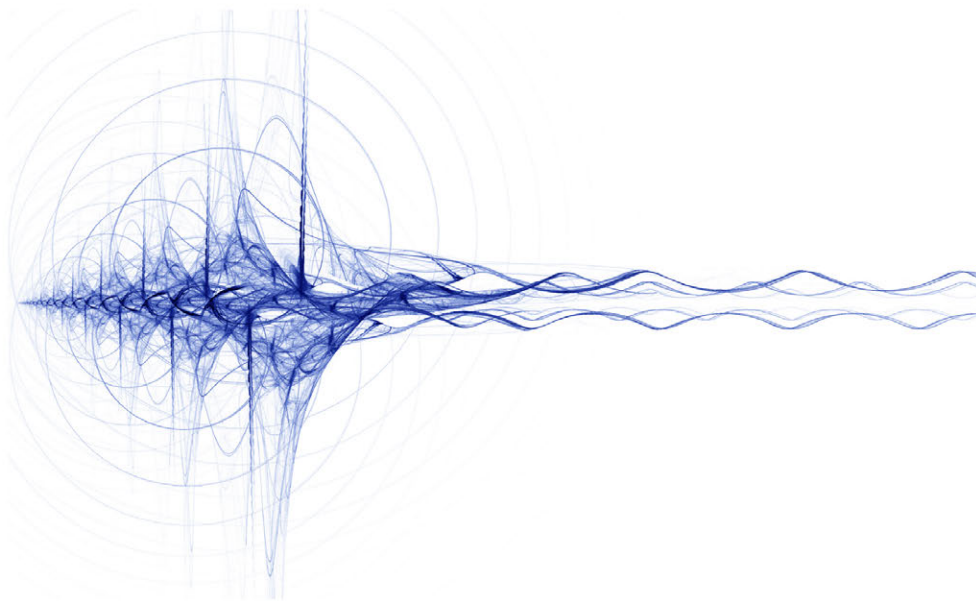


Markus Sause



**Identification of failure mechanisms  
in hybrid materials utilizing pattern  
recognition techniques applied to  
acoustic emission signals**

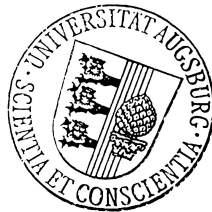


# IDENTIFICATION OF FAILURE MECHANISMS IN HYBRID MATERIALS UTILIZING PATTERN RECOGNITION TECHNIQUES APPLIED TO ACOUSTIC EMISSION SIGNALS

DISSERTATION ZUR ERLANGUNG DES DOKTORGRADES DER  
MATHEMATISCH-NATURWISSENSCHAFTLICHEN FAKULTÄT DER UNIVERSITÄT  
AUGSBURG

vorgelegt von  
Markus Sause

DEZEMBER 2010



UNIVERSITÄT AUGSBURG  
INSTITUT FÜR PHYSIK  
LEHRSTUHL FÜR EXPERIMENTALPHYSIK II

Erstgutachter: Prof. Dr. S. Horn  
Zweitgutachter: Prof. Dr. F. Haider  
Drittgutachter: Prof. Dr. M. Hamstad

Tag der mündlichen Prüfung: 16.12.2010

Bibliografische Information der *Deutschen Nationalbibliothek*

Die Deutsche Nationalbibliothek verzeichnet diese Publikation in der Deutschen Nationalbibliografie; detaillierte bibliografische Daten sind im Internet über <<http://dnb.ddb.de>> abrufbar.

ISBN: 978-3-86664-889-0

**Zugl.: Augsburg, Univ., Diss., 2010**

Dissertation, Universität Augsburg

Dieses Werk ist urheberrechtlich geschützt.

Alle Rechte, auch die der Übersetzung, des Nachdruckes und der Vervielfältigung des Buches, oder Teilen daraus, vorbehalten. Kein Teil des Werkes darf ohne schriftliche Genehmigung des Verlages in irgendeiner Form reproduziert oder unter Verwendung elektronischer Systeme verarbeitet, vervielfältigt oder verbreitet werden.

Die Wiedergabe von Gebrauchsnamen, Warenbezeichnungen, usw. in diesem Werk berechtigt auch ohne besondere Kennzeichnung nicht zu der Annahme, dass solche Namen im Sinne der Warenzeichen- und Markenschutz-Gesetzgebung als frei zu betrachten wären und daher von jedermann benutzt werden dürfen.

This document is protected by copyright law.

No part of this document may be reproduced in any form by any means without prior written authorization of the publisher.

Coverbild © Yurok Aleksandrovich - Fotolia.com

Alle Rechte vorbehalten | all rights reserved

© Mensch und Buch Verlag 2010

Choriner Str. 85 - 10119 Berlin

[verlag@menschundbuch.de](mailto:verlag@menschundbuch.de) – [www.menschundbuch.de](http://www.menschundbuch.de)



# Contents

<b>1. Introduction and Motivation</b>	<b>7</b>
<b>2. Theoretical background and developments</b>	<b>10</b>
2.1. Mechanical failure of materials . . . . .	10
2.1.1. Fracture mechanics . . . . .	10
2.1.2. Fiber reinforced plastics . . . . .	12
2.1.3. Metallic coatings . . . . .	18
2.2. Acoustic emission . . . . .	21
2.2.1. Elastic waves . . . . .	21
2.2.2. Acoustic emission sources . . . . .	24
2.2.3. Guided waves . . . . .	29
2.2.4. Attenuation . . . . .	36
2.2.5. Signal detection . . . . .	39
2.3. Signal analysis . . . . .	42
2.3.1. Prerequisites for acoustic emission interpretation . . . .	43
2.3.2. Acoustic emission features and source localization . . . .	46
2.3.3. Pattern recognition techniques . . . . .	54
2.4. Time-frequency analysis . . . . .	79
<b>3. Simulation of acoustic emission signals</b>	<b>89</b>
3.1. Model of acoustic emission source . . . . .	89
3.2. Modeling signal propagation . . . . .	100
3.2.1. Mesh resolution . . . . .	100
3.2.2. Time resolution . . . . .	104
3.3. Model of broadband sensor and signal detection . . . . .	108
3.3.1. Reciprocity calibration . . . . .	108
3.3.2. Pencil lead fracture tests . . . . .	114
3.3.3. Optimization of the sensor model performance . . . . .	116
3.4. Variation of source parameters . . . . .	120
3.4.1. Source mechanism . . . . .	121
3.4.2. Source excitation time . . . . .	130
3.4.3. Source energy . . . . .	131
3.4.4. Source position . . . . .	138

3.5. Influence of specimen geometry . . . . .	143
<b>4. Experimental results</b>	<b>148</b>
4.1. Experimental setups . . . . .	148
4.1.1. Description of specimen series . . . . .	149
4.1.2. Mechanical testing and acoustic emission acquisition . .	153
4.1.3. Microscopical investigation . . . . .	159
4.2. Variation of CFRP stacking sequence of flexural testing specimens	159
4.2.1. Loading parallel to fiber axis: Layup-0 specimens . . . .	161
4.2.2. Loading perpendicular to fiber axis: Layup-90 specimen	173
4.2.3. Loading in varied stacking sequence: Layup-0/90 specimens	176
4.3. Variation of specimen geometry and loading condition . . . . .	185
4.3.1. DCB testing of T800/913 specimens . . . . .	185
4.3.2. Tensile testing of T800/913 specimens . . . . .	193
4.4. Variation of curing degree of flexural testing specimens . . . . .	201
4.4.1. Discussion of mechanical properties and microscopic ob- servations . . . . .	202
4.4.2. Interpretation of acoustic emission results . . . . .	203
4.5. Application of pattern recognition method to T-Pull specimens	214
4.5.1. Discussion of microscopic observations . . . . .	214
4.5.2. Interpretation of acoustic emission results . . . . .	215
4.6. Application of pattern recognition method to coatings on CFRP substrates . . . . .	221
4.6.1. Microscopic investigation . . . . .	222
4.6.2. Pattern recognition approach . . . . .	225
4.6.3. Comparison with fracture mechanics . . . . .	231
4.6.4. Discussion of different coating types . . . . .	239
<b>5. Summary and Discussion</b>	<b>243</b>
5.1. Finite element simulation . . . . .	243
5.2. Pattern recognition . . . . .	247
5.3. Material Analysis . . . . .	251
<b>6. Outlook</b>	<b>254</b>
<b>A. AWARE++ User's manual</b>	<b>256</b>
<b>B. Deriving elastic coefficients from micromechanical properties</b>	<b>273</b>
B.1. Unidirectional lamina . . . . .	274
B.2. Woven fabric lamina . . . . .	277
<b>C. Finite element simulations of acoustic emission signals</b>	<b>280</b>

## *Contents*

<b>Definitions and parameter conventions</b>	<b>282</b>
<b>References</b>	<b>285</b>
<b>Acknowledgments</b>	<b>304</b>
<b>Curriculum Vitae</b>	<b>306</b>



# 1. Introduction and Motivation

Since the beginning of craftsmanship audible phenomena resulting from excitation of elastic waves are well known. These phenomena include the sound of timber fracture, rock-bursts, creaking of tin during plastic deformation and martensite transformation. In 1933 the first known scientific experiments on recording of acoustic emission signals were conducted by F. Kishinoue during tensile loading of a wood specimen. In addition to the expected audible sounds he detected many inaudible signals in the ultrasonic frequency range. This phenomenon was later entitled acoustic emission by B. H. Schofield during a reexamination of J. Kaiser's famous dissertation published in 1950. This in turn is often been quoted as start of acoustic emission science [1].

Development of modern acoustic emission analysis is closely related to the development of fast recording equipment and storage capabilities necessary for the excessive amount of data acquired during measurements. In order to resolve the acoustic emission signals within the frequency range between 20 kHz and 1 MHz a sampling rate of 2 MHz and 40 MHz is typically employed. Since the 1980s electronic equipment became available that allowed the storage of parameters derived from the detected acoustic emission signals. This important concept of "feature" extraction is still a powerful tool for the interpretation of acoustic emission data, but can lead to misinterpretations of the detected signals. Many early studies of acoustic emission analysis focused on interpretation of feature distributions or energy correlations to understand failure of engineering materials. With respect to certain types of materials and certain types of failure this approach is still valid but also can result in misleading conclusions, e. g. in the presence of noise signals. This is especially true in the field of composite materials, which typically show a vast amount of acoustic emission signals that could not be handled well in the beginning. With the development of even faster computers at the start of the 21<sup>st</sup> century it became possible to detect and capture large numbers of acoustic emission signals. Now it was possible to interpret the frequency and time-frequency distribution of the signals, which opens a completely new field of acoustic emission analysis. Finally this enabled the application of computationally complex algorithms like pattern recognition techniques.

## 1. Introduction and Motivation

One of the traditional fields of acoustic emission techniques is the monitoring of large engineered structures like dome-roofs or bridges. With large sensor arrays it is possible to monitor these constructions for damage progress and to localize the region of occurrence. This localization is based on the differences between the arrival times of the signal detected at each sensor. Another scientific application for acoustic emission analysis is the monitoring of materials under mechanical loading in order to improve the understanding of material failure. While acoustic emission resulting from mechanical failure of metallic or ceramic engineering materials is already well understood, the interpretation of failure of composite materials is still an emerging scientific field for acoustic emission analysis.

Especially in carbon fiber reinforced plastics (CFRP) several microscopic types of failure exist, that lead to complex macroscopic failure. The significance of the various failure mechanisms for the composites integrity depends on the type of application and the type of loading. In order to understand the respective contribution of these failure mechanisms to the ultimate failure of the composite it is thus necessary to record their evolution as a function of loading. Since each of the failure mechanisms is accompanied by a respective excitation of an elastic wave, acoustic emission analysis is a powerful tool for such an investigation.

The number of microscopic failure types increases further when fiber reinforced structures are combined with other materials like metals or ceramics to form functional hybrid materials. One typical application in this context is the application of a metallic coating on CFRP in order to decrease gas permeability. The characterization of adhesive strength and maximum allowable strain during mechanical loading of such metallic coatings is of great importance to optimize the method of coating application and to predict gas tightness of these coatings under real environmental conditions. The monitoring with acoustic emission analysis is a suitable method to detect the formation of cracks within the coating and delamination between coating and CFRP in dependence of loading.

Various authors have already reported on correlations between certain failure mechanisms and the characteristics of acoustic emission signals. In general these investigations are based on direct comparisons with microscopic imaging techniques or specimens series with growing complexity to induce one failure type after another. In the case of CFRP failure, several studies recently proposed to distinguish acoustic emission signals of fiber breakage and matrix cracking based on significant contributions at high frequencies (fiber breakage) or low frequencies (matrix cracking) [2–8]. For coating failure on metallic substrates various authors demonstrated that the respective acoustic emission

## 1. Introduction and Motivation

signals can be interpreted and correlated with delamination of the coating or crack formation using characteristics in wave-mode analysis and AE activity analysis [9–12]. In contrast, no reports were found on investigation of metallic coatings on CFRP substrates.

The identification of characteristics in acoustic emission signals and their classification according to similarity is a typical application for pattern recognition techniques. In general the characteristics of a recorded acoustic emission signal are not only a result of the excitation process, but also of the propagation within the material and the detection process by a respective sensor. Therefore the correlation of acoustic emission signals with failure mechanisms is a challenging task and was closely examined within the present thesis by combination of experimental techniques and finite element simulations.

Within the scope of the project “Mehrstufige Verfahren zur Herstellung von CFK-Integralstrukturen”<sup>1</sup> and in collaboration with the University of Applied Science Munich the failure process of CFRP under various loading conditions was investigated in order to develop a method to classify acoustic emission signals from CFRP failure. A new approach for pattern recognition and signal interpretation of experimental signals is introduced and is compared to the results from multi-scale finite element simulations.

Chapter 2 gives an introduction to the theoretical concepts of acoustic emission science and presents the newly introduced pattern recognition approach and signal analysis techniques. In the subsequent chapter 3 the results of finite element simulations for various experimental setups are presented and compared to results of analytical solutions. Chapter 4 presents the experimental results obtained from pattern recognition techniques applied to acoustic emission from CFRP failure and coating failure on CFRP substrates. The discussion of the presented methods and results including experiment and simulation is found in chapter 5. The final chapter 6 gives a short outlook for future investigations. Typographical conventions for symbols and abbreviations used within this thesis are summarized on pages 282–285.

---

<sup>1</sup> funded by the Bavarian Government for economy, infrastructure, traffic and technology within the research program “Neue Werkstoffe in Bayern”

## 2. Theoretical background and developments

In the following chapter theoretical concepts necessary for the understanding of acoustic emission signals occurring during material failure are presented. In addition several new approaches for signal interpretation and pattern recognition are introduced. Section 2.1 is focusing on fundamentals of mechanical failure of fiber reinforced materials and metallic coatings. Subsequently, section 2.2 is focusing on the theory of elastic waves and acoustic emission excitation during failure, guided wave propagation and the elastic wave detection process. The last section 2.3 deals with interpretation of acoustic emission signals with a main focus on pattern recognition techniques and time-frequency analysis. Generally the Einstein notation was used for index summation throughout this thesis if suitable for visualization (see page 285).

### 2.1. Mechanical failure of materials

#### 2.1.1. Fracture mechanics

The failure of a material arising from mechanical loading is described by the theory of fracture mechanics. The basic result of such failure is the formation of a crack, which is a separation within a solid due to excessive external forces which overcome the strength of atomic or intermolecular bonds. Generally, flaws are always existent within materials and fracture mechanics deals with the conditions under which flaws turn into cracks and result in material failure. As shown in figure 2.1, three different basic crack separation modes exist. These are the opening mode (mode I), the sliding mode (mode II) and the tearing mode (mode III).

In general the propagation of a crack within a material can be described by a thermodynamic approach established by A. Griffith in 1920 to describe the energetic conditions for crack propagation. He introduced the concept of the *strain energy release rate*  $G$ :

$$G = -\frac{d\Omega}{dA} \quad (2.1)$$



## 2. Theoretical background and developments

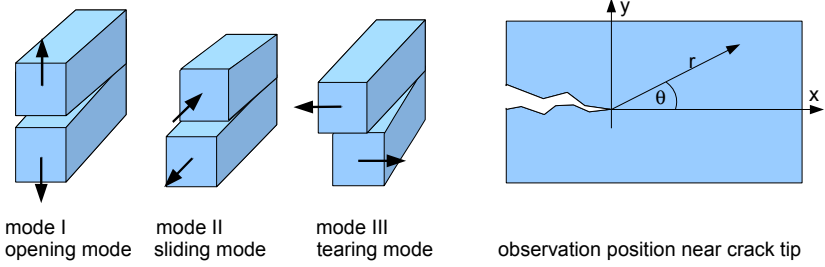


Figure 2.1.: Basic crack separation modes and coordinate system for observation position of crack tip according to [13].

This constant  $G$  is expected to be a fundamental physical quantity, which describes the amount of energy  $\Omega$  needed to extend a crack by a certain area  $A$ . In the original approach A. Griffith assumed that  $G$  equals two times the free surface energy  $\Omega_{surface}$  [14], which is only valid for very brittle materials. In general, a plastic deformation zone develops around the crack tip, which increases in size with the applied loading until the crack propagates. The formation and propagation of this plastic zone results in energy dissipation in the form of heat. To this end, A. Griffith's energy approach was modified by G. Irwin who separated  $G$  into a contribution for the formation of new surfaces and an additional contribution for energy dissipation from plastic deformation [15]:

$$G = 2\Omega_{surface} + G_{plastic} \quad (2.2)$$

The energy criterion that relates the fracture strength  $\sigma_{frac}$  of a flaw with length  $a$  in a material with Young's modulus  $E$  can then be formulated introducing the *fracture-toughness*  $G_c$  as:

$$\sigma_{frac} = \sqrt{\frac{EG_c}{\pi a}} \quad (2.3)$$

G. Irwin noticed that equation (2.3) is only applicable if the size of the plastic zone around the crack tip is small compared to the crack size and the geometry of the solid. Thus the fracture energy will not critically depend on the stress-field at the crack tip and a linear elastic approach is sufficient to describe the crack propagation. In this case equation (2.1) can be simplified in the cases with zero stress  $\sigma_z$  (plane stress) or zero strain  $\varepsilon_z$  (plane strain) in one axis

## 2. Theoretical background and developments

direction as boundary conditions.

$$G = - \left[ \frac{\partial \Omega}{\partial A} \right]_{\sigma_z=0} = - \left[ \frac{\partial \Omega}{\partial A} \right]_{\varepsilon_z=0} \quad (2.4)$$

Usually the fracture toughness  $G_c$  is used for polymer based materials. For ceramics and metals typically another quantity, namely the *critical stress-intensity factor*  $K_c$  as introduced by G. Irwin is used. In the case of mode I cracks the correlation between  $G_{Ic}$  and  $K_{Ic}$  for plane stress and plane strain conditions for a material with Young's modulus  $E$  and Poisson number  $\nu$  is defined as:

$$G_{Ic} = \begin{cases} \frac{K_{Ic}^2}{E} & \text{plane stress} \\ \frac{(1-\nu^2)K_{Ic}^2}{E} & \text{plane strain} \end{cases} \quad (2.5)$$

For the other crack separation modes similar equations exist [15]. In general, the quantity  $K$  characterizes the stress-tensor  $\sigma_{ik}$  for a linear elastic solid at observation position  $r$  and  $\theta$  in the vicinity of a crack tip as shown in figure 2.1 using the function  $Y_{ik}(\theta)$  dependent on the geometry:

$$\sigma_{ik} \approx \left( \frac{K}{\sqrt{2\pi r}} \right) Y_{ik}(\theta) \quad (2.6)$$

Since not all materials show a plastic deformation zone, which is negligible in its size or remains constant in size during loading, several new concepts were introduced to describe the stress-field around the crack tip. A review about these concepts, namely the R-curve method and the J-Integral concept is found in standard literature and is not discussed in the following [16,17].

The quantities  $G_c$  and  $K_c$  can thus both be used to describe the ability of a material containing flaws to withstand fracture and are thus material specific physical properties. For brittle materials  $G_c$  typically is dominated by the surface energy term in equation (2.2), resulting in low values. Ductile materials like metals show strong dissipative contributions and thus yield high values for  $G_c$ . Polymers instead show a wide range of intermediate values dependent on their temperature relative to their glass transition temperature.

### 2.1.2. Fiber reinforced plastics

Typically, polymers are superior to metals in terms of corrosion and their volumetric weight, but exhibit lower mechanical capacity. This makes them

## 2. Theoretical background and developments

perfect materials for certain applications, but limits their usage in other fields which require high mechanical strengths. In contrast, glass or carbon fibers exhibit high mechanical strength in tensile direction, but are very sensitive to bending and compressive loads.

The concept of fiber reinforcement of plastics is thus based on the idea of combining the advantages of both material types to form a composite. In the case of fiber reinforced plastics the functionality of the fibers is the improvement of mechanical strength of the surrounding plastic. The reinforced plastic material itself is usually called *matrix*, since it is enclosing the fibers and keeps them together. With a typical fiber-volume fraction of  $\phi = 60\%$  the fiber is the dominating part of the composite [18, 19]. As an extraordinary advantage such fiber reinforced plastics show a superior strength-to-weight and stiffness-to-weight ratio which makes them unique within the field of engineering materials. As a true disadvantage the combination of these two materials induces complex failure behavior with respect to the type of loading.

Within this thesis only a short review of failure in fiber reinforced plastics is given. Since the investigated specimens were composed of long fiber reinforced epoxy resins the section will focus on the failure mechanisms occurring in these type of materials. Especially the case of short-fiber reinforced materials is not discussed in the following. Instead, for a detailed review of mechanical failure and fracture mechanics of fiber reinforced materials the reader is referred to standard literature [18–20]. Long fiber reinforced plastics are typically provided in unidirectional rovings or as woven fabric. In both cases the plies are usually arranged in dedicated stacking sequences with different angle directions of the fiber axes in each ply. The different stacking sequences used within this thesis are given in the form<sup>1</sup> as discussed by H. Schürmann following the international conventions [18]. The different stacking sequences cause highly anisotropic elastic properties and are used to build composite structures optimized for the type of application. Since these are typically plate-like structures, a distinction is made between the *in-plane* direction and the *out-of-plane* direction, which refers to the direction perpendicular to the fiber axes and normal to the plate surface.

During mechanical loading of fiber reinforced plastics various microscopic failure mechanisms occur. The accumulated damages finally result in failure of the composite. In principle, failure within the material can occur in the matrix, the fiber or at the interface between both. From the fracture mechanics point of view, the situation grows more complex, since each of these failures can be induced by several types of loading and can form even more complex

---

<sup>1</sup> The layup given by  $[0/90_3]_{sym}$  refers to a full stacking sequence of  $[0^\circ, 90^\circ, 90^\circ, 90^\circ, 90^\circ, 90^\circ, 90^\circ, 0^\circ]$  with  $0^\circ$  and  $90^\circ$  axes orientations of the fibers

## 2. Theoretical background and developments

mechanisms on the macroscopic scale. In the following a short review is given on the different microscopic failure mechanisms, their origin and how the respective denotations are understood in the discussions within this thesis.

The most drastic type of failure within fiber reinforced plastics is fiber failure. For unidirectional tensile loading parallel to the fibers axis  $+\sigma_{||}$  fiber breakage is observed if the ultimate strength of the fiber  $\sigma_f$  is exceeded. As mentioned above the strength of the fiber  $\sigma_f$  generally is significantly higher than the matrix strength  $\sigma_m$ . As a consequence the fracture of a single fiber is accompanied by fracture of the surrounding matrix as well. This type of failure is schematically shown in figure 2.2 and denoted *fiber breakage* in the following. For comparison a respective scanning electron microscopy image of fiber breakage caused by tensile loading is shown as well. As elucidated by H. Schürmann the macroscopically measured unidirectional stress level is generally lower than the microscopic stress level of the fiber, since the macroscopic mechanical properties follow the rule of mixture [18].

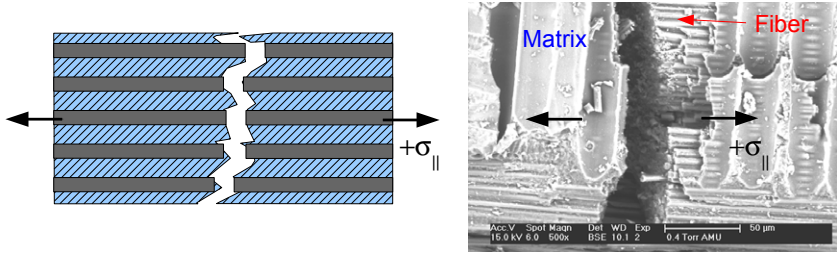


Figure 2.2.: Schematic illustration of tensile fiber breakage (according to [18]) and corresponding electron microscopy image in surface view.

While macroscopic bending loads usually result in microscopic tensile loading of the fibers at the composites elongated side, certain macroscopic load configurations can result in compressive failure of fibers. As schematically shown in figure 2.3 such compressive stress  $-\sigma_{||}$  typically results in shear buckling of the carbon fibers if their compressive strength is exceeded, but is seldom observed. For comparison a respective scanning electron microscopy image of compressive fiber failure is shown in figure 2.3. As indicated in the schematic illustration, this type of failure naturally results in vast fiber fragmentation.

The most often observed type of failure in fiber reinforced structures is *inter-fiber fracture*. As schematically shown in figure 2.4 this can result from several loading conditions. In all conditions fracture is induced within the matrix or along the interface between fiber and matrix. This type of failure is observed,

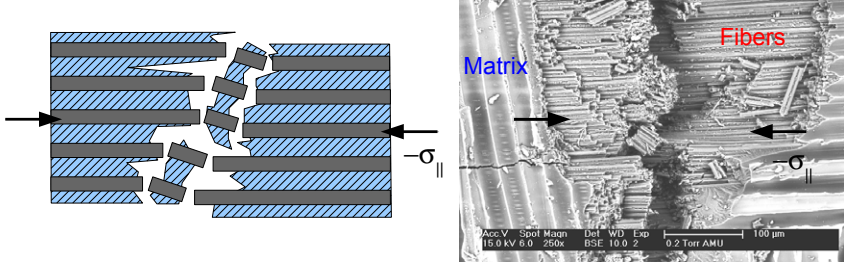


Figure 2.3.: Schematic illustration of compressive fiber failure (according to [18]) and corresponding electron microscopy image in surface view.

if the respective loading condition of normal stresses ( $\pm\sigma_{\perp}$ ) or shear stresses ( $\tau_{\perp||}$  and  $\tau_{\perp\perp}$ ) exceeds the local strength of the matrix  $\sigma_m$  or interface  $\sigma_{fm}$ . Several modern engineering theories deal with the correlation of macroscopic loading conditions to the resulting microscopic loading conditions [20–23]. Most remarkable, under certain circumstances the macroscopic stress level can even drop below the properties of the pure matrix material, since microscopic stress raisers can result in local stress step-up.

As schematically shown in figure 2.5 a typical cause for macroscopic in-plane failure is the existence of inter-fiber cracks in adjacent layers of the composite which can result in large inter-ply *delamination*. To this end, a low interfacial strength  $\sigma_{fm}$  can also dominate the inter-fiber fracture processes shown in figure 2.4. For this case the respective failure is denominated *fiber-matrix debonding* in the following. Another result of interfacial failure is the process of *fiber pullout*. This type of failure typically occurs before fiber breakage, if  $\sigma_{fm}$  is low enough to allow the fiber to slip out of the matrix.

Another process of macroscopic failure, the phenomena of *fiber-bridging* can occur as schematically shown in figure 2.6. In this stage a macroscopic crack propagates orthogonal to the fiber axis. While the matrix material fails since  $+\sigma_{||} > \sigma_m$ , the fibers are pulled out of the matrix if  $+\sigma_{||} > \sigma_{fm\perp}$  and  $+\sigma_{||} < \sigma_f$ . In this case the crack progress is constrained, since the fibers still bear the applied load. This is also visible in the scanning electron microscopy image in figure 2.6. While the layers of carbon fibers close to the surface failed due to  $+\sigma_{||}$ , the inner layers can still act as load bearing elements and stop the crack propagation.

Due to these large number of microscopic failure mechanisms, the definition of macroscopic failure of composite usually is subject to the type of application. Although inter-fiber fracture does not cause ultimate failure of the composite

## 2. Theoretical background and developments

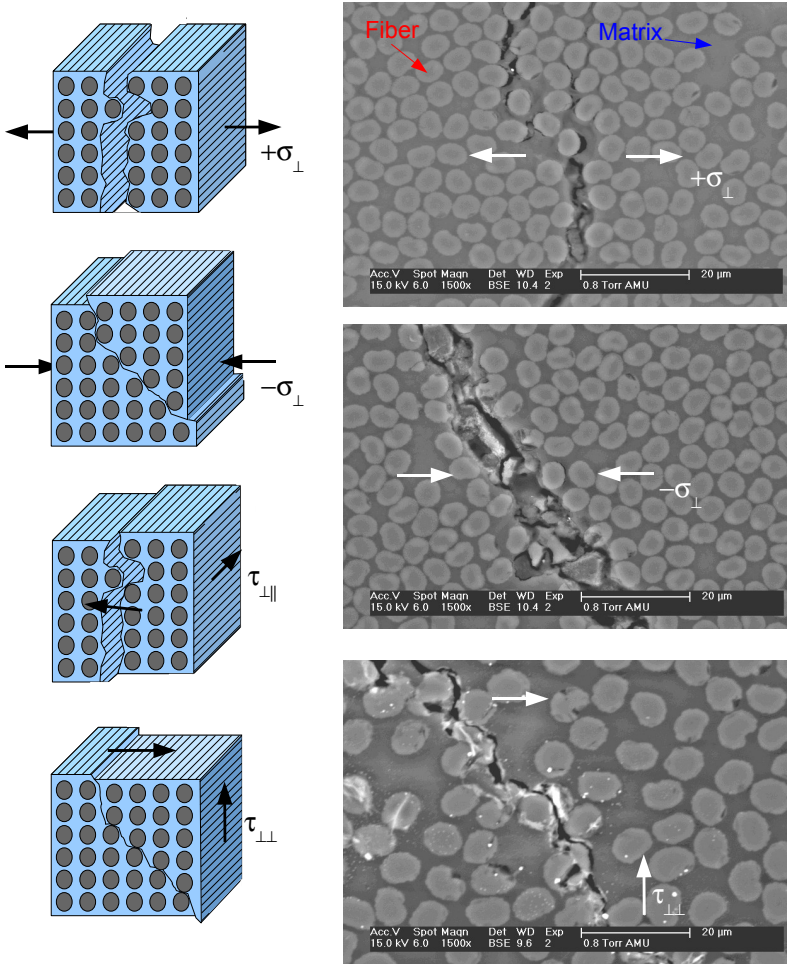


Figure 2.4.: Schematic illustration of inter fiber fracture (according to [18]) and corresponding electron microscopy cross-section images.

## 2. Theoretical background and developments

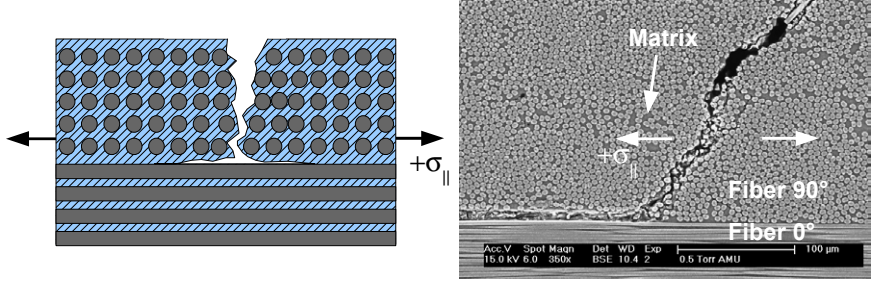


Figure 2.5.: Schematic illustration of inter-ply delamination (according to [18]) with corresponding electron microscopy images in cross-section view.

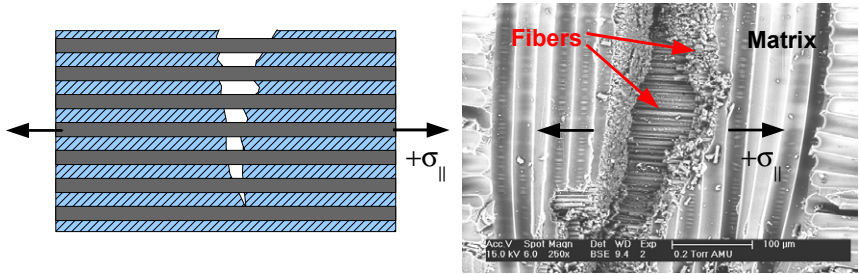


Figure 2.6.: Schematic illustration of fiber bridging (according to [18]) together with corresponding electron microscopy images in surface view.

and may be acceptable in some applications it can still alter the mechanical properties, e. g. the stiffness of the structure. In addition such failure can change the surface properties of the composite or can raise secondary damage from aggressive media penetrating the structure. Even fiber breakage does not necessarily result in ultimate failure. On the microscopic scale fibers show a broad distribution in their ultimate strength  $\sigma_f$  due to variations of the fiber diameter and internal flaws [18,24]. This can result in early failure of numerous fibers, while the remaining fibers still act as load bearing elements. In addition, most of the fiber reinforced composites are engineered with stacking sequences of differently oriented layers. Thus the global structure can often compensate the failure of one layer and thus exhibit damage tolerant behavior.

### 2.1.3. Metallic coatings

Typically the purpose of a coating is to improve the disadvantageous surface properties of a substrate by a functional surface layer with superior properties. In the case of fiber reinforced plastics the surface lacks typical metallic properties like wear resistance, high electrical conductivity or gas impermeability. The application of a metal coating can improve the properties of fiber reinforced plastics in this respect. If the coated material is subject to mechanical loading, failures like coating fracture and delamination between coating and substrate can cause disfunctionality of the coating. The following section will focus on the basics of mechanical failure of electroplated metallic coatings on CFRP, since these were investigated within this thesis. A more detailed review on adhesive failure of arbitrary coating/substrate systems is found in [25].

In the case of metallic coatings with thickness ranging from  $10\text{ }\mu\text{m}$  to  $100\text{ }\mu\text{m}$  the formation of cracks can happen either within the coating or at the interface between coating and substrate. These different failure types are schematically shown in figure 2.7 in comparison with their typical appearance in scanning electron microscopy. Fundamentally, the characterization of such coatings can thus be separated in the determination of the mode-I fracture-toughness of the coating and the mode-I/II fracture toughness of the interface, respectively.

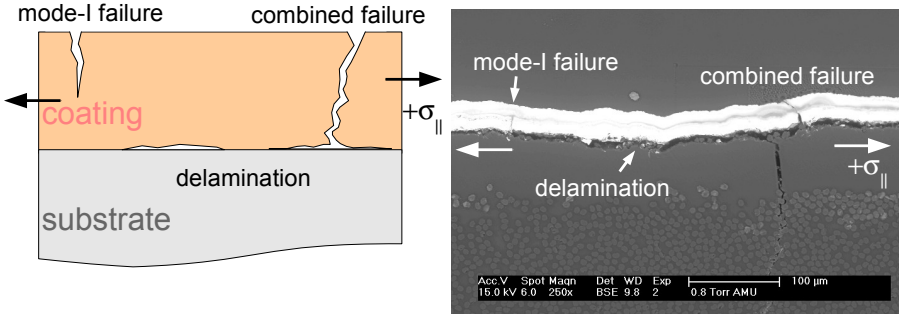


Figure 2.7.: Schematic illustration of coating cracking and delamination together with corresponding electron microscopy cross-section image.

In order to determine the critical stress-intensity factor  $K_{Ic}$  for mode-I loading various geometries are suggested in literature [26–28]. For the geometry shown in figure 2.8 with thickness  $z_{ct}$  between  $10\text{ }\mu\text{m}$  and  $50\text{ }\mu\text{m}$ , width  $2x_{ct}$  and initial crack length  $a$ , plane stress conditions can be assumed. If the coating is subject to tensile loading, the crack will start to propagate if the strain energy is sufficiently high, which is reflected by the onset of deviation from



## 2. Theoretical background and developments

linear elastic behavior as shown in the load-displacement curve in figure 2.8. According to [16] the value for  $K_{Ic}$  can then be obtained from the critical load  $F_c$  defined by a 5%-secant with reference to the linear elastic extrapolation.

$$K_{Ic} = 1.12 \frac{F_c}{z_{ct} \sqrt{2x_{ct}}} \sqrt{\frac{\pi a}{2}} \cdot Y \left( \frac{a}{2x_{ct}} \right) \quad (2.7)$$

For the specimen dimensions shown in figure 2.8 the geometric correction function  $Y \left( \frac{a}{2x_{ct}} \right)$  is defined according to [13] as:

$$Y \left( \frac{a}{2x_{ct}} \right) = \frac{1 - 0.25ax_{ct} + 0.0815(ax_{ct})^2}{\sqrt{1 - \frac{ax_{ct}}{2}}} \quad (2.8)$$

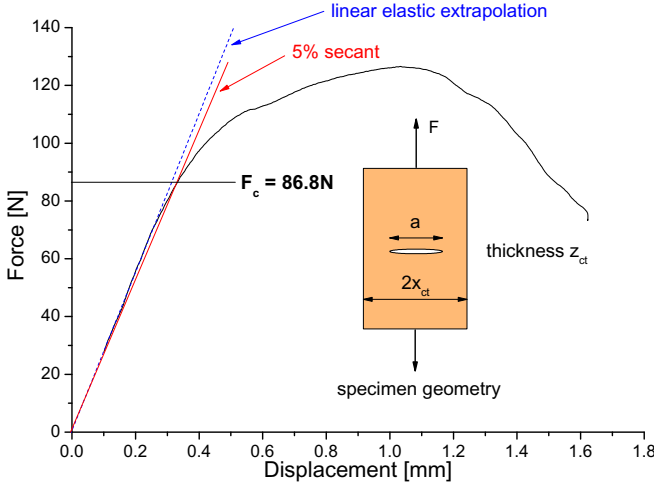


Figure 2.8.: Coating geometry for measurement of fracture toughness and typical load-displacement curve with 5%-secant defining the critical load  $F_c$ .

The value of the interfacial fracture toughness is usually determined via pull-off tests or peel-tests, like e.g. defined in ASTM B533-85 [29]. In such peeling tests the fracture toughness is calculated from the measurement of the mechanical energy during stable crack propagation. Often this reflects not pure mode-I loading conditions, but rather a mixture of mode-I and mode-II.

## 2. Theoretical background and developments

Thus the interfacial fracture toughness  $G_{I/II}$  for stable crack propagation in x-direction is given as:

$$G_{I/II} = -\frac{\partial}{\partial A} (Fdx) \quad (2.9)$$

This direct correlation of recorded force  $F$  and machine displacement  $x$  with the interfacial fracture toughness is only acceptable, if the influence of other dissipative mechanisms is negligible. As stated in [30] there are two dissipative mechanisms contributing to the measured force, which have to be taken into account. If a coating is peeled off a substrate as shown in figure 2.9 the recorded force is only representative for the interfacial fracture toughness of adhesive failure if the contributions from the plastic deformation zone and reverse plastic bending are negligible. For the investigated coating thickness this assumption is fulfilled, if the interfacial tensile adhesion is much smaller than the yield strength of the coating material [30].

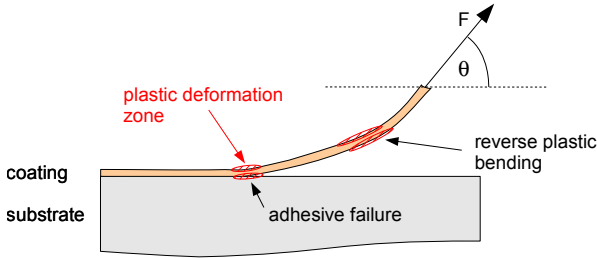


Figure 2.9.: Scheme of coating peeling process adopted from reference [30].

If the coating consists of multiple layers, interfacial failure can also take place at the interface between the respective layers. In this case mode-I crack propagation can also occur independently or correlated in each layer. In general, the formation of cracks as shown in figure 2.7 can result from different crack separation modes, not only mode-I. This makes the calculation of the fracture toughness in arbitrary shaped substrates very difficult. In addition the presence of residual stresses present after coating application can decrease the load limit of the coating-substrate system dramatically [31] and gives rise to the application of new techniques to determine the onset of failure in such complex systems.

## 2.2. Acoustic emission

In this section, the process of excitation, propagation and detection of acoustic emission signals is presented. The description starts with the fundamental theoretical bases of elastic waves in subsection 2.2.1 introducing the generalized formulation of Hooke's law. In the subsequent section 2.2.2 the current analytical theories describing the excitation process of elastic waves from acoustic emission sources are reviewed. In the section 2.2.3 the consequences of elastic wave propagation in guiding media is discussed with a focus on the propagation of Lamb waves, since these were observed in the experimentally used specimens. In addition, the propagation of elastic waves is subject to attenuation effects, whose influences are introduced in section 2.2.4. Finally, the theoretical basis of the acoustic emission signal detection with the experimentally used piezoelectric sensors is presented in section 2.2.5.

### 2.2.1. Elastic waves

B. Auld defines acoustics as “*study of time-varying deformations, or vibrations in material media*” [32]. This vibrational motion of atoms about their equilibrium positions is not only treated by acoustics but also by thermodynamics. The main distinction between these two fields is the scale of observation. While thermodynamics deals with atomistic vibration, the intention of acoustics is to describe the motion of small units consisting of many atoms. To this end acoustics theory is formulated as if solids are a continuum. Consequently, atomistic effects are completely neglected besides their influence on the macroscopic properties of the solid.

Acoustic emission signals are small elastic waves originating from microscopic deformations of a solid. In general acoustic emission sources are all sorts of rapid microscopic displacements arising e. g. from structural phase transitions, generation of surface areas but also friction inside the solid and at its surface. The frequency range of acoustic waves detectable by humans, the so-called audible range, is between 20 Hz and 20 kHz. In analogy to the electromagnetic spectra the frequency range below is denominated infrasonic and the frequency range above as ultrasonic. In the case of acoustic emission signals originating from crack growth, elastic waves with frequencies in the lower ultrasonic range are emitted (see section 2.2.2). Thus the name “acoustic emission” may even be misleading in this context since the major occurrence of signals is in the inaudible range. Consequently, the phenomenon is often also entitled “structure born ultrasound”.

According to L. Landau and E. Lifschitz the deformation of a solid causes heat to be generated at the deformation zone which fluctuates in time and

## 2. Theoretical background and developments

space. This makes an exact solution of the equations of motion very difficult. But if the spatial heat propagation is slower than the oscillatory movements within the solid, the deformations can be assumed to be adiabatic [33]. For this case, the theory of elastic waves describes the propagation of deformations within the solid for small initial deformations. This yields the basic theoretical formulation for the understanding of acoustic emission given by the theory of elastic waves, which in general requires solving the momentum balance equation in the case of negligible Lagrangian inertia:

$$\rho \frac{\partial^2 u_i}{\partial t^2} = \frac{\partial \sigma_{ik}}{\partial r_k}. \quad (2.10)$$

Here  $\rho$  is the material density,  $u$  is the displacement and  $\sigma_{ik}$  is the stress-tensor derived from the generalized formulation of Hooke's law:

$$\sigma_{ik} = C_{iklm} \varepsilon_{lm}. \quad (2.11)$$

This equation, also known as constitutive relation couples the stress-tensor  $\sigma_{ik}$  with the deformation tensor  $\varepsilon_{lm}$  using the elasticity-tensor  $C_{iklm}$  in the case of small elastic deformations in a homogeneous medium. In general  $C_{iklm}$  is a 4<sup>th</sup> order tensor with 81 elastic coefficients. Since the deformation tensor  $\varepsilon_{lm}$  is symmetric, the elasticity-tensor  $C_{iklm}$  exhibits the same symmetry constraints regarding index permutation:

$$C_{iklm} = C_{kilm} = C_{ikml} = C_{lmik} \quad (2.12)$$

This reduces the number of independent coefficients for a solid material to 21 [33]. The occurrence of symmetries within the solid reduces the number of independent coefficients further. In the case of orthotropic materials like unidirectional CFRP lamina, utilizing the Voigt notation the elasticity tensor  $C_{iklm}$  can be reduced to a 6 x 6 matrix with 9 independent elasticity coefficients. Similar, the stress-tensor  $\sigma_{ik}$  can be reduced to a vector  $\vec{\sigma}$  with six independent components composed of normal stresses  $\sigma_{ii}$  and shear stresses  $\tau_{ik}$ . The deformation-tensor  $\varepsilon_{lm}$  is represented by a vector  $\vec{\varepsilon}$  with six independent components consisting of normal components  $\varepsilon_{ll}$  and shear strain components  $\gamma_{lm}$ , respectively.

$$\begin{pmatrix} \sigma_{xx} \\ \sigma_{yy} \\ \sigma_{zz} \\ \tau_{yz} \\ \tau_{xz} \\ \tau_{xy} \end{pmatrix} = \begin{pmatrix} C_{xxxx} & C_{xxyy} & C_{xxzz} & 0 & 0 & 0 \\ C_{xxyy} & C_{yyyy} & C_{yyzz} & 0 & 0 & 0 \\ C_{xxzz} & C_{yyzz} & C_{zzzz} & 0 & 0 & 0 \\ 0 & 0 & 0 & C_{yzyz} & 0 & 0 \\ 0 & 0 & 0 & 0 & C_{xzzx} & 0 \\ 0 & 0 & 0 & 0 & 0 & C_{xyxy} \end{pmatrix} \cdot \begin{pmatrix} \varepsilon_{xx} \\ \varepsilon_{yy} \\ \varepsilon_{zz} \\ \gamma_{yz} \\ \gamma_{xz} \\ \gamma_{xy} \end{pmatrix} \quad (2.13)$$

## 2. Theoretical background and developments

If the solid is isotropic equation (2.13) is reduced to:

$$\begin{pmatrix} \sigma_{xx} \\ \sigma_{yy} \\ \sigma_{zz} \\ \tau_{yz} \\ \tau_{xz} \\ \tau_{xy} \end{pmatrix} = \begin{pmatrix} \kappa + 2\mu & \kappa & \kappa & 0 & 0 & 0 \\ \kappa & \kappa + 2\mu & \kappa & 0 & 0 & 0 \\ \kappa & \kappa & \kappa + 2\mu & 0 & 0 & 0 \\ 0 & 0 & 0 & \mu & 0 & 0 \\ 0 & 0 & 0 & 0 & \mu & 0 \\ 0 & 0 & 0 & 0 & 0 & \mu \end{pmatrix} \cdot \begin{pmatrix} \varepsilon_{xx} \\ \varepsilon_{yy} \\ \varepsilon_{zz} \\ \gamma_{yz} \\ \gamma_{xz} \\ \gamma_{xy} \end{pmatrix} \quad (2.14)$$

The remaining two independent elements  $\kappa$  and  $\mu$  are named Lamé's constants. These completely describe all elastic parameters for isotropic materials like Young's modulus  $E$ , compressive modulus  $E_C$ , shear modulus  $E_S$  and Poisson number  $\nu$ .

$$E = \mu \frac{3\kappa + 2\mu}{\kappa + \mu} \quad (2.15)$$

$$E_C = \kappa + \frac{2}{3}\mu \quad (2.16)$$

$$E_S = \frac{\kappa(1 - 2\mu)}{2\mu} \quad (2.17)$$

$$\nu = \frac{\kappa}{2(\kappa + \mu)} \quad (2.18)$$

For such isotropic materials, equation (2.10) can be simplified using the Lamé's constants to

$$\rho \frac{\partial^2 \vec{u}}{\partial t^2} = (\kappa + \mu) \nabla (\vec{\nabla} \cdot \vec{u}) + \mu \Delta \vec{u} \quad (2.19)$$

The solution of equation (2.19) can than be formulated with scalar and vector potentials as:

$$\vec{u} = \nabla \zeta + \vec{\nabla} \times \vec{\psi}. \quad (2.20)$$

This yields the two independent wave equations in solid isotropic media:

$$\Delta \zeta = \frac{1}{c_L^2} \frac{\partial^2 \zeta}{\partial t^2} \quad (2.21)$$

$$\Delta \vec{\psi} = \frac{1}{c_T^2} \frac{\partial^2 \vec{\psi}}{\partial t^2}. \quad (2.22)$$

## 2. Theoretical background and developments

Equations (2.21) and (2.22) introduce the longitudinal and transversal propagation velocities  $c_L$  and  $c_T$  for an elastic wave given as:

$$c_L = \sqrt{\frac{E(1-\nu)}{\rho(1+\nu)(1-2\nu)}} \quad (2.23)$$

$$c_T = \sqrt{\frac{E}{2\rho(1+\nu)}} \quad (2.24)$$

With respect to the boundary conditions equations (2.21) and (2.22) can be used to obtain solutions for wave-propagation in arbitrary geometries. In infinite isotropic and homogeneous media equations (2.21) and (2.22) have solutions of the form of a monochromatic plane wave with an amplitude  $u_0$ , wave number  $k$  and angular frequency  $\omega$ :

$$\vec{u}(\vec{r}, t) = u_0 \cdot e^{-i(\vec{k}\vec{r} - \omega t)} \vec{e}. \quad (2.25)$$

Here the propagation velocities  $c_L$  and  $c_T$  are identical to the respective phase velocities  $c_P$  of the plane waves. The propagation of an elastic wave in this case can thus be described by independent longitudinal wave and transversal wave propagation as shown in figure 2.10.

In general, for non monochromatic waves and anisotropic or finite media the propagation velocity of the wave is the group velocity  $c_G$  defined as:

$$c_G = \frac{\partial \omega(k)}{\partial k}. \quad (2.26)$$

Similar, the phase velocity  $c_P$  is defined by the relationship between  $k$  and  $\omega$ , which is known as dispersion-relation:

$$c_P = \frac{\omega(k)}{k}. \quad (2.27)$$

This results in dispersion if  $c_P \neq c_G$ , whose consequences are described in the following sections 2.2.3 for propagation of guided waves and in 2.2.4 for contribution to attenuation effects.

### 2.2.2. Acoustic emission sources

The excitation process of an elastic wave as a result of the crack surface movement is described by the equation of motion of the displacement vector  $\vec{u}$  in equation (2.10), as long as the deformation remains elastic, i. e. for small displacements [33]. For the present investigation the microscopic process of

## 2. Theoretical background and developments

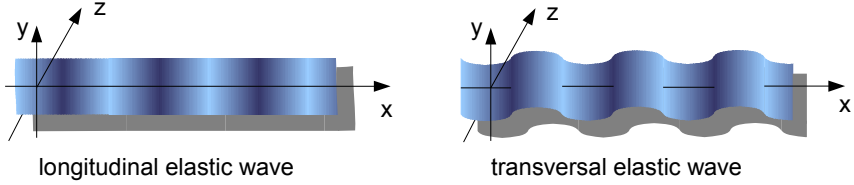


Figure 2.10.: Longitudinal and transversal elastic waves propagating in x-direction.

crack formation and crack growth is investigated and is therefore discussed in the following. The excitations of other types of acoustic emission sources can be derived accordingly.

In the case of crack growth the stress level at the newly formed surface area drops from the initial value  $\sigma_{frac}$  to zero. As a result the crack surface is deflected within a characteristic time  $T_e$  and starts to oscillate around its new energetic equilibrium state [34]. The behavior of the source can be described by the direction of the crack motion vector  $\vec{b}$  (Burgers vector) and the vector normal to the crack surface  $\vec{d}$  resulting in a total crack volume increase  $\Delta V$ . As demonstrated by K. Aki and P. Richards the characteristics of crack deflection are fully described by the moment tensor concept [35], which couples the cracks kinematic behavior with the elastic properties<sup>2</sup>:

$$M_{ik} = C_{iklm} b_l d_m \Delta V. \quad (2.28)$$

The according excitation of a small elastic wave released in the surrounding medium can then be deduced from the theory of elastic waves and results in formation of characteristic source radiation patterns as shown in figure 2.11 [36].

It is important to note that the duration for the initial deflection  $T_e$  is strictly linked to the elastic properties of the cracking material and the local loading conditions. This implies that the excited elastic wave is a characteristic fingerprint for the failure process and thus a valuable source of information that is accessible macroscopically. In general the duration for the initial deflection decreases with the brittleness of the material [37] and thus determines the oscillation frequency. Since the initial deflection time  $T_e$  typically is in the order of magnitude between  $10^{-8}$  s and  $10^{-4}$  s the frequencies of the excited

<sup>2</sup> Note that equation (2.28) only utilizes the direction of  $\vec{b}$  and  $\vec{d}$ . The source magnitude is given by  $\Delta V$ , which yields the physical unit of  $[Nm]$  for the moment tensor  $M_{ik}$ .

## 2. Theoretical background and developments

elastic waves at the crack tip are located in the ultrasonic range between 10 kHz and 100 MHz.

While the correlation of  $T_e$  to the elastic properties may seem obvious, the influence of the local loading conditions on the excited elastic wave is more complex. Since crack formation can result from all three basic loading conditions shown in figure 2.1 the oscillating displacement normal to the crack surface is strongly influenced in intensity, direction of radiation and damping behavior by the crack separation mode.

To this end, M. Ohtsu and K. Ono have examined the correlation between the response function on the surface of linear elastic solids and dislocations arising from acoustic emission sources located within [38,39]. According to the generalized theory of acoustic emission, the elastic wave amplitude observed at position  $\vec{r}$  due to a microscopic displacement  $\vec{d}(t)$  in an isotropic medium can be written as

$$u_i(\vec{r}, t) = \Gamma_{ipq}(\vec{r}, t) \otimes M_{pq}. \quad (2.29)$$

Here  $\otimes$  denotes the convolution integral between the Green function  $\Gamma_{ipq}(\vec{r}, t)$  and the moment tensor  $M_{pq}$ . The crack kinematics is described by the source-time function with a magnitude of displacement  $d_0$

$$\vec{d}(\vec{r}_{Source}, t) = \vec{r}_{Source} + d_0 \cdot \sin^4\left(\frac{\pi}{T_e}t\right) \vec{e}. \quad (2.30)$$

As a consequence of equations (2.28), (2.29) and (2.30), the amplitude of acoustic emission waves  $|\vec{u}(\vec{r}, t)|$  is expected to be proportional to the crack volume  $\Delta V$ .

Using the deconvolution analysis according to H. Wadley [41], M. Ohtsu and K. Ono demonstrated that the moment tensor from crack opening mode can be modeled by an orthogonal triad of double forces without moment, whilst the moment tensor representing sliding or tearing mode can be modeled by a double couple without moment (see [1, 35, 38, 42]). This is shown in figure 2.11 as schematic representation according to [35]. Also included are the sound radiation patterns, which are the normalized radial displacements at constant distance around the source position. The red curves indicate positive (push) displacement while the broken blue curves indicate negative (pull) displacement. E. Green lately extended this approach used in isotropic media to the needs of acoustic emission sources in composite laminates [43, 44].

As alternative to the generalized theory of acoustic emission M. Lysak and M. Giordano et al. developed theories based on fracture mechanics approaches to describe the correlation between the microscopic oscillation of a crack surface with properties of the respective acoustic emission signal in the case of isotropic



## 2. Theoretical background and developments

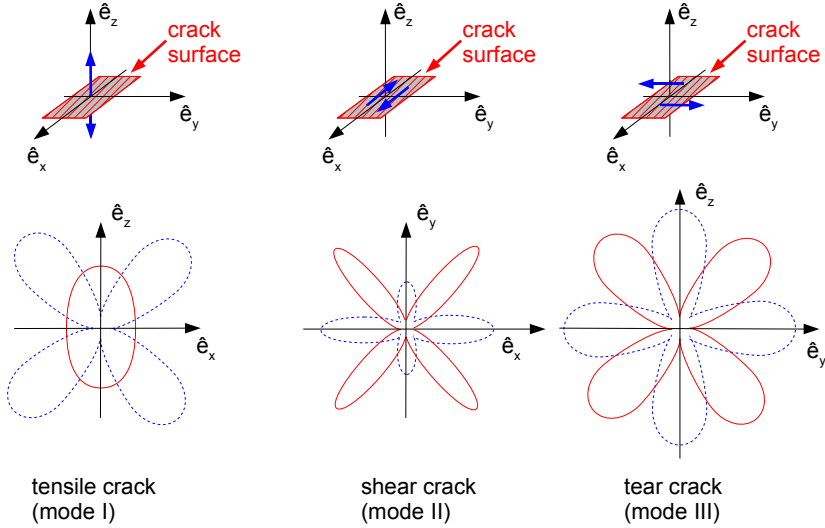


Figure 2.11.: Representation of different source mechanisms according to [40] in isotropic media. The red curves of the source radiation patterns indicate positive (push) displacement, the broken blue curves indicate negative (pull) displacement.

elastic [37] and viscoelastic materials [45]. M. Lysak provides a calculation for the elastic wave amplitude  $u$  at a distance  $r$  with observation angle  $\theta$  in the case of a crack-through process and a penny-shaped crack as seen in figure 2.12. While the penny-shaped crack is treated within a 3-dimensional approach, the symmetry of the crack-through process allows reasonable reduction in dimensionality to reach 2-dimensional description. To describe the behavior of the crack surface the Heavyside function  $H(t)$  was used. Thus the source-time function written in terms of displacement is given as:

$$\vec{d}(t) = d_0 \cdot H(t) \vec{e}. \quad (2.31)$$

Using an approach based on fracture mechanics, M. Lysak demonstrated that the elastic wave amplitude is correlated with the microscopic properties of the cracking medium:

$$u(r, \theta) = \Delta a^{3/2} \frac{\sigma_{frac}}{\rho c_L^2} \cdot \frac{v(\theta)}{\pi r} \text{ "crack-through"} \quad (2.32)$$

## 2. Theoretical background and developments

$$u(r, \theta) = \Delta A \frac{\sigma_{frac}}{\rho c_L^2} \cdot \frac{v(\theta)}{\pi r} \text{ “penny-shaped crack”} \quad (2.33)$$

In both cases the amplitude of the elastic wave is directly correlated with the fracture strength of the material  $\sigma_{frac}$  and the elastic properties given by the density  $\rho$  and the sound velocity  $c_L$ . The dependency of the crack separation mode on the elastic wave is included in the function  $v(\theta)$  which is formulated separately for the longitudinal and transversal parts of the elastic waves. While in equation (2.29) the amplitude of the elastic wave is proportional to the crack volume, it is important to point out that the amplitude in this approach is proportional to the crack-length increment to the power of 3/2 for the crack-through process and proportional to the crack surface area for a penny-shaped crack. These new proportionalities reflect the change in crack geometry acting as acoustic emission source. Thus the elastic wave is influenced most of all by the geometry of the crack and the mechanism of crack formation.

In the case of viscoelastic materials, M. Giordano et al. introduced a correlation between the frequency spectra  $\tilde{u}$  of the elastic waves observed at distance  $r$ , the initial deflection time  $T_e$ , the materials relaxation time  $T_r$  and its phase velocity  $c_P$ :

$$\tilde{u}(\omega, r, T_e, T_r, c_P) = \tilde{d}(\omega, T_e) \cdot e^{-ik(\omega, T_e, T_r, c_P) \cdot r} \quad (2.34)$$

The wave-number is dependent on the frequency and thus introduces a dispersive medium:

$$k(\omega) = \frac{1}{c_P T_r} \sqrt{\omega^2 T_r^2 - i\omega T_r}. \quad (2.35)$$

In the case of a point-like crack they applied the source-time function:

$$\vec{d}(t) = d_0 \cdot \cos\left(\frac{\pi}{2T_e} t\right) \vec{e}. \quad (2.36)$$

This finally yields the complex source frequency spectrum  $\tilde{d}$ :

$$\tilde{d}(\omega, T_e) = -2T_e \frac{\sigma_{frac}}{\rho c_P^2} \cdot \frac{\pi e^{-i\omega T_e} + 2i\omega T_e}{4\omega^2 T_e^2 - \pi^2}. \quad (2.37)$$

The result of equation (2.34) is a dependency of the elastic waves frequency spectra on the ratio between the initial deflection  $T_e$  and the materials relaxation time  $T_r$ , the so-called Deborah number.

For  $T_e \gg T_r$  viscous behavior is dominating, which strongly attenuates frequency spectra contributions above  $\omega = 2\pi T_e^{-1}$ . In contrast, materials

## 2. Theoretical background and developments

with  $T_e \ll T_r$  show almost perfect elastic behavior and therefore show little influence on the detected frequency spectra. For viscoelastic materials  $T_e \approx T_r$ , which influences the contributions at high frequencies, but almost retains the frequency spectra shape.

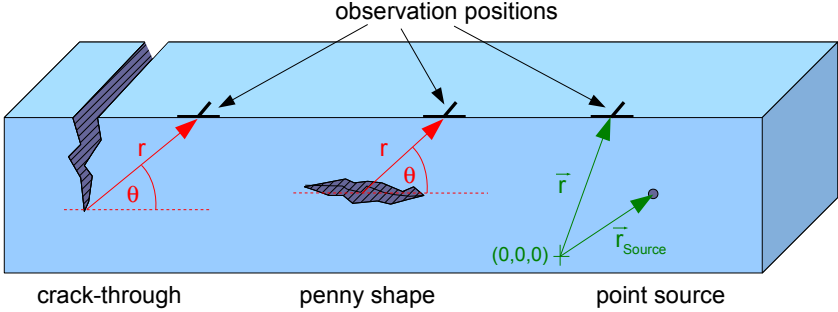


Figure 2.12.: Definition of observation position of acoustic emission sources in polar coordinates for crack-through-process and penny shape cracking and Cartesian coordinates for point source.

The present theories can thus predict the expected energy and frequency spectrum of the elastic wave released by a crack surface oscillation in dependence of the microscopic elastic properties and the crack geometry. However, all the presented theories implicitly assume partially infinite media for wave propagation. Consequently the next important step to reach realistic experimental conditions is the introduction of finite boundaries of the propagation medium.

### 2.2.3. Guided waves

For geometries of finite extent the solution of equation (2.19) has to take into account the respective boundary conditions. This ultimately results in wave propagation which is “guided” by the geometry of the propagation medium. The most prominent types of guided waves are the surface waves, which occur for a solid with free surface. These were first predicted by Lord Rayleigh in 1885 for the special case of an infinite solid with free surface. Later R. Stoneley and A. Love generalized Rayleigh’s description for a solid with an adjacent liquid halfspace and planar interfaces located between two halfspaces [46, 47]. The guided waves in such structures with liquid-solid interfaces are hence often called Stoneley- or Love waves. For infinitely extended solids with two parallel

## 2. Theoretical background and developments

free surfaces H. Lamb published the respective solutions for the wave equation in 1917 [48]. According to the shape of such geometries the respective guided elastic waves are commonly called “plate-waves” or as used in the following *Lamb waves*. In other types of geometries like rods or cylinders similar types of guided waves exist. Due to the planar structure of the experimental specimens used for the present study the propagation behavior of Lamb waves is very important and will be discussed in more detail in the following. For a closer review about Rayleigh waves the reader is referred to [49], while other types of guided waves are comprehensively discussed in [50, 51].

In order to understand guided waves it is necessary to understand the behavior of elastic waves at interfaces. The relevant physical quantity for this case is the acoustic impedance  $Z$ , which is defined by the density  $\rho$  and the respective sound velocity  $c_i$  as

$$Z = \rho c_i. \quad (2.38)$$

If a plane elastic wave arrives with orthogonal incidence to an interface the wave is partially reflected and transmitted dependent on the acoustic impedance of the two materials. If the wave propagates from medium one with impedance  $Z_1$  to medium two with impedance  $Z_2$  as shown in figure 2.13 the coefficients for reflection  $R$  and transmission  $\bar{R}$  can be written as:

$$R = \frac{Z_2 - Z_1}{Z_2 + Z_1} \quad (2.39)$$

$$\bar{R} = \frac{2Z_2}{Z_2 + Z_1}. \quad (2.40)$$

For incidence angles other than zero degree the law of refraction is applied. In contrast to electromagnetic waves, modal conversions are possible for elastic waves. Thus longitudinal waves can be completely or partially converted to transversal waves dependent on the incident angle. In the most general case, the law of refraction can be written for arbitrary combinations of longitudinal and transversal sound velocities as

$$\frac{\sin(\theta_1)}{\sin(\theta_2)} = \frac{c_1}{c_2}. \quad (2.41)$$

For certain incident angles the transmitted parts of the elastic waves are of very special nature. The most important among them are the surface waves which occur for elastic wave incidence from gaseous or liquid media to solids

## 2. Theoretical background and developments

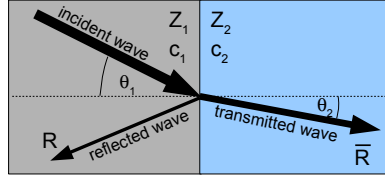


Figure 2.13.: Schematic representation of refraction law for acoustic waves.

under certain angles<sup>3</sup>. The total reflection condition for the longitudinal wave is denominated first critical angle and causes excitation of a creep wave at the solids surface that exhibits a propagation velocity identical to the longitudinal wave and a fast energetic decay. More important for practical applications is the Rayleigh wave which occurs under the second critical incidence angle resulting in total reflection conditions for the transversal wave. L. Bergmann stated an approximation formula for the sound velocity of Rayleigh waves which is in general slower than the velocity of the solids transversal wave [53]:

$$c_R \approx \frac{0.874 + 1.12\nu}{1 + \nu} c_T \quad (2.42)$$

The deformation amplitude of the Rayleigh wave decays exponentially with depth along the  $z$ -axis. This is the reason why these types of waves are called “surface” waves since they propagate and interact only close to the solids surface as shown schematically in figure 2.14.

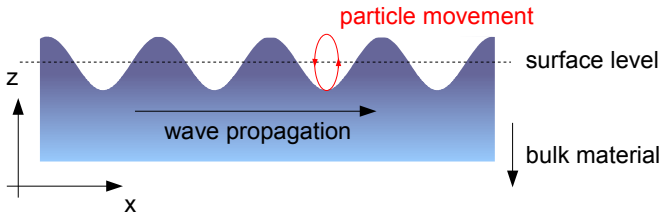


Figure 2.14.: Rayleigh-Wave propagating in  $x$ -direction

If the dimension of the solids  $z$ -axis in figure 2.14 is reduced and approaches the shape of a plate with thickness  $z_d$  the surface wave gets distorted and

<sup>3</sup> Another common technique to excite surface acoustic waves is the application of a piezoelectrical materials in the shape of an interdigital transducer [52].

## 2. Theoretical background and developments

converts to another very important type of guided wave. Such a plate with infinite extensions in the x and y direction and a finite thickness in z-direction defines boundary conditions for the solution of equation (2.19) which result in a classic eigenvalue problem. In analogy to equation (2.25) the solution of the wave equation (2.19) is given as:

$$\begin{aligned} u_x &= f_x(z)e^{-i(kx-\omega t)} \\ u_y &= 0 \\ u_z &= f_z(z)e^{-i(kx-\omega t)} \end{aligned} \quad (2.43)$$

This describes the propagation of an elastic wave in x-direction as a function of wavenumber  $k$ , frequency  $\omega$  and as function of the z-position  $f_i(z)$ . The (x,y,z) origin is located in the medial plane of the plate as shown in figure 2.15. The elastic waves described by equation (2.43) are called Lamb waves, which show no displacement in y-direction for an infinite plate. Complementary to the Lamb waves the so-called shear-horizontal waves exist, which have no displacement in the x- or z-directions, and thus propagate only in y-direction.

If the boundary condition  $\sigma = 0$  is applied at the surface level  $\pm 0.5z_d$  of a plate with thickness  $z_d$  this results in two characteristic periodic equations for symmetrical and anti-symmetrical motions with respect to the plane  $z = 0$  as schematically shown in figure 2.15:

$$\text{Symmetric: } \frac{\tan(0.5\eta z_d)}{\tan(0.5\xi z_d)} = -\frac{4\xi\eta k^2}{(k^2-\eta^2)^2} \quad (2.44)$$

$$\text{Antisymmetric: } \frac{\tan(0.5\eta z_d)}{\tan(0.5\xi z_d)} = -\frac{(k^2-\eta^2)^2}{4\xi\eta k^2} \quad (2.45)$$

with abbreviations  $\xi$  und  $\eta$

$$\xi^2 = \frac{\omega^2}{c_L^2} - k^2 \quad (2.46)$$

$$\eta^2 = \frac{\omega^2}{c_T^2} - k^2 \quad (2.47)$$

The equations (2.44) and (2.45) implicitly relate the wavenumber  $k$  and frequency  $\omega$  to the plate thickness  $z_d$ . This results in dispersion, since the velocity of propagation depends on the frequency. For Lamb waves the relation

## 2. Theoretical background and developments

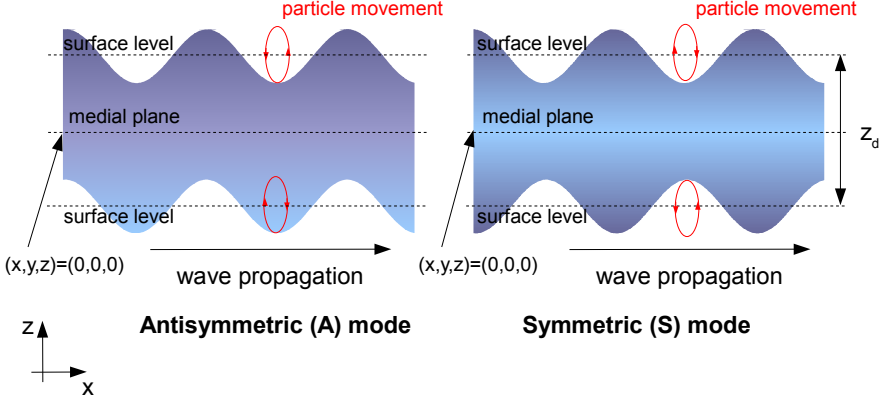


Figure 2.15.: Schematic representation of antisymmetric and symmetric Lamb wave modes propagating in x-direction (strongly emphasized surface motion).

between phase velocity  $c_P$  and group velocity  $c_G$  is thus given by:

$$c_G = c_P(f z_d) \left( 1 - \frac{1}{1 - \frac{c_P}{f z_d \frac{dc_P}{d(f z_d)}}} \right). \quad (2.48)$$

The relationship between frequency, plate-thickness and phase- or group-velocity is typically visualized within a set of dispersion curves for *symmetrical* ( $S_i$ ) and *anti-symmetrical* ( $A_i$ ) Lamb wave modes. A typical set of such dispersion curves for a 4.7 mm thick Aluminum plate is shown in figure 2.16 presented in the form according to F. Firestone and J. and H. Krautkrämer [50].

The diagram shows the dependency of the phase velocity and group velocity on the product  $f \cdot z_d$  for the symmetric and antisymmetric modes. The two fundamental modes exhibiting the lowest frequency for a given wave-number starting at index  $i = 0$ , whereas higher order modes are iterated consecutively. The diagram in figure 2.16 is of high practical usage, since Lamb waves are typically excited by a plane elastic wave with appropriate incidence angle  $\varphi$  as schematically shown in figure 2.17. The excitation process in turn depends on the used frequency and plate thickness. Figure 2.17-a shows a schematically representation of the transversal component of the incident wave, which is reflected at the top and bottom boundaries and propagates in the same manner as in a bulk medium. If the incidence angle, the thickness  $z_d$  or the frequency are

## 2. Theoretical background and developments

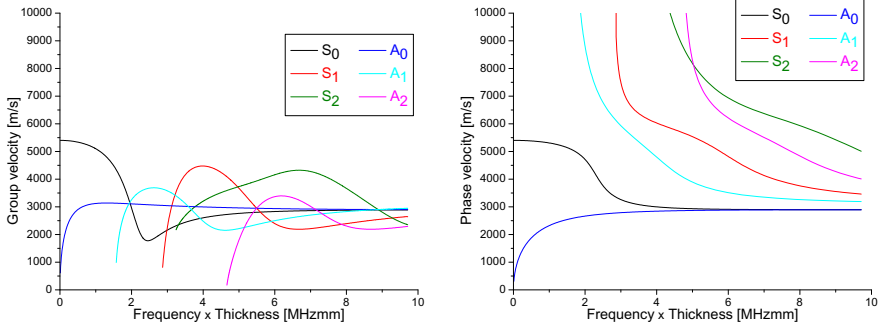


Figure 2.16.: Set of dispersion curves calculated for a 4.7 mm Aluminum-Plate with longitudinal sound velocity 6320 m/s and transversal sound velocity 3100 m/s.

chosen appropriately, interference of transversal and longitudinal components occurs and results in excitation of Lamb waves (figure 2.17-b). Similar to the longitudinal or transversal waves the wavelengths of the Lamb waves are typically in the order of a few mm and are thus typically slightly larger than the thickness  $z_d$  of the investigated plate structures.

In the case of Lamb waves originating from acoustic emission sources the excitation process is different. Here the internal microscopic displacement described in section 2.2.2 results in spherical radiation of longitudinal and transversal waves, which are now subject to the boundary conditions given by the plate structure. The reflection of longitudinal and transversal waves at the top and bottom of the plate causes similar interference to those shown in figure 2.17-b and, consequently, results in excitation of Lamb waves. Since the modal composition of the excited Lamb wave is an important factor for identification of failure mechanisms in CFRP this correlation will be discussed in more detail in chapter 3.

Especially in the case of CFRP-plates an acoustic anisotropy is introduced by the orientation of the carbon fibers. Their dominating elastic modulus results in highly anisotropic sound velocities and can cause the effect of beam steering. Since the wavelengths of the Lamb waves are much larger than the typical carbon fiber diameter this results in a preferential guidance of the Lamb waves along the fiber direction as if the propagation medium was an homogeneous medium. This results in distorted, non radial-symmetric propagation of the Lamb waves as schematically shown in figure 2.18. For the non-uniform stacking sequences typically used in CFRP, this can result in



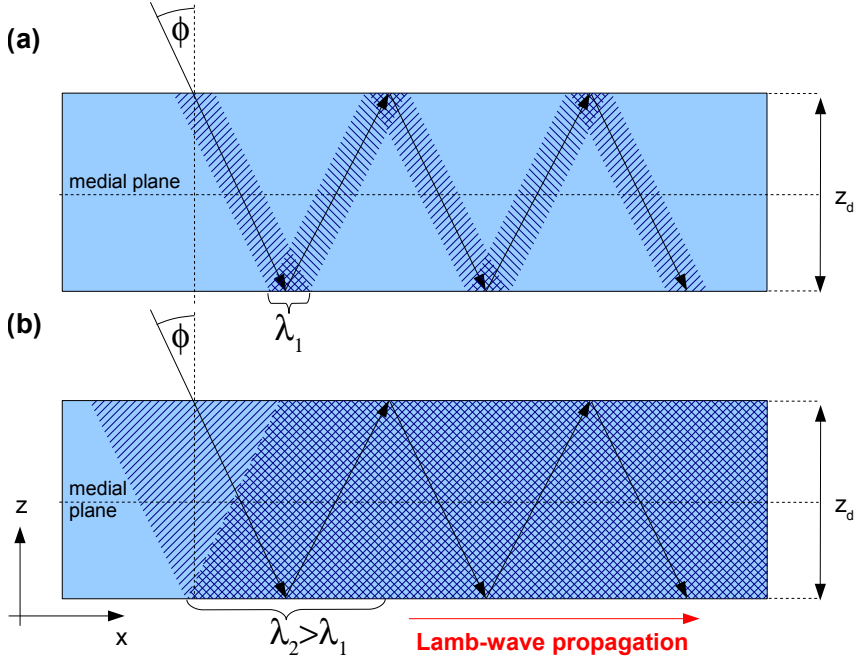


Figure 2.17.: Visualization of transversal wave with incidence angle  $\varphi$  and inappropriate transversal wavelength  $\lambda$  (a) and larger transversal wavelength  $\lambda$  causing Lamb wave excitation due to interference (b).

complex propagation behavior of the acoustic emission signals and has to be taken into account for localization and interpretation [54].

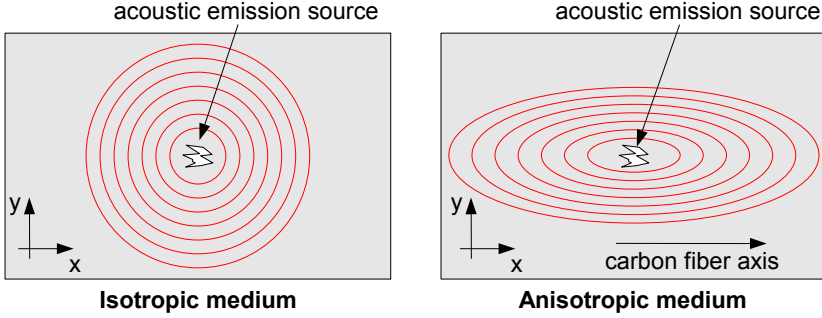


Figure 2.18.: Scheme of beam-steering effect observed in media with elastic anisotropy.

For even more complex geometries like rods or cylinders other types of guided waves exist, which can be excited by acoustic emission sources. Since these types of geometries were not investigated within this thesis these guided waves will not be closely examined, instead more information on this topic is found in [1, 50, 51].

In general, the propagation of acoustic emission signals is subject to the boundary conditions formed by the propagation mediums geometry. In addition, the propagation of elastic waves is subject to attenuation which significantly alters the appearance of the waves in dependence of their propagation distance and is therefore discussed in the next section.

#### 2.2.4. Attenuation

The propagation of elastic waves according to the constitutive relation (2.10) in an infinite isotropic medium exhibits no loss of energy. For real solids, lossless propagation is not fulfilled, instead the elastic wave suffers from attenuation effects. As shown by B. Auld, acoustic losses of solids at room temperature can sufficiently be described by a viscous damping term [32]. This is introduced in equation (2.11) by a second term including the time derivative of the deformation tensor  $\epsilon_{lm}$  as:

$$\sigma_{ik} = C_{iklm}\epsilon_{lm} + C'_{iklm}\frac{\partial\epsilon_{lm}}{\partial t} \quad (2.49)$$

## 2. Theoretical background and developments

As shown in [32] equation (2.49) can be represented by a formulation equivalent to equation (2.11) in the form:

$$\sigma_{ik} = C_{iklm}^* \epsilon_{lm} \quad (2.50)$$

This introduces complex elastic coefficients if the respective elastic wave field has  $e^{i\omega t}$  time dependence.

$$C_{iklm}^* = (C_{iklm} + i\omega C'_{iklm}) \quad (2.51)$$

The acoustic attenuation is then defined as decay of amplitude  $u_1$  and  $u_2$  of an elastic wave between two observation positions.

$$\text{Attenuation} = 10 \log (e^{-\alpha(u_1 - u_2)})^2 \text{dB} \quad (2.52)$$

This introduces the attenuation coefficient  $\alpha$  used as measure for the attenuation properties of a material. The attenuation is typically expressed in the dB scale to reflect the large range of attenuation effects. As discussed by A. Pollock [55] and W. Prosser [56] from the viewpoint of acoustic emission science there are five contributions for attenuation of acoustic emission signals, which are discussed in more detail in the following:

1. geometric spreading
2. thermoelastic and Akhieser dissipation
3. dispersion
4. scattering
5. dissipation into adjacent media

In the near-field range, close to the acoustic emission source, geometric spreading is the main reason for attenuation. This is caused by the spherical radiation of energy into the solids volume, which results in an energetic decay per dihedral angle with inverse propagation distance  $r$ . If Lamb waves are excited, the attenuation in the near-field range will even be more pronounced, since the elastic waves energy is separated into the distinct symmetrical and antisymmetrical modes. In addition, these suffer from velocity dispersion as will be described below. According to [56] in the case of Lamb waves, the distance dominated by attenuation caused by geometric spreading is given by  $r < 4.34/\alpha$ .

In the far-field of the acoustic emission source the main contributions for attenuation at room temperature originate from the thermoelastic mechanism

## 2. Theoretical background and developments

and the Akhieser mechanism. The first one results from irreversible heat conduction arising from compression during propagation of the longitudinal wave. The second mechanism arises from the disturbance of the equilibrium distribution of thermal acoustic waves (phonons). The propagation of a coherent acoustic wave disturbs the equilibrium positions of the phonons and thus leads to a dissipative energy contribution. For homogeneous isotropic solids, the thermoelastic and the Akhieser mechanism result in attenuation for elastic waves proportional to  $\omega^2$ .

For guided waves in anisotropic solids even more effects contribute to the total acoustic attenuation. In the case of Lamb waves, additional contributions arise from spatial dispersion and frequency dispersion [57]. For dispersive media the phase velocity is directly linked to the attenuation by Kramers-Kronig relations deduced from the principle of causality [58]. Thus attenuation from spatial dispersion is caused by the dependency between phase velocity and wave-vector inherent in equations (2.44) and (2.45). The effect of attenuation due to frequency dispersion is also inherent in propagation of non-monochromatic wave-packages. Since each frequency component travels at a distinct velocity an initially short pulse begins to spread in time during propagation. This causes attenuation with propagation length. In the case of Lamb waves this is of great importance since the different modes exhibit different attenuation coefficients. For CFRP-plates the attenuation of the antisymmetrical modes is still higher, than the attenuation of the symmetrical modes [56]. This effect superimposes the thermoelastic effect, since the  $S_0$  Lamb wave mode typically shows higher frequencies than the  $A_0$  Lamb wave mode.

In addition, scattering of the elastic waves caused by inhomogeneities can occur. Typical examples are the grain structure within metals, fibers in composites or voids. This can result in severe attenuation and has to be taken into account when discussing attenuation effects.

In experimental environments acoustic emission signals propagate within a material under testing, which typically is in contact with additional structures like e.g. fixtures or supply pipes. Since a partial transmission of the acoustic emission signal into adjacent media results in a respective loss of the reflected wave, such losses can be considerably high and thus even dominate the acoustic attenuation.

As a consequence, the information included in the amplitude and frequency composition of the acoustic emission signal formed during excitation is altered during propagation. Consequently, the detection and identification of a failure mechanism is limited to a certain distance around the position of acoustic emission excitation.

### 2.2.5. Signal detection

The detection of an elastic wave released by an acoustic emission excitation takes place at the surface of a solid as shown in figure 2.19. In most cases a piezoelectric element is used for detection, which is included within a protective housing and is connected to the surface by a viscous coupling medium [59]. There is a large variety of acoustic emission sensors available today, which are almost completely based on lead zirconate titanate  $\text{Pb}[\text{Zr}_x\text{Ti}_{1-x}]\text{O}_3$  (PZT) as detector material [60] whose lattice structure is also shown in figure 2.19. The purpose of the acoustic emission sensor is the conversion of surface motion of the solid to an electric signal. This conversion is based upon the piezoelectric effect which is closely related to the occurrence of electric dipole moments within piezoelectric materials. In the case of PZT the dipole moments originate from the asymmetric charge density located within the oxygen octahedron. The magnitude of the dipole moment along the octahedrons main axis is directly linked to the applied mechanical stress in the same direction.

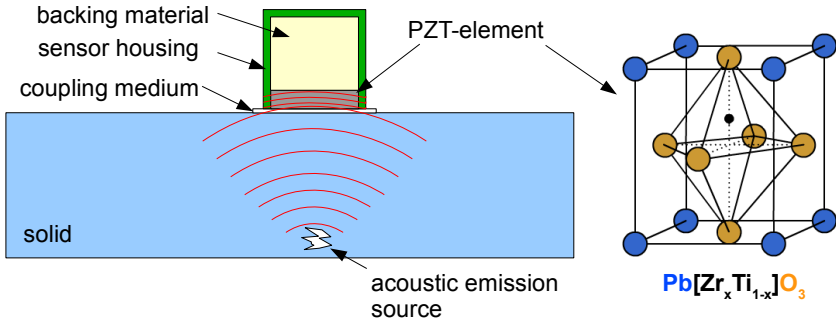


Figure 2.19.: Detection of acoustic emission signals (left) and crystal structure of lead zirconate titanate (right).

The fundamental equation for the electrical displacement  $D_i$  of a material with electrical permittivity  $\chi_{im}$  within an electric field with strength  $\Phi_m$  is given by

$$D_i = \chi_{im} \cdot \Phi_m. \quad (2.53)$$

In combination with Hooke's law from equation (2.11) this yields the coupled equations of the piezoelectric effect in stress-charge form. The coupling matrix

## 2. Theoretical background and developments

is given by the direct  $S_{ikm}$  and inverse  $S_{ikm}^{-1}$  piezoelectric constants:

$$D_i = S_{ikm} \cdot \epsilon_{km} + \chi_{im} \cdot \Phi_m \quad (2.54)$$

$$\sigma_{ik} = C_{iklm} \cdot \epsilon_{lm} - S_{ikm}^{-1} \cdot \Phi_m \quad (2.55)$$

Thus the lattice deformation of a piezoelectric solid results in an electric field, which is called the direct piezoelectric effect and is typically used in sensor applications. Complementary the application of an electric field over a piezoelectric material results in a mechanical displacement known as inverse piezoelectric effect which is instead often used in actuator elements.

Although such piezoelectric sensors are very sensitive to detection of surface displacements down to  $10^{-12}$  m in the ultrasonic frequency range [61], they show intrinsically resonant behavior. This resonant frequency response is caused by the piezoelectric materials properties and the finite dimensions of the sensor. These effects superimpose the frequency characteristic of the detected elastic wave. Consequently, for interpretation of the frequency distribution of the acoustic emission signals the effect of the sensor has to be taken into account.

The concept which deals with such characteristic system responses is the transfer function. In the frequency domain the dependency between the output function  $\tilde{h}_A(\omega)$  and the input function  $\tilde{h}_E(\omega)$  is given by the transfer function  $\tilde{J}(\omega)$

$$\tilde{h}_A(\omega) = \tilde{h}_E(\omega) \cdot \tilde{J}(\omega) \quad (2.56)$$

Thus in the frequency domain the system output is simply given by multiplication of the input function and the transfer function. Moreover, transfer functions of concatenated systems can be written as product of each singular transfer function. With respect to the previous sections, the case of acoustic emission detection can be expressed according to [1, 45, 62] as

$$\tilde{u}_{AE}(\omega) = \tilde{d}_{source}(\omega) \cdot \tilde{J}_{medium}(\omega) \cdot \tilde{J}_{geometry}(\omega) \cdot \tilde{J}_{sensor}(\omega) \cdot \tilde{J}_{amplifier}(\omega). \quad (2.57)$$

This includes the acoustic emission source-time function  $\tilde{d}_{source}(\omega)$  in the frequency domain, the influence of the propagation medium  $\tilde{J}_{medium}(\omega)$ , its geometry  $\tilde{J}_{geometry}(\omega)$ , the sensors response  $\tilde{J}_{sensor}(\omega)$  and the characteristic of the amplifier  $\tilde{J}_{amplifier}(\omega)$  of the recording equipment. Figure 2.20 shows exemplary frequency spectra of these transfer functions illustrating their influence on the final acoustic emission signal.

## 2. Theoretical background and developments

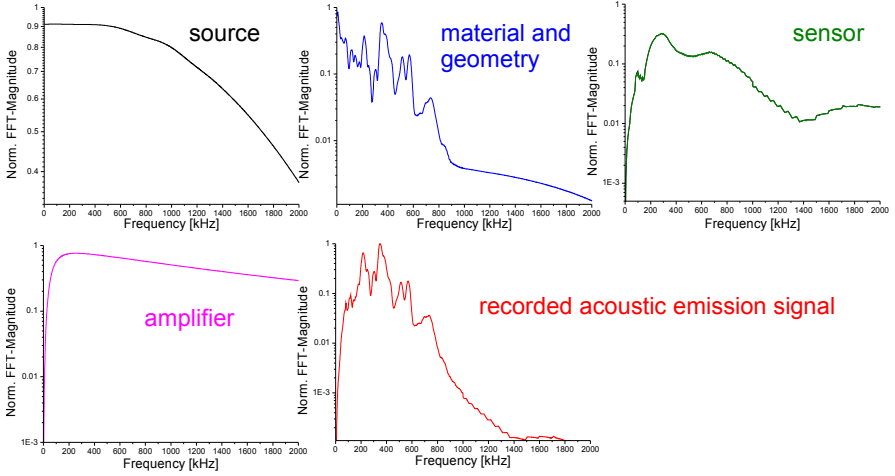


Figure 2.20.: Contributions of the different transfer-functions of source, material and geometry, sensor and acoustic emission equipment obtained from FEM-simulations to the final acoustic emission signals, visualized according to J. Bohse et al. [62].

In principle it is possible to evaluate each transfer function of equation (2.57) independently as already pointed out by M. Giordano et al. and P. Wilcox et al. [45,63]. Consequently an application of the deconvolution analysis according to [41] to equation (2.57) can deduce the source function  $\tilde{d}_{source}(\omega)$  from the recorded signal  $\tilde{u}_{AE}(\omega)$  if all other transfer functions are known.

Usually the influence of the propagation medium  $\tilde{J}_{medium}(\omega)$  and its geometry  $\tilde{J}_{geometry}(\omega)$  cannot be separated sufficiently. Moreover their exact solutions are also correlated to the propagation distance of the signal and its path of propagation. Therefore analytical solutions for these two contributions are usually approximated by idealistic assumptions on the mediums influence and approximations of the real geometry, typically with infinite extensions [38,39,43,44].

In contrast, the estimation of the transfer function of the sensor and the amplifier are better established experimental techniques. Whilst the characteristic of the amplifier can easily be obtained by a network analyzer, the measurement of the transfer function of acoustic emission sensors, also known as primary calibration is more difficult.

Several experimental methods are thus established for primary calibration of

acoustic emission sensors. The most common are the step-function calibration [64] and the reciprocity calibration [65]. In addition F. Breckenridge et al. applied a capacitance sensor for primary calibration of piezoelectric sensors [66]. In recent years laser vibrometers are widely applied to the same purpose [40,67]. As pointed out by L. Goujon et al. there is no expectation for an absolute transfer function of the sensor, since the frequency sensitivity characteristic of the sensor also depends on the elastic properties of the medium it is applied on. This effect is caused by the mismatch of acoustic impedance between sensor and medium [67]. Usually the transmissive properties and the impedance mismatch is improved by application of a viscous or fluid coupling medium. As recently reported by P. Theobald et al. the couplants show slight influence on the sensors reception sensitivity [68], but are negligible compared to the other contributions in equation (2.57).

In summary, the individual contributions to equation (2.57) have to be understood very well if the characteristics of the recorded acoustic emission signals want to be correlated with the respective acoustic emission excitation process. Besides analytical calculations one powerful tool to analyze and interpret these contributions is finite element simulation as presented in chapter 3.

### 2.3. Signal analysis

In the following section all experimentally used techniques for analysis of acoustic emission signals are introduced. The first subsection 2.3.1 will shortly review the experimental prerequisites for interpretation of acoustic emission signals. Subsequently, the feature based interpretation and source localization techniques will be introduced in section 2.3.2 and discussed with a focus on the experimental setups used within this thesis. More advanced types of analysis of signal features are pattern recognition techniques, which focus on identification of characteristic similarities of the acoustic emission signals. Section 2.3.3 will review current techniques and present new approaches established within this thesis to detect natural clusters of acoustic emission signals. As alternative approach to interpretation of acoustic emission signals, the time-frequency behavior is widely used. In the present thesis one new approach is the interpretation of the averaged (mean) time-frequency behavior of the recorded signals which will be presented in detail in section 2.4 together with a review on the established time-frequency interpretation techniques.



### 2.3.1. Prerequisites for acoustic emission interpretation

Typically not all recorded signals originate from failure mechanisms, but instead originate from different acoustic emission sources. Examples of such experimentally acquired signals are shown in figure 2.21. One example are “non-transient” signals arising from friction as shown in figure 2.21-a. Another source of signals completely unrelated to microstructural changes within the material are electromagnetically induced signals as in figure 2.21-b. The type of signal which will be termed *acoustic emission signal* in the following is shown in figure 2.21-c. These are well defined transient signals, which do not interfere with other signals and show a clear signal onset and a convenient decay.

In most practical applications, the sensors signals are not recorded continuously<sup>4</sup>, but instead the acquisition of a signal is triggered by exceeding a given threshold level, which is advantageous for the acquisition system performance. Typically the incoming reflections from boundaries of the specimen superimpose with the direct part of the transient wave and result in difficult abortion criteria for the acquisition. In order to separate such signals an additional analysis step subsequent to signal acquisition is often required.

A further prerequisite for signal analysis is a sufficient data acquisition rate, which is given by the Nyquist-criteria. To be adequate the sampling rate should be at least twice as high as the highest frequency within a frequency range of interest. For higher accuracy this minimum requirement for the sampling rate is often exceeded, e.g. to better resolve the signal onset. The consequences arising from digitalization, like aliasing effects and data storage and data throughput are not discussed in the following. Instead a good review about this aspect of acoustic emission science is found in [1, 40].

The different established methods for analysis of acoustic emission signals are schematically shown in figure 2.22. In general there are two different approaches for acoustic emission analysis:

1. Analysis of features extracted from the signals
2. Direct analysis of the obtained signals

The interpretation of signal features is a well established procedure which originates from the beginning of acoustic emission science. Due to low computational capacity only signal features were stored on the harddisc and were interpreted subsequently. The most direct approach is the accumulation of the number of signals detected or their associated energy to obtain a degree

---

<sup>4</sup> There are certain applications which require continuous acquisition of acoustic emission signals. The advantage of this approach is the extensive capability for offline analysis.

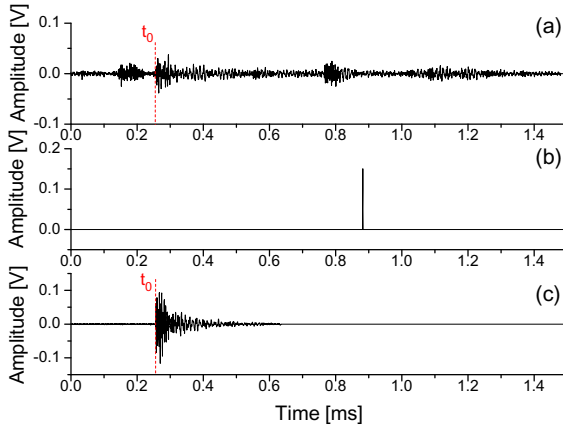


Figure 2.21.: Typical signals recorded during measurement. Signals arising from friction (a), typical electromagnetically induced signal (b) and transient acoustic emission signal (c).

of damage within the material under investigation. Another important concept for interpretation of acoustic emission signals is the localization of the acoustic emission source position based on threshold based evaluation of the run-time difference (see section 2.3.2). Based on a multitude of features, pattern recognition techniques are widely used to find similarities within the recorded signals. These are often used for identification of acoustic noise, but also allow identification of particular source mechanisms as demonstrated within this thesis.

As an alternative approach, the possibility to analyze the acquired signals directly enabled new techniques for interpretation of acoustic emission signals. Most of the new techniques focus on correlations between the characteristics of the acoustic emission signals and the respective source mechanism, but can also be used to improve source localization accuracy [69, 70]. Most noteworthy the moment-tensor inversion was widely applied to concrete specimens to deduce the characteristics of the source mechanism [40]. As an alternative approach in specimens with plate-like geometry an analysis of the frequency and time-frequency behavior can yield distinct characteristics for typical failure mechanisms.

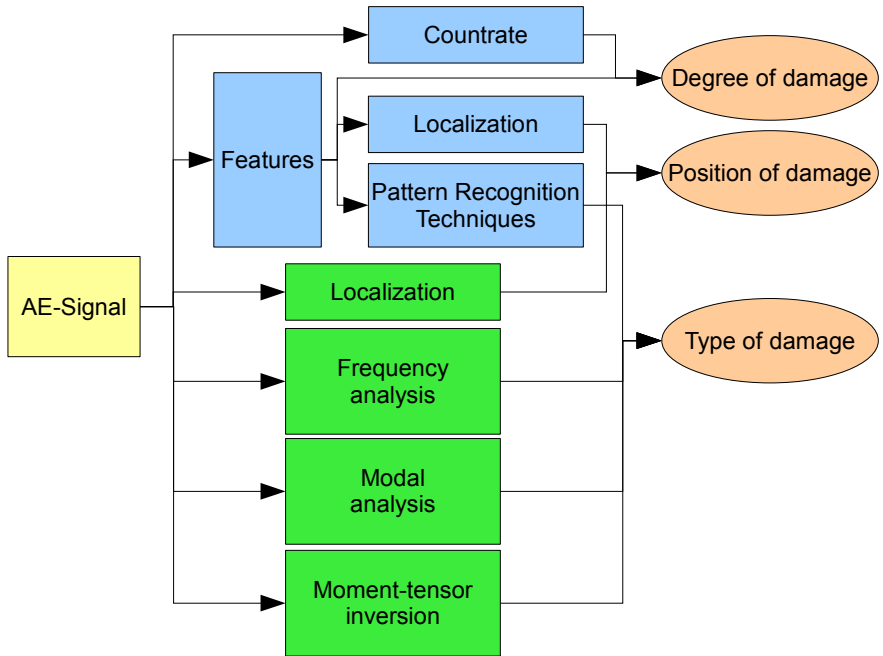


Figure 2.22.: Overview of feature based (blue) and signal based (green) analysis techniques applied to acoustic emission signals.

### 2.3.2. Acoustic emission features and source localization

Counting the number of acquired transient signals is a straight forward method for interpretation of acoustic emission. Since growth of damage in discrete steps of microscopic deformation is accompanied by the release of transient elastic waves, the accumulated number of acoustic emission signals yields a good estimation of the degree of damage within the material. The accumulated number of acoustic emission signals and its time derivative, the acoustic emission activity has long been used for interpretation of material failure [71–75]. If the activity level changes, the type of failure is expected to change accordingly. This can result from contributions of additional failure mechanisms, or a fundamental change in the activity of the same type of failure. The scheme in figure 2.23 shows a comparison of the typical acoustic emission activities in the case of a coated material. As long as the cracks within the coating grow stable, a constant acoustic emission activity is observed. The type of failure (crack growth) does not change (figure 2.23-a). In later stages the initial crack growth can induce delamination between the coating and the substrate, which results in an additional type of failure with additional contribution to the acoustic emission activity. Accordingly the slope of accumulated acoustic emission signals over time changes (figure 2.23-b).

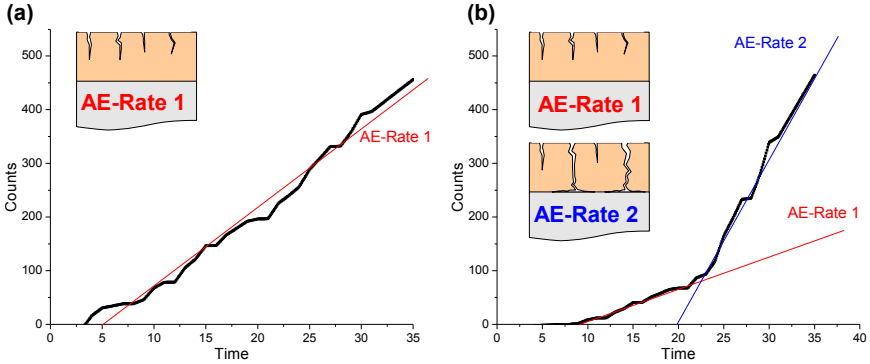


Figure 2.23.: Comparison of acoustic emission activity for different steps of coating failure.

Fundamentally, the direct correlation between crack progress and the number of acoustic emission signals is only valid, if the discrete energy release during growth of the crack is of equal magnitude and the fracture toughness of the material does not change during crack propagation (see equations (2.29),(2.32),(2.33) and (2.34)). If this is not the case, a better relation is

## 2. Theoretical background and developments

given by the acoustic emission signals energy  $W_{AE}$ , which is proportional to the strain energy  $\Omega$  consumed during crack progress under certain boundary conditions (see section 3.4.3).

$$\frac{\partial W_{AE}}{\partial t} = \beta \frac{\partial \Omega}{\partial t} \quad (2.58)$$

Since the mechanical energy of the acoustic emission signal is difficult to obtain it is often replaced by the electrical energy of the detected acoustic emission signal. In the following the electrical energy will always be understood as acoustic emission signal energy.

The majority of the energy necessary for crack growth is consumed by plastic deformation, formation of new surfaces and dissipative processes. Release of elastic waves constitutes only a small fraction of this energy which is expressed by a suitable proportionality constant  $\beta \ll 1$ . The absolute value for  $\beta$  depends on the shape of the crack tip and on the mechanical properties of the material. Different types of failure result in different source radiation patterns. The relative orientation between acoustic emission source and detector can thus lead to different detected acoustic emission signal energies. Especially for thin plate specimens, the source radiation patterns can result in different ratios of Lamb wave modes, which in turn influence the overall energy content of the recorded signal [76]. Additionally, the energy of the signal is reduced due to attenuation and dispersion and thus depends on the path of propagation between acoustic emission source and point of detection. Therefore  $\beta$  should only be treated as a constant for stable growth of one specific type of failure within one type of material composition within a limited observation distance.

### Feature extraction

The definition of a characteristic feature like an energy obtained from a transient signal introduces the important concept of feature extraction. In acoustic emission science these signal features have long been used to interpret the type of failure. Basically, a feature (parameter) is used to reduce the amount of information carried by the signal to a single value. As shown in figure 2.24 for a typical voltage signal in the time domain  $U(t)$  and frequency domain  $\tilde{U}(f)$  large numbers of features are available to describe the signal. Although many features are already part of national and international standards [77, 78] the exact feature definitions of different providers for acoustic emission equipment slightly differ. Further, for the interpretation of acoustic emission signals with pattern recognition techniques it is useful to define new features like the Weighted Peak Frequency. Since the definition and calculation of signal features is an important step preceding to the presented pattern recognition

## 2. Theoretical background and developments

methods in section 2.3.3 all features used in this thesis are shortly summarized. While the basic signal features in table 2.1 are almost self explanatory and covered by the above mentioned standards, this is not necessarily the case for the derived features presented in table 2.2. These show discrepancies between the different providers of acoustic emission software and are hence defined here in the way used within this thesis.

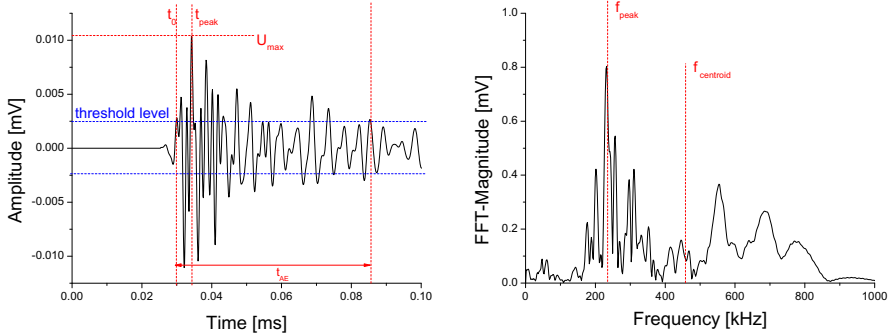


Figure 2.24.: Examples of acoustic emission signals features in the time and frequency domain as described by [77, 78].

Feature	Definition	Unit
$t_0$	time of first threshold crossing (arrival time)	[s]
$N_{AE}$	number of signals threshold crossings	[#]
$t_{AE}$	time between first and last threshold crossing of signal	[ $\mu$ s]
$U_{max}$	maximum signal voltage	[mV]
$t_{peak}$	time of maximum signal voltage	[ $\mu$ s]
$f_{peak}$	frequency of maximum signal contribution	[Hz]
$N_{peak}$	number of threshold crossings between $t_0$ and $t_{peak}$	[#]

Table 2.1.: Basic signal parameters used for feature definition

Most of the features used to describe an acoustic emission signal are composed of extreme values, derived from the signal in time- or frequency domain as shown in figure 2.24. The “RMS”- and “ASL”-values are used in a similar manner like in electrical engineering, were these describe the effective voltage within a characteristic time interval. The three different count-based frequencies “Initiation-“, “Reverberation-“ and “Average-Frequency” are used to provide an

## 2. Theoretical background and developments

Feature	Definition	Unit
Amplitude	$dB = 20 \log(U_{\max}/1\mu V) - dB_{preamplifier}$	[dB]
Counts	$N_{AE}$	[#]
Duration	$t_{AE}$	[ $\mu s$ ]
Rise Time	$t_0 - t_{peak}$	[ $\mu s$ ]
Counts To Peak	$N_{peak}$	[#]
Root mean square (RMS)	$RMS = \sqrt{\frac{1}{T_{RMS}} \int_{t_0}^{t_0+T} U^2(t) dt}$ with a characteristic time $T_{RMS}$ for averaging between 10 - 1000 ms	[mV]
Average signal level (ASL)	$ASL = \sqrt{\frac{1}{T_{ASL}} \int_{t_0}^{t_0+T} Amplitude dt}$ with a characteristic time $T_{ASL}$ for averaging between 10 - 1000 ms	[dB]
Average Frequency	$\langle f \rangle = N_{AE}/t_{AE}$	[Hz]
Reverberation Frequency	$f_{rev} = \frac{N_{AE} - N_{peak}}{t_{AE} - t_{peak}}$	[Hz]
Initiation Frequency	$f_{init} = \frac{N_{peak}}{t_{peak}}$	[Hz]
Rise Angle	$\varphi_{rise} = \tan\left(\frac{U_{\max}}{t_{peak}}\right)$	[rad]
Decay Angle	$\varphi_{decay} = \tan\left(\frac{U_{\max}}{t_{AE} - t_{peak}}\right)$	[rad]
Absolute Energy	$W_{AE} = \int_0^{t_{AE}} \frac{(U(t))^2}{10k\Omega} dt$ with 10 k $\Omega$ input impedance of the recording equipment	[aJ]
Peak Frequency	$f_{peak}$	[Hz]
Frequency Centroid	$f_{centroid} = \frac{\int f \cdot \tilde{U}(f) df}{\int \tilde{U}(f) df}$	[Hz]
Weighted Peak-Frequency	$\langle f_{peak} \rangle = \sqrt{f_{peak} \cdot f_{centroid}}$	[Hz]
Partial Power	$\int_{f_1}^{f_2} \tilde{U}^2(f) df \bigg/ \int_{f_{start}}^{f_{end}} \tilde{U}^2(f) df$ Frequency range of interest [f <sub>1</sub> ;f <sub>2</sub> ] Frequency range of investigation [f <sub>start</sub> ;f <sub>end</sub> ]	[%]

Table 2.2.: Definition of acoustic emission signal features used within this thesis.

## 2. Theoretical background and developments

estimate of the characteristic frequency before and after the peak-maximum and as average of the complete signal. This should not be understood as exact frequency analysis since the number of threshold crossings is often very low and thus yields very inaccurate results. Instead the different ratios obtained from these three frequencies can be used as a measure of symmetry of the signal. A similar measure can be obtained from the “Rise-“ and “Decay Angle”. These are used to describe the angle of the slope formed by the point of first threshold crossing and the signal maximum (rise) and the angle of the slope from signal maximum to the last threshold crossing (decay). The “Absolute Energy” is an absolute measure of the electrical energy of an acoustic emission signal and is given in Atto-Joule [ $10^{-18}$  J] due to the small energy amount. The “Frequency Centroid” is used to characterize the overall frequency content of an acoustic emission signal in a similar manner like the center of mass is used to describe the properties of geometric object with uniform density. Thus it can be understood as additional information on the characteristic average frequency of the signal and is in general not equal to the “Peak Frequency”. This in turn is a highly efficient feature for discrimination of acoustic emission signals, since it is very discrete in its nature. To improve the representation of a characteristic frequency associated with an acoustic emission signal the “weighted Peak Frequency” was introduced to combine the discriminative efficiency of the “Peak Frequency” with the information on the average frequency content of the signal expressed by the “Frequency Centroid”. A very similar approach is used by the different “Partial Power” levels. They measure the signals frequency contribution within a given interval and are thus used to capture the frequency composition of the signal in more than one characteristic value.

### Acoustic emission source localization

Another important concept for interpretation of acoustic emission signals is localization of the acoustic emission source position. Once the acoustic emission source is localized, its origin can be correlated with microscopic observations and usually is called an *acoustic emission event*. The calculation of the source position is based on differences of the arrival time at several sensor positions. As shown in figure 2.25-a, the elastic wave originating from an acoustic emission source radiates into the solids volume and “arrives” at the respective sensors positions at distinct times.

The main experimental problem is the exact determination of the arrival time of a transient signal. As depicted in figure 2.24 the first occurrence of a threshold crossing is used as onset of the signal. The so obtained arrival time is obviously linked to the chosen threshold level and consequently can falsify the localization process.



## 2. Theoretical background and developments

As alternative approaches other methods for determination of the arrival time of elastic waves were adopted from seismology in the past. The most important techniques to mention are the autoregressive methods. The modified Hinkley criteria uses the position of the energetic minimum of transient signals at the onset [79] while the AIC (Akaike Information Criterion) is obtained from the signals envelope after applying a Hilbert transformation [80]. In comparison to threshold based techniques, the accuracy for determination of the signal onset is drastically increased. This effect on the obtained arrival time using the modified Hinkley criteria is also shown for the exemplarily signal in figure 2.25-b. Further techniques focus on determination of the arrival time using wavelet spectra [69] or determine runtime differences from attenuation effects or utilize beam forming [70]. Since the determination of the signal onset is a fundamental part in acoustic emission science, but is not extensively used in the current thesis the reader is referred to a more advanced review on the different established techniques which is found in [1]. Instead for the following investigations conventional threshold based techniques were found to provide sufficient accuracy for source localization.

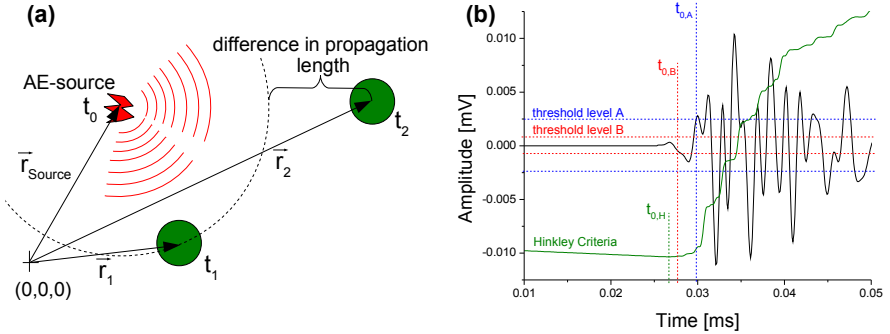


Figure 2.25.: Scheme for localization of acoustic emission source position (a) and determination of arrival time showing influence of threshold level in comparison to modified Hinkley-Criteria (b).

Once the arrival times are obtained, the source position  $\vec{r}_{source}$  and time of acoustic emission  $t_0$  can be calculated:

$$|\vec{r}_i - \vec{r}_{source}| = c \cdot (t_i - t_0). \quad (2.59)$$

This equation relates the positions of the different sensors  $\vec{r}_i$  and their arrival times  $t_i$  to the acoustic emission source location using the sound velocity  $c$ . Since equation (2.59) is the definition of a hyperbola this technique is called

hyperbolic localization. The localization of acoustic emission signals in isotropic media is closely related to the problems faced in GPS (Global Positioning System) applications. Consequently, the corresponding algorithm of S. Bancroft is typically applied to obtain the acoustic emission source position in a direct algebraic approach [81]. In alternative, algorithms adapted from seismology science are often applied, which use an inverse approach. Here the specimen is subdivided into elements with finite resolution and hypothetical runtimes are calculated for each element. The element showing sufficient agreement with the measured runtimes is chosen as source position [1].

In general, equation (2.59) applies to arbitrary dimensions. Since the unknowns are the source position  $\vec{r}_{source}$  and the time of occurrence  $t_0$  for localization in  $N$ -dimensions  $N + 1$  sensors are required to solve equation (2.59). Thus for a 3-dimensional localization at least 4 sensors are necessary to obtain solutions. Typically more than  $N + 1$  sensors are used to localize the source positions which results in overdetermined equation systems. This additional information can be used to estimate the source localization error or to improve the accuracy of localization by multiple regression analysis.

In practice the localization accuracy depends on the sampling rate  $\Delta T^{-1}$  used to record the acoustic emission signals, the aperture of the used sensors and the validity of the assumptions made on signal propagation. The basic inaccuracy of the measured signal runtime can be calculated from the inverse sampling rate. This is directly correlated to a metric localization error via multiplication of the sampling interval  $\Delta T$  with the sound velocity. The physical size of the sensor results in an additional inaccuracy of the determination of the arrival time caused by aperture effects. If the sensor radius is small in comparison to the signal propagation length (e.g. if the sensor can be assumed as point sensor) this error contribution can be neglected. For complex geometries and anisotropic media the largest errors arise from deviations in the assumed signal propagation. If the used algorithm does not take into account the reflections at specimen boundaries the assumed signal propagation velocity might be over- or underestimated. In the case of planar specimens 2-dimensional localization of acoustic emission sources generating Lamb waves can be treated in this respect by using the propagation velocity of the  $S_0$ -mode for localization. As depicted in figure 2.16, for the frequency range of acoustic emission signals and reasonable plate thickness the  $S_0$ -mode shows higher group velocity than the other Lamb wave modes and thus arrives first at the sensor position.

If the propagation medium exhibits elastic anisotropy equation (2.59) is no longer valid and should be replaced by a respective approach for anisotropic sound velocities. In general this boosts the complexity of the equations. For simple 2-dimensional localization problems like in CFRP-plates the varying ply layups result in elastic anisotropy. In this case a common approach is to scale

## 2. Theoretical background and developments

the geometry to the ratio of anisotropy in the sound velocities. Afterwards the common algorithms are used to infer the source location based upon equation (2.59).

Once the source positions of the acoustic emission signals are obtained, they can be correlated to microscopic observations. Typically, scatterplots are used to visualize the acoustic emission events, which have several disadvantages. First, a projection of 3-dimensional localization results on a 2-dimensionsal plane can result in overlapping points which results in distorted or hidden information. Second, the accuracy of localization results is hardly reflected in scatterplots using error-bars. As a contribution to the visualization of such localization results the software “DensityVille” was developed within this thesis. To this end the localization results are displayed as a density diagram instead of a scatterplot as visualized in figure 2.26 in direct comparison [82,83]. Thus overlapping points increase the local density, which is adequately captured by the pseudo-color range. In addition the software also features time-resolved and spatial-resolved picture series which can be converted to videos and compared to other volumetric imaging techniques like computer- or ultrasonic-tomography.

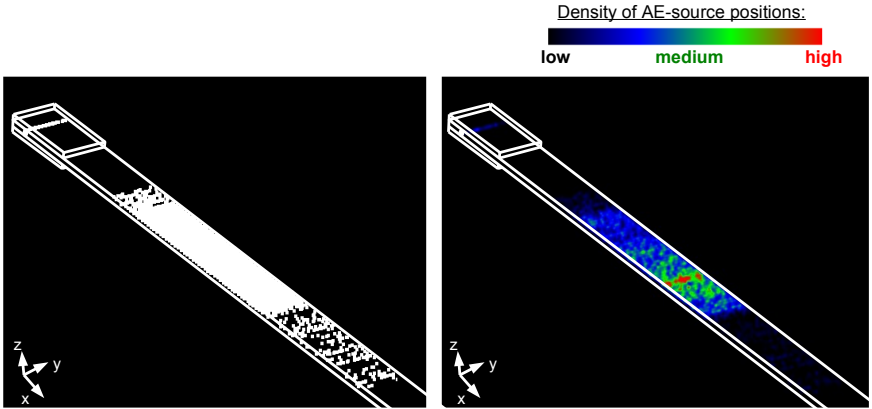


Figure 2.26.: Comparison of typical scatterplot (left) and density diagram (right) for the acoustic emission source positions of a DCB-testing specimen. The specimen dimensions are marked by the white wire frame.

### 2.3.3. Pattern recognition techniques

In the context of acoustic emission analysis, the purpose of pattern recognition techniques is the identification of similarities in the recorded acoustic emission signals. In contrast to conventional feature based interpretation of the signals, pattern recognition techniques use a multitude of features and consequently can identify distinct signal types even if they cannot be described by fixed feature limits. Thus for the present thesis unsupervised pattern recognition is an elementary part of the investigative methods applied to acoustic emission signals. The task of the presented methodology is to find similarities within the recorded signals using characteristic signal features. This is not directly equivalent to detection of specific types of failure associated with the signals, since this requires additional knowledge about the signals characteristics for a certain type of failure. Thus the correlation between distinct acoustic emission signal types and a certain type of failure is completely separated from the pattern recognition process and is discussed instead in chapters 3 and 4.

In general, the purpose of pattern recognition techniques is automated object recognition and application of a decision criterion on the given objects in order to separate them into distinct groups. Fundamentally the methods can be separated into two approaches, namely *supervised* and *unsupervised pattern recognition*. Figure 2.27 shows an abstract example of  $N = 8$  objects to be treated by pattern recognition. The task of unsupervised pattern recognition is to separate the given objects into distinct groups according to their similarity to each other without any previous knowledge, e. g. into groups of rectangles, triangles and circles. In the following an assignment of the given objects into distinct groups will be termed *partition*. Here the groups of an arbitrary partition will be denoted *clusters*, while the final partition of the pattern recognition techniques will be termed *classes*. This emphasizes the difference between an intermediate partitioning of the given objects and the final result. Therefore the whole pattern recognition process is often termed *classification*.

In contrast, supervised pattern recognition techniques consist of two stages. In the supervised stage a set of objects with known assignment to the respective classes is prepared. This known assignment is usually denoted *label*. Here an algorithm is trained to recognize these types of objects based on a given set of features. In the subsequent stage the algorithm is applied on objects with unknown assignment and classifies them based upon their similarity to the object classes provided in the supervised stage. In the example in figure 2.27 the algorithm learns e. g. how to recognize quadrilateral objects based on the features of object 1, 5 and 8.

Obviously, in the given example the application of pattern recognition can

## 2. Theoretical background and developments

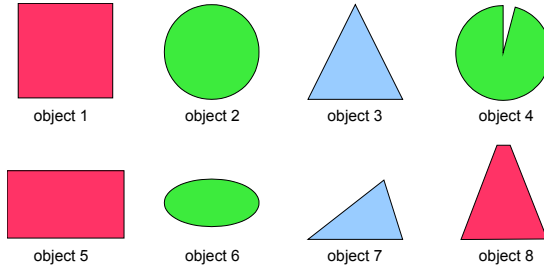


Figure 2.27.: Example of geometric objects as classification problem.

give biased or false results if the features used to describe the problem are chosen inappropriate. Since the idea of the example in figure 2.27 is the identification of distinct geometric object types, based upon the feature “colour” a pattern recognition algorithm will yield strongly separated classes, but the result is arguable. In the given example the algorithm would assign red objects of any geometry to the geometric type rectangle. The combination with other features like the “number of edges” or “area” can improve the result. However no single feature is sufficient to allow a distinct separation of the presented geometries in general. Intrinsically this problem is the major strength of all pattern recognition techniques. Instead of single features, the distinction of the given objects is based on a multitude of features. Such combination of several features of a given object is usually termed *feature vector*  $\vec{q}$ . In the  $Q$ -dimensional feature space spanned by the individual  $Q$  features axis the feature vector defines each objects position. Figure 2.28 shows the respective 2-dimensional feature space of the example in figure 2.27 for the feature axis “area” over “number of edges”. Now the purpose of a pattern recognition algorithm is to determine optimal solutions for the decision boundaries within the feature space, which allow correct classification of the individual objects. In general, the mathematical solutions of these decision boundaries are non-linear functions. In this context pattern recognition is often discussed as function approximation problem.

Although it is an easy task for most cluster algorithms to obtain valid decision boundaries for the feature distribution in the given example, this is not generally the case. Since the mathematical definition of the geometry type is by no means affected by its area there is a large numerical distribution along the feature axis “area”. In practice the numerical range of the “area” feature is expected to exceed the numerical range of “number of edges”. In order to

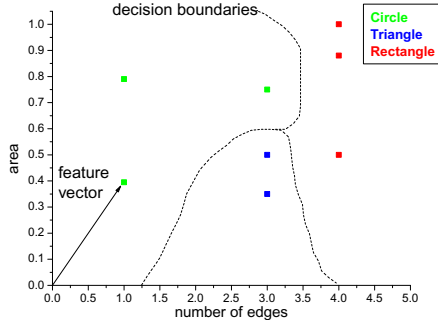


Figure 2.28.: Classification problem in feature space with typical non-linear decision boundaries. The class labels of the different geometric objects are given by the color of the data points.

deal with such unequally distributed features, an adequate *preprocessing* of the chosen features is commonly applied.

### Data preprocessing

In general, data preprocessing includes outlier removal, feature selection, feature normalization and if applicable a feature vector transformation. The main reason for this is the improved performance of the classification algorithms if the numerical range of the individual feature axis is comparable and the significance of the chosen feature axes is high [84].

Implicitly the removal of outliers and noise included in the objects to be classified is one of the best possibilities to boost the performance of pattern recognition. Since this is a crucial step including deletion of experimental data this has to be used carefully. In the context of this thesis the approach is the classification of acoustic emission signals as defined in section 2.3.1. Noise signals as shown in figure 2.21 will result in characteristically different features than acoustic emission signals. If the correlation between distinct features and the noise signals is very strict, these can easily be detected and deleted. This is the case for electromagnetically induced signals, which e. g. can be distinguished by their very low values for  $N_{AE}$  or  $t_{AE}$ . Other types of noise like friction signals are more difficult to detect and often cannot be distinguished by a single feature. For this case supervised pattern recognition techniques can be applied to find and delete the respective noise signals. In any case the input

## 2. Theoretical background and developments

for a pattern recognition procedure used for identification of signals correlated with failure mechanisms should only consist of features extracted from defined acoustic emission signals.

While for the example presented in figure 2.27 the amount of reasonable features used to describe a single object is almost straightforward, this is not necessarily the case for less abstract problems. In the case of acoustic emission signals, tables 1 and 2 already summarized the features used within this thesis. However, this list is by no means exhaustive and could easily be extended by a number of features. Although a more detailed description of the individual objects by an extended feature vector may seem advantageous, this comes with the cost of increased computational complexity for the classification algorithm<sup>5</sup>. In practice the number of features should be minimized as much as possible, while the chosen features should be descriptive enough to allow successful distinction between the given objects. Such selection can be achieved by usage of parallel coordinates or mosaic plots as described in [85]. Another very popular technique to find and exclude redundant features are *correlation dendrograms*. These dendrograms are used to visualize the correlation between the features describing the objects in the dataset (see figure 2.29). The calculation of such dendrograms is based upon a series of hierarchical agglomeration steps. At each step the feature combination with “closest distance”<sup>6</sup> is merged together to form an equivalent combined feature. Thus the correlation between two features is given by their inverse merging distance. To this end highly redundant features can easily be identified, since they merge at very close distances. For acoustic emission signals this is often the case for energetic features and is represented in figure 2.29 by the features 4 and 12, which merge at an inverse distance of 1. This similarity is also observable in the respective feature plot, since both features describe the objects within the dataset almost equally. In contrast features which are highly uncorrelated are often useless. Feature 8 in figure 2.29 shows no correlation with the other features at all, since it merges at an inverse distance of zero. This is indicative for a constant feature as shown in the respective feature plot. To this end, correlation dendrograms can be used to select features within a useful inverse merging distance range as marked in figure 2.29. This reduces the dimension of the feature vector without losing too much of its discriminative power.

However, there is no guarantee that the chosen features will be sufficient to achieve a significant partitioning of the given objects. Thus the main disad-

---

<sup>5</sup> This problem is commonly known as “curse of dimensionality”.

<sup>6</sup> For single linkage the “closest distance” is chosen as minimum distance between the respective features of two objects, while complete linkage uses the “closest distance” between the minimum feature values of the two most remote objects [86].

## 2. Theoretical background and developments

vantage of correlation dendrograms is the missing feedback of the respective clustering algorithm applied to the chosen feature set. Since the result of a clustering algorithm is closely linked to the given features an alternative approach to feature selection for pattern recognition of acoustic emission signals was established within this thesis and is discussed in the subsection “2.3.3 Semi-automated feature selection and cluster validation”.

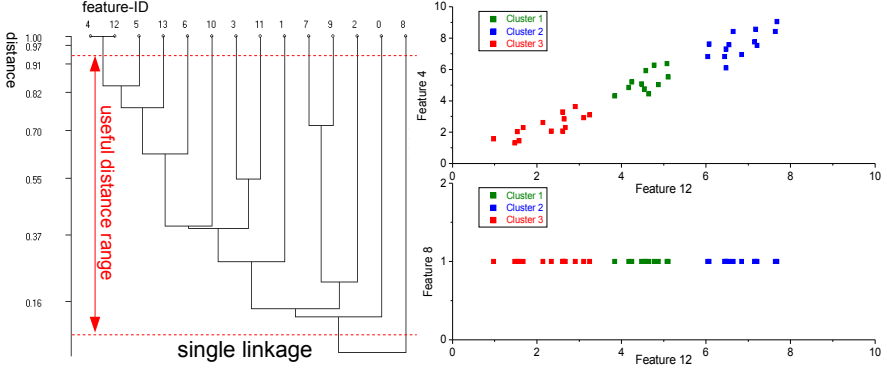


Figure 2.29.: Selection of features using correlation dendrograms for an example with  $Q = 12$  features (left) and corresponding feature plots for selected features (right).

Subsequent to the feature selection, depending on the type of classification different normalization procedures are applied to the individual features. The most common are the normalization of the entries within the vector of each feature  $\vec{g}$  to zero mean, by its unit variance  $var(\vec{g})$  or to a fixed numerical range like  $[-1,1]$ .

$$\vec{g}' = \vec{g} - \langle \vec{g} \rangle \quad (2.60)$$

$$\vec{g}' = \frac{\vec{g}}{var(\vec{g})} \quad (2.61)$$

$$\vec{g}' = \frac{\vec{g}}{\sum_{j=1}^N (g_j)^2} \quad (2.62)$$

The application of a normalization is thus particularly useful if the chosen features are characteristic, but exhibit drastically different numerical ranges. With respect to the chosen clustering algorithm and the distribution of the



features several normalization procedures should be investigated to yield the best performance by empirical means.

The final preprocessing step consists of an adequate feature vector transformation. Typically either a *principal components analysis* (PCA) or a linear discriminant analysis is used. The first one, also known as Karhunen-Loève transformation [87, 88] is one of the oldest techniques in multivariate analysis. Typically the PCA is used to reduce the number of features by an orthogonal linear axes transformation to achieve maximum variance along the first coordinate. Thus the principal axes are directed along the eigenvectors of the covariance matrix of the given features as shown in figure 2.30. After application of a PCA, the new number of features can be reduced by subsequent removal of the highest order principal axes, which in turn contribute little to the discrimination efficiency. Complementary the lower order principal axes provide highest discrimination efficiency in terms of variance along the principal axes. The suitability of this projection method is also confirmed by recent investigations which demonstrated, that PCA intrinsically projects to a feature space which facilitates the k-means algorithm to find almost optimal separations [89, 90]. Since the k-means algorithm was widely used within this thesis, the PCA was generally chosen as projection method. More information on other types of feature vector projections are given in [84, 91, 92].

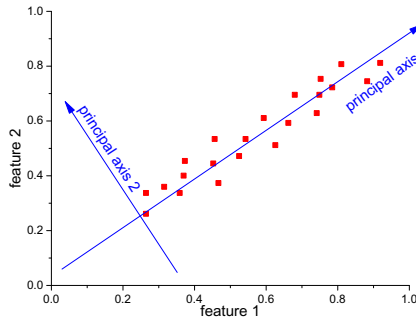


Figure 2.30.: Principal components axes along the eigenvectors of the covariance matrix of the features (according to [84])

## Unsupervised pattern recognition

Subsequent to data preprocessing a cluster algorithm is applied to calculate the decision boundaries as shown in figure 2.28 and to assign the individual objects to the respective cluster. In the case of unsupervised pattern recognition this is done without any previous knowledge on the number of classes and the objects labels. While the detection of similarities in the given example is easy to obtain by most cluster algorithms, in practice the separation into distinct classes is more difficult. As a consequence, a wide range of cluster algorithms are established, which are typically adopted to the faced pattern recognition problem. For classification of acoustic emission signals A. Anastassopoulos et al. investigated the performance of a variety of commonly used cluster algorithms [93]. The most promising among them are the well known *k-means* algorithm and its derivatives, as well as cluster algorithms based on neuronal networks [94,95]. In the following, only a review of the k-means algorithm and the Kohonen map based *learning vector quantizer* (LVQ) will be given, since no other unsupervised cluster algorithms were used within this thesis. In other publications variations of fuzzy c-means [96], vector quantization [97–99], adaptive resonance theory networks [100], Kohonen networks [98,99] and several variations of self organizing maps [98] are also applied to similar classification problems of acoustic emission signals [7, 94, 95, 101].

Based upon the idea of H. Steinhaus in 1956, J. MacQueen established the name “k-means” in 1967 for one of the most universally applicable cluster algorithms [102, 103]. For a given number of clusters  $P$  the k-means algorithm is used to assign each object to a cluster based upon its distance to the cluster centre and optimize the so obtained partition. Mathematically this is expressed as minimization of the within-cluster sum of squares for a partition  $\vec{B} = \{B_1, B_2, \dots, B_P\}$

$$\min \sum_{l=1}^P \sum_{\vec{q} \in B_l} |\vec{q} - \langle \vec{q}_l \rangle|^2 \quad (2.63)$$

For computation of the k-means algorithm, S. Lloyd proposed a standard algorithm in 1982, which is schematically shown in figure 2.31 [104].

The first step consists of random or heuristic definition of initial cluster centers  $\langle \vec{q}_l \rangle$ , marked in color in figure 2.31-a. In the second step, the individual objects are assigned to the cluster centre with closest mean distance (figure 2.31-b). It is noteworthy, that this requires the definition of a metric to measure the mean distance, which is chosen to be the Euclidean distance metric in this investigations. In the next step, the new position of the cluster centers is recalculated based upon the assignment in the previous step. The respective

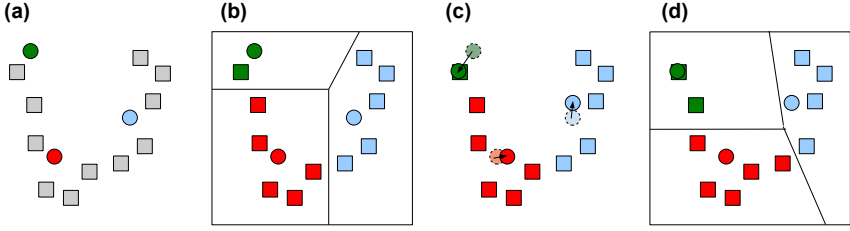


Figure 2.31.: Schematic principle of k-means algorithm in four steps. Initialization of cluster centers (a), assignment of objects to clusters (b), recalculation of cluster centers (c) and reassignment of objects to clusters (d).

recalculation of cluster centers is shown in figure 2.31-c and is calculated for the iteration step  $m + 1$  as

$$\langle \vec{q}_l \rangle^{(m+1)} = \frac{1}{|B_l^{(m)}|} \sum_{\vec{q} \in B_l^{(m)}} \vec{q} \quad (2.64)$$

Subsequently the objects are assigned to their new classes with respect to the distance between the object and the new cluster centers as shown in figure 2.31-d. The last two steps are repeated iteratively until no changes in the assignment occur and thus the algorithm converges.

While the k-means algorithm is computationally very efficient, it is not necessarily the best algorithm to find natural clusters of objects. The main problem of the k-means algorithm is the selection of the initial cluster centers and their iterative optimization. A variety of approaches deals with improvement of this task [105], one of them is the application of a learning vector quantizer based on a Kohonen neuronal network map [98], which is conceptual similar to the k-means algorithm [106]. As major difference of this algorithm, the cluster centers  $\vec{q}_l$  are not obtained directly from the mean vector  $\langle \vec{q}_l \rangle$ . Instead learning vector quantization is used to adjust the cluster centers in an optimization process based on neural networks.

In general, neural networks try to mimic the structure of the nervous system. This is schematically shown in figure 2.32 for the structure of the Kohonen LVQ algorithm. Neural networks typically consist of an input layer, one or more hidden layers of artificial neurons and an output layer. The concept of the network is the “mapping” of the data structure provided at the input

## 2. Theoretical background and developments

layer to another data structure at the output layer. For the present case of unsupervised pattern recognition, the neural network maps the feature vector of an object to a respective cluster label. This “mapping” is based on the functionality of the artificial neurons, which is explained in more detail in the following.

The response of the node  $h_A$  of a single neurons to various inputs  $h_{E_i}$  with weights  $w_i$  is formulated using the activation function  $f_{activation}$  as:

$$h_A = f_{activation} \left( \sum_i w_i h_{E_i} \right). \quad (2.65)$$

The activation function is used to modify the linear decision boundary given by  $\sum w_i h_{E_i}$  and is used as criteria if the neuron is active or inactive. This can either be realized by a threshold function (hard limit function) or by continuous (linear or sigmoidal) functions. Fundamentally, the task of the neural network is the adaptive adjustment of the node weights  $w_i$  to generate an optimized mapping between the input layer and the output layer.

For the variant of the Kohonen LVQ used in this thesis this optimization is achieved by a feed forward net with one hidden layer of neurons fully connected with the input layer (see figure 2.32). The output of the neurons maps directly to the output layers, which holds the associated clusters label for the given features at the input layer. For LVQ the rule for optimization is based on the winner-take-all Hebbian learning approach.

At first an initial set of weights is generated for each neuron. These neurons and their weights  $w_i$  to the feature vector elements  $q_i$  form the prototype centers of the associated clusters in the given feature space. These are usually called *codebook vectors*. Now the algorithm determines which codebook vector is closest<sup>7</sup> to the input feature vector  $\vec{q}$ , which is called the winning codebook vector. Based on the winner-take-all principle, only the weights of this codebook vector are increased, while the weights to the other codebook vectors are decreased. This increase and decrease is called Hebbian learning [107]. Based on this adaptive change of the neuron weights the codebook vectors are iteratively refined until they represent optimized cluster centers  $\vec{q}_l$ . This optimization of cluster centers is often more tolerant for the subsequent classification in terms of convergence and less dependent on the position of the initial cluster centers than other methods used for the k-means algorithm.

One of the major difficulties of pattern recognition techniques is an adequate evaluation of the classification results from different clustering approaches. To quantify the quality of a dataset partition, several methods

---

<sup>7</sup> As measure of distance typically the Euclidean metric is used.

## 2. Theoretical background and developments

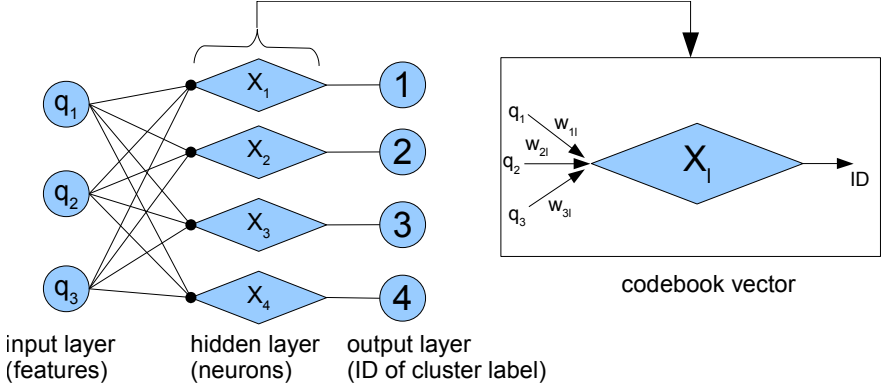


Figure 2.32.: Scheme of learning vector quantization architecture used in this thesis and codebook vector representation.

are used. A comparison of two partitions  $B_X = \{B_{X1}, B_{X2}, \dots, B_{XP}\}$  and  $B_Y = \{B_{Y1}, B_{Y2}, \dots, B_{YP}\}$  of the same objects can be obtained by the *Rand index* [108]:

$$RAND = \frac{\Lambda + \bar{\Lambda}}{\binom{N}{2}}. \quad (2.66)$$

Here  $\Lambda$  is the number of pairs of all objects that are in the same cluster in  $B_X$  and in the same cluster in  $B_Y$ , while  $\bar{\Lambda}$  is the number of pairs of all objects that are in different clusters in  $B_X$  and in different clusters in  $B_Y$ . To this end the Rand index can only be used to measure the similarity between two partitions, but cannot give a numerical evaluation of a single partition. Such measure is instead achieved by the *multivariate Wilks  $\lambda$ -value* using the *within-class scatter matrix*  $\vec{\vec{X}}_W$  and the *total-scatter matrix*  $\vec{\vec{X}}_T$ .

$$WILK = \frac{\det(\vec{\vec{X}}_W)}{\det(\vec{\vec{X}}_T)}. \quad (2.67)$$

$$\vec{\vec{X}}_W = \sum_{l=1}^P \vec{\vec{X}}_l = \sum_{l=1}^P \sum_{\vec{q} \in B_l} (\vec{q} - \langle \vec{q} \rangle) \cdot (\vec{q} - \langle \vec{q} \rangle)^t \quad (2.68)$$

$$\vec{\vec{X}}_T = \sum_{\vec{q}} (\vec{q} - \langle \vec{q} \rangle) \cdot (\vec{q} - \langle \vec{q} \rangle)^t. \quad (2.69)$$

## 2. Theoretical background and developments

Here the scatter matrices are defined for partitions of  $P$  clusters with mean vector  $\langle \vec{q}_l \rangle$  for the  $l$ -th cluster. The superscript  $t$  indicates the transposed vector. As consequence of the definition in equation (2.67), Wilks  $\lambda$ -value is only suitable to compare the efficiency of different algorithms applied to the same feature selection, number of clusters and projection method. In order to evaluate the numerical separation of partitions from arbitrary approaches, several other *cluster validity indices* were proposed.

In general the cluster validity indices used in the following are based on different measures derived from the distance<sup>8</sup> between objects in feature space, which is defined as

$$X_{ij} = \|\vec{q}_i - \vec{q}_j\|. \quad (2.70)$$

One of the oldest cluster validity indices, proposed by J. Dunn in 1974 is used to identify partitions, where clusters are compact and well separated [109]. This is based on *intercluster* (distance measure between different clusters) and *intracluster* (distance measures within a cluster) distances as visualized in figure 2.33-a for an example of three clusters. The marked distance measures are only used to visualize the usage of the indices in equations (2.71), (2.72) and (2.73) and are not reflecting the corresponding extreme values used for calculation of the different indices. The *Dunn-Index* for  $P$  clusters is defined as:

$$DUNN = \min_{i \neq j} \left( \min_{1 < j < P; i \neq j} \left( \frac{X_{ij}}{\max_{1 < l < P} (X_l)} \right) \right). \quad (2.71)$$

This relates the intercluster distances  $X_{ij}$  to the maximum intracluster distances  $X_l$ . Naturally, compact clusters are reflected by a minimum intracluster distance  $X_k$  and well separated clusters are reflected by a maximum intercluster distance  $X_{ij}$ . The Dunn-Index is now defined as minimum of these ratios from all cluster combinations. Thus, the Dunn-Index indicates well separated partitions by a numerical maximum.

A conceptional similar index was proposed by J. Tou in 1979 [110]. The *Tou-Index* is calculated from the global minimal distance  $\min(X_{ij})$  between objects of clusters  $i$  and  $j$  and the global maximum distance  $\max(X_l)$  of objects

---

<sup>8</sup> Typically the used metric for calculation of the distance value is Euclidean.

## 2. Theoretical background and developments

within cluster  $l$  as shown in figure 2.33-b.

$$TOU = \frac{\min(X_{ij})}{\max(X_l)}; \quad i, j, l = 1, \dots, P; \quad (2.72)$$

Same as the Dunn-Index, the Tou-Index maximizes for well separated and compact clusters. The main difference to the Dunn-Index is the interpretation of the intercluster distance.

Another cluster validity index was proposed by D. Davies and D. Bouldin in 1979, which is based on the ratio of within-class scatter and the between-class scatter [111]. The *Davies-Bouldin-Index* is defined as:

$$DB = \frac{1}{P} \sum_{i=1}^n \max_{i \neq j} \left( \frac{\langle X_i \rangle + \langle X_j \rangle}{X_{ij,0}} \right). \quad (2.73)$$

Here  $\langle X_i \rangle$  and  $\langle X_j \rangle$  are defined as the average distance between objects within clusters  $i$  and  $j$ , while  $X_{ij,0}$  is defined as the distance between the respective cluster centers as shown in figure 2.33-c. The Davies-Bouldin-Index is then calculated from the maximum values of all cluster combinations divided by the number of cluster  $P$ . A small ratio of the Davies-Bouldin-Index thus indicates a partition with compact clusters and largest distance of cluster centers.

The cluster validity index based on Hubert's  $\Gamma$  statistic is often used in clustering methods with low-similarity or high-similarity of the individual objects [112, 113]. *Hubert's  $\Gamma$ -Index* is defined by the equation:

$$GAMMA = \frac{1}{P(P-1)/2} \sum_{i=1}^{P-1} \sum_{j=i+1}^P \left( \frac{X_{ij} - \langle X_{ij} \rangle}{stdev(X_{ij})} \right) \left( \frac{\Xi_{ij} - \langle \Xi_{ij} \rangle}{stdev(\Xi_{ij})} \right). \quad (2.74)$$

Here  $X_{ij}$  is defined as distance between two feature vectors and  $\langle X_{ij} \rangle$  as the average distance of all feature vectors. This is normalized by the standard deviation of  $X_{ij}$  [114]. The function  $\Xi_{ij}$  is defined as:

$$\Xi_{ij} = \begin{cases} 1 & \text{if } i, j \text{ in same cluster} \\ 0 & \text{else} \end{cases} \quad (2.75)$$

Thus the  $\Gamma$ -Index evaluates the deviation of the distances of all feature vector combinations from their average distance divided by their standard deviation. In addition the function  $\Xi_{ij}$  provides additional weight depending on the respective cluster label of the selected two different feature vectors.

## 2. Theoretical background and developments

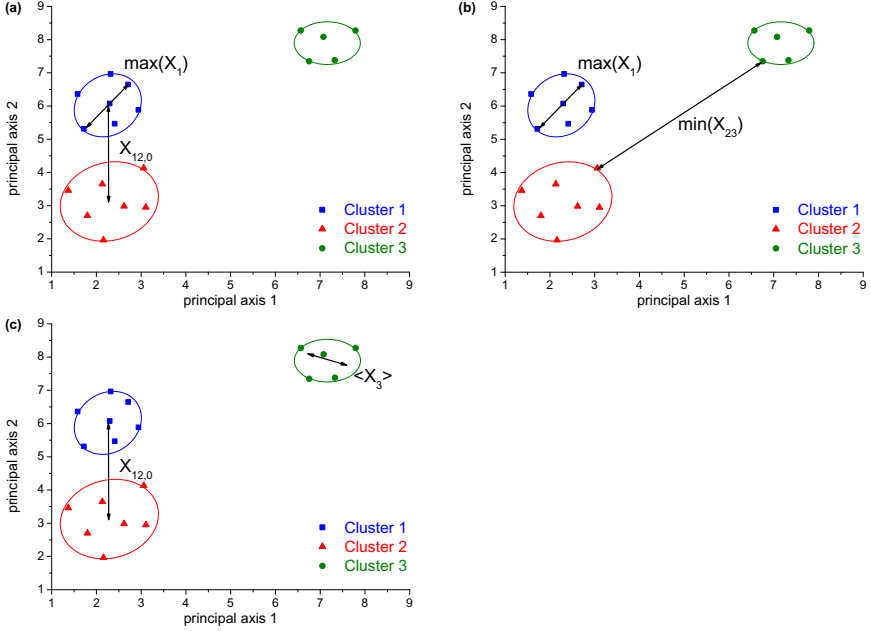


Figure 2.33.: Visualization for definition of the distance measures used for the Dunn-Index (a), the Tou-Index (b) and the Davies-Bouldin-Index (c). The marked distance measures only visualize the usage of the indices and are not the corresponding extreme values used for calculation of the different indices.

Consequently, the  $\Gamma$ -Index is higher if feature vectors in the same cluster are close together, which indicates better separated cluster.

Other cluster validity indices used to assess the quality of a partition independent of the number of clusters include the C-Index [115], the Silhouette validation technique [116] and the Goodman-Kruskal Index [117] which were not used in the present thesis and therefore are not discussed in detail.

In the case of acoustic emission science, A. Anastassopoulos and T. Philipidis were the first who used cluster validity indices in order to identify similarities in acoustic emission signals [93]. They used the Davies-Bouldin-Index and the Tou-Index to determine the number of clusters for a given set of features which yields best separation. Such an investigation using the Kohonen LVQ algorithm is shown exemplarily in figure 2.34. The maximum in the Tou-Index and the minimum in the Davies-Bouldin-Index for a partition with 4 clusters



indicates the best separation of the clusters for this data set. One typical prerequisite for application of this technique is the usage of features with high discrimination efficiency. If these are basically unknown or no previous assumptions are desired, an exhaustive search of promising features in combination with cluster validity indices can be used as presented in this thesis in section 2.3.3.

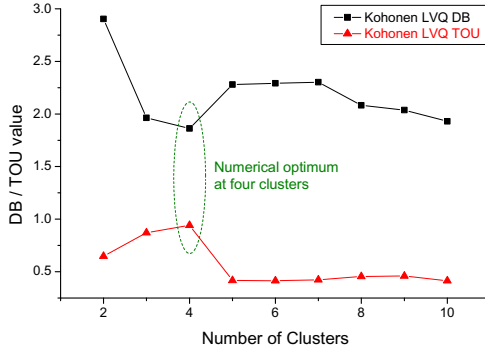


Figure 2.34.: Method according to A. Anastassopoulos and T. Philippidis to identify the number of clusters with highest separation using the Davies-Bouldin and the Tou-Index.

A common problem faced in screening of numerically optimal partitions with ab-initio unknown number of clusters is shown in figure 2.35. Following strict optimization rules, the given set of objects is found to be optimal for a number of clusters  $P = 2$  by evaluation of most of the cluster validity indices. This is caused by the large distance and the great compactness of cluster 2. Consequently this cluster “dominates” the value of the cluster validity index. In the worst case, the objects of this cluster consist of outliers of similar nature. Thus a numerical evaluation of the separability of the remaining objects is often superimposed by their strong dissimilarity to the objects of one specific cluster. Figure 2.35 also shows a separation of the same objects in a partition with  $P = 3$  clusters. For an increased number of clusters, the dominating cluster usually is composed of the same objects, while the remaining clusters split. If one cluster is dominating the numerical range of the cluster validity indices and does not split for a reasonable increase in the number of clusters this phenomenon will be named *super-dominating cluster* in the following.

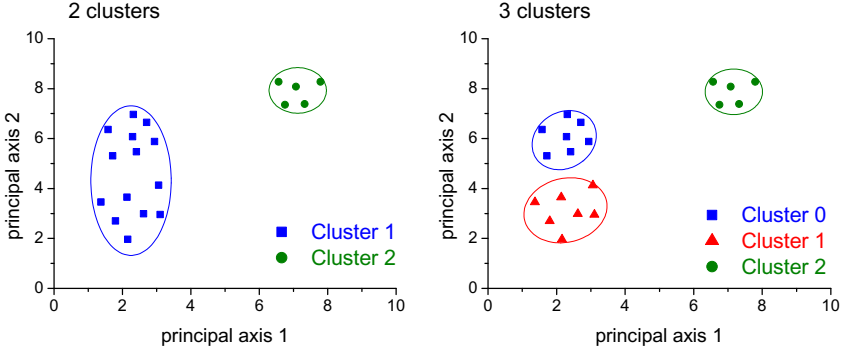


Figure 2.35.: Appearance of a super-dominating cluster in unsupervised pattern recognition.

### Supervised pattern recognition techniques

For classification of acoustic emission signals supervised pattern recognition techniques can be used very efficiently, if a reasonable amount of reference signals is available and the number of clusters is known. Supervised pattern recognition can be subdivided in two parts:

1. Training of an algorithm based on reference objects with known class labels
2. Application of this algorithm to objects with unknown class labels

From the view-point of acoustic emission science, signals with validated correlation to a certain physical origin are required for the first step. This in turn is the greatest drawback in application of supervised pattern recognition techniques to classification of acoustic emission signals, since this is rarely the case in practical applications. A straight-forward approach to overcome this problem was presented by A. Anastassopoulos and T. Philippidis who used the validated result of an unsupervised clustering approach as reference dataset [118–120]. Another option is manual classification of the signals. In this context, supervised pattern recognition techniques are well suited to identify noise-signals as described in section 2.3.1. Due to their appearance noise-signals can easily be selected manually and act as reference signals.

Among the algorithms available for supervised classification a subdivision can be made between statistical algorithms, like the *Bayes Classifier* and

## 2. Theoretical background and developments

its derivative the *Naïve Bayes Classifier* and the neural network types [84]. Within the class of neural network based cluster algorithms two types are used more often than any other, which are the *multilayer perceptron* (MLP) and the *radial basis function* (RBF). In addition, time-delay neural networks [121], recurrent networks [97], neuro-fuzzy algorithms [122], ARTMAP [123], genetic algorithms [124], swarm intelligence [125] and decision-tree based approaches [126] are applied to similar classification problems. In the following a review of the back-propagating multi-layer perceptron is given, since this was the only cluster algorithm applied for supervised pattern recognition within this thesis.

The architecture of a multi-layer perceptron is a neural network as schematically shown in figure 2.36. The training of an algorithm for supervised pattern recognition using such neural network structures can be understood as function approximation problem, where the “function” maps object features given at the input nodes to class labels at the output nodes. Since this correlation is a non-linear problem, multiple artificial neurons are typically used, arranged in a number of hidden layers between input and output nodes (see figure 2.36), powerful enough to allow approximation of arbitrary functions. This is done by adjusting the weights of the nodes in order to find a global minimum of the quadratic error surface function  $L$ .

$$L(\vec{w}_{tot}) = \frac{1}{2} \sum_{i=1}^{N_{train}} \sum_{j=1}^N (P_{ref,j} - P_j)^2 \quad (2.76)$$

Here  $\vec{w}_{tot}$  represents the vector of all node weights,  $P_{ref,j}$  the class label from the reference objects and  $P_j$  the actual class label. The dependency of the error surface function on  $\vec{w}_{tot}$  is implicitly given in equation (2.76), since the node weights strictly depend on the values of  $P_j$ . The back-propagating multilayer perceptron now updates these weights  $\vec{w}_{tot}$  iteratively based upon a gradient search of the global minimum with a *learning-rate*  $\iota$ :

$$\vec{w}_{tot}(i+1) = \vec{w}_{tot}(i) - \iota \frac{\partial L(\vec{w}_{tot})}{\partial \vec{w}_{tot}}. \quad (2.77)$$

In order to achieve convergence of this iterative process a minimum in  $L(\vec{w}_{tot})$  is necessary. As pointed out by R. Polikar, such minima of the error surface function can either be local or global [84]. Thus convergence of equation (2.76) is dependent on the initial settings of the weights and does not necessarily converge to the global minimum.

Other typical problems faced in back-propagating MLPs are the appropriate choices of the learning-rate, the network structure and the threshold level of the error function. The latter one is used as abortion criteria, which assumes that the network is sufficiently trained when this threshold level is reached.

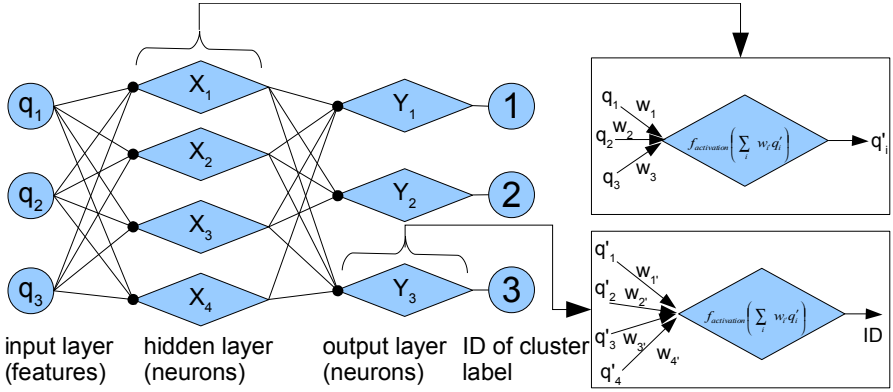


Figure 2.36.: Schematic structure of a back-propagating multi-layer perceptron with one hidden layer.

While the learning-rate and the network structure can often be determined empirically, a low threshold level of the error function can result in *over-training* of neural networks. Then the neural network tries to capture the characteristics of the input objects very detailed. In practice this often comes close to learning the “noise” in the feature distributions of the given objects.

After successful training of neural networks, their ultimate strength is the computationally fast reapplication of complex decision boundaries to objects with unknown class identifier.

### Semi-automated feature selection and cluster validation

The goal of the presented unsupervised pattern recognition methodology is to introduce a semi-automated technique to detect promising feature combinations for feature based clustering of acoustic emission signals. In contrast to subsequent reduction of features based on correlation dendrograms an exhaustive search of global optimal combinations of the used signal features is performed, which is schematically shown in the flowchart in figure 2.37.

As already pointed out by R. Polikar such exhaustive search methods are conceptionally simple but computationally devastating since the number of feature combinations to investigate grows combinatorial [84]. Consequently, before application of the presented exhaustive search method an educated preselection of promising features for description of the respective acoustic emission signals is suggested. This in turn can be done by subsequent reduction of redundant features identified in correlation dendrograms as described in

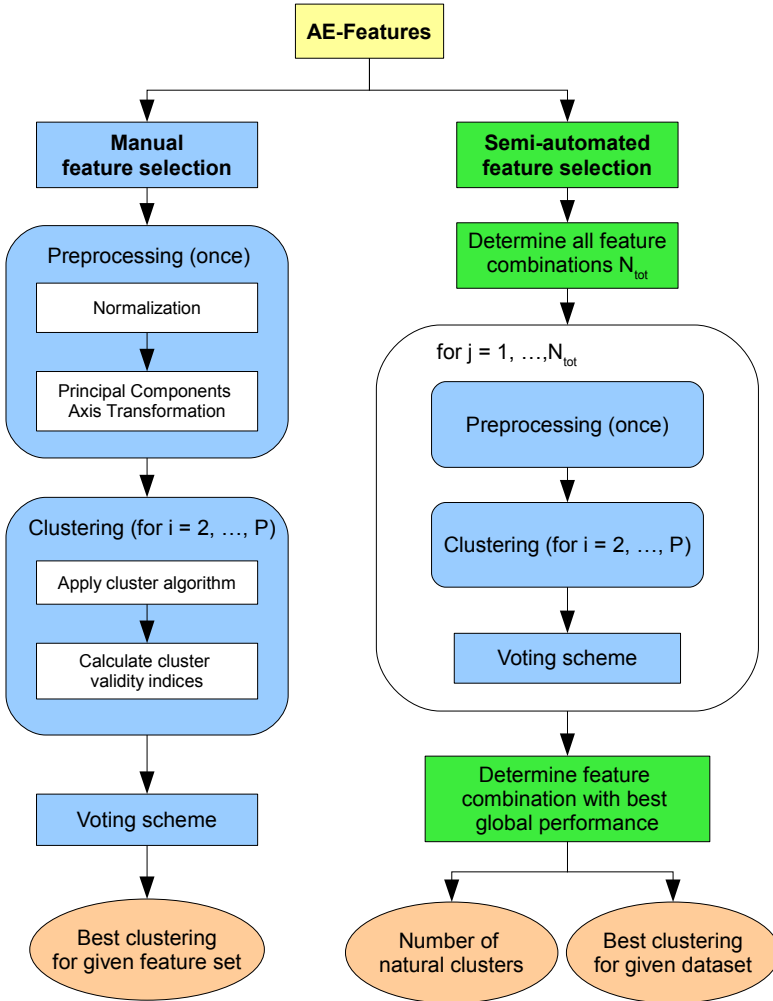


Figure 2.37.: Flowchart of the pattern recognition process with manual feature selection (left) and semi-automated feature selection (right).

## 2. Theoretical background and developments

section 2.3.3, by their physical relevance for the distinction process (see chapters 3 and 4) or their reliability<sup>9</sup>.

In order to screen all possible feature combinations with a given minimum number of features  $Q_{min}$  to be used for clustering, the total number  $N_{tot}$  of combinations for  $Q$  features is thus:

$$N_{tot} = \sum_{i=Q_{min}}^Q \binom{Q}{i}. \quad (2.78)$$

Whilst for many pattern recognition application the value of  $Q$  can reach hundred or thousand features, for description of acoustic emission signals this can be reduced to an amount  $Q < 20$  by reasonable efforts. For larger numbers of  $Q$  more efficient search algorithms, like the depth-first, the breadth-first or the hill-climb algorithm are used to avoid exhaustive search procedures [84,91]. However, none of them is guaranteed to find the optimal feature combination to separate natural clusters of objects within the dataset [84]. For unsupervised pattern recognition of acoustic emission signals, the proposed feature selection method proceeds as depicted in figure 2.37.

After calculation of the total number  $N_{tot}$  of feature combinations, all preprocessing options, like normalization or principal components projection are applied for each feature combination. Subsequently the cluster algorithm calculates the respective partitions for 2, 3, 4, ...,  $P$  clusters, with  $P$  as maximum chosen number of clusters. For each partition four cluster validity indices are calculated and evaluated in the following modified voting scheme adapted from S. Günter and H. Bunke [127]:

1. The number of clusters with the best index performance is given  $P$  points.
2. The number of clusters with second-best performance is given  $(P - 1)$  points.
3. The number of clusters with third-best performance is given  $(P - 2)$  points.
- ⋮

( $P-1$ ). The number of clusters with worst performance is given 2 points.

For the present investigations the Dunn-Index (*DUNN*), the Tou-Index (*TOU*), the Davies-Bouldin-Index (*DB*), and the  $\Gamma$ -Index (*GAMMA*) was

---

<sup>9</sup> Features obtained relative to the arrival time are strongly correlated to the trigger process and should be used carefully.

## 2. Theoretical background and developments

used. Afterwards the voting points from all validity indices are cumulated in dependence of cluster number and evaluated for the global maximum in points. If two cluster numbers have an equal value of voting points, the lower number of clusters wins. The respective number of clusters is defined as numerical optimal and thus is selected for the current feature set. This evaluation is schematically shown in figure 2.38 for one feature combination.

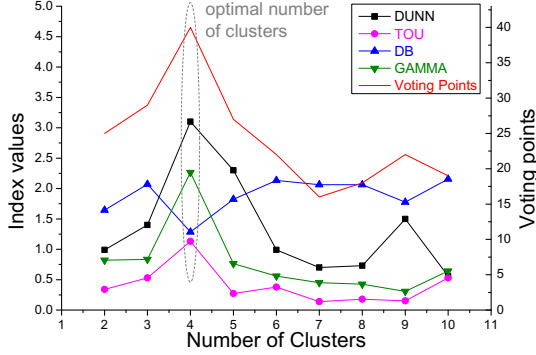


Figure 2.38.: Evaluation of optimal number of clusters for one feature combination using voting scheme with *DUNN*, *TOU*, *DB* and *GAMMA* indices and  $P = 10$  clusters.

In the current investigation the clustering approach shown in figure 2.37 is based on a fixed scheme including normalization by unit variance, principal components projection and subsequent clustering by the k-means algorithm. The suitability of these settings is based on preceding investigations on classification of acoustic emission signal types [93, 128, 129]. It is worth to point out, that the so obtained optimal feature combinations are inevitably linked to the chosen preprocessing and the chosen cluster algorithm. Consequently, these settings should be modified fitting the specific needs of the classification problem investigated.

To demonstrate the suitability of the presented approach the method is tested using an artificial dataset composed of 1000 objects with  $Q = 10$  features and 4 hidden<sup>10</sup> classes. To reflect realistic conditions with unequally distributed classes, class 1 holds 600 objects, class 2 holds 250 objects, class three only 100 objects and class 4 merely 50 objects. Only the first five features are

<sup>10</sup> The term “hidden” reflects that the cluster algorithm has no information about the class labels of the individual objects.

characteristic for the identification of the hidden classes. Further three features do not contain discriminative information since they are solely uniformly distributed “scatter”. The remaining two features are not useful either, since they are a squared normal distributed feature and one normal distributed feature superimposed by an uniform distribution. The so prepared set of objects is shown in figure 2.39 for the five characteristic features in a scatterplot matrix and exemplarily for one scattering feature and one distribution feature in figure 2.40. The colour of the data points in both figures reflects the class labels of the individual objects.

As depicted in figure 2.39 a single characteristic feature is not sufficient to distinguish all hidden classes, since each characteristic feature has an overlapping range of at least two hidden classes, as e.g. shown in the plot of feature 1 over feature 2. Clearly, the scatter and distribution features are not useful for the discrimination between the hidden classes. Instead they could cause formation of new artificial clusters, like composed of the top three data points in figure 2.40b. Thus the proposed method should be robust against such inappropriately chosen features.

If a lower limit  $Q_{min} = 5$  of features is used, from the prepared set of objects and features a clear identification of the first five features with a partition into 4 clusters is expected as optimal selection. In general, less than five features can also provide sufficient discriminative power to separate the hidden classes. Consequently, the minimum number of features  $Q_{min}$  used for the clustering procedure has to be chosen adequately to the faced pattern recognition problem. In particular, low values for  $Q_{min}$  can result in better values for the cluster validity indices. On the contrary, this can also originate from a dominant contribution of only one single feature, which is not related to the natural clusters within the dataset.

The result of the exhaustive search with  $Q_{min} = 5$  is shown in figure 2.41 in a scatterplot of all cluster validity index combinations. Each data point corresponds to a distinct feature combination. The optimal number of clusters obtained for the respective feature combination is encoded by the color of the data point. In addition, the positions of the numerically best separated clusters are marked by gray ellipses for the respective index combination.

As combined result of all index values (high *DUNN*, low *DB*, high *TOU*, high *GAMMA*) only one feature combination was found with best global performance. This is the expected combination of the five characteristic features as marked in figure 2.41. Instead, all other feature combinations are numerically worse and refer to feature combinations, which should not be used for clustering, since their respective clusters are less distinctly separated. This is demonstrated by the respective positions of one feature combination associated with a separation into two clusters. This feature combination is marked in figure 2.41 by a black



## 2. Theoretical background and developments

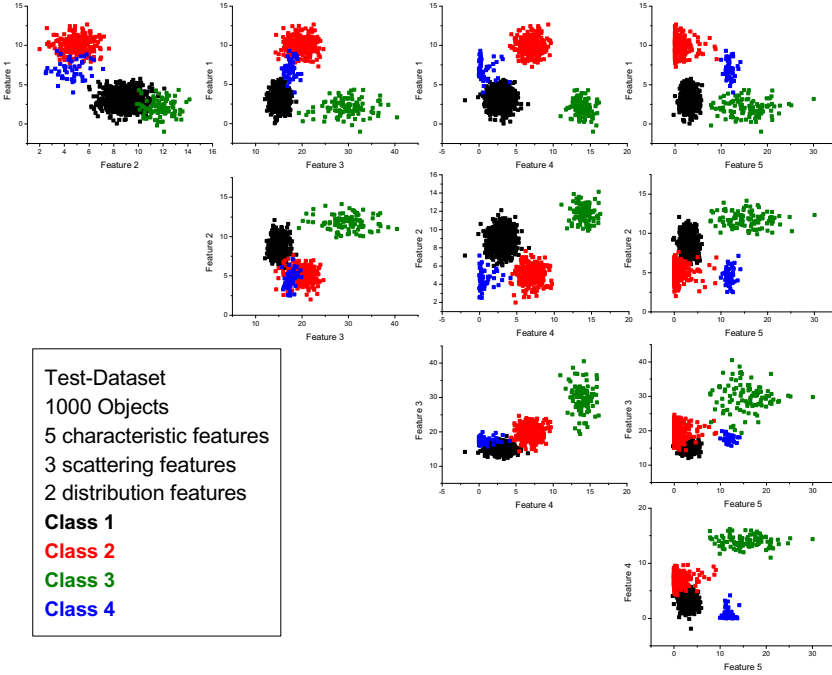


Figure 2.39.: Scatterplot representation of the first five features of an artificial dataset used to evaluate the performance of the feature selection procedure. The four hidden classes are marked in colour.

frame around the data point. While values for *DB* and *DUNN* are well located within the optimal ranges, this is not the case for the *GAMMA* index value. This result is representative for the rest of the clusters located within the numerical optimal ranges of the different validity indices. In summary, only the marked feature combination shows best global performance, where “global” refers to the combined evaluation of all cluster validity indices values. It is worth to point out, that the majority of the feature combinations suggest a separation into two classes, as indicated by the color of the data points. This is completely irrelevant for the global feature selection procedure, since the numerical indices of the respective data points are all worse than those of the globally optimal feature combination.

However, for application of this approach to acoustic emission signals often less pronounced optimal feature combinations are found. Thus for realistic

## 2. Theoretical background and developments

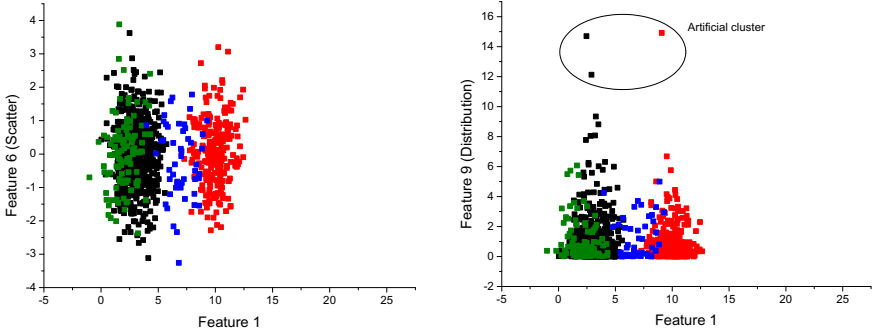


Figure 2.40.: Exemplarily representation for the scattering feature (left) and the distribution feature (right) plotted over the characteristic feature 1. The four hidden classes are marked in colour.

applications the various near-optimal partitions should be investigated as well. For pattern recognition of features from acoustic emission signals, the plot *DB* over *GAMMA* was found to be best for selection of the optimal feature combination. Consequently, this diagram is used in the following for identification of promising feature combinations for classification of acoustic emission signals.

In order to decrease the computational complexity of the exhaustive search procedure, it can be useful to apply the procedure to a statistically representative subset instead of the complete dataset. Figure 2.42 shows a comparison of the results obtained for a random subset of 100, 250 and 500 objects and the complete dataset with 1000 objects in plots of *DB* over *GAMMA*. Clearly all investigation results indicate the same optimal feature combination consisting of the five characteristic features. Although the absolute numerical value scatters in dependence of the subset size, the relative positions of the optimal feature combinations are very comparable. Thus a random reduction of the number of objects belonging to a dataset does not drastically influence the performance of the method, as long as classes with a low number of objects are not over-reduced and vanish in the scatter of the adjacent clusters. For the given artificial dataset, cluster four is statistically reduced to 1/10 of its original size, which results in merely 5 objects to be identified as separate cluster.

In summary, pattern recognition techniques used for acoustic emission signals require a careful feature selection. The presented approach is capable of an automated selection of promising feature combinations in terms of numerical

## 2. Theoretical background and developments

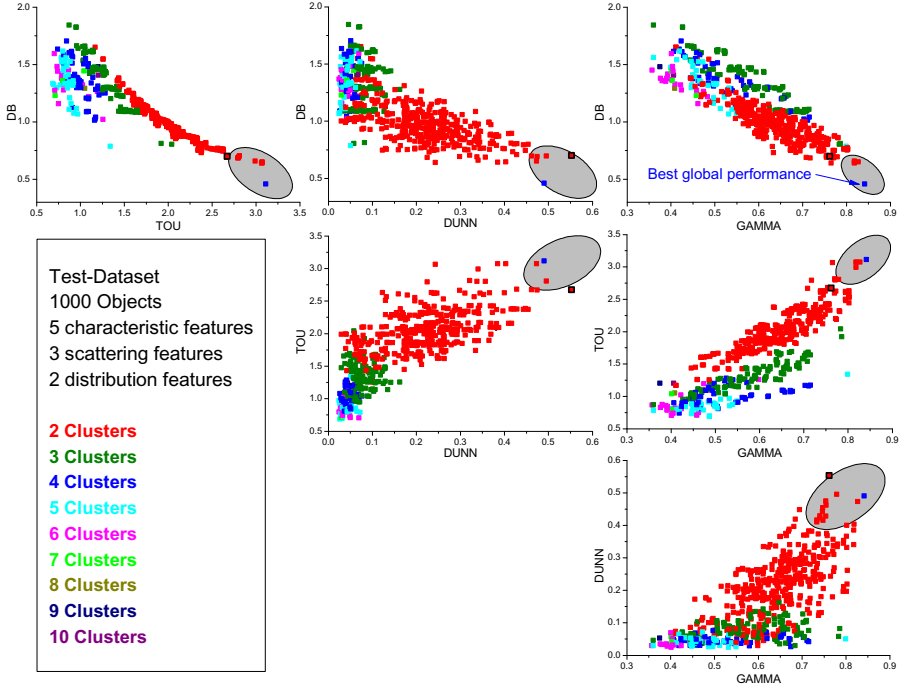


Figure 2.41.: Result of the exhaustive search procedure. The different feature combinations are shown in a scatterplot matrix of the cluster validity indices. The optimal number of clusters for each feature combination is encoded in color.

separation of the respective partition. If the detected features are suitable for the description of similarities of the signals in terms of their physical origin is not evaluated in the approach. For the present investigation the approach shown in the flowchart of figure 2.37 utilizing normalization by unit variance, principal components axes projection and the k-means algorithm yields reasonable results for acoustic emission signals originating from composite failure.

## 2. Theoretical background and developments

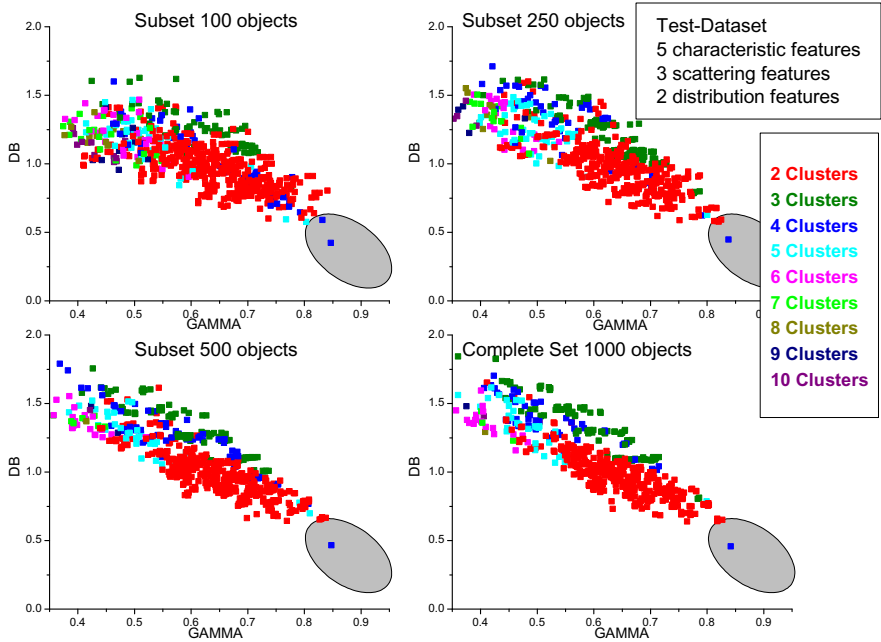


Figure 2.42.: Result of the exhaustive search procedure with various subset sizes. The different feature combinations are shown in plots of  $DB$  over  $GAMMA$ . The optimal number of clusters for each feature combination is encoded in color.

## 2.4. Time-frequency analysis

In order to understand the information carried by a transient acoustic emission signal it is often useful to analyze the signal in the frequency domain. This reveals the characteristic frequency range of the signal and can be used to interpret its origin. Usually the Fourier-Transformation is used to achieve the transformation from signals in the time domain to the frequency domain<sup>11</sup>, which is defined as

$$\tilde{U}_{CFT}(\omega) = \frac{1}{\sqrt{2\pi}} \int_{-\infty}^{+\infty} U(t) \cdot e^{-i\omega t} dt. \quad (2.79)$$

This can also be written in polar form

$$\tilde{U}_{CFT}(\omega) = \tilde{U}(\omega) \cdot e^{-i\theta(\omega)}. \quad (2.80)$$

The result of the transformation is typically presented as continuous amplitude spectra  $\tilde{U}(\omega)$  and phase spectra  $\theta(\omega)$ . Since experimental signals are typically finite in extent and sampled in discrete time intervals, one major problem of the continuous Fourier-Transformation as defined in equation (2.79) is the integration within the boundaries from  $-\infty$  to  $+\infty$ . To this end usually the discrete Fourier-Transformation in combination with suitable window functions is used. The window functions are used to provide a convenient decay of a finite signal, which is required to minimize the effect of spectral leakage [71]. This occurs when the signal is non-periodic within the recorded duration  $[-N_S; N_S]$  using  $2N_S + 1$  samples. In the case of transient signals a multitude of window functions exist which can be used to achieve these boundary conditions. A closer review on this topic is thus found in [71], since the different window functions are typically chosen specifically for the type of signal under investigation. The discrete Fourier-Transformation for a transient signal with  $2N_S + 1$  discrete values  $U_j$  sampled in time intervals  $\Delta T$  is given as:

$$\tilde{U}_{DFT}(\omega) = \frac{1}{\sqrt{2\pi}} \sum_{j=-N_S}^{N_S} U_j \cdot \Delta T \cdot e^{-i\omega \Delta T}. \quad (2.81)$$

In the following investigation the term Fourier-Transformation is always understood as discrete Fourier-Transformation. In particular, the computationally efficient algorithm known as Fast Fourier-Transformation was used. As a prerequisite to the application of the discrete Fourier-Transformation,

---

<sup>11</sup> Sometimes the Fast-Hartley Transformation is applied as well [40].

## 2. Theoretical background and developments

the signal under investigation has to be sampled sufficiently high within the frequency range of interest. This requirement is formulated by the Nyquist-Shannon sampling theorem, which defines the minimum sampling rate  $\Delta T_{\min}^{-1}$  necessary to resolve a given frequency [130]:

$$\Delta T_{\min}^{-1} > 2(f_{\max} - f_{\min}). \quad (2.82)$$

While the information of the frequency distribution is particularly useful for the interpretation of transient signals, a simple Fourier-Transformation still cannot provide any information on the temporal evolution of the frequencies of a transient signal.

To overcome this limitation, transformations from time domain to the time-frequency domain are used to obtain further information of the signal behavior. For acoustic emission signals the typical transformations used to calculate this behavior are the *Short-Time-Fourier-Transformation* (STFT), the *Wavelet-Transformation* (WT) and *Choi-Williams-Distributions* (CWD) [76, 131, 132]. In the following only a short introduction to these time-frequency distributions is given, while a more detailed review on Wavelet-Transformations is instead found e. g. in [133, 134] and on Choi-Williams-Distributions in the original work by H.-I. Choi and W. Williams [135].

The Short-Time-Fourier-Transformation is a straight-forward approach to provide time-dependent frequency information of a signal. Before application of the discrete Fourier-Transformation the signal is convolved with a Gaussian window to remove the signal information outside the time interval spanned by the window as shown in figure 2.43. Subsequently the FFT is calculated for the convolved signal and plotted versus the center position of the Gaussian window. To reach quasi-continuous temporal resolution, the position of the Gaussian window is shifted along the time axis of the signal and the result of each FFT is plotted over time. This process is schematically shown for a typical acoustic emission signal in figure 2.43. Clearly the time-frequency content is very discrete along the time and frequency axis, but the dominant time-frequency behavior is reflected in the obtained diagram. This discretization is caused by the finite temporal resolution given by the size of the Gaussian window and the finite frequency resolution given by the intervals of the discrete Fourier-Transformation. Thus the time-frequency domain is subsampled in a rectangular array with finite extent as shown schematically in figure 2.44.

For most transient signals it is advantageous to change the temporal resolution adaptive to the frequency, based upon the different wave-lengths associated with different frequencies. This can be done by Wavelet-Transformations. The basic idea of a Wavelet-Transformation is to provide a suitable scaled function for convolution at each point in the time-frequency domain. These func-

## 2. Theoretical background and developments

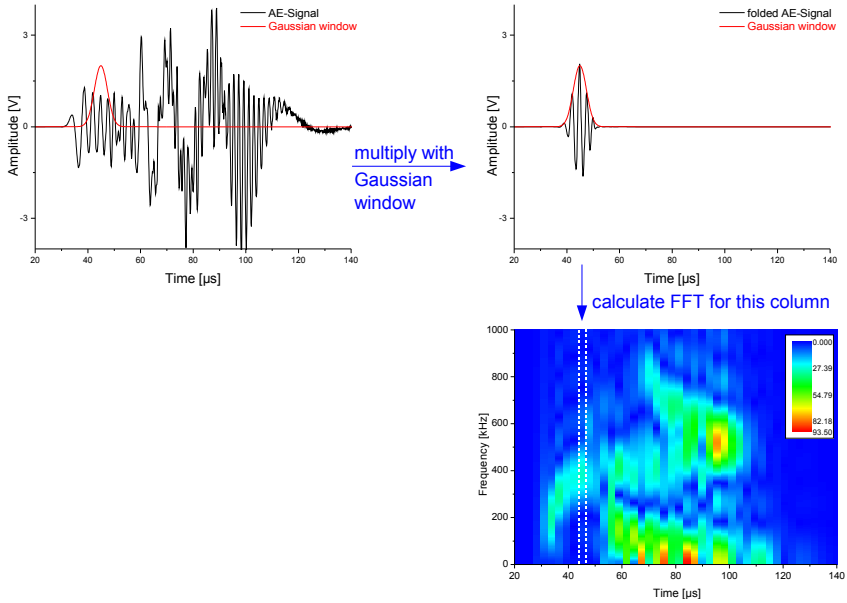


Figure 2.43.: Calculation of time-frequency transformations for the Short-Time-Fourier-Transformation.

## 2. Theoretical background and developments

tions, the so-called *wavelets*, are based on a specific prototype-function termed *mother-wavelet*.

As schematically shown in figure 2.44 the time-frequency resolution is not equally distributed as for the STFT, but instead changed adaptively. Thus the temporal resolution for higher frequencies (small wave-lengths) is increased to provide better temporal accuracy, while the temporal resolution at lower frequencies (long wave-lengths) is decreased to provide more accurate frequency resolution. Thus the overall resolution within the time-frequency domain is more adaptive to the nature of transient signals. In this context it is important to point out, that the area contained within each box in figure 2.44 has to be equal for each position in the time-frequency domain. This is a consequence of Heisenberg's inequality. Thus the absolute value for the chosen size of the area (time-frequency resolution) can be changed by different Gaussian windows and FFT-resolutions for the STFT or other mother wavelet types for the WT, but the lower boundary for the area is always given by  $\pi/4$  based on Heisenberg's uncertainty principle. As for the Fourier-Transformation, there is a continuous Wavelet-Transformation (CWT) and a discrete Wavelet-Transformation (DWT). While the DWT is often used for obtaining quantitative information using the discrete wavelet-coefficients [7, 136], this was not used in the present thesis. Instead, the discretized version of CWT (which is not equivalent to the DWT) was used for interpretation and visualization of acoustic emission signals.

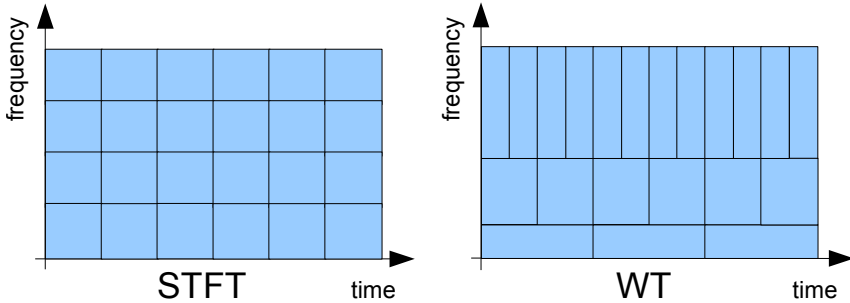


Figure 2.44.: Comparison of time-frequency resolution for Short-Time-Fourier-Transformation and Wavelet-Transformation.

The discrete continuous Wavelet-Transformation coefficients  $\aleph_{CWT}(\vartheta, \varsigma)$  for



## 2. Theoretical background and developments

a discrete transient signal are given by equation:

$$\aleph_{CWT}(\vartheta, \varsigma) = \sum_{i=0}^{N_S} U_i \Delta T \cdot \Psi_{\vartheta, \varsigma}(t). \quad (2.83)$$

$$\Psi_{\vartheta, \varsigma}(t) = \frac{1}{\sqrt{\vartheta}} \Psi\left(\frac{t - \varsigma}{\vartheta}\right) \quad (2.84)$$

The function  $\Psi_{\vartheta, \varsigma}(t)$  is called the *wavelet-function* of scale  $\vartheta > 0$  and location parameter  $\varsigma \in \mathbb{R}$ . The wavelet-function has to fulfill the admissibility condition, which is required for the wavelet-functions to provide an orthonormal base:

$$0 < \int_{-\infty}^{+\infty} \frac{|\tilde{\Psi}(\omega)|^2}{|\omega|} d\omega < \infty. \quad (2.85)$$

For the present investigation a Gabor-type wavelet was used, which was shown to be appropriate for analysis of acoustic emission signals by H. Suzuki et al. [137]. The Gabor mother-wavelet with centre frequency  $\omega_c$  is given as

$$\Psi(t) = \pi^{-1/4} \sqrt{\left(\frac{\omega_c}{\pi \sqrt{2/\ln(2)}}\right)} \cdot e^{-\frac{t^2}{2} \left(\frac{\omega_c}{\pi \sqrt{2/\ln(2)}}\right)^2 + i\omega_c t}. \quad (2.86)$$

The result of the discrete CWT for a typical acoustic emission signal obtained from pencil-lead fracture on a 4.7 mm thick Aluminum plate as provided by [138] is shown in figure 2.45. Here, the magnitudes of the WT-coefficients  $\aleph_{CWT}(\vartheta, \varsigma)$  are given as pseudo-color diagram. The adaptive change of time- and frequency-resolution of the CWT yields a smoother result than those obtained from the STFT. But as consequence of the adaptive time-frequency resolution shown in figure 2.44, spikes along the time-axis for lower frequencies and along the frequency-axis for higher frequencies can occur. Recently M. Hamstad used Choi-Williams-Distributions to visualize the time-frequency behavior of acoustic emission signals [139]. In comparison to the CWT-results, these yield even sharper results of the time-frequency behavior as shown in figure 2.46 in a direct comparison of STFT, CWT and CWD of the same acoustic emission signal.

In addition, the dispersion curves for the first two fundamental Lamb wave modes, as calculated for a 4.7 mm thick Aluminum plate are superimposed to the CWT-result in figure 2.45. Such comparison can be done for signals with

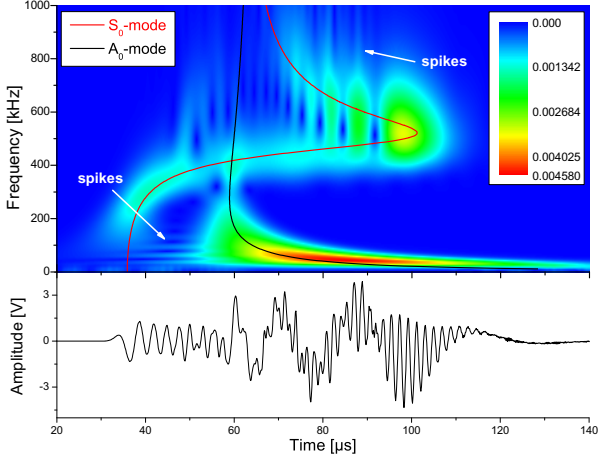


Figure 2.45.: Comparison between AE-signal in time-domain, continuous Wavelet-Transformation based on Gabor-Wavelet and dispersion curves for the first two fundamental Lamb wave modes for an Aluminum plate with 4.7 mm thickness, longitudinal sound velocity 6320 m/s and transversal sound velocity 3100 m/s.

known distance  $r$  between source and point of detection utilizing the dispersion curves of the group velocity as:

$$t = \frac{c_G^{-1}}{r}. \quad (2.87)$$

These scaled dispersion curves agree well with the intensity of the CWT in the time-frequency domain. Such comparison can thus be used to analyze the composition of Lamb wave modes of the signal and their individual intensity. Although various early studies realized, that propagation of acoustic emission signals in plate-like structures is realized by guided waves [55, 140–142], the valuable information carried by these were not addressed before the investigations of M. Gorman and W. Prosser [56, 143, 144]. These investigations introduced a new field of acoustic emission science called *Modal Analysis*. In general, this technique is not fixed to analysis of Lamb waves, but can also be applied to other types of guided waves, like those observed in shells, pipes and rods. Modal analysis is often used to improve the localization accuracy in such structures, since it is able to take into account the difference in propagation

## 2. Theoretical background and developments

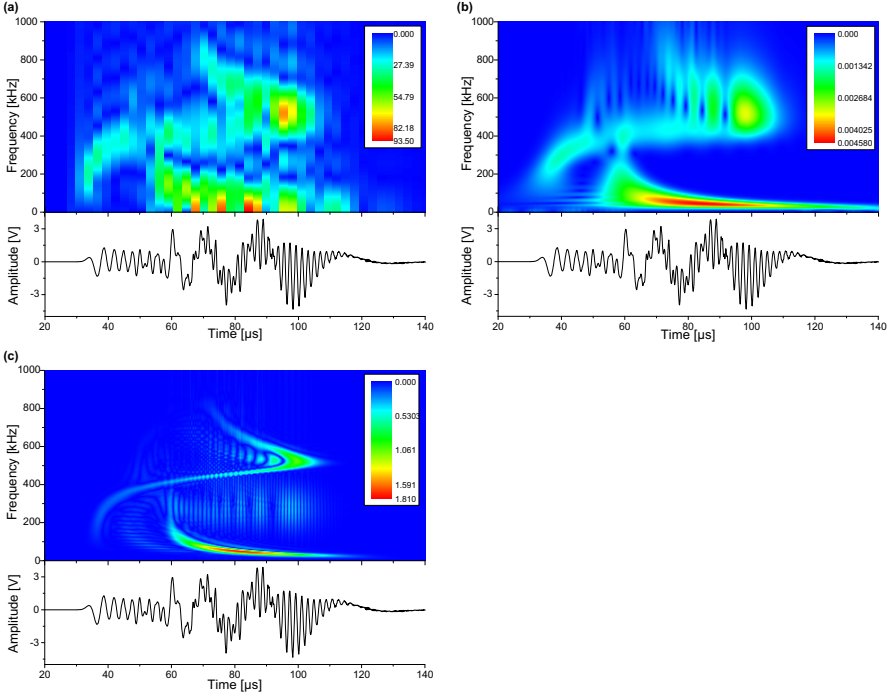


Figure 2.46.: Comparison of different time-frequency transformations applied to the same acoustic emission signal provided by [138]. Result of STFT (a), CWT (b) and CWD (c).

behavior of guided waves compared to those of bulk-waves [69]. In the case of Lamb waves as shown in the example in figure 2.45 the propagation velocity of the  $S_0$ -mode is usually required for localization of acoustic emission sources based upon the initial arrival time, since it is propagating faster than the other Lamb wave modes.

Furthermore, modal analysis can be used to identify source mechanism of acoustic emission based on the intensity ratios of the different propagation modes of guided waves. An exhaustive investigation on such identification procedures is given by M. Hamstad et al. [76], who compared the CWT of signals obtained from FEM-simulations in dependence of source position and source type. For an isotropic planar geometry it was demonstrated that the intensity of the  $S_0$ - and the  $A_0$ -mode are characteristic for a certain type of failure, as long as the changes in source position are relatively small and no

## 2. Theoretical background and developments

dominant reflections from the boundaries occur. In particular it was shown, that a change in the depth position of the source can yield similar CWT diagrams like those originating from different failure types.

The correlation between the occurrences of dominant  $S_0$ - or  $A_0$ -modes and the source type is caused by the characteristic source radiation patterns as discussed in section 2.2.2 [144–146]. Thus source radiation patterns with dominant in-plane components show a dominant excitation of the  $S_0$ -mode. In contrast, source radiation patterns with large out-of-plane components result in excitation of a dominant  $A_0$ -mode. During propagation in CFRP the different modes show different attenuation [56], which intrinsically limits the usage of the intensity-ratio  $A_0/S_0$  to characterize the source mechanism to a certain propagation distance. The frequency distributions of the detected signals in turn are correlated to the intensity-ratio  $A_0/S_0$ . This is caused by the characteristic propagation frequency, which is higher for the  $S_0$ -mode than for the  $A_0$ -mode. Consequently, the different contributions in the Fourier-spectra can be understood to originate from different  $A_0/S_0$  intensity ratios.

Whilst the calculation of DFT or CWT of a single transient signal can easily be done by various software packages, a typical requirement in acoustic emission analysis is the interpretation of the mean information carried by a multitude of signals, which were classified to represent a certain type of acoustic emission source.

Inspired by the calculation of the average FFT presented by J. Bohse [147] the software package AWARE++ was realized within the scope of this thesis<sup>12</sup>. Although the software is capable of numerous analyzation routines, which are commonly applied to transient signals, its main purpose is the calculation of average FFT spectra and average CWT diagrams to yield a mean representation of a group of acoustic emission signals. Since the full manual of AWARE++ is found in Appendix A, only a short explanation of the calculations used for the averaging process is given in the following.

Following the definition of the discrete Fourier-Transformation in equation (2.81), the average FFT spectra  $\langle \tilde{U}_{FFT}(\omega) \rangle$  for  $n$  transient signals is defined as

$$\langle \tilde{U}_{FFT}(\omega) \rangle = \frac{1}{n} \sum_{i=1}^n \tilde{U}_{FFT,i}(\omega) \quad (2.88)$$

with  $\tilde{U}_{FFT,i}(\omega)$  being the complex Fourier-coefficients of the  $i$ -th transient signal. In addition to the average value of the Fourier-coefficients, their

---

<sup>12</sup> **A**dvanced **W**aveform **A**nalysis and **R**esearch **E**ngine (written in C++)

## 2. Theoretical background and developments

standard deviation and extreme values can be calculated as explained in detail in Appendix A.

Similar in its concept, the average complex CWT coefficients  $\langle \aleph_{CWT}(\vartheta, \varsigma) \rangle$  for  $n$  transient signals are defined as

$$\langle \aleph_{CWT}(\vartheta, \varsigma) \rangle = \frac{1}{n} \sum_{i=1}^n \aleph_{CWT,i}(\vartheta, \varsigma) \quad (2.89)$$

with  $\aleph_{CWT,i}(\vartheta, \varsigma)$  being the complex CWT coefficients of the  $i$ -th signal. The implementation of the averaging process uses the convolution theorem applied to the definition of the Wavelet-Transformation in equation (2.83) and is described in more detail in Appendix A. An exemplary result of the calculated average CWT of two transient signals is shown in figure 2.47. Clearly, the average CWT diagram exhibits the time-frequency characteristics of both signals and thus can act as measure of the common time-frequency behavior of the two signals.

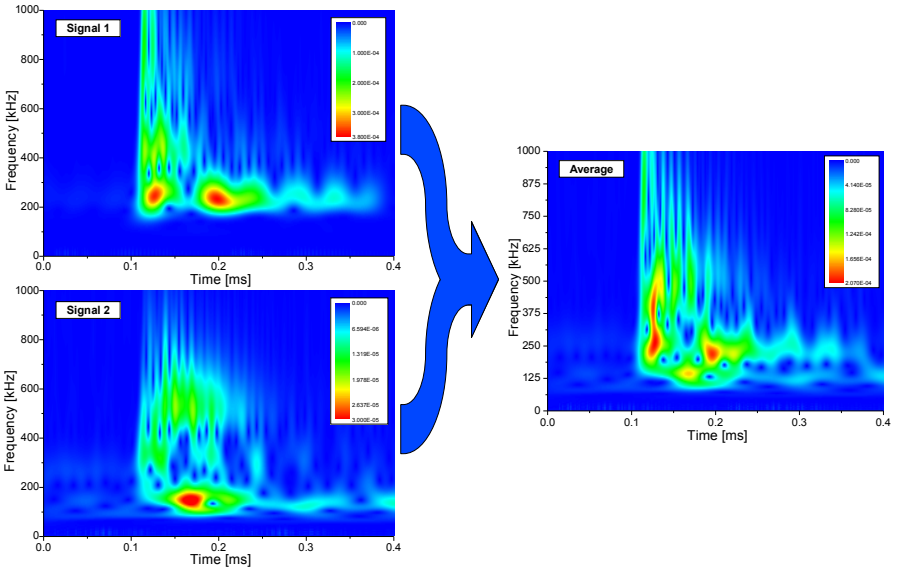


Figure 2.47.: Calculation of average CWT using AWARE++, for an example of two transient signals.

In summary, the visualization in time-frequency representation is very useful to analyze the physical origin of the acoustic emission signals. In order to

## *2. Theoretical background and developments*

correlate the experimentally recorded signals to certain failure mechanism based on frequency or time-frequency characteristics requires fundamental knowledge of the correlation between the signal characteristics and the failure type. To understand the different factors which influence the experimentally observed acoustic emission signal, finite element simulations of acoustic emission signals as discussed in the following chapter are used.

## 3. Simulation of acoustic emission signals

In this section the results of a finite element method (FEM) approach for simulation of acoustic emission signals are presented. Section 3.1 starts with a new concept of acoustic emission source model, which takes into account the microscopic elastic properties in the vicinity of the crack tip. This is used to model the typical failure mechanisms observed in CFRP and coatings on CFRP substrates. The consecutive section 3.2 describes modeling of signal propagation within CFRP-plates with a focus on the formation of Lamb waves. Section 3.3 deals with the detection process of acoustic emission signals. Here a detailed model of the experimentally used broadband sensor is introduced and its influence on the signals shape and frequency content is discussed. Section 3.4 holds a systematic investigation of the source excitation parameters, which influence the properties of the detected acoustic emission signals. Here, the source excitation time, the source energy and the influence of the source position relative to the point of detection are investigated and compared to the predictions from the theories introduced in section 2.2.2. In the last section 3.4.4, the influence of the geometry of the propagation medium is investigated. The possibility to distinguish the distinct failure types occurring in CFRP based on frequency characteristics of the signals is discussed.

In the following sections only the model descriptions and their results will be presented. In addition, the basic differential equations used within the “Structural Mechanics Module” of the software environment “COMSOL” are found in Appendix C.

### 3.1. Model of acoustic emission source

For the present investigation, the microscopic acoustic emission source of interest is crack formation and crack progress within a material. As discussed in section 2.2.2 such acoustic emission sources are typically modeled by point sources with complex radiation patterns adapted to the type of failure as shown in figure 2.11. As formulated within the generalized theory of acoustic emission the according excitation of a small elastic wave, which is released

### 3. Simulation of acoustic emission signals

into the surrounding medium can than be deduced from the theory of elastic waves [36]. Although these currently used source representations are well established to model the excitation of acoustic emission signals [38, 39, 43, 45, 146, 148], they do not focus in detail on the microscopic elastic properties of the cracking medium and the exact geometry of the crack with respect to the surrounding medium. There are two ways to obtain a more realistic model for acoustic emission excitation. On the one hand, the source can be described by the force distribution around the crack tip, on the other hand realistic parameters describing crack propagation are the time-dependence and displacement amplitude of the newly formed crack surface. As will be demonstrated in the following not only the geometry of the crack, but also the inhomogeneous elastic properties of the cracking medium around the crack influence the characteristics of the excited elastic waves. Therefore the term acoustic emission source will always refer to the crack geometry, the temporal behavior of the crack surface movement and the elastic properties of the surrounding medium.

To describe the release of elastic waves from such crack progress a new acoustic emission source model is used. The presented source geometry includes spatial dimensions of the crack located within the cracking medium. In the case of coating failure and CFRP failure this is shown schematically on the left panels in figures 3.1-a and 3.1-b including the different materials surrounding the source. The corresponding geometric implementation as acoustic emission source model is shown on the right panels of figures 3.1-a and 3.1-b, respectively. For simulation of the crack a cross-shaped volume is cut out of the cracking medium. This enables quasi-independent movement of the “cracks” surfaces in x, y, or z direction and allows simulation of all possible combinations of displacement directions without changing the mesh of the model. This is advantageous, since minor changes in the mesh resolution can influence the exact comparability of the calculation result.

For the investigated double layered coating systems mode-I cracks typically propagate in a crack-through process of the respective layer. Here the size of the acoustic emission source model is in the range of the coatings thickness ( $10\text{ }\mu\text{m}$  to  $50\text{ }\mu\text{m}$ ). Therefore the cross-shaped volume is scaled to fit the thickness of the investigated coating layer as shown in figure 3.1-a. The crack surface displacement is directed along the x-axis to simulate mode-I cracking. Coating delamination is modeled with an enclosed cross-shaped volume located at the interface between the two coating layers and crack surface displacement in z-direction. The microscopic elastic anisotropy is taken into account by the elastic properties of the different coating layers and the CFRP substrate.

For the different failure mechanisms in CFRP this microscopic anisotropy is more pronounced. Here the acoustic emission source is modeled by a resin



### 3. Simulation of acoustic emission signals

cube surrounding one embedded carbon fiber. This can be used to simulate fiber breakage, or interfacial failure, when choosing appropriate crack surface deflections (see below). For stacking sequences with other fiber axis orientations than along the x-axis, the embedded carbon fiber was rotated respectively. The resin cube and the carbon fiber in turn are enclosed in an adjacent cube acting as perfectly matched layer (PML). Within this PML the microscopic elastic properties are gradually adjusted to those of the surrounding macroscopic medium (CFRP) in order to provide a gradient free transition of elastic properties. For simulation of pure matrix cracking, the model-fibers elastic properties were replaced by the elastic properties of the resin cube.

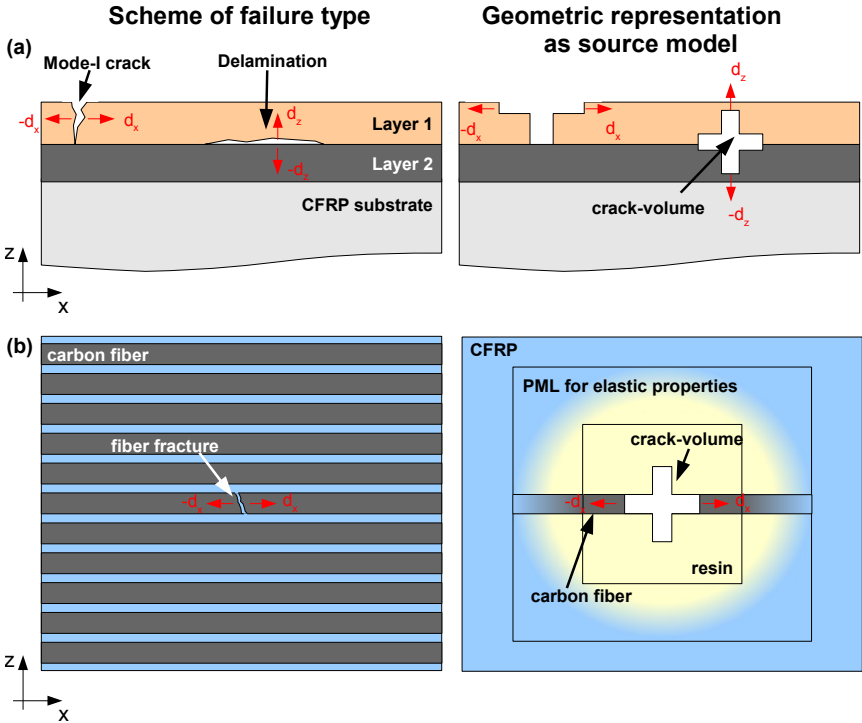


Figure 3.1.: Scheme of coating failure (a) and single fiber-fracture (b) with respective 2-dimensional representation as acoustic emission source model (right panels).

A typical quarter-volume representation of the acoustic emission source

### 3. Simulation of acoustic emission signals

model for CFRP failure is shown in figure 3.2-a in three dimensions. For the quarter-volume case the  $yz$ - and the  $xz$ -plane were chosen as symmetry-plane. For simulation of all failure types in CFRP the dimensions of the source are usually given by a rectangular model-fiber with cross-section  $(10 \times 10) \mu\text{m}^2$  and  $35 \mu\text{m}$  length, which is embedded in a resin cube of  $100 \mu\text{m}$  edge length. The surrounding PML cube has an edge length of  $200 \mu\text{m}$ . The gradual change of elastic properties realized by the PML is shown exemplarily in figure 3.2-b as diagram of the density in the vicinity of the source. This was realized by a gradual change of the elastic coefficients of carbon fiber and resin  $C_{iklm,0}$  to the macroscopic properties of the CFRP  $C_{iklm,1}$  according to:

$$C_{iklm}' = \begin{cases} C_{iklm,0} & \Delta r < r_{cube} \\ C_{iklm,0} + \left( \left( \frac{\Delta r}{r_{cube}} - 1 \right) \cdot (C_{iklm,1} - C_{iklm,0}) \right) & r_{cube} \leq \Delta r \leq 2r_{cube} \\ C_{iklm,1} & \Delta r > 2r_{cube} \end{cases}$$

Here  $r_{cube}$  denotes the length of the used resin cube and  $\Delta r$  the current distance to the source models center position. Dependent on the source position and the chosen specimen geometry different symmetry-planes were used. Consequently, the source model was either used in its full volumetric representation, as half-volume model or as quarter-volume model.

The simulations of metal cracking were done for copper and nickel coatings applied on CFRP substrates. All simulations of failure mechanisms in CFRP were done for the unidirectional T800/913 CFRP-prepreg system consisting of HexPly 913 resin and Torayca T800S carbon fibers. The elastic properties for copper and nickel were obtained from the material library provided within the software COMSOL, while the properties of carbon fiber and resin were taken from the manufacturer's datasheets. The full elastic coefficient matrix for the unidirectional T800/913 layer was subsequently calculated using the approach described in Appendix B. The elastic properties used are summarized in table 3.2.

To excite an elastic wave a displacement  $d_{(xyz)}$  of the model crack surface which increases linear in time for a time interval  $T_{e,(xyz)}$  was introduced. The  $(xyz)$  subset indicates the respective displacement direction. Since the present case utilizes a linear elastic material model, this is equivalent to the application of respective force couples. However, due to the finite extent of the current source model, the usage of absolute force or displacement values has to take into account the dimensions of the source. As a consequence of the current source model, reasonable values for the crack surface displacement  $d_{(xyz)}$  are more accessible than the respective forces.

As a response to such a short temporal displacement with  $T_{e,x} = 100 \text{ ns}$

### 3. Simulation of acoustic emission signals

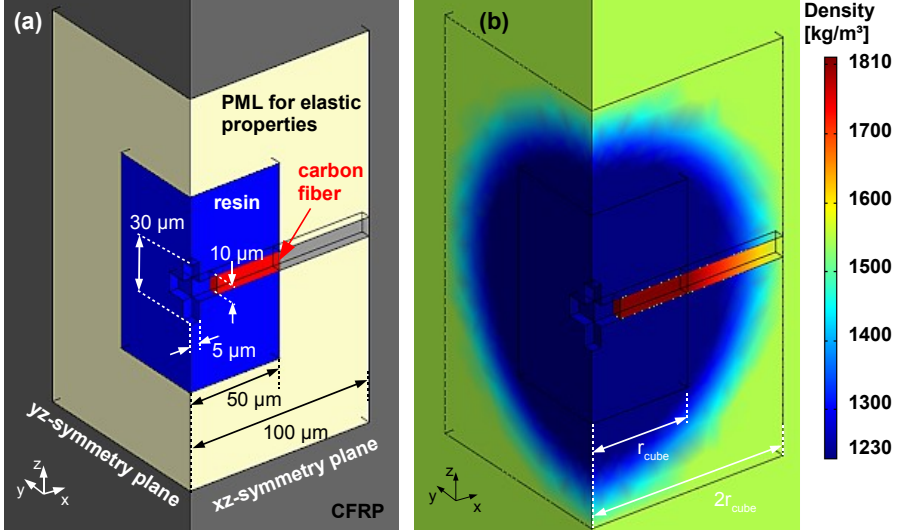


Figure 3.2.: Quarter-volume representation of acoustic emission source model including typically used length scales (a). Gradual change of material density in quarter-volume representation achieved by PML (b).

### 3. Simulation of acoustic emission signals

	Copper	Nickel	T800/913 (UD)	Resin HexPly 913	Carbon Fiber T800S
Density $\rho$ [kg/m <sup>3</sup> ]	8700	8900	1550	1230	1810
Poisson-Ratio	0.35	0.29	-	0.35	0.20
Elastic coefficients [GPa]	$E=110.0$	$E=205.0$	$C_{xxxx}=154.0$ $C_{xxyy}=3.7$ $C_{xxzz}=3.7$ $C_{yyyy}=9.5$ $C_{yyzz}=5.2$ $C_{zzzz}=9.5$ $C_{yzyz}=2.5$ $C_{zxzx}=4.2$ $C_{xyxy}=4.2$	$E=3.39$	$E=294.0$
Source	[149]	[149]	Appendix B	[150]	[151]

Table 3.2.: Summary of material properties used for the simulation of failure mechanisms and signal propagation.

### 3. Simulation of acoustic emission signals

and  $d_x = 50$  nm the crack surface starts to oscillate and is damped out as the energy is propagating into the solids volume (see figure 3.3). It is important to point out that the oscillating response of the crack surface shown in figure 3.3 is caused solely by the chosen geometry and the materials elastic properties. In particular it is not caused by a driving force like commonly used in other publications [152–154].

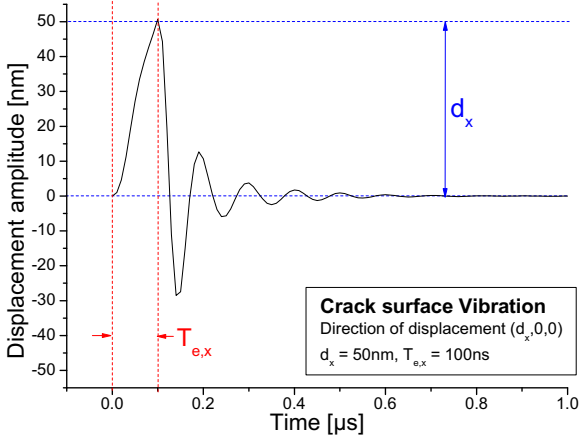


Figure 3.3.: Vibration of the model cracks surface with resin elastic properties for an excitation with  $T_{e,x} = 100$  ns and displacement  $d_x = 50$  nm. The oscillating response is attributed solely to the geometry and the elastic properties of the cracking medium and was not introduced by an oscillating driving force.

### 3. Simulation of acoustic emission signals

Thus the only input parameters required for the simulation of the presented source model are:

1. direction of crack surface displacement
2. magnitude of crack surface displacement
3. time of initial crack surface displacement.

Critically reviewed in terms of the underlying physics, the direction of crack surface displacement is strictly given by the type of failure. As discussed by [1, 38, 39], mode-I cracking results in a displacement direction perpendicular to the crack surface. In a similar way, mode-II and mode-III cracking result in components acting parallel to the crack surface (see figure 2.11). The magnitude of crack surface displacement is directly correlated to the strain-energy accumulated before fracture and the elastic properties of the cracking medium. Solely the time of initial crack surface displacement is subject to assumptions, since it is difficult to access by experimental means. Thus in the following, the range of excitation times investigated varies between 50 ns and 1  $\mu$ s. These values are based on the reported excitation times by H. Hatano et al., M. Giordano et al. and M. Ohtsu et al. who employed various source rise times. The suitability of these rise times were confirmed in various comparisons between experimental data and analytical solutions [36, 45, 155].

While the influence from anisotropies in the vicinity of the crack tip is completely negligible for homogeneous materials like metals<sup>1</sup>, this influence can be crucial for composite materials like CFRP. In the presented source model the effect of the elastic properties in the vicinity of the crack tip are included. Based on identical excitation times  $T_{e,x} = 50$  ns and displacements  $d_x = 100$  nm the different elastic properties of fiber and resin and their geometric arrangement as cracking medium result in characteristic crack surface displacements. These are shown in figures 3.4 and 3.5 as comparisons between the crack surface displacement obtained from the FEM-model and analytical solutions for the different source-time functions of M. Ohtsu et al., M. Giordano et al. and M. Lysak as described in section 2.2.2 [36, 37, 45]. For all analytical models the magnitude of the surface displacement was first scaled to match the simulated  $d_x = 100$  nm. Afterwards the respective excitation time was obtained from a fit between the analytical solution and the simulated surface displacement.

Obviously, the Heaviside function used by M. Lysak is only a very rough approximation as source-time function. A better agreement is observed between the result obtained from the FEM-model and the analytical solutions

---

<sup>1</sup>Unless the local microstructure close to the crack tip is drastically different in its elastic properties those of the bulk material and cannot be approximated by homogeneous elastic properties.

### 3. Simulation of acoustic emission signals

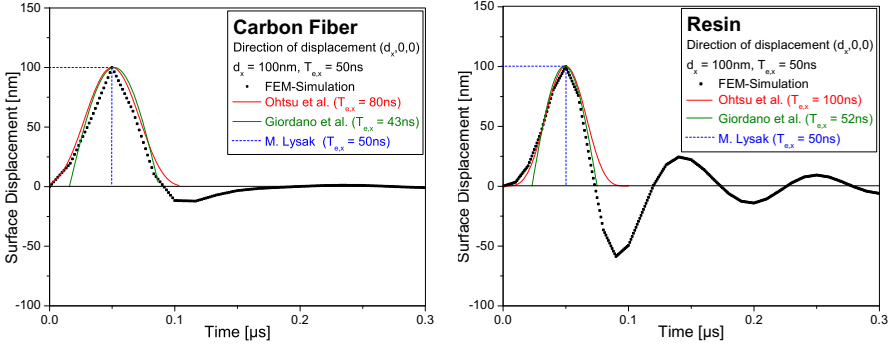


Figure 3.4.: Crack surface displacement in x-direction for an excitation with  $T_{e,x} = 50\text{ ns}$  and displacement  $d_x = 100\text{ nm}$  for fiber (a) and resin elastic properties (b) in comparison with different analytical solutions.

of M. Giordano et al. and M. Ohtsu et al. for carbon fiber elastic properties. However, this is not the case for the results obtained for resin elastic properties. Here the damped oscillation of the crack surface is a vital part of the source behavior. Based on physical considerations the crack surface oscillation is expected and was already predicted by L. Freund et al. within an elastodynamic approach [34]. During crack progress, the system under investigation moves from one equilibrium state (before crack progress) to another equilibrium state (after crack progress). The behavior to reach the new equilibrium state is found to be an underdamped oscillation for the present FEM-simulations, while the analytical solutions would all assume a critically damped oscillation. In the FEM-simulations a strict correlation between the elastic properties and the damping ratio is observed. In the investigated materials a higher ratio of Young's modulus to material density results in a higher damping ratio. Thus the source descriptions provided by the analytical models are accurate enough to describe the source-time behavior for materials with quickly decaying crack surface vibration as carbon fibers or metals (see figures 3.4-a, 3.5-a and 3.5-b).

The different damping behavior of the different materials crack surface oscillation causes different source spectra. These are obtained by Fast-Fourier-Transformation of the crack surface displacement of the FEM-simulations and are shown in figure 3.6 for carbon fiber and resin in comparison with the analytical solution for the source spectrum according to M. Giordano et al. [45]. Again the source spectrum for fiber elastic properties agrees reasonable with the analytical solution, while the source spectrum for resin elastic properties

### 3. Simulation of acoustic emission signals

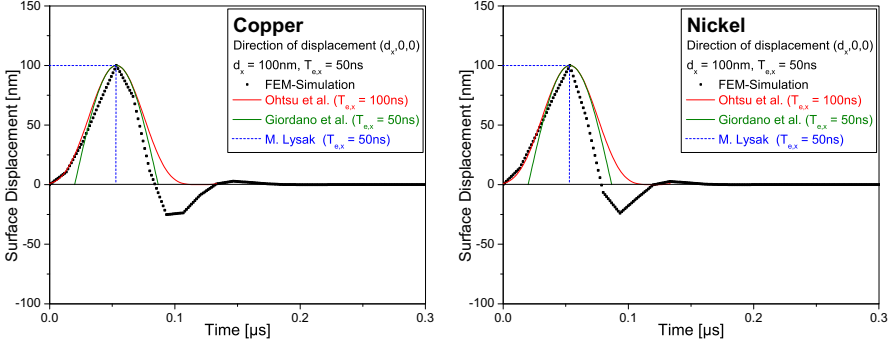


Figure 3.5.: Crack surface displacement in x-direction for an excitation with  $T_{e,x} = 50$  ns and displacement  $d_x = 100$  nm for copper (a) and nickel elastic properties (b) in comparison with different analytical solutions.

is strictly different from the analytical solution. This difference is caused by the significant oscillations shown in figure 3.4-b, which are not reflected in the analytical description. This source behavior causes an additional resonance contribution around 9 MHz and results in a faster decay towards higher frequencies than for the fiber breakage simulation. Consequently, matrix cracking shows source spectra with significantly lower bandwidth than source spectra of fiber breakage.

It is worth to point out, that for the identification of source mechanisms and comparison with experimental data such substantial differences in the source characteristic are very important for the resulting characteristics of the respective acoustic emission signals. Although the broad frequency spectra of the acoustic emission sources suffer from significant bandwidth reduction during propagation and especially during detection with a bandwidth limited sensor (see figure 2.20 and equation (2.57)) the source spectra are still an important contribution to the final acoustic emission signal spectra.

Since various failure mechanisms were modeled, an overview of all displacement schemes used is given in figure 3.7. For the type of cracks found within metallic coatings, mode-I failure was assumed. Thus the modeled displacement is applied perpendicular to the crack surface as indicated by the arrows in figure 3.7. The color plot shows the magnitude of the simulated displacement vector  $\vec{u}$  in the xz-plane at  $y = 0$  of a plate with length in x- and width in y-direction. The z-axis direction is chosen normal to the plate surface. For copper and nickel cracking this yields a displacement field, which is best described by a



### 3. Simulation of acoustic emission signals

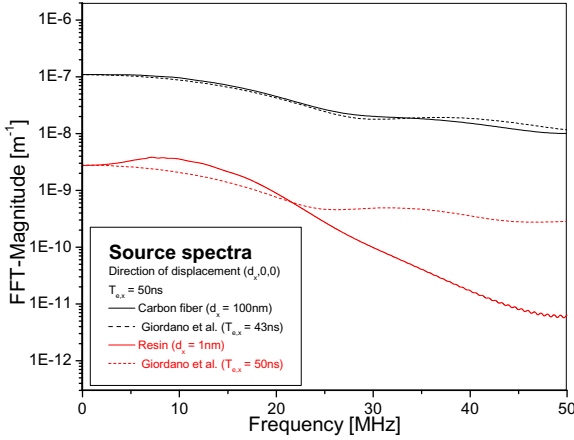


Figure 3.6.: Source spectra obtained from the crack surface vibration in x-direction for an excitation with  $T_{e,x} = 50$  ns and displacement  $d_x = 100$  nm for fiber and resin elastic properties.

dipole-characteristic, as expected for an in-plane tensile crack as schematically shown in figure 2.11 [38, 39, 43, 56, 76, 148]. In contrast to figure 2.11, the plot uses the same color for the same magnitude of push- and pull-displacements. Here no significant differences are observed in the radiation patterns of copper and nickel cracking. The difference in elastic properties for these materials is more emphasized in the displacement pattern for interfacial failure at the copper-nickel interface. The influence of the different elastic properties is causing strong anisotropy of the displacement field, which is best described as distorted out-of-plane dipole. The distortion ratio depends on the ratios of the longitudinal sound velocity of the materials. Here nickel shows higher sound velocities than copper, which results in a faster spreading of energy into the surrounding bulk medium.

For all models of CFRP failure shown in figure 3.7 the fiber axes are oriented along the x-axis. For fiber breakage the major displacement is directed along the fiber axis, i.e. the dominant source radiation direction is in the xy-plane (in-plane). This is again best approximated by a dipole characteristic. The only difference to the mode-I cracks in copper and nickel are the small spikes directed along the fiber axis. This is caused by the high Young's modulus of the carbon fiber with respect to the surrounding medium and results in a faster

### 3. Simulation of acoustic emission signals

propagation of the elastic wave within the carbon fiber. For matrix cracking the crack surface normal can be directed along any axis. This was modeled by short temporal displacement along the x-, y- or z-axis. The displacement vector magnitudes show source radiation patterns which can also be approximated by a dipole characteristic. For displacement in x- or y-direction (equivalent) this is an in-plane dipole, for displacement in z-direction this is an out-of-plane dipole. The in-plane dipole typically represents inter-fiber matrix cracking, while the out-of-plane dipole represents inter-ply delamination in matrix rich areas. During crack progress all interface processes which involve fiber and matrix (e.g. debonding) should contribute to in-plane and out-of-plane radiations. In this case, the crack formation at the interface is simulated as a y-axis and z-axis displacement perpendicular to the crack surface. In addition, due to the loss of contact between fiber and matrix a relaxation of the fiber occurs. This is taken into account by an additionally simulated x-axis displacement component (along the fiber axis). The amplitude of this displacement depends on the shear stress between fiber and matrix at the start of debonding. Consequently, a higher adhesive strength between fiber and matrix results in a higher expected shear stress, which translates in a higher displacement component along the fiber axis. The obtained displacement field is best approximated by a quadrupole characteristic, which is a result of these two different displacements and the anisotropic properties of the sources surrounding. The change in displacement ratio ( $d_x$ ):( $d_y, d_z$ ) of these two contributions results in a shift of the observed displacement field from matrix cracking on one end to fiber breakage on the other.

## 3.2. Modeling signal propagation

After excitation of an elastic wave by the crack surface displacement of the presented source model, an elastic wave starts to propagate into the adjacent medium. In finite element simulations the propagation of elastic waves is modeled based on time dependent solutions of differential equations of the equilibrium states. For the planar geometries investigated within this thesis this results in formation and propagation of Lamb waves.

### 3.2.1. Mesh resolution

In order to model this propagation accurately it is necessary to use a density of the finite elements which is sufficient to resolve the shortest wavelength of the elastic waves used in the model [156, 157]. The geometric arrangement of the finite elements is usually called *mesh* and the respective density of finite

### 3. Simulation of acoustic emission signals

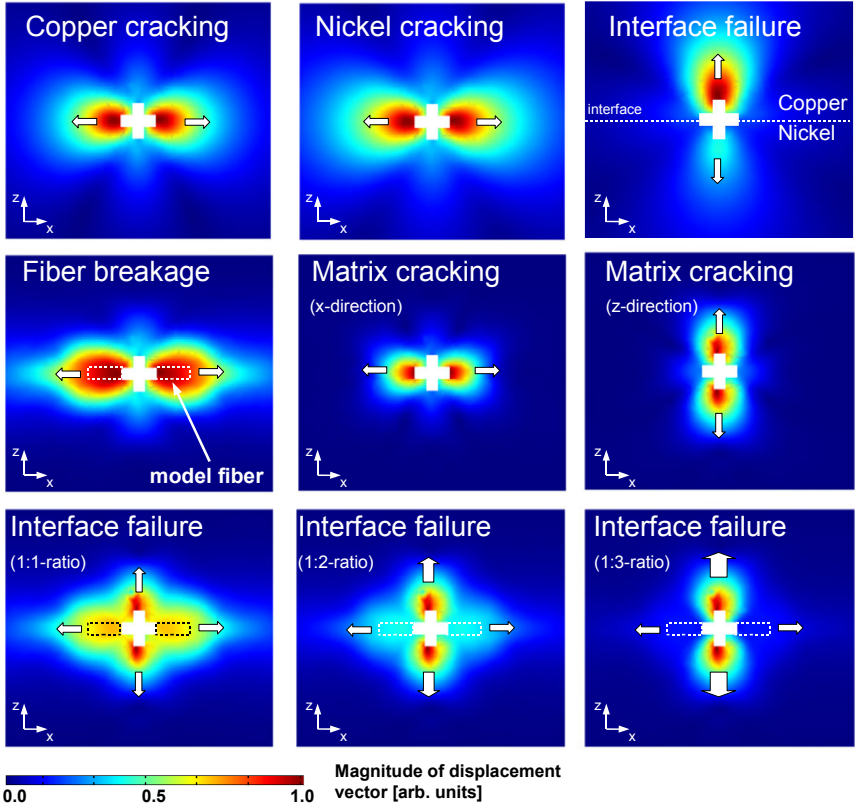


Figure 3.7.: Magnitude of the displacement vector in  $xz$ -cross-section plane for the different simulated failure mechanisms obtained from a half-volume source model at  $t = 50$  ns. The arrows indicate the direction of the chosen initial displacement  $d_{(xyz)} = 100$  nm, while the excitation time for all processes was kept constant at  $T_e = 50$  ns.

### 3. Simulation of acoustic emission signals

elements is directly linked to the resolution of the mesh. Various authors already established FEM-models for simulation of elastic wave propagation in CFRP specimens [152–154]. Based upon their considerations a basic investigation of the mesh influence in the model specimen geometries was done. Similar to J. Nieuwenhuis et al. and M. Castaings et al. a sinusoidal force pulse was applied to the boundary of the CFRP-plate for  $t < 10\pi/\omega$  and a temporal resolution of  $\Delta T = 0.1 \mu\text{s}$  (see figures 3.8-a and 3.8-b) [152, 154].

$$F(t) = \begin{cases} |F| \sin(\omega t) \cdot \sin^2\left(\frac{\omega t}{10}\right) & t \leq 10\pi/\omega \\ 0 & t > 10\pi/\omega \end{cases} \quad (3.1)$$

The angular frequency  $\omega$  was chosen to match the “highest” frequency parts of 1 MHz observed in the experimental signals. Assuming a sound velocity of 3000 m/s for the epoxy resin this corresponds to an approximate wavelength of 0.003 m for 1 MHz frequency. Consequently, the mesh resolution was varied starting with an initial resolution of 0.003 m and was increased to a final resolution of 0.0005 m. According to references [156, 157] the mesh resolution is sufficient if no changes in the pulse shape are observed when the mesh resolution is further increased. The simulated surface displacement caused by the sinusoidal force pulse was obtained at a distinct position after propagation through the CFRP-plate. For simulation of the model geometry with 100 mm  $\times$  15 mm  $\times$  1.4 mm (length  $\times$  width  $\times$  thickness), the T800/913 elastic properties as given in table 3.2 and two planes of symmetry (xz-plane and yz-plane) were used to reflect the experimentally used specimen geometries according to DIN-EN-ISO 14125 [158].

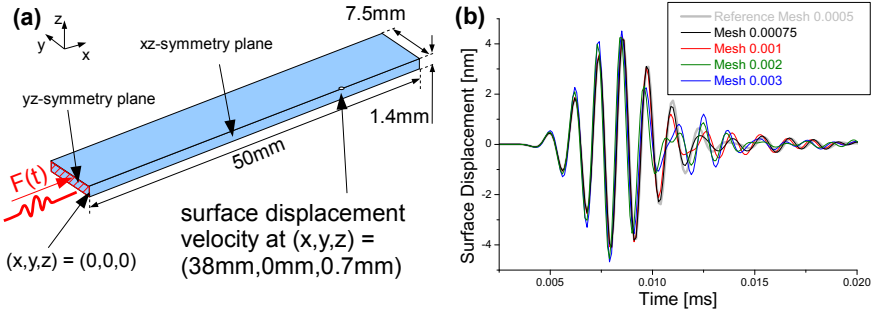


Figure 3.8.: CFRP-geometry used for investigation of mesh resolution (a) and shape of force pulses detected at observation position in dependency of mesh resolution (b).

As shown in figure 3.8-b, for increasing mesh resolution, the shape of the

### 3. Simulation of acoustic emission signals

pulse converges to the shape given by the highest resolution of 0.0005 m. For even higher resolutions no further changes in the appearance of the pulse were detected, so 0.0005 m is defined as mesh resolution, which is necessary to simulate the elastic wave propagation accurately. While such accuracy may be desirable, it is definitely not the best solution in terms of computational efficiency. To this end, M. Castaings et al. established an alternative approach to simulate elastic wave propagation, which is very effective for description of signals with limited bandwidth, but less applicable to the case of acoustic emission signals. Instead of the computationally burdensome approach in the time domain, they solved the time dependent equations of the equilibrium states in the frequency domain for a limited number of frequencies. The temporal propagation was subsequently deduced using Fourier-Transformations [152]. This can successfully reduce the number of calculation steps for signals with distinct frequency content, but is not very effective for the investigation of acoustic emission signals which show reasonable bandwidth and would require almost the same number of calculations in the frequency domain as in the time domain. Consequently, the temporal approach was used in the following. The required computational resources of this approach are directly linked to the Degrees of Freedom (DOF) encountered in the model. These in turn are directly correlated to the mesh resolution and the volume of the model under investigation. As shown in figure 3.9 the dependency between the mesh resolution and the DOF are best described by a power law. These can act as measure for the required computational resources, since the DOF are directly proportional to the computation time and the amount of memory. The maximum capacity of current personal computers is marked with a gray hachured rectangle in figure 3.9. Thus it is very obvious, that the size of the model volume which can be treated with the most accurate mesh resolution is limited. As a compromise for the following simulations the reference mesh resolution of 0.0005 m was used for the simulations of the influence from source parameters presented in section 3.1, while the simulations of the different larger experimental geometries in section 3.5 used the mesh resolution of 0.002 m. This decreased resolution is still sufficient to capture the overall shape of the 1 MHz pulse shown in figure 3.8-b.

Compared to the specimen dimensions the size of the source model is very small. This requires a multi-scale approach, which means that the mesh resolution is increased, when approaching the acoustic emission source within the specimen geometry. The mesh resolution of the source model in turn is always kept constant and is drastically higher ( $\approx 10^{-6}$  m) than the resolution in the remaining specimen. The accuracy of the source models mesh resolution was also investigated by a gradual refinement of resolution, until no changes in the excited elastic waves were observed for further increase of the mesh

resolution.

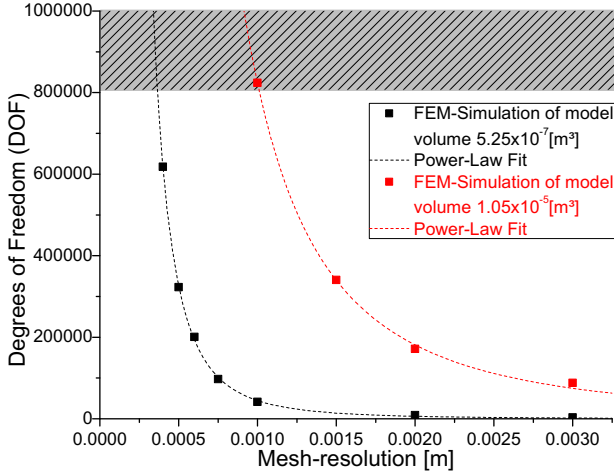


Figure 3.9.: Dependency between degrees of freedom and mesh resolution for the modeled volume of figure 3.8 (black) and the modeled volume from DCB-specimens shown in figure 3.44 (red). Gray hachured rectangle marks current maximum capacity of personal computers.

#### 3.2.2. Time resolution

In order to temporally resolve the smallest chosen excitation time of  $T_e = 50$  ns used within the source model, the initial time step of the model was set to 10 ns. To increase the computational efficiency, the time steps were gradually increased after a convenient decay of the crack surface oscillation, as visible in figure 3.3 at around  $1 \mu s$  to reach a final temporal resolution of  $\Delta T = 0.1 \mu s$ . This corresponds to the experimentally used sampling rate of 10 MHz and is sufficient to resolve the signals frequency content in the range up to a maximum frequency of 5 MHz.

As described in sections 2.2.3 and 2.2.4, the propagation of guided waves in viscoelastic specimens is influenced by attenuation and dispersion which, consequently, should be included in the model. According to M. Castaigns et al. this can be achieved by complex elastic coefficients [152]. In computational terms this doubles the amount of memory required for the calculation and thus decreases the efficiency. As discussed by W. Prosser et al. the dominating

### 3. Simulation of acoustic emission signals

part for attenuation in planar specimens in the near-field range within the distance  $r < 4.34/\alpha$  is geometric spreading [56]. For all specimens investigated, the propagation distance between source and area of detection is below 45 mm, while the attenuation  $\alpha$  for the T800/913 prepreg was measured to be  $(100 \pm 10)$  dB/m (see section 4.3.2). As a consequence the attenuation is dominated by geometric spreading, which is intrinsically included within the model. Consequently, in the following, the elastic properties of unidirectional CFRP-specimens were modeled by real anisotropic elastic coefficients. This is a sufficient approximation to simulate guided waves in viscoelastic media if the attenuation effects arising from thermoelastic and Akhiezer dissipation are negligible during propagation.

Finite element simulations by M. Hamstad et al. already have shown that different source radiation patterns result in different ratios of symmetric and antisymmetric plate wave modes in isotropic materials [76]. This in turn causes different frequency compositions of the detected acoustic emission signals, as the propagation of the  $S_0$ -mode occurs at higher frequency than the  $A_0$ -mode [56] (see figure 2.45). As described in section 3.1 due to the microscopically anisotropic nature of fiber reinforced composites, depending on the failure mechanism strong differences in the source radiation patterns are found.

The temporal development of the magnitude of the displacement vector shown in figure 3.10 compares the propagation of the excited Lamb waves of a simulation with excitation time  $T_e = 1.0 \mu\text{s}$  and displacement of  $d_x = 100$  nm for in-plane fiber breakage versus out-of-plane matrix cracking with  $d_z = 100$  nm. As model geometry, the plate specimen shown in figure 3.10 with elastic properties of T800/913 and model source position at  $(x,y,z) = (0,0,0)$  mm was used. In addition, the  $xz$ - and  $yz$ -plane were chosen as symmetry-planes. For comparison the propagation is shown at four distinct time steps in top-view of the  $xy$ -plane in identical color ranges for fiber breakage and in the same color range for matrix cracking. As clear difference in figure 3.10, the fiber breakage source model stimulates higher intensity  $S_0$  plate wave modes than the out-of-plane matrix cracking. For visualization of the  $S_0$ -mode for out-of-plane matrix cracking, the color range was adapted. The distortion of the  $S_0$ -mode along the  $x$ -axis is caused by the unidirectional orientation of the carbon fibers, causing anisotropic elastic properties with the highest elastic coefficient  $C_{11}$  directed along the  $x$ -axis. This excitation of different Lamb wave modes by internal acoustic emission sources is very similar to the observations reported by M. Hamstad et al. for isotropic materials [76]. Although strong dependencies on the acoustic emission source position are observed, the different Lamb wave ratios can be used to characterize the respective source mechanisms, as discussed in section 3.4. For the investigated materials and specimen geometries

### 3. Simulation of acoustic emission signals

a high intensity of antisymmetric modes generally corresponds to frequency contribution in the lower frequency range, while a high intensity of symmetric modes generally corresponds to contributions in the high frequency range, as visualized in the WT-diagram in figure 2.45.

In addition, figure 3.11 shows the dispersion curves calculated with [138] according to equation (2.48) for a T800/913 plate with 1.4 mm thickness. The group velocities of 3800 m/s for the  $S_0$ -mode and 1900 m/s for the  $A_0$ -mode obtained from the simulations at the respective propagation frequencies agree well to the calculated group velocities as extracted from the dispersion curves.

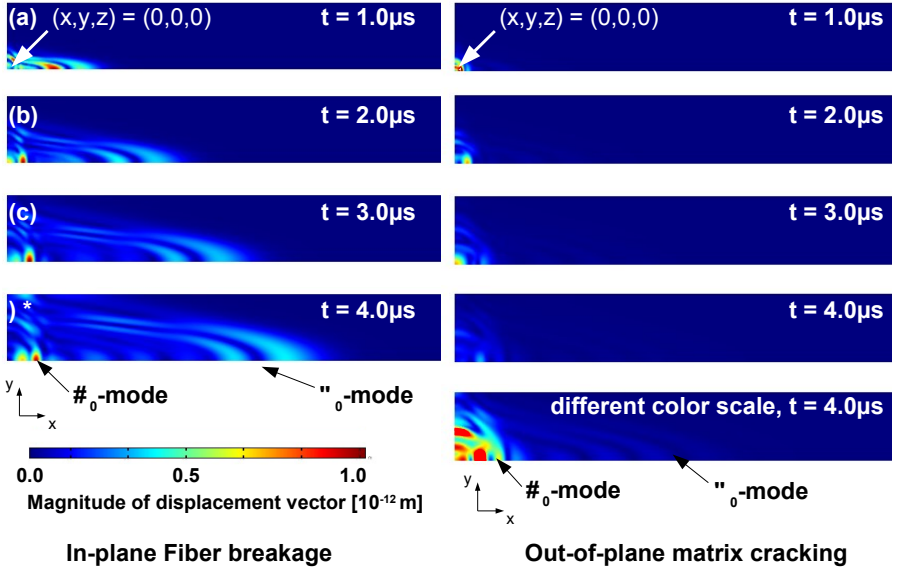


Figure 3.10.: Temporal development of the magnitude of the displacement vector in the near-field region of the acoustic emission source model for a simulation of fiber breakage (left) and out-of-plane matrix cracking (right). Times shown are  $1.0 \mu\text{s}$  (a),  $2.0 \mu\text{s}$  (b),  $3.0 \mu\text{s}$  (c) and  $4.0 \mu\text{s}$  (d) after excitation (excitation time  $T_e = 1.0 \mu\text{s}$ , displacement  $d_x = 100 \text{ nm}$  and  $d_z = 100 \text{ nm}$ ).

Compared to analytical solutions for signal propagation obtained for infinite volumes, infinite half-spaces or infinite plates, the advantage of the presented FEM-simulations is the possibility to include the reflections arising from the



### 3. Simulation of acoustic emission signals

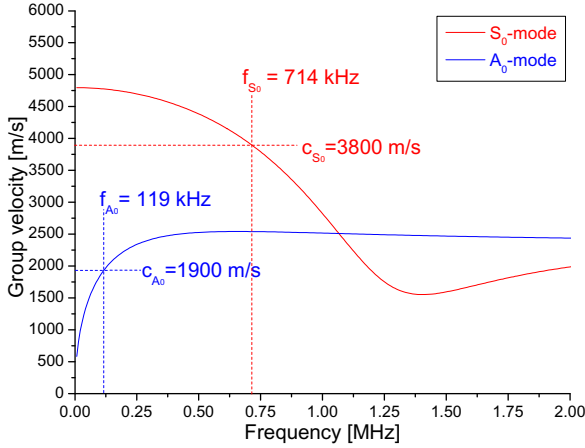


Figure 3.11.: Dispersion curves of S<sub>0</sub>- and A<sub>0</sub>-mode calculated with [138] for a 1.4 mm thick plate with T800/913 properties. The propagation velocities and frequencies of the S<sub>0</sub>- and the A<sub>0</sub>-mode obtained from the simulations are marked by dashed lines.

specimen boundaries implicitly by definition of the specimen geometry. The reflections in turn can play an important role in signal propagation, as demonstrated by the formation of Lamb waves in the present case. In addition, reflections from the boundaries of the specimen can cause characteristic contributions to the acoustic emission signals appearance, if the sensor position is located close to the boundary [159, 160].

While it is still possible to use analytical descriptions for signal propagation within the simple planar model geometry shown in figure 3.8 such analytical descriptions grow less practicable for more complex geometries. In addition, an accurate analytical description of the signal propagation in CFRP requires an extension of the approaches presented in section 2.2.2, which overcome crucial limitations by introducing anisotropy [43] and a dissipative medium for wave propagation [44, 45].

### 3.3. Model of broadband sensor and signal detection

The final step in the present simulation is the detection process of the acoustic emission signal by a suitable sensor model. Under certain circumstances, the influence of the sensor may be negligible, which is the case when the transfer function of the sensor is almost constant within the investigated frequency range. For sensor types like the capacitance transducer of C. Scruby et al. [161] or the widely applied laser vibrometers [40,67,162] this assumption is sometimes fulfilled. In contrast, for piezoelectric sensors, the frequency and energy content of the measured signals depends significantly on the sensor geometry and the sensor material. For these sensor types, L. Goujon et al. already pointed out that the influence of the aperture effect on the detected signals appearance is not negligible [67]. In addition, piezoelectric sensors can be designed to respond either to the surface displacement, the surface displacement velocity or the surface displacement acceleration [60]. For a more detailed description of the differential equations used for the simulation of piezoelectric conversion, the reader is again referred to Appendix C.

In the case of acoustic emission sensors, K. Ono et al. investigated the response behavior of a broad range of commonly used acoustic emission sensors. For the sensor of type WD manufactured by Physical Acoustics, which is used in the current investigation they have elucidated the fact that this type primarily responds to the surface displacements velocity  $\vec{v}$  rather than to surface displacement  $\vec{u}$  [163]. For comparison of results obtained from the FEM-simulations with experimental data it is thus necessary to include the influence of this experimentally used sensor in a respective simulation. In the following investigation a full three dimensional model of the type WD broadband sensor was established. For validation of the applicableness of the model geometry shown in figure 3.12 and the material composition given in tables 3.4 and 3.5 the results of the simulations were compared to experimental data in two approaches. Firstly the sensor model was evaluated within a simulation of a setup typically used for reciprocity calibration of acoustic emission sensors as described by H. Hatano et al. [155]. Secondly, the sensor models signal was compared to respective experimental signals within a setup used for detection of signals from pencil lead fracture tests.

#### 3.3.1. Reciprocity calibration

The typical experimental setup used for reciprocity calibration is shown in figure 3.13. The sensor is placed on a cylindrical calibration block with 400 mm

### 3. Simulation of acoustic emission signals

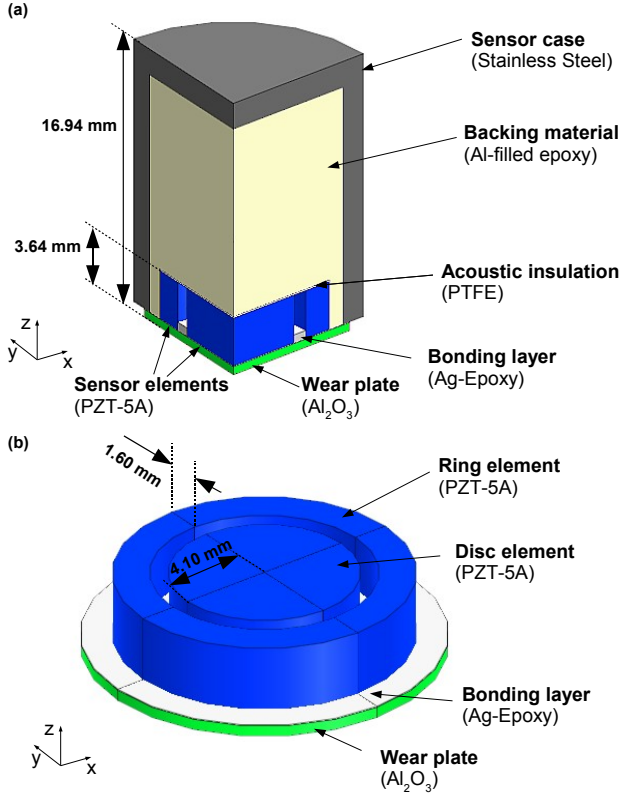


Figure 3.12.: Quarter-volume representation of the WD sensor type used in this investigation (a). Full volumetric representation of the bottom sensor part with removed sensor case, backing material and acoustic insulation (b).

diameter and 150 mm height, which is used as propagation medium. Due to the radial symmetry of the problem the z-axis was used as axial symmetry axis for isotropic propagation media. In contrast to the experimental reciprocity calibration, no additional transmitter is required and thus no reciprocity correction due to its characteristic has to be made. Instead, a sinusoidal force pulse as given by equation (3.1) with different center frequencies was applied at the bottom of the propagation medium to excite a plane wave propagating towards the sensor position. The chosen geometry of the propagation medium

### 3. Simulation of acoustic emission signals

avoids interference of the incident boundary reflections at the sensor position as shown in figure 3.14 at three different time steps. For calculation of the sensor response, the voltage signal, the surface pressure and the surface displacement velocity at the interface between sensor and calibration block was simulated as a function of the center frequency.

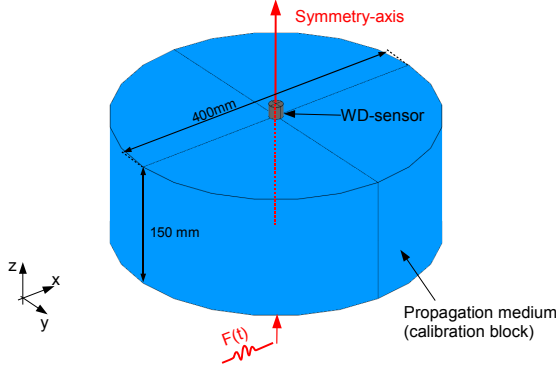


Figure 3.13.: Modeled setup for simulation of reciprocity calibration. The sensor model is placed centered on top of a cylindrical propagation medium block. The plane wave is excited on the opposite side. The symmetry axis used for the simulations is marked as well.

To obtain the frequency dependent sensitivity curve of the WD sensor, the ratio of voltage per surface pressure or surface displacement velocity is required. These were obtained from the simulated peak-values of the voltage signals and the surface pressure signals as shown in figures 3.15-a and 3.15-b. To obtain these signals, the surface pressure  $p(t)$  and surface displacement velocity  $v(t)$  in  $z$ -direction was averaged within the contact area  $A_{contact}$  between sensor and calibration block:

$$p(t) = \frac{1}{A_{contact}} \int_{A_{contact}} p_z(t) \, dx dy \quad (3.2)$$

$$v(t) = \frac{1}{A_{contact}} \int_{A_{contact}} v_z(t) \, dx dy \quad (3.3)$$

Similar, the voltage signal  $U(t)$  is obtained from the average electric potential

### 3. Simulation of acoustic emission signals

	Sensor case	Backing material	Acoustic Insulation	Bonding	Wear plate	Sensor elements
Material	Stainless Steel	Al-filled Epoxy	PTFE	Ag-filled Epoxy	Al <sub>2</sub> O <sub>3</sub>	PZT-5A
Density $\rho$ [kg/m <sup>3</sup> ]	7970	2700	2200	1700	3965	7750
Poisson-Ratio	0.29	0.4	0.33	0.45	0.22	-
Elastic coefficients [GPa]	$E=219$	$E=30.0$	$E=0.4$	$E=2.7$	$E=400.0$	$C_{xxxx}=120.3$ $C_{xxyy}=75.2$ $C_{xxzz}=75.1$ $C_{yyyy}=120.3$ $C_{yyzz}=75.1$ $C_{zzzz}=110.9$ $C_{yzyz}=21.1$ $C_{zxzx}=21.1$ $C_{xyxy}=22.6$
Source	[149]	estimate	[149]	[149]	[149]	[149]

Table 3.4.: Summary of material properties of the WD sensor model.

### 3. Simulation of acoustic emission signals

	Coupling constants [ $C/m^2$ ]	Relative Permittivity
	$S_{zzxx} = -5.4$	$\chi_{xxxx} = 919.1$
	$S_{zzyy} = -5.4$	$\chi_{yyyy} = 919.1$
	$S_{zzzz} = 15.8$	$\chi_{zzzz} = 826.6$
	$S_{yyyz} = 12.3$	
	$S_{xxzz} = 12.3$	
Source	[149]	[149]

Table 3.5.: Piezoelectric properties of PZT-5A.

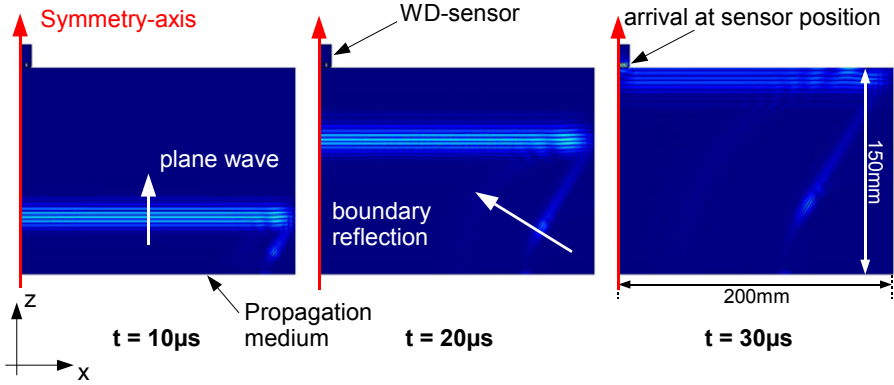


Figure 3.14.: Cross sectional plot of axial symmetry plane of the setup used for reciprocity calibration. The color value indicates the magnitude of the displacement vector in the same color range for  $t = 10 \mu s$ ,  $t = 20 \mu s$  and  $t = 30 \mu s$ .

at the top surface of the disc and ring sensor elements shown in figure 3.12-b:

$$U(t) = \frac{1}{A_{disc}} \int_{A_{disc}} U_z(t) dx dy + \frac{1}{A_{ring}} \int_{A_{ring}} U_z(t) dx dy \quad (3.4)$$

The sensitivity curve of the WD sensor as obtained from the FEM-simulation of calibration blocks with elastic properties of steel, aluminum and T800/913 in comparison to calibration curves provided by the manufacturer are shown in figure 3.16 as sensor response  $U(t)/p(t)$  given in dB with reference to [1 V/ $\mu$ bar]. Similar sensitivity curves are obtained from the simulations of the

### 3. Simulation of acoustic emission signals

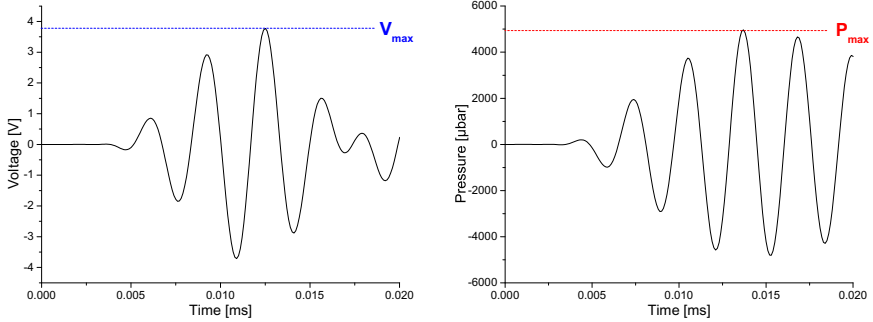


Figure 3.15.: Typical voltage signal (a) and surface pressure signal (b) obtained from the simulation of the reciprocity calibration for 300 kHz center frequency.

sensor response with reference to the surface displacement velocity  $U(t)/v(t)$  measured in [V/mm/s]. For the sensitivity curve obtained on a calibration block with steel properties, good agreement of the sensor characteristic is found relative to the scattering range observed for the two different reference sensors. In particular, the absolute value of the voltage to surface pressure ratio is reflected very well in the simulation.

As discussed by L. Goujon et al., the sensitivity curves of acoustic emission sensors are strictly dependent on the acoustic impedance of the medium the sensor is attached to [67]. This is caused by the dependency of the transmission and reflection coefficients at the interface between the wear-plate of the sensor and the propagation medium on the respective acoustic impedance as approximated by equations (2.39) and (2.40). In the current investigation this is reflected in the different simulated sensitivity curves shown in figure 3.16 for steel, aluminum and CFRP calibration blocks. While the calibration curve for aluminum was obtained by simple replacement of the steel block by an aluminum block, due to the anisotropic elastic properties the sensitivity curve for CFRP is more difficult to obtain.

Here a full three dimensional simulation was used including the full anisotropic properties of unidirectional T800/913 as given in table 3.2 with a fiber axis orientation along the x-axis. The arbitrarily chosen fiber axis direction in the xy-plane does not influence the appearance of the sensitivity curve, since the sensor is radial symmetric around the z-axis. Thus the fiber axis direction within the xy-plane reflects the typical configuration in planar CFRP-structures, where the fiber axis is typically oriented parallel to the sensors wear plate. Due

to the drastic increase in demand of computational resources for the three dimensional model, the height of the calibration block was reduced to 16 mm.

As a consequence of the dependency of the sensitivity curve on the material the direct application of sensor-calibration curves is obviously limited to the material used for the calibration process. This can be of great disadvantage for materials like CFRP, since it is not possible to manufacture calibration block geometries similar to the steel block shown in figure 3.13. Unfortunately these geometric dimensions are still required for experimental calibration of the sensor response to incident longitudinal waves, since only such geometries provide a reflection free arrival of the planar wave at the sensor position.

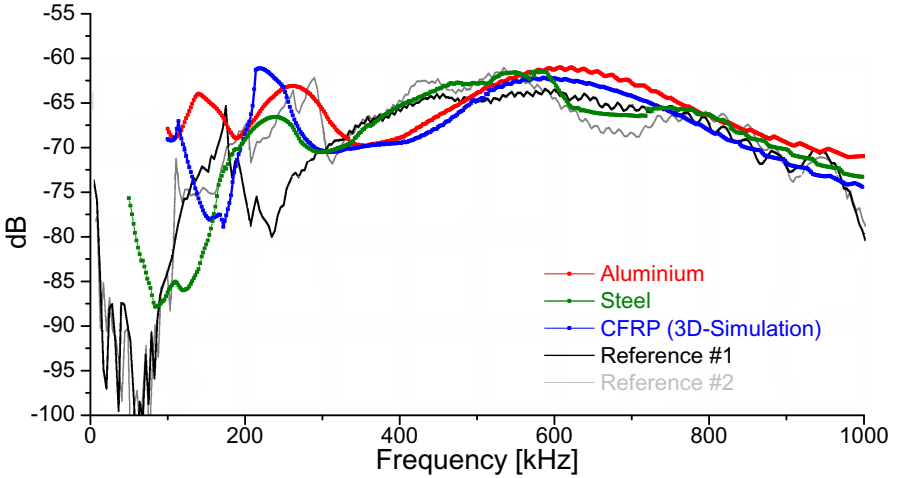


Figure 3.16.: Frequency dependent response of the WD-sensor model in dB with reference to  $[1 \text{ V}/\mu\text{bar}]$  obtained from the simulation of the reciprocity calibration on steel, aluminum and CFRP blocks in comparison with two reference curves provided by the manufacturer.

#### 3.3.2. Pencil lead fracture tests

As second test of the suitability of the presented WD sensor model, a comparison between experimental signals obtained from a pencil-lead fracture test on a 1.1730 steel plate and a respective FEM-simulation was made. The experimental signal was obtained from a pencil lead fracture, commonly known as Hsu-Nielsen source [164] at a distance of 60 mm away from the sensor applied on a 50 mm



### 3. Simulation of acoustic emission signals

$\times 16 \text{ mm} \times 300 \text{ mm}$  (width  $\times$  height  $\times$  length) steel plate. The simulated pencil lead fracture was realized as 3 N point force with a rise time of 300 ns according to [161] in a respective geometry using the  $xz$ -plane as symmetry plane (see figure 3.17).

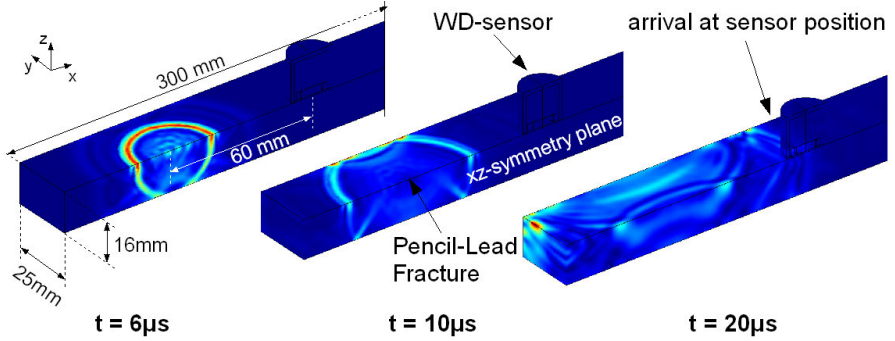


Figure 3.17.: Plot of the displacement vector magnitude for a pencil-lead fracture on a steel plate at  $t = 6 \mu\text{s}$ ,  $t = 10 \mu\text{s}$  and  $t = 20 \mu\text{s}$ .

The strong influence of the chosen acoustic emission sensor on the simulated acoustic emission signals becomes especially clear, when the experimental pencil lead fracture signal is compared to simulated signals obtained without any sensor model. This means any contribution arising from specimen-sensor interaction and any contributions from aperture or material response within the sensor are neglected. The respective signals simulated for the mid-point of the sensor position are shown in figure 3.18. In summary, neither the surface displacement nor the surface displacement velocity show reasonable resemblance to the experimentally obtained signal. At least the surface displacement shows better agreement to the experimental signal at the initial part (see figure 3.18-a), while the surface displacement velocity reflects the experimental signal better for  $t > 0.035 \text{ ms}$  (see figure 3.18-b).

The quantified simulated surface displacement at the sensor position arising from pencil lead fracture is 0.5 nm, which agrees well with experimental values from other authors, who report surface displacements of the order of 1 nm [61, 161]. The simulated surface displacement velocity of 0.07 mm/s is also well comparable to the experimental values reported by other authors during sensor calibration [155, 163].

In clear contrast, the voltage signal obtained from the WD-sensor model in the same simulation approach is shown in figure 3.19-a compared to the same experimental acoustic emission signal as above. In this case the experimental

### 3. Simulation of acoustic emission signals

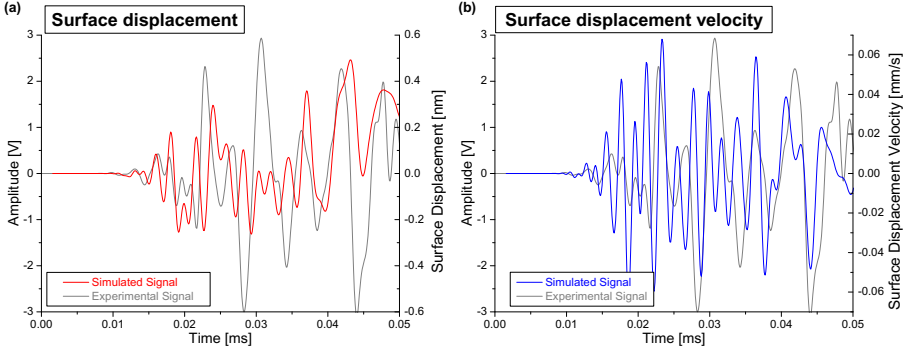


Figure 3.18.: Comparison of experimental pencil lead fracture signals (marked in grey) simulated signals of surface displacement (a) and surface displacement velocity (b) at midpoint location of the sensor.

signal is reflected well by the simulated signal and especially the absolute signal voltage is very close to the experimental value. The deviation in the observed signal amplitudes between simulation and experiment increases at the end of the investigated time range. This difference can originate from attenuation effects, like structural damping within the sensor or loss effects during piezoelectric conversion, which were not taken into account for the current model. In addition, minor discrepancies between the simulated signal and the experimental signal can well be attributed to statistical scattering of the experimental pencil lead fracture signals. As discussed by T. Boczar the pencil lead fracture test produces well reproducible signals as shown in figure 3.19-b in a comparison of three experimental signals [165]. For the purpose of comparison with the simulated signals, their distribution range is still high enough to cover the deviations between the signals shown in figure 3.19-a.

#### 3.3.3. Optimization of the sensor model performance

While such accurate representation of the signal detection process is very valuable for some applications, the increase in computation time caused by the present sensor model is not reasonable for simulation of a large amount of signals. Instead a reduced representation, which is computationally more efficient is thus of great practical value. In the following the reduction of the sensor is discussed using simulated and experimental signals obtained from the pencil lead break setup.

First of all, the piezoelectric conversion process can be taken into account by

### 3. Simulation of acoustic emission signals

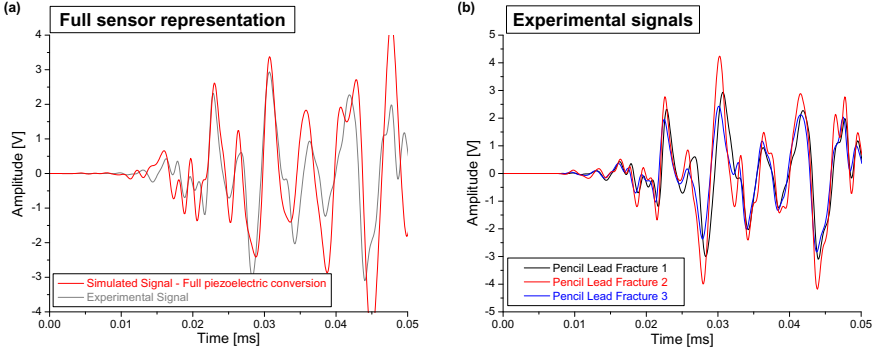


Figure 3.19.: Comparison between pencil lead fracture signals obtained from simulation using full sensor model and experiment (a) and comparison of three experimental signals recorded during pencil lead fracture test (b).

a fixed transfer function for the used sensor and material under investigation, while the geometry of the sensor model is retained. To this end, the simulated sensitivity curve  $U(t)/v(t)$  of the WD-sensor as defined by equations (3.3) and (3.4) obtained from reciprocity calibration on a steel block was used as transfer function. Since no simulations were performed for frequencies below 100 kHz the missing values were assumed to equal the value of the sensitivity obtained for 100 kHz. Similar, the range above 1 MHz was extended by the constant value obtained for the simulation with 1 MHz center frequency.

The signal obtained from this reduced model is shown in figure 3.20-a compared to the voltage signal from simulated piezoelectric conversion. In addition the same experimental pencil lead fracture signal as above is shown. The agreement between both simulated signals is remarkably good, which offers the possibility to replace the simulation of piezoelectric conversion by a subsequent application of the sensors transfer function to the simulated surface displacement velocity signal. In terms of computational efficiency this decreases the duration for one simulation by an approximate factor of two.

As second reduction step, the model geometry itself can be improved to provide a computationally more efficient representation. Here the goal is the identification of the governing contributions arising from the various geometric elements within the sensor. In this context, an earlier attempt [166] already demonstrated that the characteristic of the WD-sensor is dominated by the aperture effect of the piezoelectric elements. This strong influence is again demonstrated by a comparison of two simulated signals to the respective

### 3. Simulation of acoustic emission signals

experimental signal in figure 3.20-b. Here the red curve is the result of an integration of the volumetric displacement velocity within the volume of the piezoelectric elements:

$$v_{tot}(t) = \frac{1}{V_{disc}} \int_{V_{disc}} v(t) dV + \frac{1}{V_{ring}} \int_{V_{ring}} v(t) dV. \quad (3.5)$$

Similar, the blue curve is obtained from the surface displacement velocity in the contact area between wear-plate and piezoelectric elements:

$$v_{tot}(t) = \frac{1}{A_{disc}} \int_{A_{disc}} v(t) dxdy + \frac{1}{A_{ring}} \int_{A_{ring}} v(t) dxdy. \quad (3.6)$$

In summary, both simulated signals show closer resemblance to the experimental signal than similar signals obtained from the surface displacement velocity at the sensors midpoint (see figure 3.18-b). Thus it is clear, that the geometry of the piezoelectric elements causes a dominant contribution to the signals appearance, although the deviations to the experimental signal are slightly larger than for the sensor-model using the approaches which take into account the piezoelectric conversion (see figure 3.20-a). As a consequent reduction step towards larger computational efficiency the complex geometric model of the WD-sensor can be reduced further, neglecting the sensors housing, backing material, acoustic insulation and the bonding between wear-plate and PZT-elements.

The simulated signal of this drastically reduced sensor geometry is shown in figure 3.21-a, as obtained from the surface displacement velocity in the contact area with subsequent application of the sensors transfer function. There is good agreement observed between the simulated signal using the full volumetric representation of the WD-sensor and the signal obtained for the reduced geometry. In addition, the simulated signal of the reduced geometry is at least as comparable to the experimental signal, as the approach taking into account the full piezoelectric conversion process as shown in figure 3.19-a. But more advantageous, this geometric reduction of the sensor model results in a decrease in the duration of simulation of an approximate factor of three.

An even more abstract geometric representation of the WD-sensor was already reported in [166]. This drastically reduced representation takes into account only the aperture effect of the sensor, but is not meant to be a full-scale simulation of the detection process. To this end the complex geometry of the sensors interior and the piezoelectric conversion was completely neglected. Instead, the characteristic of the acoustic emission signal  $U(t)$  of the sensor is obtained from the average surface displacement velocity in the contact area  $A$

### 3. Simulation of acoustic emission signals

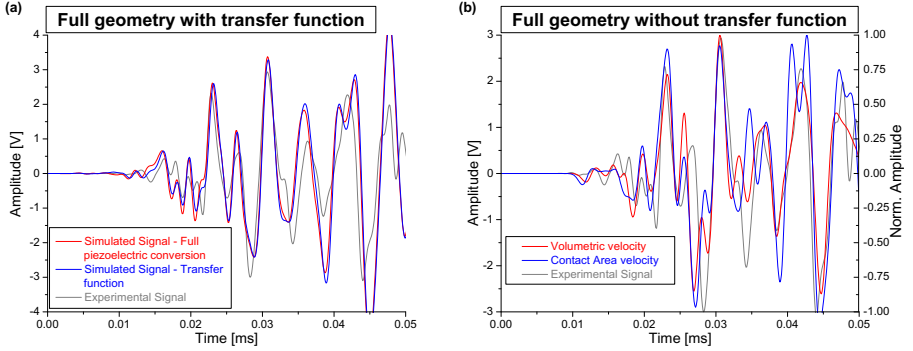


Figure 3.20.: Comparison of pencil lead fracture signals obtained from experiment and simulation with simulated piezoelectric conversion and application of the transfer function of the WD-sensor obtained from reciprocity calibration (a). Two simulated velocity signals obtained from the sensor geometry without piezoelectric conversion in comparison with experimental signal (b).

defined by the two sensor elements (disc and ring). This is done by integration of the z-component of the surface displacement velocity  $v_z$  within the respective area  $A$  and subsequent normalization:

$$U(t) = \frac{1}{A_{disc}} \int_{A_{disc}} v_z(t) \, dxdy + \frac{1}{A_{ring}} \int_{A_{ring}} v_z(t) \, dxdy \quad (3.7)$$

The comparison of this drastically reduced sensor model with the experimental signal obtained from pencil lead fracture is shown in figure 3.21-b. Still there is noticeable resemblance between the simulated and the experimental signal. Again this indicates the importance of the contribution of the sensors aperture to the signals appearance.

In summary, the large range of computational resources required for the different sensor models forces selective usage of the different reduction steps. For direct comparison with experimental data, the best compromise between accuracy and computational efficiency was found to be the full-geometric representation with subsequent application of the sensors transfer function of the respective material, as obtained from the simulations of reciprocity calibration. In the following this sensor model will be named *full-sensor representation*.

As computationally faster alternative, simulations for large number of sig-

### 3. Simulation of acoustic emission signals

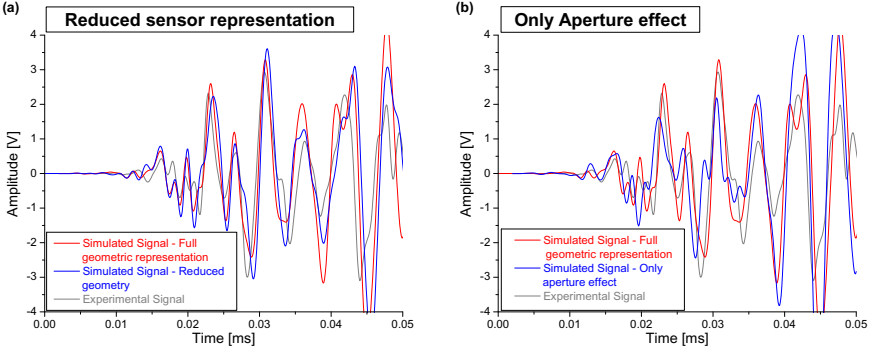


Figure 3.21.: Comparison of simulated signals using full geometry and reduced geometry both with subsequent application of the WD-sensors transfer function obtained from reciprocity calibration (a) and influence of the aperture effect of the piezoelectric elements (b).

nals will be done using the reduced geometry model of the WD-sensor with subsequent application of the sensors material specific transfer function as obtained from the simulations of reciprocity calibration. This model will be referred to as *reduced-sensor representation* in the following. Although this model is not as efficient as the sensor representation proposed in [166] it is still reasonable in computational costs compared to those of the propagation mediums volume. For the specimen volume given in figure 3.8-a with the reference mesh resolution of 0.0005 m the reduced sensor model contributes only 1.2 % to the overall computational resources.

### 3.4. Variation of source parameters

In this section the correlation between the input parameters for description of the microscopic failure process and the simulated acoustic emission signal is investigated. To this end the source excitation time  $T_{e,(xyz)}$ , the displacement amplitude  $d_{(xyz)}$  and the acoustic emission source mechanism is varied systematically. In addition, the changes of the simulated acoustic emission signals in dependence of the position of the acoustic emission source model within the plate and the CFRP stacking sequence is investigated. Since these are fundamental investigations of acoustic emission formation and propagation no sensor model was included, which could influence the result of the simulation due to its characteristic frequency dependent sensitivity. For most investigations in

### 3. Simulation of acoustic emission signals

this section the simulated signals were obtained from the surface displacement velocity at distinct point locations on the specimen surface. Only for simulation of the acoustic emission signal voltage the full sensor representation was used selectively in subsections 3.4.1 and 3.4.3.

In the following the Fast-Fourier-Transformation (FFT) of the simulated acoustic emission signals is calculated for comparison of the influence caused by the different source model parameters. To compare the frequency spectra of different simulations the resulting magnitude-spectra are normalized to their absolute value. This compensates the effect of different source excitation energies and yields frequency spectra which are comparable in their frequency weight to each other. In addition, continuous Wavelet Transformations (CWT) are calculated based on a Gabor mother wavelet to visualize the time-frequency behavior of the simulated signals.

#### 3.4.1. Source mechanism

For identification of a particular failure mechanism, it is necessary to investigate the dependency between the different source mechanisms (e.g. matrix cracking, fiber breakage, interface failure) and the characteristics of the respective simulated acoustic emission signal. For the plate-like geometries investigated within this thesis, these acoustic emission sources excite Lamb waves with different ratios of symmetric and antisymmetric propagation modes as described in section 3.2. In the following the simulations are conducted for a CFRP-specimen with  $100 \text{ mm} \times 15 \text{ mm} \times 1.4 \text{ mm}$  (length  $\times$  width  $\times$  height) as shown in figure 3.22-a using  $xz$  - and  $yz$  - symmetry planes marked by the white hachured areas. The encoding of the respective stacking sequences follows the scheme introduced on page 13. For simulation of coating failure a respective CFRP-specimen of  $100 \text{ mm} \times 15 \text{ mm} \times 2 \text{ mm}$  (length  $\times$  width  $\times$  height) with additional  $25 \text{ mm} \times 15 \text{ mm}$  (length  $\times$  width) Nickel and Copper coating layers with various thicknesses are modeled as shown in figure 3.22-b. Also remarked in figure 3.22 are the standard positions of the simulated acoustic emission sources for CFRP-failure at  $(x,y,z) = (0,0,0) \text{ mm}$  and coating failure at  $(x,y,z) = (0,0,1.01) \text{ mm}$ . The respective acoustic emission signals are obtained from the surface displacement velocity at  $(x,y,z) = (38,0,0.7) \text{ mm}$  and  $(x,y,z) = (38,0,1) \text{ mm}$ , respectively. These observation positions were chosen at the respective  $(x,y)$  - midpoints of the experimentally used sensor positions.

In planar geometries the frequency content of acoustic emission signals will depend on the ratio of the excited Lamb wave modes. For fiber reinforced structures the different failure mechanisms naturally result in acoustic emission sources with specific oriented sound radiation directions as already described in section 3.1. To this end simulations of inter-fiber matrix cracking, fiber breakage

### 3. Simulation of acoustic emission signals

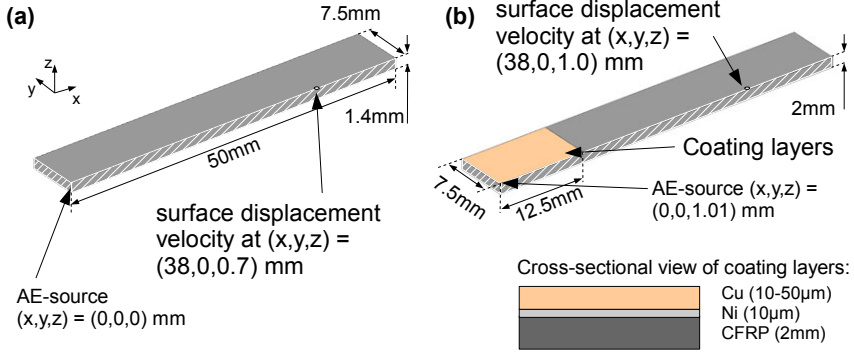


Figure 3.22.: Model specimen geometries used for simulation of different failure mechanisms in CFRP (left) and coated CFRP (right).

and interfacial failure with various crack surface displacement orientations were investigated in the following.

#### Inter-fiber matrix cracking

Inter-fiber matrix cracking is expected to appear perpendicular to the fiber axis direction. The result of a simulation of matrix cracking for an unidirectional  $[0_5]_{sym}$  layup with fiber axis along the x-direction is shown in figure 3.23 for the y- and z-displacement direction. For all these simulations the excitation time  $T_e = 100$  ns and displacement amplitude  $d = 100$  nm was kept constant. The elastic properties of the carbon fiber model were replaced by those of resin (see figure 3.1). The strong low frequency parts observed in the frequency spectra of figure 3.23 suggest strong  $A_0$ -mode intensities of the respective acoustic emission signals. This is only partially the case, since the slowly propagating  $A_0$ -mode is superimposed at the chosen observation position by boundary reflections. Both simulated frequency spectra show good agreement with only small deviations for frequencies above 200 kHz. This gives rise to the assumption, that the characteristic frequency spectra of acoustic emission signals from matrix cracking are independent of the displacement direction. In experimental data of transverse matrix cracking of W. Prosser et al. less intense  $A_0$ -modes are reported [145]. This variation in intensity of the  $A_0$ -mode contribution can be caused by different stacking sequences of the CFRP-specimen, which is a major factor of influence on the overall frequency spectra of the detected acoustic emission signal. This influence is shown in figure 3.24 and 3.25 for additional simulations of matrix cracking in an unidirectional



### 3. Simulation of acoustic emission signals

$[90_5]_{sym}$  layup and an  $[0/90_4]_{sym}$  stacking sequence with displacement in x- or z-direction and equal excitation time  $T_e = 100$  ns and equal displacement amplitude  $d = 100$  nm. In all cases, simulation of matrix cracking results in major frequency contributions below 400 kHz. Furthermore, for each individual layup reasonable agreement is observed between the two matrix cracking displacement directions perpendicular to the fibers axis.

However, the simulations of the different layups show less agreement to each other. These significant differences are caused by the major changes in the elastic properties of the propagation medium and the additional vertical (out-of-plane) anisotropy introduced by variations in the stacking sequence of the CFRP. Thus strong dependencies of the individual frequency spectra on the CFRP layup can be expected in experiments. Consequently, frequency signatures of different failure mechanisms can even be superimposed by such effects. For correlation of distinct failure mechanisms with distinct types of acoustic emission signals a careful investigation of this influence is thus required.

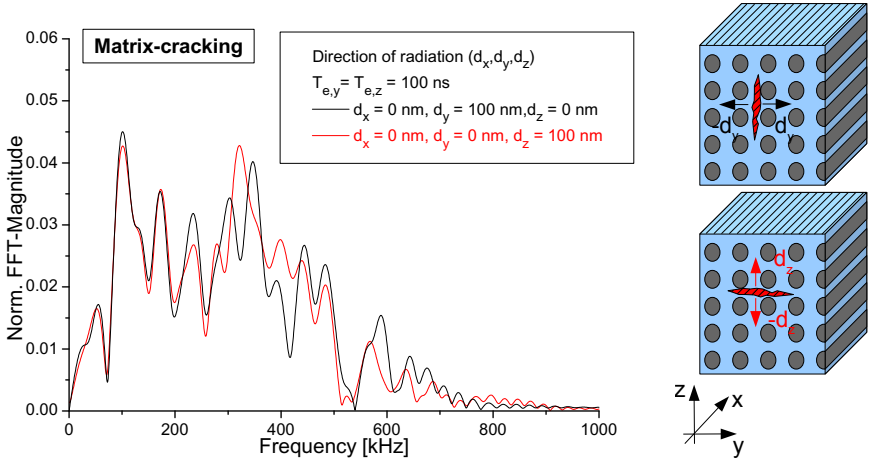


Figure 3.23.: Influence of displacement direction on frequency spectra of simulated signals for excitation time  $T_{e,y} = T_{e,z} = 100$  ns and displacement in y- and z-direction with  $d_y = d_z = 100$  nm for resin elastic properties in an unidirectional  $[0_5]_{sym}$  layup.

### 3. Simulation of acoustic emission signals

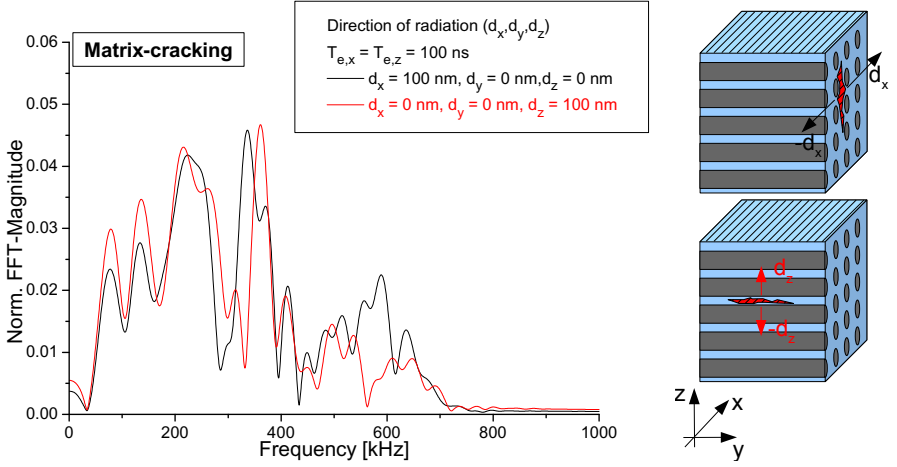


Figure 3.24.: Influence of displacement direction for excitation time  $T_{e,x} = T_{e,z} = 100$  ns and displacement in x- and z-direction with  $d_x = d_z = 100$  nm for resin elastic properties in an unidirectional  $[90_5]_{sym}$  layup.

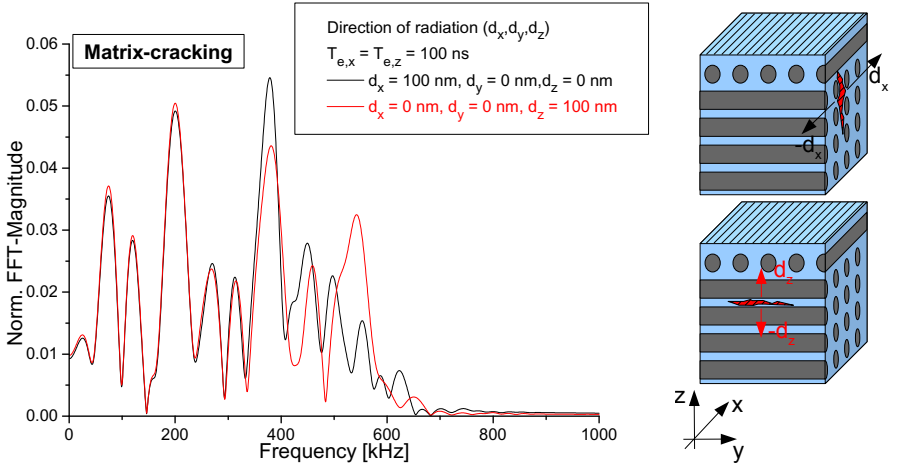


Figure 3.25.: Influence of displacement direction on frequency spectra of simulated signals for excitation time  $T_{e,x} = T_{e,z} = 100$  ns and displacement in x- and z-direction with  $d_x = d_z = 100$  nm for resin elastic properties in a  $[0/90_4]_{sym}$  layup.

### Fiber breakage

Due to the orientation of carbon fibers in the in-plane direction, no fiber breakage is expected to occur in the out-of-plane direction. In the simulations of fiber breakage the intensity of the  $S_0$ -mode dominates, which results in characteristically higher contributions at frequencies above 400 kHz. This is shown in figure 3.26 for a simulated frequency spectrum in an  $[0_5]_{sym}$  layup. For comparison of the influence arising from different stacking sequences an additional simulated frequency spectra of fiber breakage in x-direction for an  $[90/0_4]_{sym}$  stacking sequence is shown. As in the case of matrix cracking, the different CFRP stacking sequences cause distinct differences in the frequency spectra. Although the shifts in frequency contribution caused by different stacking sequences result in less comparable acoustic emission signals for the simulation of fiber breakage, the contributions above 400 kHz are still significantly higher than for matrix cracking.

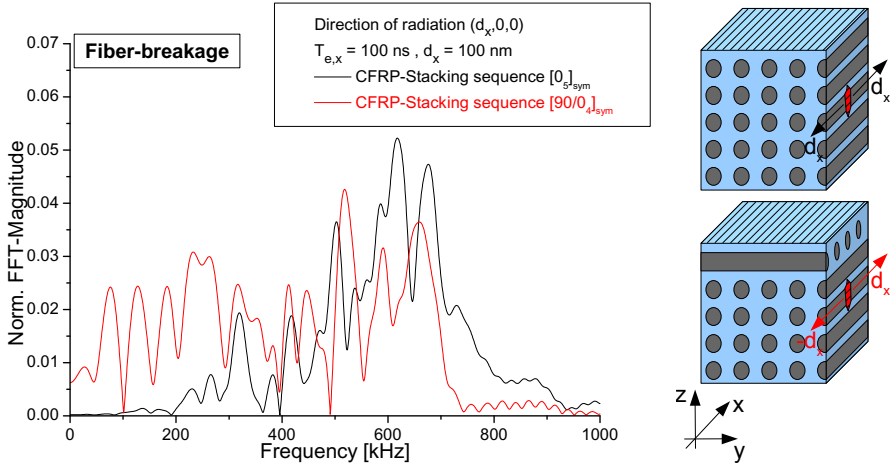


Figure 3.26.: Influence of CFRP-layup on frequency spectra of simulated signals for excitation time  $T_{e,x} = 100 \text{ ns}$  and displacement in x-direction with  $d_x = 100 \text{ nm}$  for fiber elastic properties in an unidirectional  $[0_5]_{sym}$  layup and an  $[90/0_4]_{sym}$  stacking sequence.

The occurrence of different frequency spectra for matrix cracking and fiber breakage are in good agreement with experimental observations of various authors [2, 4–8]. All these studies proposed to distinguish acoustic emission signals of fiber breakage and matrix cracking based on significant contributions at high frequencies (fiber breakage) or low frequencies (matrix cracking), which

is in good agreement with the results obtained from the simulation.

#### Interface failure

Failure in CFRP can also occur at the interface between fiber and matrix. As described in section 3.1 this is modeled by simultaneous displacements along and perpendicular to the fiber axis. Figure 3.27 shows the simulated frequency spectra for systematic variation of the ratio between the displacement components directed in x- and (y,z)-direction. The simulated frequency spectra corresponding to interface failure are different to those observed for fiber breakage or matrix cracking. In contrast to fiber breakage, the signals corresponding to interface failure show stronger contributions for frequencies below 500 kHz. As a consequence the signals can be distinguished from fiber breakage signals. On the other hand, the distinction to matrix cracking is based on stronger contributions of the interface failure signals for frequencies above 450 kHz. Changes in the ratio of the displacement amplitude in x- and (y,z)-direction influences the frequency spectrum of the simulated acoustic emission signal significantly. With increasing displacement in x-direction, the contribution at frequencies above 500 kHz increases, which originates from a stronger excitation of the  $S_0$ -mode.

A better visualization of the results for simulations of different failure mechanisms in CFRP is shown in figure 3.28. The WT-diagrams show three representative signals obtained from simulations of matrix cracking and fiber breakage with  $T_{e,x} = 100$  ns and  $d_x = 100$  nm and interface failure with  $T_{e,x} = T_{e,y} = T_{e,z} = 100$  ns,  $d_z = 100$  nm and  $d_x = d_y = 10.0$  nm in an unidirectional  $[0_5]_{sym}$  stacking sequence. Clearly all signals show high frequency contributions originating from the  $S_0$ -mode at the initial part of the signal and lower frequency parts after  $t = 0.02$  ms. The lower frequency parts are attributed to the propagation of the  $A_0$ -mode superimposed by boundary reflections. The characteristic frequency spectra of the different failure mechanisms shown in figures 3.23 - 3.27 are a direct consequence of the different ratios of high frequency  $S_0$ -mode and the low frequency components as already discussed by M. Hamstad et al. [76]. In general, the parts of the signal after the initial arrival of the  $S_0$ - and  $A_0$ -mode are less characteristic for the source mechanism, since they are most of all caused by boundary reflections. Consequently, signal features obtained from the frequency domain are most characteristic, when obtained only from the initial part of the signal. This should include the full  $S_0$ -mode and a comparable amount of the  $A_0$ -mode. While this can be achieved by a fixed time scale for constant source-sensor distances, this is more difficult for practical applications. Here, as consequence of the signal propagation,

### 3. Simulation of acoustic emission signals

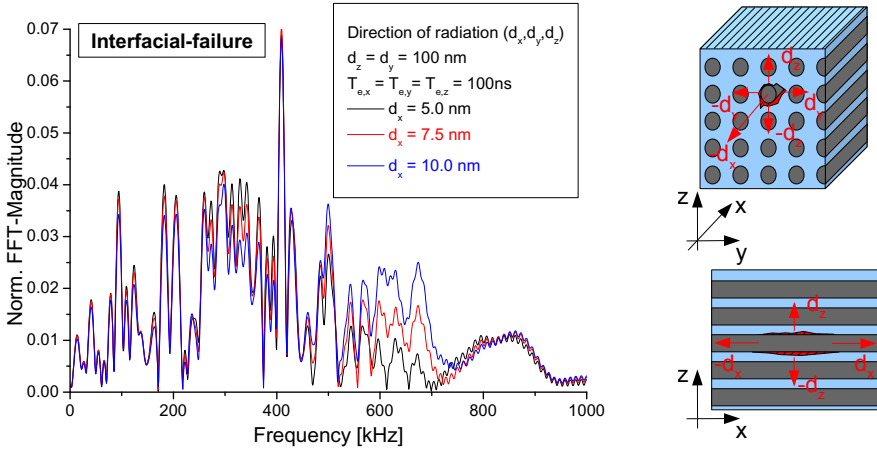


Figure 3.27.: Influence of the ratio between displacement components directed in x- and (y,z)-direction on frequency spectra of simulated signals. The excitation times are  $T_{e,x} = T_{e,y} = T_{e,z} = 100$  ns, the displacement amplitudes in y- and z-direction are  $d_y = d_z = 100$  nm and  $d_x$  is varied from 5.0 nm to 10.0 nm.

### 3. Simulation of acoustic emission signals

the different Lamb wave modes suffer from dispersion and will broaden after short propagation distances. Thus a careful investigation of the capabilities of distinction of different failure mechanisms in the chosen specimen geometry is strongly recommended. For the present specimen geometry a time scale between 0.05 ms and 0.10 ms yields a reasonable value for distinction of the presented failure mechanisms.

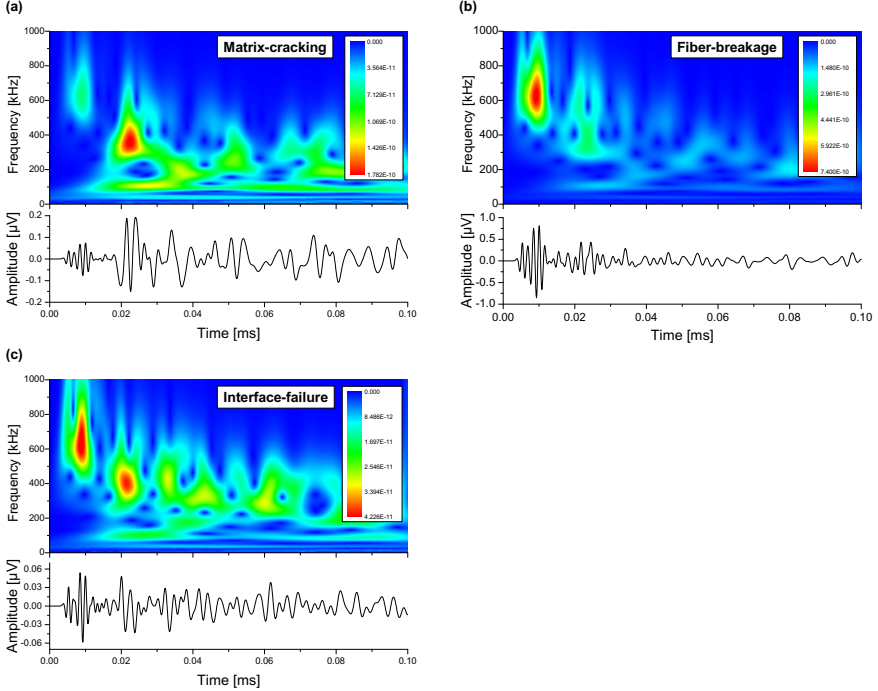


Figure 3.28.: WT-diagrams of matrix cracking (a) and fiber breakage (b) with  $T_{e,x} = 100$  ns and  $d_x = 100$  nm and interface failure (c) with  $T_{e,x} = T_{e,y} = T_{e,z} = 100$  ns,  $d_z = 100$  nm and  $d_x = d_y = 10.0$  nm.

#### Coating failure

The simulation of coating failure was done for three different source mechanism as presented in section 3.1. These are mode-I cracks in nickel, mode-I cracks in copper and mode-I delamination between nickel and copper-coatings. Since the anisotropic elastic coefficients of the experimentally used KDK 8054/120

### 3. Simulation of acoustic emission signals

CFRP substrates were not obtained experimentally, these were calculated from the microscopic properties as provided by the manufacturer following the approach given in Appendix B. The resulting anisotropic elastic coefficients of the KDK 8054/120 CFRP substrates and the elastic properties of the coating materials are summarized in table 3.6. For simulation of the acoustic emission signal voltage the full sensor representation was used with sensor mid-point at the position  $(x,y,z) = (38,0,0.7)$  mm.

	Copper	Nickel	KDK 8054/120 (woven fabric)
Density $\rho$ [kg/m <sup>3</sup> ]	8700	8900	1550
Poisson-Ratio	0.35	0.29	-
Elastic coefficients [GPa]	$E=110.0$	$E=205.0$	$C_{xxxx}=67.5$ $C_{xxyy}=7.6$ $C_{xxzz}=7.6$ $C_{yyyy}=67.5$ $C_{yyzz}=8.1$ $C_{zzzz}=16.9$ $C_{yzyz}=4.9$ $C_{zxzx}=4.6$ $C_{xyxy}=4.6$
Source	[149]	[149]	Appendix B

Table 3.6.: Summary of material properties used for the simulation of failure mechanisms in coatings applied on KDK 8054/120 substrates.

In contrast to the simulations of matrix cracking and fiber breakage, the magnitude of displacement for coating failure was calculated to match the different fracture strengths  $\sigma_{frac}$  of the materials. The orientation of  $\sigma_{frac}$  is given by the  $(x,y,z)$  subset as  $\sigma_{(x,y,z)}$ . For copper cracking the fracture strength was chosen as  $\sigma_{frac} = 200$  MPa, for nickel cracking as  $\sigma_{frac} = 140$  MPa and for interfacial failure as  $\sigma_{frac} = 9$  MPa. While the first two values were adapted from literature [149], the value for interfacial strength was obtained from the measured fracture toughness value (see section 4.6). The normalized frequency spectra of the simulated signals for all three failure mechanisms are shown in figure 3.29-a. Overall the three normalized frequency spectra show strong similarities to each other. Only the frequency spectrum of copper cracking shows slightly higher contributions at frequencies above 300 kHz. In direct comparison, the frequency spectra of nickel cracking and nickel-

### 3. Simulation of acoustic emission signals

copper delamination are not clearly distinguishable. A more characteristic difference for the failure mechanisms is instead observed in the magnitude of the simulated acoustic emission signals (see figure 3.29-b). The different energies of the acoustic emission signals reflect the differences in the associated strain energy release. Consequently, a distinction between the three failure mechanisms is possible based upon their energy level, if the strain energy release and the crack volume are similar for each acoustic emission excitation (see also section 3.4.3).

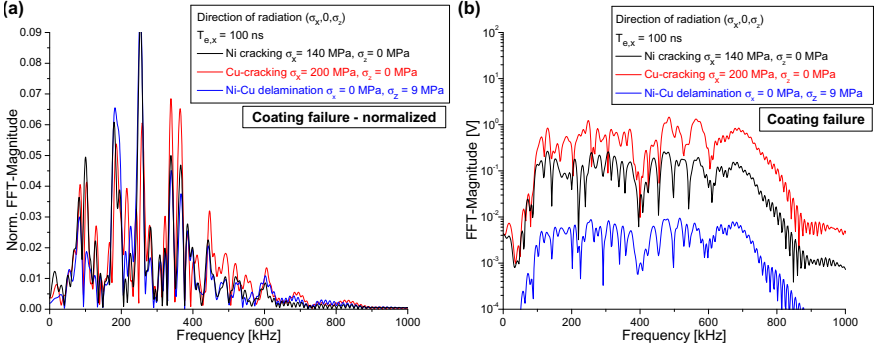


Figure 3.29.: Comparison of frequency spectra of copper-cracking, nickel-cracking and nickel-copper delamination with various fracture strengths and constant excitation time  $T_{e,x} = T_{e,z} = 100$  ns after normalization by absolute value (a) and without normalization (b).

#### 3.4.2. Source excitation time

As already pointed out by M. Giordano et al. and M. Hamstad et al. the frequency spectra of acoustic emission signals are strongly influenced by the response of the cracking material to the source excitation time [45, 167]. This influence is caused by the mismatch between the relaxation time of the (viscoelastic) material and the excitation time of the crack progress. Based on the frequency spectra of the source model shown in figure 3.6 this effect is expected to be most pronounced for the elastic properties of resin in comparison to the elastic properties of carbon fibers. In figure 3.30 the effect of the different elastic properties of these materials on the frequency spectra are shown for an excitation in x-direction for various excitation times obtained within a simulation of an unidirectional  $[0_5]_{sym}$  layup with T800/913 elastic properties.



### 3. Simulation of acoustic emission signals

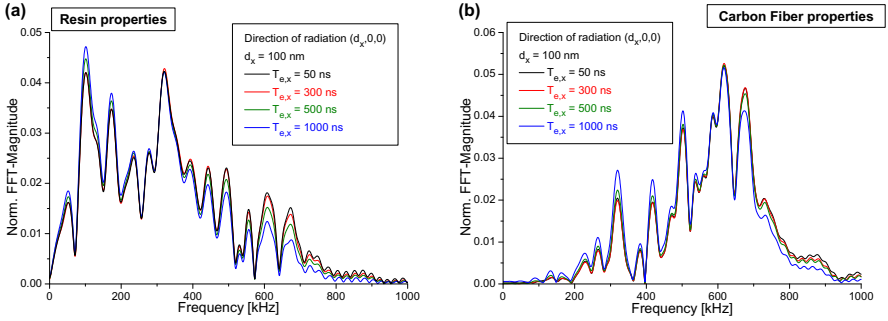


Figure 3.30.: Influence of excitation time  $T_{e,x}$  for displacement in x-direction with  $d_x = 100$  nm for resin elastic properties (a) and carbon fiber elastic properties (b) on frequency spectra of simulated signals.

For both material properties shown in figure 3.30 an influence of the source excitation time  $T_{e,x}$  is observed. When  $T_{e,x}$  increases (i.e. the crack surface moves slower) the frequency content shifts to lower frequencies, which results from a shift of energy contributions to the  $A_0$ -mode. In direct comparison of matrix cracking and fiber breakage this effect is slightly more pronounced for resin elastic properties.

The same systematic shift of frequency contributions was also observed for matrix cracking with excitation in y- and z-direction as shown in figure 3.31. This demonstrates that the spectral changes resulting from different excitation times do not depend on the chosen crack surface displacement direction. Instead this effect is solely caused by the elastic properties of the cracking medium and the ratio between the materials relaxation and the excitation time, which is the magnitude of the Deborah-number. The additional influence of the materials viscoelastic response as described by M. Giordano et al. was not included in the current linear elastic material model, but is expected to increase the influence of the source excitation time drastically [45].

#### 3.4.3. Source energy

To investigate the correlation between the source energy and the energy of the respective acoustic emission signals, the size of the acoustic emission source model and the magnitude of displacement were varied in the FEM-model. The simulations were performed for two propagation media and three different failure types. The first type is copper cracking within an isotropic copper plate. The second and third type are matrix cracking and fiber breakage in

### 3. Simulation of acoustic emission signals

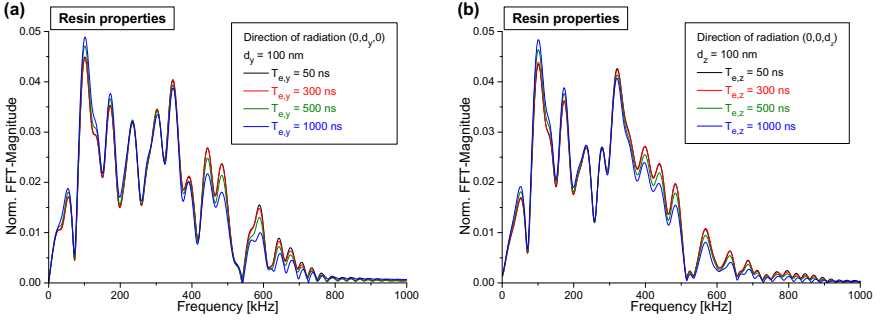


Figure 3.31.: Influence of excitation time  $T_{e,x}$  for displacement in  $y$ - and  $z$ -direction with  $d_x = 100$  nm for resin elastic properties on frequency spectra of simulated signals.

an anisotropic CFRP plate with T800/913 properties with  $[0_5]_{sym}$  layup. The geometry of both plates corresponds to those in figure 3.22 with the  $xz$ - and the  $yz$ -plane chosen as symmetry planes. The size of the source model with scale 1 is equivalent to the dimensions given in figure 3.2, while all other scales are understood as multiplier to these dimensions. For instance, scale 2 doubles all dimensions. To simulate different crack volumes at constant source model scale, the magnitude of displacement  $d_x$  was varied at constant excitation time  $T_{e,x}$ .

As prerequisite for the investigation, the formation process of the acoustic emission signal has to be independent of the chosen excitation energy and source scale. Consequently, results obtained for the signal energies or the maximum signal voltages are only comparable if the ratio of symmetric and antisymmetric Lamb wave modes is constant. This requirement is expressed in identical normalized frequency spectra, as shown in figure 3.32-a for copper cracking. Clearly, the different frequency spectra are almost identical besides minor deviations at higher frequencies. These deviations are attributed to the slight differences of mesh density in the vicinity of the different scaled source models. The same behavior was obtained for simulations of matrix cracking in  $x$ - and  $z$ -direction, as well as for fiber breakage.

As exemplarily shown in figure 3.32-b for a simulation of copper cracking, the acoustic emission signal amplitude shows strict correlation to the inverse propagation length. This agrees with the reported analytical dependencies found in equations (2.32), (2.33) and (2.34) [37,45]. To avoid this influence all acoustic emission signals were obtained at a constant propagation distance to the sensors mid-point at  $(x,y,z) = (38,0,0.7)$  mm. The signal voltages were

### 3. Simulation of acoustic emission signals

obtained from the reduced WD-sensor model.

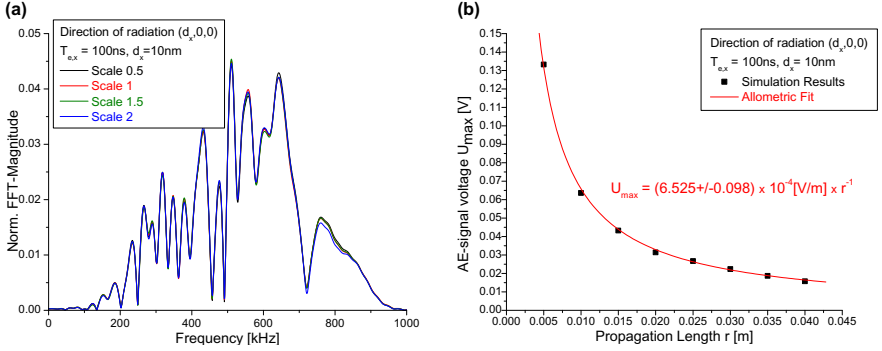


Figure 3.32.: Normalized frequency spectra for copper cracking in dependency of the source model scale at constant excitation time  $T_{e,x} = 100$  ns (a) and correlation between propagation length and maximum amplitude of acoustic emission signals (b).

As given in equation (2.29), the amplitude of the detected acoustic emission signal is expected to be proportional to the crack volume, when assuming direct proportionality between the elastic wave amplitude and the electrical signal voltage. Consequently, the total crack volume increment  $\Delta V$  is expected to be proportional to the maximum signal amplitude  $U_{max}$ .

Figures 3.33-a, 3.33-b and 3.33-c show the simulation results for the investigation of this relation for all three failure mechanisms investigated. For every source scale and displacement magnitude a strict correlation between  $U_{max}$  and the crack volume  $\Delta V$  is observed. The minor deviation from the exact linear proportionality is again attributed to the differences in the mesh resolution in the vicinity of the source models. This is confirmed by the fact, that for constant source model scale almost exact linear correlation between  $U_{max}$  and  $\Delta V$  is observed. In addition the proportionality factor between  $U_{max}$  and  $\Delta V$  is found to be dependent on the cracking mediums elastic properties. As shown in figure 3.33-d for the three material systems a linear correlation between  $U_{max}$  and the squared longitudinal sound velocity  $c_L^2$  at constant  $\Delta V = 10^{-18}$  [m<sup>3</sup>] was observed. Thus for a higher longitudinal sound velocity, higher signal voltages are obtained for the same crack volume increment.

From the above relations, the dependencies of  $U_{max}$  can thus be written as

$$U_{max}(\Delta V, c_L^2, r) = \beta(c_L^2) \cdot \frac{\Delta V}{r}. \quad (3.8)$$

### 3. Simulation of acoustic emission signals

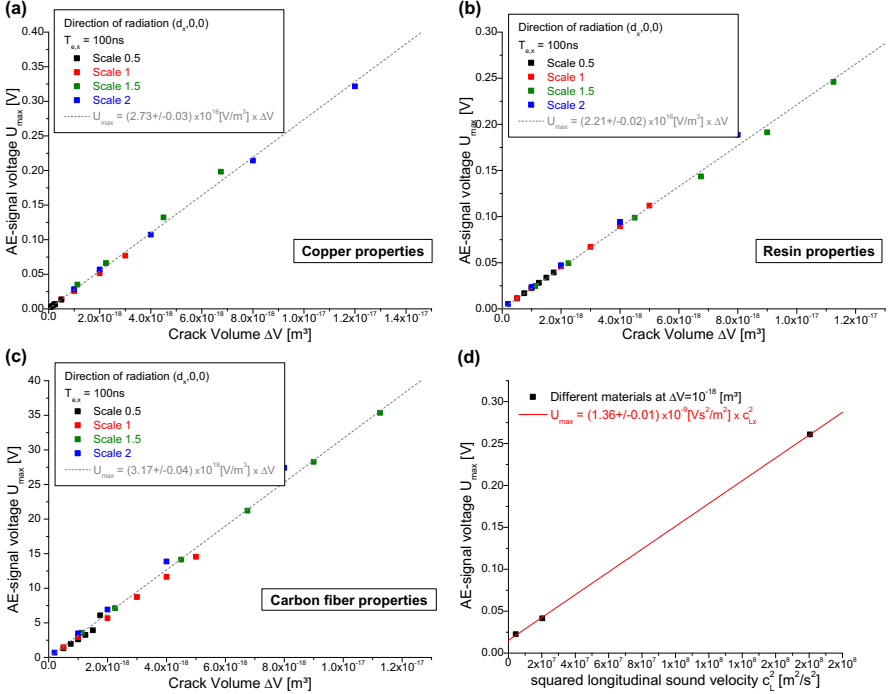


Figure 3.33.: Dependency between crack volume  $\Delta V$  and maximum amplitude of acoustic emission signals for copper cracking (a), matrix cracking (b) and fiber breakage (c). Dependency between maximum amplitude  $U_{max}$  of acoustic emissions signals and squared longitudinal sound velocity  $c_L^2$  at constant crack volume (d).

This introduces a material specific proportionality constant  $\beta(c_L^2)$  dependent on the longitudinal sound velocity of the cracking medium. This correlation between  $U_{max}$  and  $\Delta V$ ,  $r$  and  $c_L^2$  obtained from the FEM-model agrees with the analytical relations reported by the different authors mentioned in section 2.2.2. The generalized theory of acoustic emission describes the same dependency between the amplitude of the detected acoustic emission signal at the specimen surface  $U_{max}$  and the size of the crack volume  $\Delta V$  [38, 39]. The theory of M. Lysak derived from a fracture mechanics approach in turn assumes a correlation between the crack's surface area (crack length) and the amplitude of the acoustic emission signal [37]. The discrepancy of both theories can be attributed to the reduction in dimensionality of the source model description,

### 3. Simulation of acoustic emission signals

which means both theories report a dependency between the geometric size of the crack increment and the acoustic emission amplitude.

For experimental applications the correlation between the detected acoustic emission signal energy and the microscopic strain energy release during crack propagation is of great interest. The strain energy release is the quantity which describes the amount of energy required for a crack volume increment within a material. Thus  $\Delta V$  and  $\Omega$  are only direct proportional, if the value of the fracture toughness is constant (see eq. (2.1)) and the aspect ratio of the crack increment is kept constant. The first condition typically also requires similar loading conditions during crack progress. The second condition is less important for isotropic materials, but is a dominating contribution in anisotropic materials as demonstrated in the following.

The dependency  $W_{AE}$  and  $\Omega$  is shown in figure 3.34 for the three failure mechanisms investigated. In an isotropic propagation medium, like the investigated copper plate the simulated acoustic emission energy  $W_{AE}$  shows strict linear proportionality to the strain energy release  $\Omega$  for all source model scales (see fig. 3.34-a). This proportionality is obviously not fulfilled for the simulations of matrix cracking and fiber breakage within an anisotropic propagation medium (see figs. 3.34-b and 3.34-c). For these simulations, the linear proportionality between  $W_{AE}$  and  $\Omega$  is only fulfilled at constant source model scale. To analyze the origin of this correlation, the simulations were repeated in an anisotropic plate with T800/913 properties with a reduced source representation. For this simulation only the cross was cut out of the anisotropic propagation medium. The only difference to the simulations of the copper plate in figure 3.34-a is the change from isotropic to anisotropic elastic properties. In these simulations, again a strict dependency of the source model scale on the proportionality between  $W_{AE}$  and  $\Omega$  was found. Consequently, this correlation is solely attributed to the anisotropic elastic properties of the propagation medium and is not caused by the acoustic emission source model.

A closer look at the simulations of matrix cracking and fiber breakage instead reveals an approximate linear correlation between  $W_{AE}$  and the strain energy release  $\Omega$  times the crack surface area  $A$  (see figure 3.35). This correlation is caused by the symmetry break introduced by the orientation of the crack surface displacement. Within an isotropic medium the deformation directed along each axis is equal and thus the magnitude of displacement only depends on the crack volume, given by magnitude of displacement  $d$  times crack surface area  $\Delta A$ . For an anisotropic medium, the displacement magnitudes along the different axes are not equal. Here an increase in  $\Delta A$  is not comparable to an increase in displacement  $d$ , since the different directions show different elastic properties and thus result in different energy contributions. Consequently, higher crack surface areas result in higher acoustic emission signal energies for

### 3. Simulation of acoustic emission signals

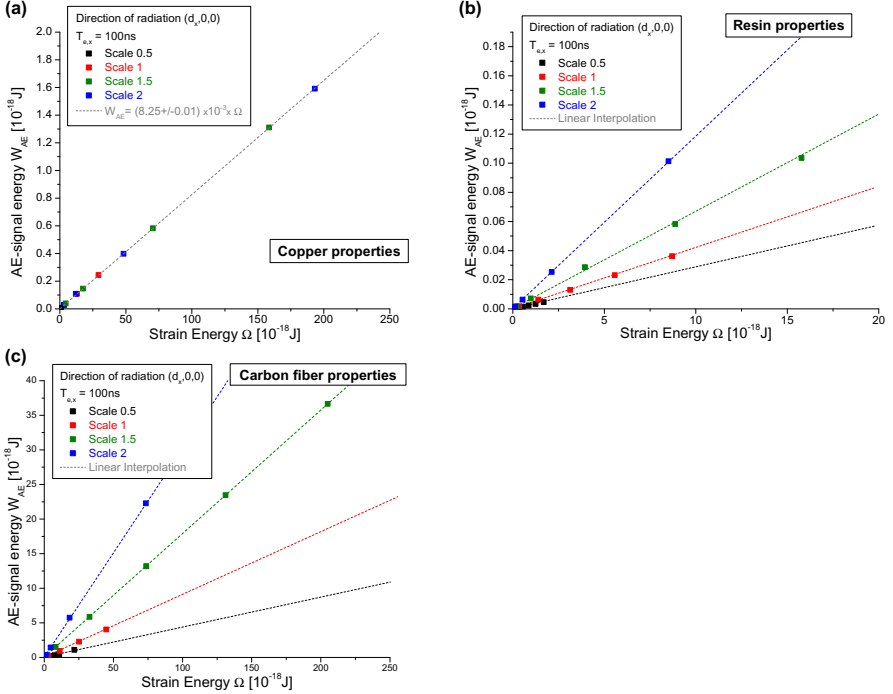


Figure 3.34.: Dependency between strain energy release  $\Omega$  and acoustic emission signal energy  $W_{AE}$  for copper cracking (a), matrix cracking (b) and fiber breakage (c) at various source scales.

the same microscopic strain energy release.

Based upon these investigations equation (2.58) can be written for isotropic media:

$$\frac{\partial W_{AE}}{\partial t} = \beta \frac{\partial \Omega}{\partial t} = \beta \frac{\partial \Omega}{\partial V} \frac{\partial V}{\partial t}. \quad (3.9)$$

For the special case of a planar mode-I crack growth in x-direction this can also be written as:

$$\frac{\partial W_{AE}}{\partial t} = \beta \frac{\partial \Omega}{\partial A \partial x} \frac{\partial A \partial x}{\partial t} = \beta \frac{\partial \Omega}{\partial A} \frac{\partial A}{\partial t} = \beta G_{Ic} \frac{\partial A}{\partial t}. \quad (3.10)$$

This equation relates the energy of the observed acoustic emission signals to the materials fracture toughness  $G_{Ic}$  and the size of planar crack growth  $\partial A / \partial t$ .

### 3. Simulation of acoustic emission signals

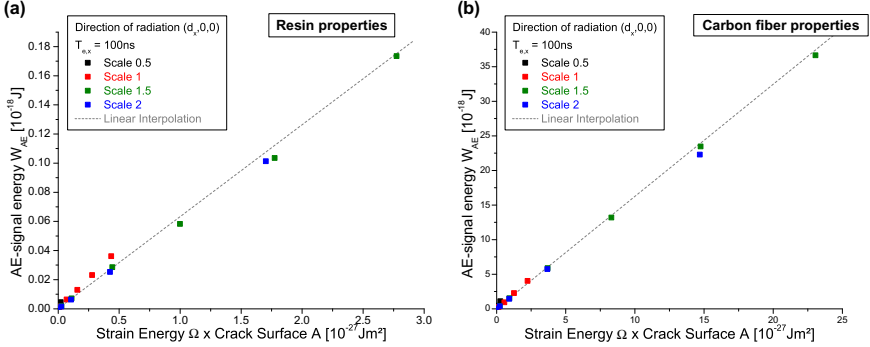


Figure 3.35.: Dependency between strain energy release  $\Omega$  times crack surface area  $A$  and acoustic emission signal energy  $W_{AE}$  for matrix cracking (a) and fiber breakage (b) at various source scales.

A similar formulation of equation (2.58) for anisotropic propagation media has to reflect the dependency of the proportionality constant  $\beta$  on the crack surface area  $\Delta A$ :

$$\frac{\partial W_{AE}}{\partial t} = \beta(\Delta A) \frac{\partial \Omega}{\partial t}. \quad (3.11)$$

Thus the acoustic emission signal energy is directly related to the microscopic strain energy release and the crack surface area. Measurement of the acoustic emission energy can, consequently, only be used as measure for the strain energy release, if the crack surface area of the microscopic failure mechanism is constant for all crack increments. In terms of fracture mechanics this condition can be understood as stable crack growth.

In summary, within the presented variation of source scale and source energy the frequency spectra of the simulated acoustic emission signals show no significant changes in their appearance. Consequently frequency spectra can be used as characteristic fingerprint of the acoustic emission source type. This agrees well with results from M. Hamstad et al., who observed a similar behavior for simulations of dipole-type point sources in isotropic material. They reported that the ratio of  $S_0$ - and  $A_0$ -magnitude is independent of the acoustic emission source strength [76].

In contrast, the correlation between the microscopic strain energy release during crack propagation and the energy of the acoustic emission signals is only direct proportional for isotropic propagation media. In the case of anisotropic elastic properties the correlation shows additional dependency on the size of

the acoustic emission source. In general, the measurement of the microscopic strain energy release is thus only feasible for stable crack growth, and especially when the acoustic emission sources show narrow distributions of crack volume increments and similar fracture toughness.

#### 3.4.4. Source position

So far the results of matrix cracking and fiber breakage were obtained for a position symmetrically centered with respect to all three axes (center-point of the used specimen). In order to use frequency criteria obtained from acoustic emission signals to distinguish different failure mechanisms, only a limited dependence of the frequency spectra on the source position is acceptable. However, the propagation distance between acoustic emission source and point of detection has great influence on the frequency composition of acoustic emission signals due to mode specific attenuation and dispersive signal propagation [56, 159, 168, 169]. In addition, M. Hamstad et al. already pointed out, that especially the z-position of the acoustic emission source in planar geometries is crucial for the ratio of stimulated plate wave modes [76]. Consequently, the distance between acoustic emission source and point of detection along the x- and y-axis were varied to investigate the influence of attenuation and dispersion. In addition the position of the source was varied along the z-axis. The simulations were performed for CFRP-specimen geometries with dimensions of 100 mm  $\times$  15 mm  $\times$  1.4 mm (length  $\times$  width  $\times$  height) and elastic properties as given in table 3.2. The acoustic emission signals were obtained from the surface displacement velocity at the position  $(x,y,z) = (38,0,0.7)$  mm. For all simulations the excitation time  $T_{e,x} = 100$  ns and the displacement amplitude  $d_x = 100$  nm were kept constant. As investigation range for the source positions, the x-, y- and z-positions were chosen similar to the microscopically observed damaged regions within the specimen.

#### Inter-fiber matrix cracking

For these simulations the source position was varied along the x-axis within a distance of  $(\pm 15, 0, 0)$  mm. The resulting normalized frequency spectra of the two extreme values are shown in figure 3.36 in comparison to the frequency spectra of matrix cracking obtained at  $(x,y,z) = (0,0,0)$  mm. The shift in frequency contributions to higher frequencies for the source model position  $(x,y,z) = (15,0,0)$  mm is caused by the closer distance to the point of detection. As result from the reduced propagation distance, the  $S_0$ -mode is attenuated less and causes higher frequency contributions than at the reference position at  $(x,y,z) = (0,0,0)$  mm. The same effect is observed for the position at  $(x,y,z)$



### 3. Simulation of acoustic emission signals

= (-15,0,0) mm, although this reflects an increased propagation distance and thus results in a shift of frequency distributions to lower frequencies. For all three simulations the characteristic frequency distribution of matrix cracking with higher intensity at frequencies below 500 kHz is observed.

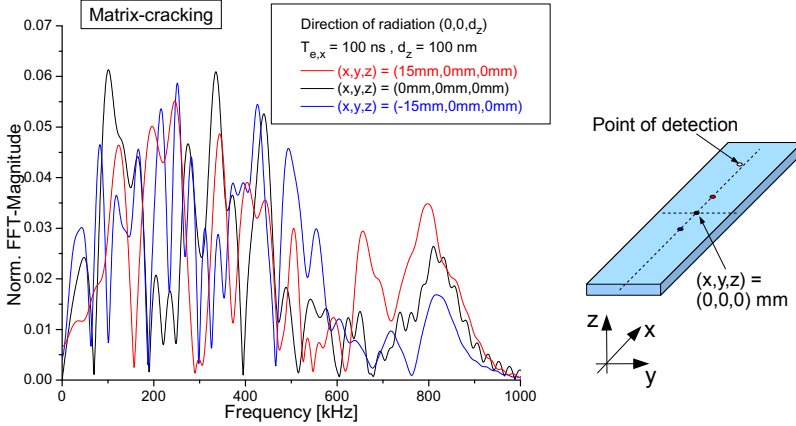


Figure 3.36.: Comparison of normalized frequency spectra for matrix cracking with  $T_{e,x} = 100 \text{ ns}$  and  $d_x = 100 \text{ nm}$  at different positions along the specimens x-axis.

In addition, the source position was varied along the y-axis of the specimen geometry starting at the reference position at  $(x,y,z) = (0,0,0) \text{ mm}$ . The frequency spectra shown in figure 3.37 are obtained at the marked positions increasing up to  $y = 7.5 \text{ mm}$ . In comparison to the observations for variations along the x-axis, the found influence of the y-position is less intense. This is caused by the very similar source-sensor distances of all four positions. Source positions closer to the specimen edge show less intense  $S_0$ -modes. This is expressed in the vanishing contributions around 800 kHz visible in figure 3.37. Since the specimen is fully symmetric around the xz-plane, the same effect is observed for source positions with decreasing y-components down to  $y = -7.5 \text{ mm}$ .

Finally, the source position was varied along the z-axis for the positions given in figure 3.38. The simulated frequency spectra show a decrease of intensity of the  $S_0$ -mode when the source position approaches the surface of the specimen. This is most pronounced at the position  $z = 0.6 \text{ mm}$ . In summary, for all source positions investigated the frequency distribution characteristic of matrix cracking is retained and is not completely superimposed by the effects

### 3. Simulation of acoustic emission signals

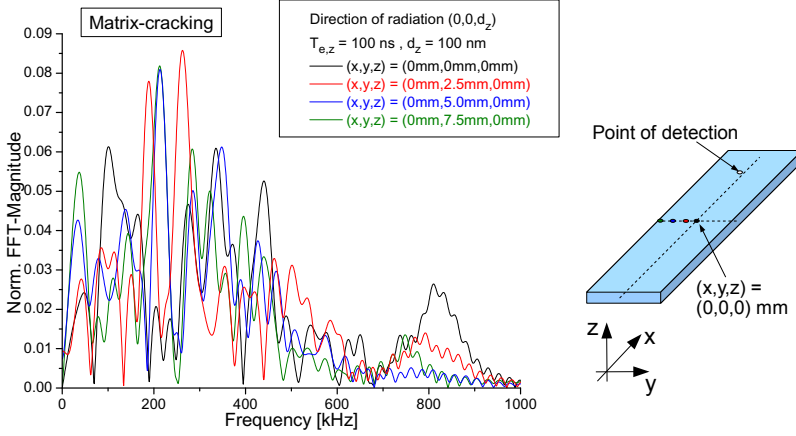


Figure 3.37.: Comparison of normalized frequency spectra for matrix cracking with  $T_{e,x} = 100$  ns and  $d_x = 100$  nm at different positions along the specimens y-axis.

of dispersive Lamb wave propagation.

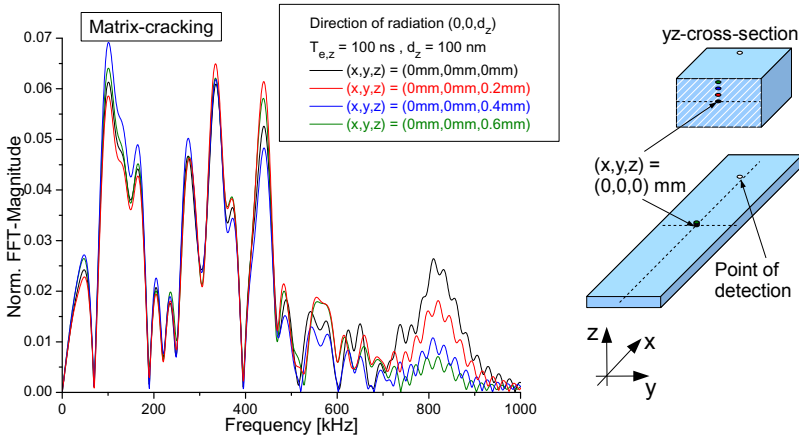


Figure 3.38.: Comparison of normalized frequency spectra for matrix cracking with  $T_{e,x} = 100$  ns and  $d_x = 100$  nm at different positions along the specimens z-axis.

#### Fiber breakage

In the case of fiber breakage the source position was again varied along the x-, y- and z-axis. The resulting normalized frequency spectra of the two extreme values at a distance of  $x = \pm 15$  mm are shown in figure 3.39 in comparison to the spectra obtained at the reference position at  $(x,y,z) = (0,0,0)$  mm. Similar to the investigation above, the shift in frequency contributions to higher frequencies for the source model position  $(x,y,z) = (15,0,0)$  mm is caused by the closer distance to the point of detection, while the position  $(x,y,z) = (-15,0,0)$  mm causes shifts to lower frequencies, respectively. Independent of these effects, for all three simulations the characteristic frequency distribution for fiber breakage with high intensities at frequencies above 500 kHz is observed.

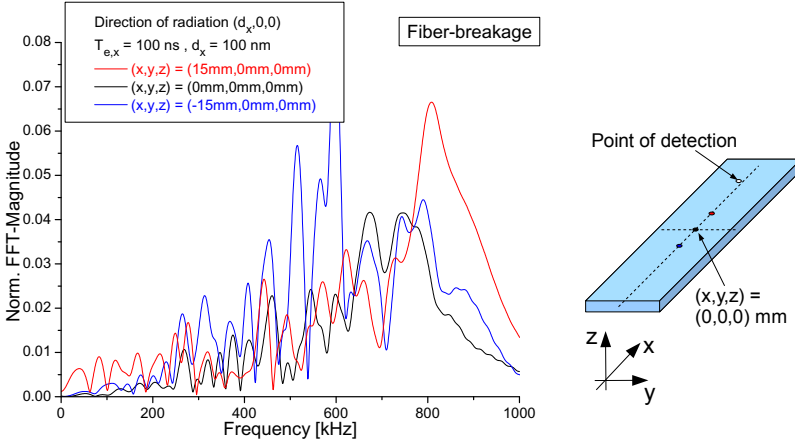


Figure 3.39.: Comparison of normalized frequency spectra for fiber breakage with  $T_{e,x} = 100$  ns and  $d_x = 100$  nm at different positions along the specimens x-axis.

As second investigation, the source position was varied along the y-axis up to a distance of  $y = 7.5$  mm located close to the specimens edge. The resulting normalized frequency spectra of the extreme and two intermediate positions are shown in figure 3.40 in comparison to the spectra obtained at  $(x,y,z) = (0,0,0)$  mm. Similar to the case of matrix cracking above, a decrease of the contributions from the  $S_0$ -mode is observed when approaching the edge of the specimen. This results in increased contributions at frequencies below 500 kHz, but cannot hide the frequency distribution characteristic of fiber breakage with highest intensities above 500 kHz.

### 3. Simulation of acoustic emission signals

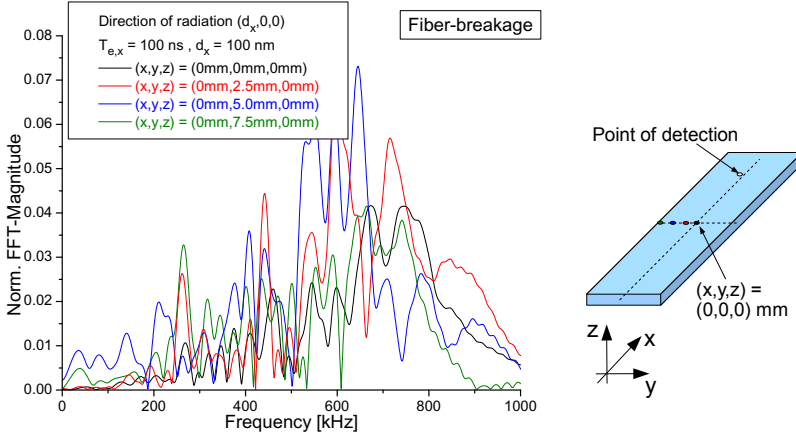


Figure 3.40.: Comparison of normalized frequency spectra for fiber breakage with  $T_{e,x} = 100$  ns and  $d_x = 100$  nm at different positions along the specimens y-axis.

The simulated frequency spectra of a systematic variation of the source position along the specimens z-axis is shown in figure 3.41. Starting at the reference position at  $(x,y,z) = (0,0,0)$  mm the z-position was varied at three steps up to  $z = 0.61$  mm, which locates the acoustic emission source practically at the specimen surface, since the z-length of the source model is  $100 \mu\text{m}$ . In comparison to the variations along the x- and y-axes the influence of the source models z-position is more pronounced. With increasing z-position, the spectral contributions above 500 kHz decrease significantly, while the contributions around 400 kHz and below increase. Despite the shifts in the weight of the frequency distribution the spectra remain characteristic of fiber breakage due to the significant contributions above 550 kHz.

The strong dependence of the frequency spectra of the signals on the source position demonstrates, that identification of distinct failure mechanisms is not possible based on one single frequency criteria like, e. g. the maximum peak frequency. Instead the identification procedure should generally rely on several characteristic frequency based criteria, like FFT-magnitude contributions in different frequency intervals or similar descriptors derived from wavelet-transformations.

### 3. Simulation of acoustic emission signals

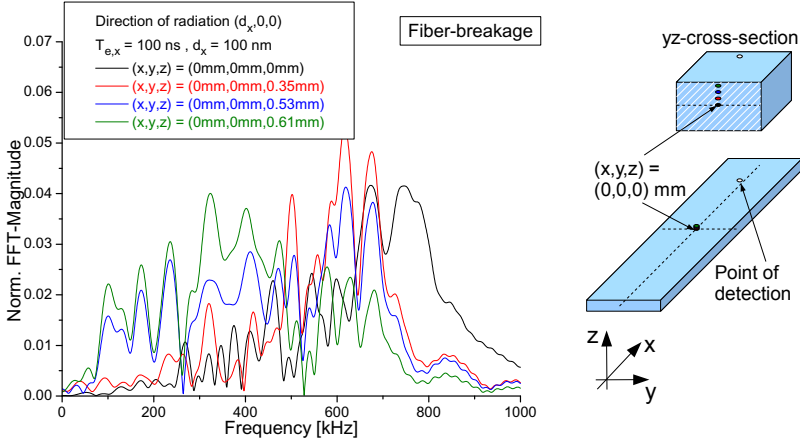


Figure 3.41.: Comparison of normalized frequency spectra for fiber breakage with  $T_{e,x} = 100$  ns and  $d_x = 100$  nm at different positions along the specimens z-axis.

#### Coating failure

For coating failure the influence on the frequency spectra for variations along the x- and y-axis position was not investigated. Here the influence of the source is expected to be similar to those observed for fiber breakage and matrix cracking. Thus no strong deviations in dependence of the (x,y)-position are expected. In particular, the acoustic emission sources z-position is almost fixed due to the coatings position at the CFRP-substrates surface. Consequently, no influence from the slight variations in the z-position is expected either.

### 3.5. Influence of specimen geometry

In addition to the source mechanism and the source position, the geometry of the propagation medium is expected to have significant influence on the signal characteristics as well. For the present investigation, the most obvious influence arises from the planar geometry, which causes formation of Lamb waves as described in section 3.2. Consequently, the thickness of the planar specimens is a major factor of influence for the obtained acoustic emission signals. An additional influence is expected to arise from the different reflections at the boundaries of the specimen in x and y-direction. As demonstrated in section 3.4.1 the stacking sequence of the CFRP-specimens also shows

### 3. Simulation of acoustic emission signals

significant influence on the frequency spectra of the acoustic emission signals. To investigate all these influences the typical failure mechanisms occurring in CFRP as presented in section 3.1 were investigated in three different types of experimentally used CFRP specimens.

These are bending specimen, tensile specimen and Double Cantilever Beam (DCB) specimen as shown in figures 3.42 - 3.44 in photographic images of the used specimens in combination with the volumetrically reduced geometries used in the simulations. The respective geometries symmetry planes are marked by white hachured areas. For comparison with experimentally recorded acoustic emission signals in chapter 4, the full WD-sensor model was included in the simulations at the annotated positions. To avoid any influences arising from the source position and the excitation parameters, the source model position was chosen at  $(x,y,z) = (0,0,0)$  mm for all geometries with constant excitation time  $T_{e,x} = 100$  ns and displacement amplitude  $d_x = 100$  nm. As representative example for the flexural testing geometries an unidirectional  $[0_5]_{sym}$  layup was modeled, while for the tensile testing geometry the experimentally used  $[0/90_3/0]_{sym}$  layup was used. The DCB testing geometry was simulated as unidirectional  $[0_{12}]_{sym}$  layup.

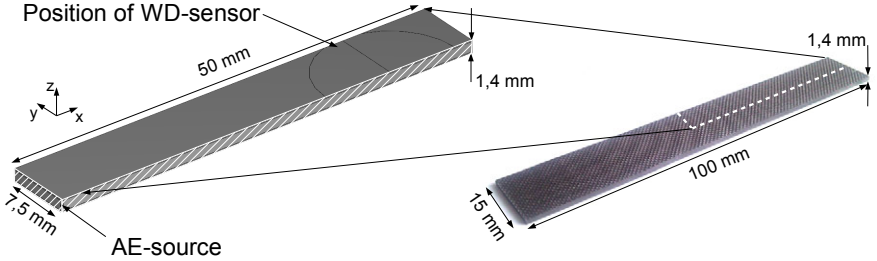


Figure 3.42.: Model geometry of bending specimen geometry (left) and photographic image of experimentally used bending specimen (right). The geometry is adapted to DIN-EN-ISO 14125.

A comparison of the simulated frequency spectra of matrix cracking with displacement  $d_z = 100$  nm and constant excitation time  $T_{e,z} = 100$  ns for the three different specimen geometries is shown in figure 3.45. Despite the noticeable differences in the frequency spectra, all signals show highest frequency contributions at frequencies around 200 kHz. In the time domain this is expressed in small contributions to the  $S_0$ -mode and strong contributions to the  $A_0$ -mode. This is clearly visible for the DCB testing geometry, while for the flexural and tensile testing geometry the  $A_0$ -mode is superimposed by

### 3. Simulation of acoustic emission signals

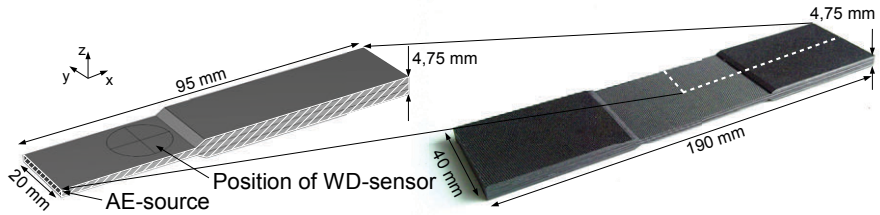


Figure 3.43.: Model geometry of tensile specimen geometry (left) and photographic image of experimentally used tensile specimen (right).

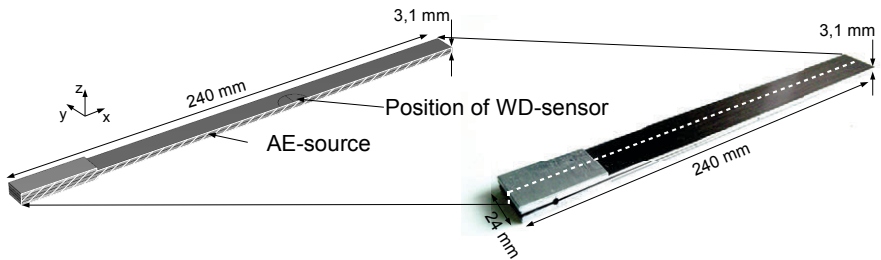


Figure 3.44.: Model geometry of DCB specimen geometry (left) and photographic image of experimentally used DCB specimen (right). The geometry is adapted to the requirements of ASTM D 5528 [170].

### 3. Simulation of acoustic emission signals

boundary reflections. In combination with the different stacking sequences this explains the different ratios between low and high frequency parts in the simulated frequency spectra.

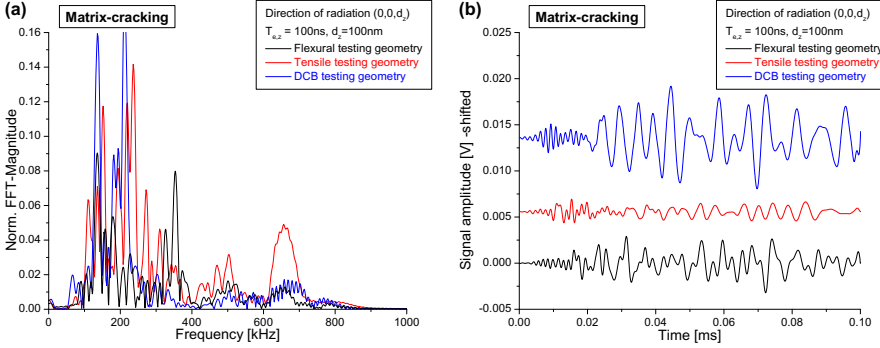


Figure 3.45.: Influence of specimen geometry for excitation time  $T_{e,z} = 100$  ns and displacement in z-direction  $d_z = 100$  nm for resin elastic properties in frequency domain (a) and time domain (b).

A very similar common characteristic is observed in the frequency spectra of simulated fiber breakage in the three geometries as shown in figure 3.46. For all three frequency spectra noticeable contributions at high frequencies are observed, which correspond to the strong excitation of the  $S_0$ -mode in comparison to the  $A_0$ -mode as observed in the respective signals in the time domain.

For the simulations of interface failure shown in figure 3.47 again similar signals are found for all three geometries. As described in section 3.4.1 interface failure causes higher contributions to the  $S_0$ -mode than matrix cracking, but lower contributions than those observed for fiber breakage. These intermediate ratios of  $S_0/A_0$ -contributions are found in the signals of all geometries in the time domain and are reflected in the stronger pronounced contributions at frequencies above 400 kHz in comparison to the simulations of matrix cracking shown in figure 3.45.



### 3. Simulation of acoustic emission signals

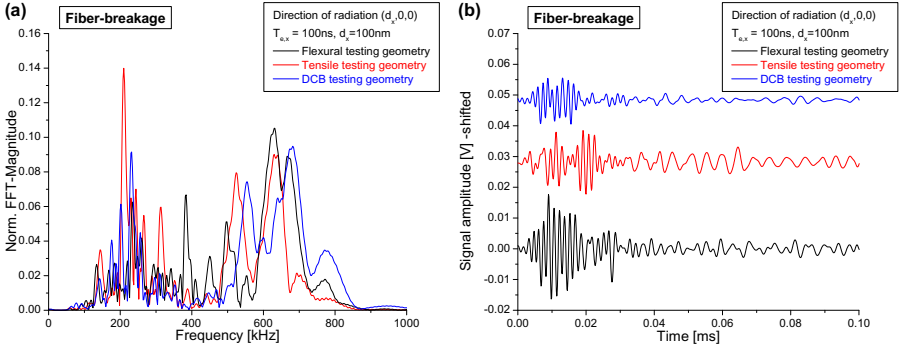


Figure 3.46.: Influence of specimen geometry for excitation time  $T_{e,x} = 100$  ns and displacement in x-direction  $d_x = 100$  nm for fiber elastic properties in frequency domain (a) and time domain (b).

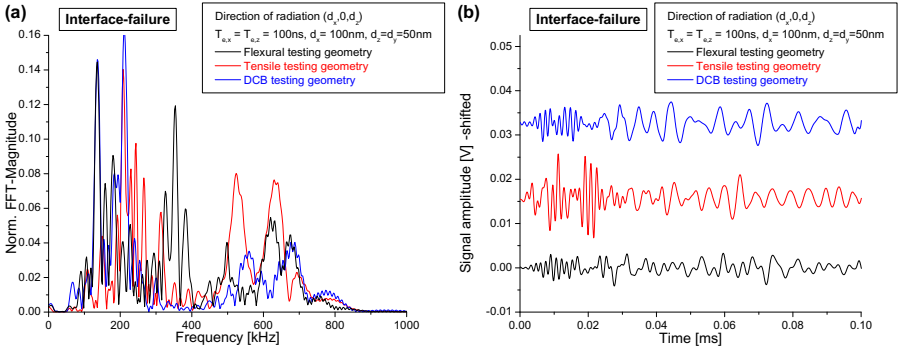


Figure 3.47.: Influence of specimen geometry for simulation of interface failure with excitation time  $T_{e,x} = T_{e,y} = T_{e,z} = 100$  ns and displacement  $d_x = 100$  nm and  $d_y = d_z = 50$  nm in frequency domain (a) and time domain (b).

## 4. Experimental results

In this chapter a comprehensive description of the experimentally used setups and their results is given. The first section 4.1 will focus on the technical aspects of the specimen preparation, the setups for mechanical testing and acoustic emission acquisition and the methods used for microscopic assessment of the failure mechanisms occurring in the different specimen types. The subsequent sections 4.2 and 4.3 deal with different stacking sequences and mechanical loading conditions applied to various specimen geometries of the T800/913 material system. The purpose of these specimen series is to induce different ratios of failure mechanisms by changes of the specimen geometry, stacking sequence and loading condition. This is used to assign the natural clusters detected by the presented pattern recognition method to respective failure mechanisms as observed by microscopy. In addition the validity of the assignment is verified by qualitative and quantitative comparison with simulation results as obtained from the FEM-approach introduced in chapter 3. The specimen series presented in section 4.4 is used to demonstrate the broad capabilities of interpretation of the recorded acoustic emission signals. Here the variation of the curing degree of the specimens of the HTS/RTM6 material system introduces dominant changes in the failure mode of the specimen. In addition, section 4.5 describes T-Pull experiments on the same material type and is used as representative investigation to evaluate the presented pattern recognition method in a 3-dimensional geometry with complex stacking sequence. The last section 4.6 describes the experimental results of acoustic emission analysis obtained for metallic coatings applied on CFRP substrates. Such hybrid materials naturally exhibit more than one type of acoustic emission source and are, consequently, hard to interpret by conventional acoustic emission techniques. The section demonstrates how pattern recognition methods can be used to improve the interpretation of acoustic emission and to assess the quality of such coating systems.

### 4.1. Experimental setups

In general, for observation of material failure in dependency of certain mechanical properties a dedicated experimental setup for mechanical loading is

## 4. Experimental results

required to induce the failure progress in a controlled manner. In the case of carbon fiber reinforced plastics, a variety of standardized tests are established to determine the fundamental engineering properties of the material. This is not the case for acquisition of acoustic emission signals during mechanical loading and thus this aspect is described in more detail in the following. In addition, the investigation of failure mechanisms is supported by digital optical microscopy (DOM), scanning electron microscopy (SEM) and scanning acoustic microscopy (SAM). While the first two methods are limited to either surface investigation or destructive investigation by cross-sectional imaging of a specimen, SAM is a nondestructive technique capable to provide volumetric information about the failure progress within the specimen.

### 4.1.1. Description of specimen series

The basic investigations used to establish the process of failure identification in CFRP were performed using the prepreg sytem T800/913. This prepreg system consists of an unidirectional arrangement of continous Torayca T800S intermediate modulus high-tensile carbon fibers and the HexPly 913 epoxy resin. All T800/913 specimens were manufactured using the curing cycle as shown in figure 4.1 under vacuum conditions as  $320 \text{ mm} \times 320 \text{ mm}$  (length  $\times$  width) plates with stacking sequences as summarized in table 4.2. Subsequently these plates were cut to three different specimen geometries (see figure 4.2) as follows:

1. For investigation of acoustic emission signals arising from different failure mechanisms a series of bending specimens with varying ply-layup was used. These were rectangular specimens according to the requirements of DIN-EN-ISO 14125 [158] with dimensions of  $(100 \pm 1) \text{ mm} \times (15 \pm 0.5) \text{ mm} \times (1.4 \pm 0.2) \text{ mm}$  (length  $\times$  width  $\times$  height). For this geometry three different stacking sequences were used, namely  $[0_5]_{sym}$ ,  $[90_5]_{sym}$  and  $[0/90_4]_{sym}$  ply-layup. These specimen series will further be addressed as Layup-0, Layup-90 and Layup-0/90 with reference to the used stacking sequence.
2. An additional specimen series of T800/913 DCB specimens is used to investigate the influence of the specimen geometry on the pattern recognition and failure identification process. For the DCB-specimens the dimensions are  $(240 \pm 2) \text{ mm} \times (24 \pm 0.5) \text{ mm} \times (3.0 \pm 0.2) \text{ mm}$  (length  $\times$  width  $\times$  height) according to the requirement of ASTM D 5528 [170]. In the following, these will be termed DCB specimens.
3. The T800/913 tensile specimens are made of  $(190 \pm 2) \text{ mm} \times (40 \pm 0.5) \text{ mm}$

#### 4. Experimental results

$\times (1.5 \pm 0.1)$  mm (length  $\times$  width  $\times$  height) plates in  $[0/90_3/0]_{sym}$  layup with  $(60 \pm 1)$  mm  $\times$   $(40 \pm 0.5)$  mm  $\times$   $(1.1 \pm 0.1)$  mm (length  $\times$  width  $\times$  height) reinforcements in  $[45/135/0_2]_{sym}$  layup at the edges as visible in figure 4.2. Similar as above, these will be termed Tensile specimens.

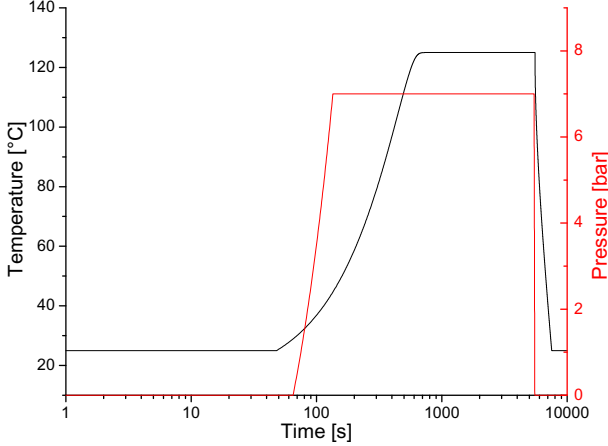


Figure 4.1.: Curing cycle for T800/913 system.

The second material type investigated is made of dry Toho-Tenax HTS carbon fibers and the infusion resin system Hexcel RTM6. This CFRP system was investigated within the scope of the project “Mehrstufige Verfahren zur Herstellung von CFK-Integralstrukturen”. All HTS/RTM6 specimens were manufactured by the Premium Aerotec Company in a vacuum assisted resin infusion process using the VAP<sup>®</sup>-technique. While the stacking sequence was identical  $[0/(0,90)_{f2}]_{sym}$  for all specimens, the curing degree of the resin was systematically varied. To achieve curing degrees of 60 %, 70 % and 80 % the temperature profile was shortened compared to the 100 % reference specimens as shown in figure 4.3-a. The cross-linking degree was evaluated after curing using dynamic differential scanning calorimetry (DSC), as shown exemplarily in figure 4.3-b. Subsequently specimens for flexural testing were cut to dimensions of  $(100 \pm 1)$  mm  $\times$   $(15 \pm 0.5)$  mm  $\times$   $(2.3 \pm 0.1)$  mm (length  $\times$  width  $\times$  height) as shown in figure 4.4. These different specimen types will be referred to as HG60%, HG70%, HG80% and HG100% according to their cross-linking degree. The focus of this specimen series is the demonstration of analysis capabilities

#### 4. Experimental results

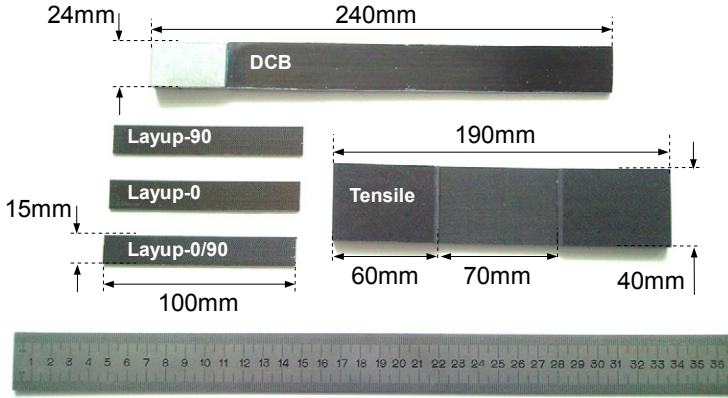


Figure 4.2.: Image of T800/913 bending specimen, DCB specimen and Tensile specimen series including dimensions.

using acoustic emission for investigation of the microscopic origin causing the different performance of the various curing degrees during mechanical loading.

As additional specimen series of the HTS/RTM6 material system, T-Pull specimens subjected to the full curing cycle in figure 4.3-a were investigated. These consist of a stringer and a base plate (see figure 4.4). The stringer is manufactured as  $[(45,135)_f/(0,90)_f]_{sym}$  layup with  $(165 \pm 1) \text{ mm} \times (50 \pm 0.5) \text{ mm} \times (2.1 \pm 0.1) \text{ mm}$  (length  $\times$  width  $\times$  height) plate and an enclosure for the wedge located at the interface to the base plate. The base plate in turn consist of an  $[45/90/(135,45)_f/135]_{sym}$  layup with additional intermediate layers of  $[0/(135/45)_f]$ ,  $[(135/45)_f]$ ,  $[0]$  and  $[90]$  below the wedge to increase the height of the cross-section profile gradually as shown in figure 4.4. The dimensions of the base plate are  $(300 \pm 1) \text{ mm} \times (50 \pm 0.5) \text{ mm}$  (length  $\times$  width) and  $(3.0 \pm 0.1) \text{ mm}$  height in the region outside the increased cross-section.

The last specimen series is used to investigate failure of metallic coatings applied on KDK 8054/120 CFRP-substrates. The matrix consists of a polyurethane based epoxy resin (Araldite: LY 564 / HY 2954). The carbon fibers of type SIGRATEx KDK8054/120 are arranged in six plies ( $0^\circ$ -  $90^\circ$  textured) of woven fabric. All specimens were provided and manufactured by BMW-Group “Research and Technology” and were investigated within the scope of the project “StorHy” (Hydrogen Storage Systems for Automotive Application). The CFRP-substrates were cut to rectangular CFRP-specimens according to DIN-EN-ISO 14125 (class IV type), with dimensions  $(100 \pm 10) \text{ mm}$

## 4. Experimental results

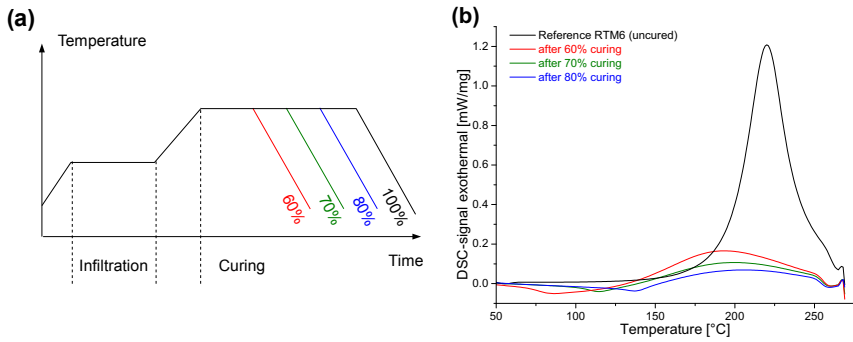


Figure 4.3.: Shortened curing cycles (a) and evaluation of curing degree of RTM-6 resin by DSC measurements (b).

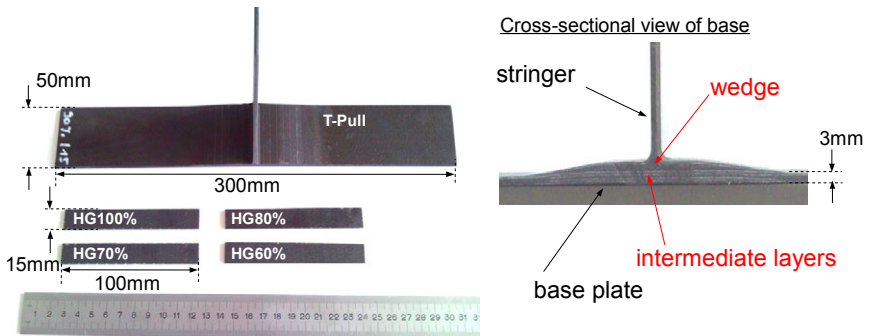


Figure 4.4.: Image of HTS/RTM6 bending specimen and T-Pull specimen series including dimensions.

## 4. Experimental results

$\times (15 \pm 0.5) \text{ mm} \times (2 \pm 0.2) \text{ mm}$  (length  $\times$  width  $\times$  height) [158]. The CFRP substrates were coated by subsequent chemical deposition of a  $10 \text{ }\mu\text{m}$  nickel or copper layer and afterwards electroplated with copper layers of  $10 \text{ }\mu\text{m}$ ,  $30 \text{ }\mu\text{m}$  and  $50 \text{ }\mu\text{m}$  thickness with lateral dimensions of  $(25 \pm 1) \text{ mm} \times (15 \pm 0.5) \text{ mm}$  ( $l \times w$ ) as shown in figure 4.5. More information on the coating application process is provided in detail by [171]. In the following, these different types of coatings will be termed Ni, NiCu10, NiCu30, NiCu50 and CuCu50-specimens.

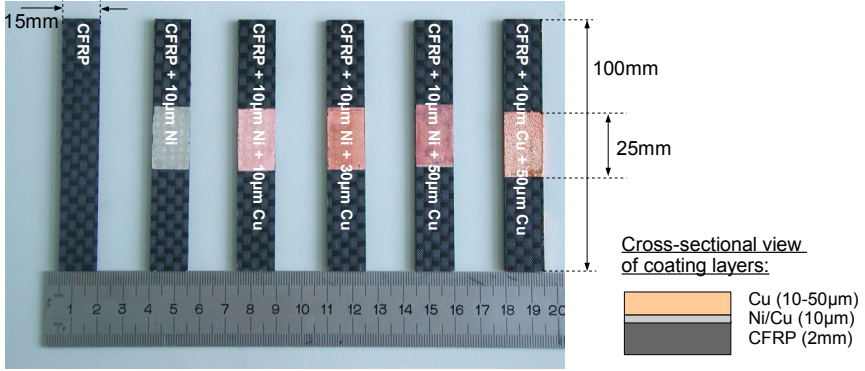


Figure 4.5.: Image of KDK8054/120 specimen series with various coatings including dimensions and cross-section scheme.

In the following, all subscripts “\_00N” attached to the specimen identifier refer to the number  $N$  of the individual specimen within the series.

### 4.1.2. Mechanical testing and acoustic emission acquisition

For investigation of acoustic emission signals arising from several types of failure all specimens were loaded in experimental setups suitable to induce the intended failure mode. All these mechanical tests were carried out on a type 8502 servo-hydraulic machine<sup>1</sup> and a type 1464<sup>2</sup> spindle driven machine.

The acoustic emission signals were detected by broadband sensors of type WD<sup>3</sup> applied directly to the specimen surface with Baysilone silicone grease<sup>4</sup> of medium viscosity as acoustic coupling medium. As reported by P. Theobald et al. deviations in the thickness of the used coupling medium can have significant

<sup>1</sup> Manufacturer: Instron GmbH

<sup>2</sup> Manufacturer: Zwick/Roell AG

<sup>3</sup> Manufacturer: Physical Acoustics Corporation

<sup>4</sup> Manufacturer: Bayer Material Science AG

#### 4. Experimental results

Test setup	Material	Stacking sequences / Coating type	Shortcut	Statistics
Flexural	T800/913	$[90_5]_{sym}$	Layup-90	5
	T800/913	$[0_5]_{sym}$	Layup-0	8
	T800/913	$[0/90_4]_{sym}$	Layup-0/90	6
DCB	T800/913	$[0_{12}]_{sym}$	DCB	5
Tensile	T800/913	Plate: $[0/90_3/0]_{sym}$ Reinforcement: $[45/135/0_2]_{sym}$	Tensile	7
Flexural	HTS/RTM6	$[0/(0,90)_{f2}]_{sym} - 60\%$	HG60%	3
	HTS/RTM6	$[0/(0,90)_{f2}]_{sym} - 70\%$	HG70%	3
	HTS/RTM6	$[0/(0,90)_{f2}]_{sym} - 80\%$	HG80%	3
	HTS/RTM6	$[0/(0,90)_{f2}]_{sym} - 100\%$	HG100%	3
T-Pull	HTS/RTM6	Stringer: $[(45,135)_f/(0,90)_f]_{sym}$ Base plate: $[45/90/(135,45)_f/135]_{sym}$ with additional layers of $[0/(135/45)_f]$ , $[(135/45)_f]$ , $[0]$ and $[90]$ in base region	T-Pull	7
Flexural	KDK 8054/120	$[(0,90)_{f3}]_{sym} - 10\mu\text{m Ni}$	Ni	5
	KDK 8054/120	$[(0,90)_{f3}]_{sym} - 10\mu\text{m Ni, } 10\mu\text{m Cu}$	NiCu10	8
	KDK 8054/120	$[(0,90)_{f3}]_{sym} - 10\mu\text{m Ni, } 30\mu\text{m Cu}$	NiCu30	8
	KDK 8054/120	$[(0,90)_{f3}]_{sym} - 10\mu\text{m Ni, } 50\mu\text{m Cu}$	NiCu50	8
	KDK 8054/120	$[(0,90)_{f3}]_{sym} - 10\mu\text{m Cu, } 50\mu\text{m Cu}$	CuCu50	5

Table 4.2.: Summary of specimen series investigated. The stacking sequence encoding follows the suggestions by [18] (see page 13).



#### 4. Experimental results

influence on the sensitivity spectra of the sensors [68]. To take this effect into account, all experimental setups used suitable clamp systems to provide mechanical contact between sensor and specimen. This yields reproducible acoustic coupling, when the pressure of the clamps and the dose of silicone grease is kept comparable for all experiments. All acoustic emission signals were recorded by threshold based triggering with 40 dB preamplification using a PCI-2 data acquisition system<sup>5</sup> and the software AEwin<sup>6</sup> with a sampling rate of 10 MSPs. Only for the tensile tests 20 dB preamplification was used to avoid signal cutoffs due to the intense acoustic emission signals observed in this experimental setup. The trigger parameters were optimized to the respective specimen geometries to inhibit triggering of noise signals and reflections of the specimen boundaries. In addition, a bandpass range between 20 kHz and 1-3 MHz was used to reduce detection of low frequency friction signals and high frequency electromagnetic noise signals. For interpretation of the recorded signals, the software package Noesis<sup>7</sup> was used for data reduction and postprocessing steps like feature extraction and pattern recognition.

For all flexural tests the specifications follow DIN-EN-ISO 14125, as schematically shown in figure 4.6 [158]. For these four-point-bending tests, the crosshead speed in z-direction was 0.01 mm/s with an inner distance between supports of  $(27 \pm 1)$  mm and an outer distance of  $(81 \pm 2)$  mm, respectively. For all measurements of coated specimens the position of the coating was on the tensile loading side (specimen bottom). During mechanical loading the acoustic emission was detected by two WD broadband sensors in linear arrangement as shown in figure 4.6. The sound velocity was obtained from the difference in the arrival time of test signals propagating between sensor 1 and sensor 2 and the respective metric distance.

The DCB-tests were carried out in an experimental setup according to ASTM D 5528 as schematically shown in figure 4.7 with a cross-head speed in z-direction of 10 mm/min [170]. Due to the larger specimen geometry it was possible to mount three sensors to measure the sound velocity. Since this method is more accurate than the usage of two sensors it was used in all following setups. For measurement of the sound velocity of the specimens, WD sensor 1 was used as pulse emitter. The sound velocity was calculated from the difference in the arrival time of the signal between sensor 2 and the supplementary sensor 3 and the respective difference in propagation distance. During mechanical loading the acoustic emission signals were detected solely

---

<sup>5</sup> Manufacturer: Physical Acoustics Corporation

<sup>6</sup> Manufacturer: Physical Acoustics Corporation

<sup>7</sup> Manufacturer: Enviroacoustics S.E.

#### 4. Experimental results

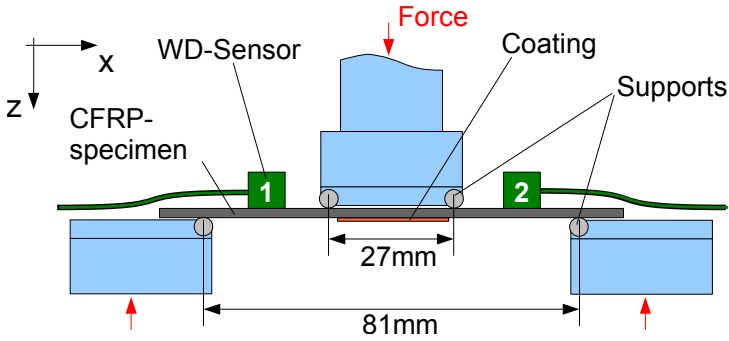


Figure 4.6.: Scheme of experimental setup for flexural tests according to DIN-EN-ISO 14125 including sensor positions (side view).

by sensor 1 and sensor 2 in linear geometry as shown in figure 4.7.

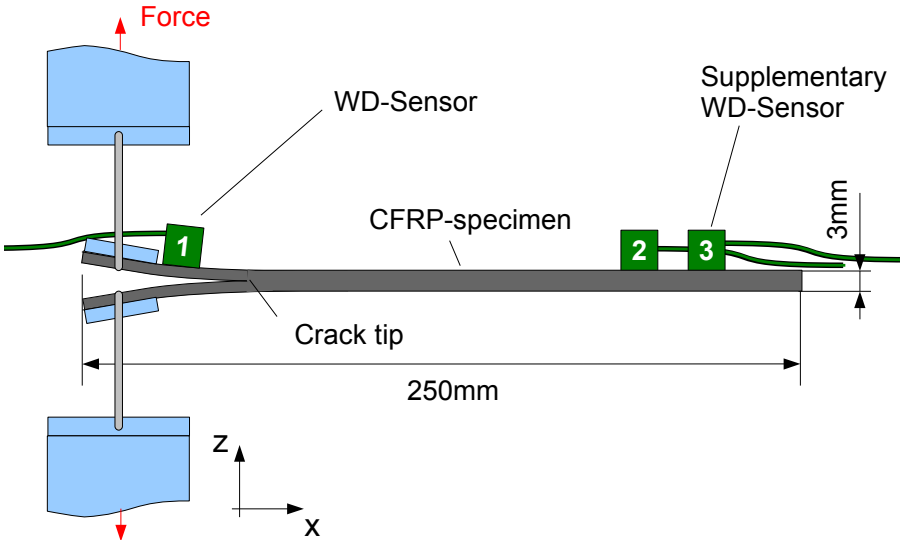


Figure 4.7.: Scheme of experimental setup for DCB tests according to ASTM D 5528 including sensor positions (side view).

The tensile tests were conducted in an experimental setup as schematically

#### 4. Experimental results

shown in figure 4.8. All specimens were loaded with a constant deformation speed in x-direction of 1 mm/min. To inhibit acoustic emission arising from clamped strain gauges (friction) or glued strain gauges (glue failure) the strain level was measured using a VideoXtens optical extensometer<sup>8</sup> using the marker positions shown in figure 4.8. During loading the acoustic emission was recorded by four WD-sensors in planar geometry. The sound velocities in x- and y-direction were obtained from measurements conducted on the complete 320 mm × 320 mm CFRP-plate before cutting of the specimen geometries. Here a linear arrangement of three WD-sensors was chosen. The first sensor was used as emitter, while the sound velocity was obtained from the difference in the arrival time of the signal between the second and third sensor and the respective difference in propagation length. Similar, the attenuation coefficient  $\alpha$  was determined from the loss of maximum amplitude between the second and the third sensor with respect to the difference in propagation length. These measurements were conducted for the x- and y-direction of the CFRP-plate.

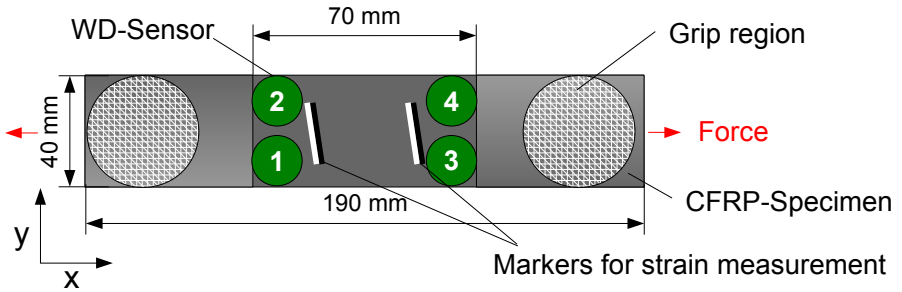


Figure 4.8.: Scheme of experimental setup used for tensile testing including sensor positions (top view).

For testing of the T-Pull specimens an experimental setup as schematically shown in figure 4.9 was used. The position of the stringer was kept constant and the base-plate was moved in negative z-direction with a constant deformation rate of 1 mm/min until specimen failure due to pull-off between base plate and stringer. The strain level at the wedge of the specimen was measured by a VideoXtens optical extensometer as remarked in figure 4.9. During loading the acoustic emission signals were recorded with six WD-sensors at the positions annotated in figure 4.9. The sound velocities in x- and z-direction were each measured by a combination of three WD-sensors arranged in linear geometry

<sup>8</sup> Manufacturer: Zwick/Roell AG

#### 4. Experimental results

with one emitter and two receivers. To obtain the sound velocity in y-direction, the difference in arrival time of test signals from pencil lead fractures were measured with two WD-sensors in a linear arrangement along the y-axis.

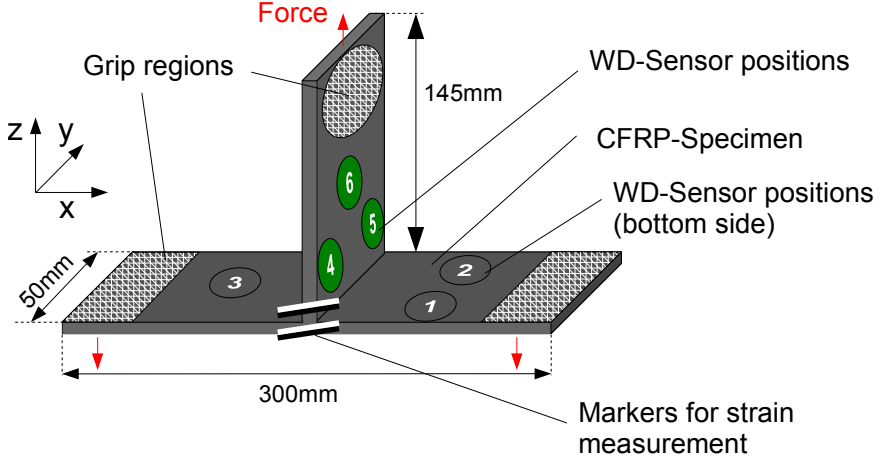


Figure 4.9.: Schematic drawing of experimental setup configuration used for T-Pull tests of HTS/RTM6 specimens including sensor positions (perspective side view).

In addition, several mechanical tests were carried out to measure mechanical properties of the different materials, which were not accompanied by acoustic emission measurements. Tests according to DIN-EN 2563 for determination of the apparent interlaminar shear strength were conducted for the different curing degrees of the HTS/RTM6 specimens [172]. To determine the critical stress-intensity factor  $K_{Ic}$  of the different copper coatings a centre-notched specimen as shown in the inset of figure 2.8 was prepared. The critical load  $F_c$  necessary for calculation of  $K_c$  is then obtained from the intersection of the load-displacement curve and the 5%-secant of the linear-elastic range analogous to ASTM-E399 (see also figure 2.8 on page 19) [173]. Further, the strain energy release rate for mode-I/II delamination of the copper coatings was obtained from peeling tests according to ASTM B533-85 [29].

### 4.1.3. Microscopical investigation

For imaging of the failure progress and correlation with the localized positions of acoustic emission sources, a VHX-100 digital optical microscope<sup>9</sup> (DOM), a XL30 environmental scanning electron microscope<sup>10</sup> (ESEM) and a WIN-SAM Vario-I scanning acoustic microscope<sup>11</sup> (SAM) were used. The different microscopy methods were used to assess the failure progress in the CFRP qualitatively. In addition quantitative measurement of the failure progress in the investigated coating systems was carried out utilizing the software package ImageJ [174]. Since the used techniques for microscopic imaging of material failure are commonly used, no detailed description is given in the following. Instead a comprehensive review on optical and electron microscopy is found in [175], while a good review on scanning acoustic microscopy is given in [176].

## 4.2. Variation of CFRP stacking sequence of flexural testing specimens

The goal of this specimen series is the investigation of failure mechanisms occurring in CFRP laminates with acoustic emission analysis and the evaluation of the proposed pattern recognition methodology. The different specimen layups described in section 4.1.1 are used to control the number of failure mechanisms and their frequency of occurrence. For the  $[90_5]_{sym}$  stacking sequence no fiber failure is expected, since these specimens are loaded perpendicular to the fiber axis. In clear contrast, loading of bending specimens with  $[0_5]_{sym}$  stacking sequence is expected to result in significant contributions of fiber failure and inter-ply delamination. Finally, for the  $[0/90_4]_{sym}$  stacking sequence failure in form of inter-ply delamination and fiber breakage is expected as well, but with different contributions than in  $[0_5]_{sym}$  stacking sequences.

The steps used to analyze the detected acoustic emission signals follow the same scheme for all layups investigated. First the acoustic emission signals are localized using a hyperbolic localization technique with the linear sensor geometry shown in figure 4.6. Only localized signals are taken into account for further analysis. In the simulation of acoustic emission signals it was observed that boundary reflections at the experimentally used sensor positions dominate the characteristic of the acoustic emission signal at  $t > 100 \mu s$  after the first arrival of the  $S_0$ -mode. Consequently the acoustic emission signal features as defined in table 2.2 were extracted solely from the initial  $100 \mu s$  of the recorded

---

<sup>9</sup> Manufacturer: Keyence GmbH

<sup>10</sup> Manufacturer: FEI Company

<sup>11</sup> Manufacturer: PVA Tepla Analytical Systems GmbH

#### 4. Experimental results

acoustic emission signals. This strong influence of boundary reflections on the signal features is demonstrated exemplarily for the frequency spectra obtained from the complete signal and obtained from the initial 100  $\mu\text{s}$  of the signal as remarked in figure 4.10-a. Obviously this results in drastically different feature values, as exemplarily shown for the frequency of maximum signal contribution  $f_{peak}$  in figure 4.10-b. In particular, the usage of the complete signal for feature extraction can result in emphasized self-similarity of the acoustic emission signals, since boundary reflections contribute to each signal and are very similar in their intensity.

As subsequent step, only the frequency features proposed in table 2.2 (Average Frequency, Reverberation Frequency, Initiation Frequency, Peak Frequency, Frequency Centroid, Weighted Peak-Frequency, Partial Powers 1-6) were investigated with the pattern recognition method described in section 2.3.3. This focus on frequency based features is a consequence of the simulation results for CFRP failure, which demonstrate that frequency features generally can act as characteristics for the failure mechanisms in CFRP better than energy based features (see also [166]). For the six different partial power features the frequency ranges marked in figure 4.10-b were used, which were chosen to reflect the characteristic frequency contributions in the experimentally observed frequency spectra. Finally the results of the pattern recognition process are compared to the results of the FEM-simulations and are discussed in terms of fracture mechanics.

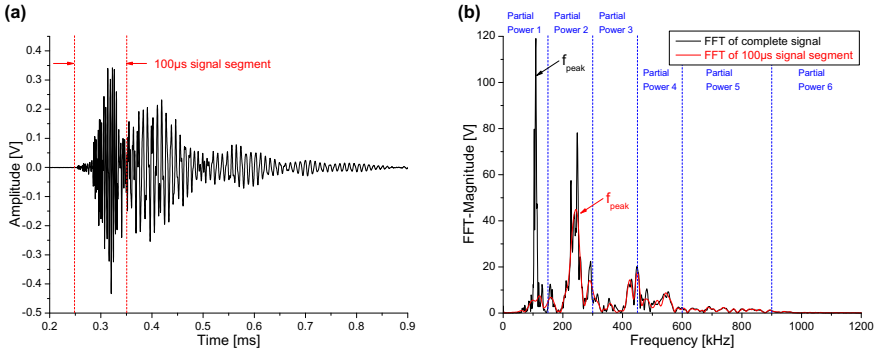


Figure 4.10.: Comparison of feature extraction process based on complete signal and initial 100  $\mu\text{s}$  of the signal (a). The dashed lines in the frequency spectra mark the chosen frequency intervals for definition of the partial power levels 1-6 (b).

#### 4.2.1. Loading parallel to fiber axis: Layup-0 specimens

The typical macroscopic appearance of the accumulated damage in these specimen types with  $[0_5]_{sym}$  layup after loading in four-point bending (see section 4.1.2) is exemplarily shown in figure 4.11. Most damage is observed at the positions of the upper supports which results in complete crack-through of the specimen in combination with large inter-ply delamination taking place in the region located between the upper supports. As acoustic emission sources, inter-fiber matrix cracking, fiber-breakage and interface failure in the form of inter-ply delamination are expected.

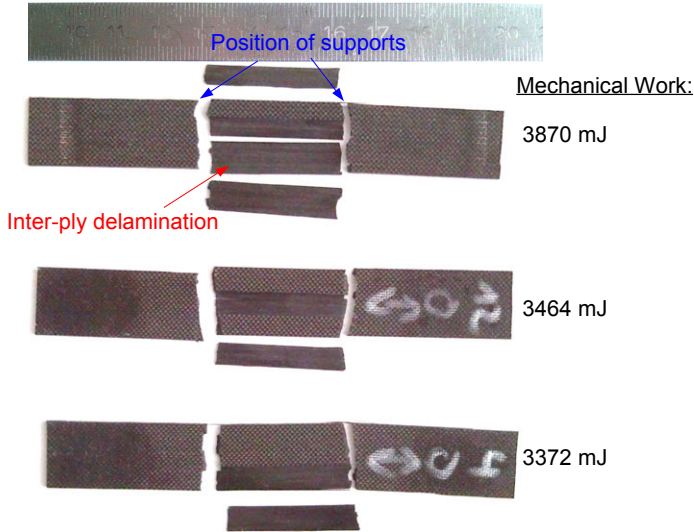


Figure 4.11.: Images of macroscopically observed damage in three  $[0_5]_{sym}$  layup specimens. The value of mechanical work recorded till failure is noted on the right.

#### Pattern recognition

The result of the investigation of the acoustic emission signal features with the proposed pattern recognition methodology is shown in diagrams of the Davies-Bouldin (DB) over Gamma (GAMMA) index in figure 4.12 (see equations (2.73) and (2.74)). The lower boundary value for the number of features for

#### 4. Experimental results

the investigations was chosen to be  $Q_{min} = 5$ . For the  $Q = 12$  frequency features this results in a total number of feature combinations  $N_{tot} = 3302$ . The associated optimal number of clusters for the clustering procedure with variance normalization, principal components projection and the k-means algorithm is given by the color of the data points in figure 4.12 for each feature combination. As discussed in section 2.3.3 numerical optimal feature combinations are located at low *DB*- and high *GAMMA*-values. As indicated by the color value of the marked optimal feature combinations the associated number of clusters is found to be either three or four. As combined result of the same investigation on all Layup-0 specimens the only feature combination always located in the numerical optimal range is given in table 4.3. The respective classification result of this feature combination is shown figure 4.13-a as result in principal components projection and in figure 4.13-b as diagram of Partial Power 4 over Weighted Peak-Frequency.

The remaining optimal feature combinations indicating three clusters as optimal value result in partitions with great similarity to those shown in figure 4.13. In fact, two other feature combinations did not even show any different assignment of the acoustic emission signals to the respective clusters. The reason of their worse cluster validity index values compared to those of the feature combination in table 4.3 is solely the different numerical performance of the different features to describe the clusters shown in figure 4.13. In contrast, the feature combinations indicating four clusters as optimal value are unique in their result for each specimen. Consequently, these feature combinations are not suitable to separate the natural clusters of acoustic emission signals.

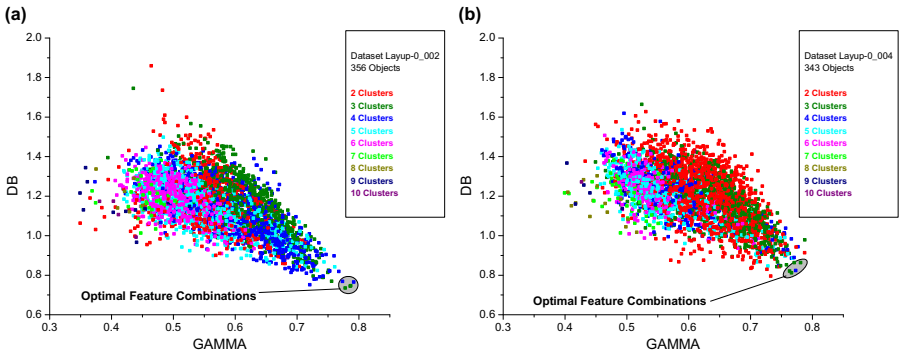


Figure 4.12.: Result of the proposed pattern recognition method for two representative investigations shown as diagram of Davies-Bouldin over Gamma Index for all feature combinations.



#### 4. Experimental results

Feature	Remark
Peak Frequency [Hz]	
Weighted Peak-Frequency [Hz]	
Partial Power 1 [%]	Frequency range 0-150 kHz
Partial Power 2 [%]	Frequency range 150-300 kHz
Partial Power 4 [%]	Frequency range 450-600 kHz

Table 4.3.: Optimal feature combination for clustering of acoustic emission signals from Layup-0 specimens (see also table 2.2 for definition).

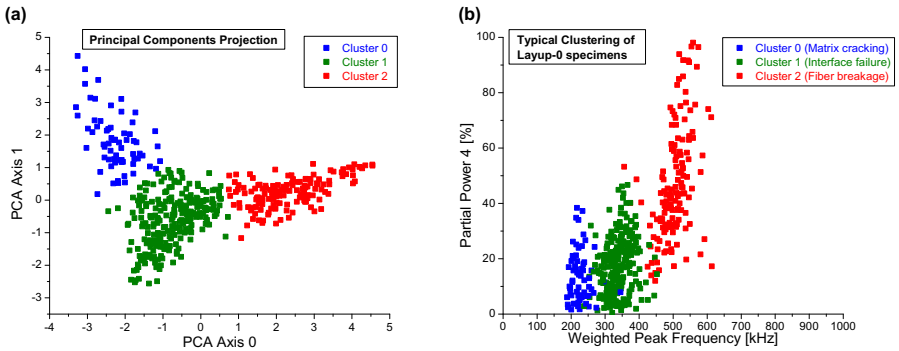


Figure 4.13.: Exemplarily result of cluster location in principal components projection (a) and as diagram of Partial Power 4 over Weighted Peak-Frequency (b).

### Discussion of the signal clusters

The next step is the correlation of the obtained distinct acoustic emission signal types with certain source mechanisms. To this end, the average Wavelet-Transformation of the obtained signal clusters was calculated and is shown in figure 4.14. Clearly, the three different diagrams show distinct time-frequency behavior. Here signals belonging to cluster 0 show strongest contributions at frequencies below 250 kHz caused by a strong  $A_0$ -mode. This behavior changes for signals of cluster 1, whose average WT-diagram shows a noticeable shift of contributions to higher frequencies. Finally, signals of cluster 2 show strongest contributions at frequencies above 450 kHz, which in turn correspond to a strong  $S_0$ -mode.

Before discussing the physical origin of these different time-frequency appearances it is important to consider the dispersive propagation of the Lamb wave modes. This results in a strict dependency of the appearance of an acoustic emission signal on its propagation length from the source position to the point or area of detection. In this investigation, the correspondence of one signal type to a certain cluster shows no direct correlation to the calculated propagation distance of the signal, i. e. the signals contributing to one cluster were recorded by both sensors. Thus the formation of the different signal clusters shown in figure 4.13-b is not simply caused by distinctly different propagation lengths of the recorded acoustic emission signals. Instead the observed differences are expected to be correlated to distinct differences in the microscopically source mechanism.

Based on the experimental observations of various authors [4–8], a phenomenological assignment of cluster 0 to the occurrence of inter-fiber matrix cracking and cluster 2 to fiber breakage is possible. In addition [3–5] attribute signals with frequency contributions similar to those of cluster 1 to the occurrence of interface failure. However, these assignments are only of empirical nature and shall be investigated closer by a direct comparison between experimental signals and simulated signals of the assumed failure type.

### Comparison with simulation results

For the present specimen geometry all signals were localized at distances between 5 mm to 55 mm away from the respective sensor. This causes a broader appearance of the  $S_0$  and  $A_0$ -mode in the averaged WT-diagrams in figure 4.14 than typically observed for one individual signal. For the purpose of an one on one comparison of experimental signals and simulated signals in the following only selected representative experimental signals are used. These experimental signals were localized approximately at the position  $x = 0$  mm

## 4. Experimental results

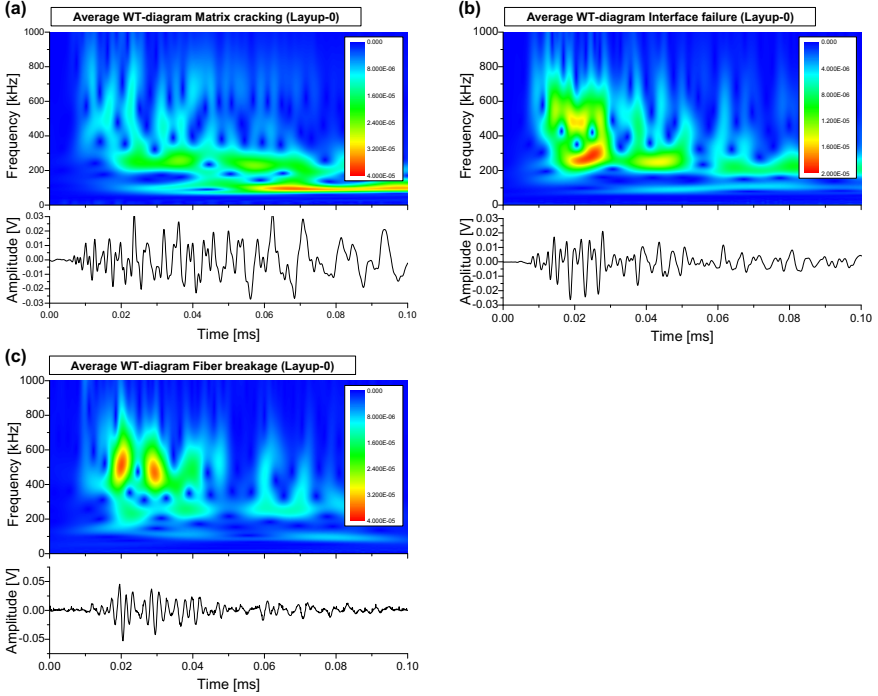


Figure 4.14.: Comparison of the average WT-diagrams for signals from cluster 0 (a), cluster 1 (b) and cluster 2 (c) as obtained by pattern recognition.

but undefined (y,z)-position. This means that the experimental signals have a propagation distance comparable to the simulated signals. Nevertheless, differences between simulated and experimental signals can still originate from the unknown (y,z) position of the experimental signals. In addition, pre-existing cracks within the propagation path can influence the appearance of the experimental signal, due to changes in the Lamb wave propagation [177–179]. In the following the simulated signals were obtained using the bending specimen geometry with respective layup as described in section 3.5 with the full sensor representation.

An experimental signal of cluster 0 is shown in figure 4.15 in comparison to a simulated signal for matrix cracking with excitation in z-direction ( $T_{e,z} = 1000$  ns,  $d_z = 100$  nm). The value of the excitation time was chosen based on the proposed Deborah numbers for epoxy resin between 62 and 108 [45],

#### 4. Experimental results

which imply typical excitation times around  $1 \mu\text{s}$ . For both diagrams low frequency parts below 200 kHz dominate the signals which are attributed to an  $A_0$ -mode superimposed by the reflections from the adjacent boundaries. Within the expected accuracy, the simulated signal agrees satisfactory with the experimental signal.

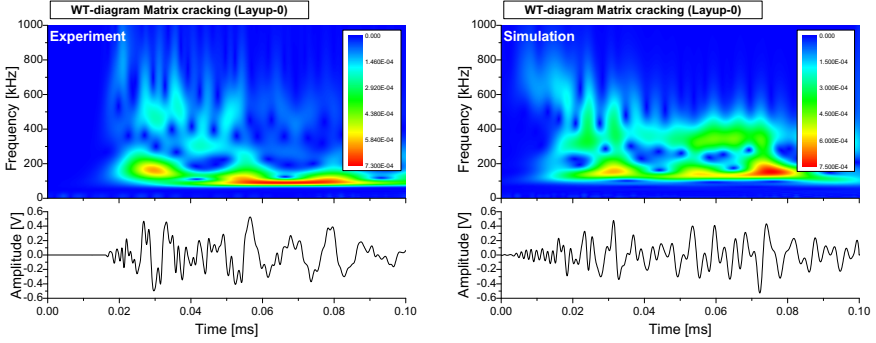


Figure 4.15.: Comparison of WT-diagrams for one representative signal of cluster 0 and the simulated result for matrix cracking at  $(x,y,z) = (0,0,0)$  mm with  $d_z = 100$  nm and  $T_{e,z} = 1000$  ns.

In the case of interface failure an additional short stimulation of the carbon fiber with low displacement amplitude in x-direction is expected. Therefore a lower displacement was chosen in x-direction ( $d_x = 50$  nm) than for the displacement in y- and z-direction ( $d_y = d_z = 100$  nm). All displacements are expected to occur simultaneously. An experimental signal of cluster 1 is compared to a simulated signal of a fiber-matrix interface failure in figure 4.16. The strongest frequency contribution is observed around 200 kHz. At the beginning of the time axis for  $t < 20 \mu\text{s}$  additional contributions arise from the excitation of the  $S_0$ -mode between 400 kHz and 800 kHz. A contribution in the intermediate frequency range between 300 kHz and 600 kHz is observed over a broad time interval ( $20 \mu\text{s} < t < 80 \mu\text{s}$ ). With the chosen excitation parameters a reasonable match between simulated and experimental signals was found.

Figure 4.17 shows the comparison between an experimentally obtained signal from cluster 2 and a simulated signal of fiber-breakage with  $d_x = 100$  nm and  $T_{e,x} = 100$  ns. Both wavelet-diagrams show good agreement in their overall temporal evolution of frequency contributions. Here the  $S_0$ -mode is the dominant contribution as seen by the high frequency contributions up to 1000 kHz at the beginning of the time axis.

#### 4. Experimental results

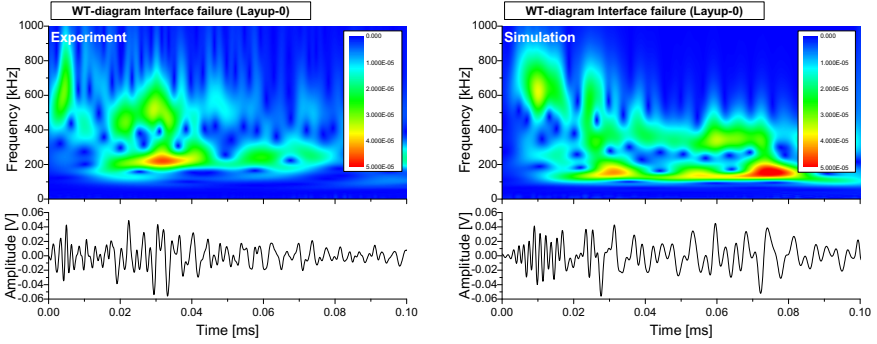


Figure 4.16.: Comparison of WT-diagrams for one representative signal of cluster 1 and the simulated result for interface failure at  $(x,y,z) = (0,0,0)$  mm with  $d_x = 50$  nm,  $d_y = d_z = 100$  nm and  $T_{e,x} = T_{e,y} = T_{e,z} = 100$  ns.

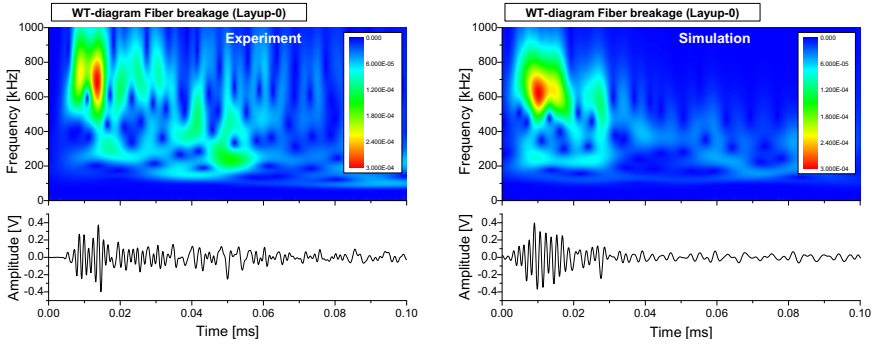


Figure 4.17.: Comparison of WT-diagrams for one representative signal of cluster 2 and the simulated result for fiber breakage at  $(x,y,z) = (0,0,0)$  mm with  $d_x = 100$  nm,  $T_{e,x} = 100$  ns.

Due to the strong influences arising from the relative source sensor distance found in the simulated signals, the above comparison is only of indicative nature. To yield a quantitative comparison between the experimental acoustic emission signals and the simulated signals the source models position was varied within the specimen volume to reflect the microscopically observed positions of the different failure mechanisms. Here simulations for matrix cracking, interface failure and fiber breakage were performed at the respective

#### 4. Experimental results

microscopically observed positions and the simulated signals were obtained using the reduced sensor model. Subsequently the same feature extraction was applied to the simulated signals as to the experimental signals.

The direct comparison of the feature values obtained from the experimental signals and the simulated signals is shown in figure 4.18 in a plot of Partial-Power 4 over Weighted Peak-Frequency. The general agreement of the value ranges for simulated signals and experimental signals is remarkably high. Solely the feature range of interface failure is hard to reflect by the simulated data points. Here the exact positions for occurrence of interface failure are difficult to assess by microscopic analysis, since this microscopic type of crack surface displacement is attributed to various failure mechanisms. In addition the presented source model may not fully represent all of them and consequently might not be able to excite the right combination of Lamb wave modes to yield exactly identical signal features.

Due to the combined indications of experimental observations [3–8] and the systematic qualitative and quantitative agreement between the different signal classes and the simulated signals of different failure mechanisms, the three distinct types of signals are attributed to matrix cracking, interface failure and fiber breakage in the following.

##### **Interpretation of pattern recognition results**

Using this assignment, the results of the measurements of all Layup-0 specimens are summarized in figure 4.19 as diagram of relative number of signals (a) and relative amplitude of signals (b) contributing to one signal class plotted over the specimen identifier. The relative number of signals is defined as number of signals belonging to the respective clusters divided by the total number of signals and is reported in percent. This is understood as measure of the amount of occurrence of these types of signals during specimen failure. The normalization by the total number of signals is required, since different specimens typically show large differences in their absolute number of acoustic emission signals. The relative amplitude of signals is defined similar, but instead of the number of signals, the accumulated maximum acoustic emission amplitude  $U_{max}$  for the investigated cluster was used. This value is normalized by the total accumulated  $U_{max}$  and thus also reported in percent. With reference to section 3.4.3 this reflects the combined contributions of crack surface area and the surface displacement magnitude of the respective failure mechanisms. This is deduced from the strict correlation between  $U_{max}$  and the crack volume  $\Delta V$  as given by equation (3.8).

Besides the low contribution of matrix cracking, the behavior of the identically prepared and tested specimens seems not to be very systematic. The

#### 4. Experimental results

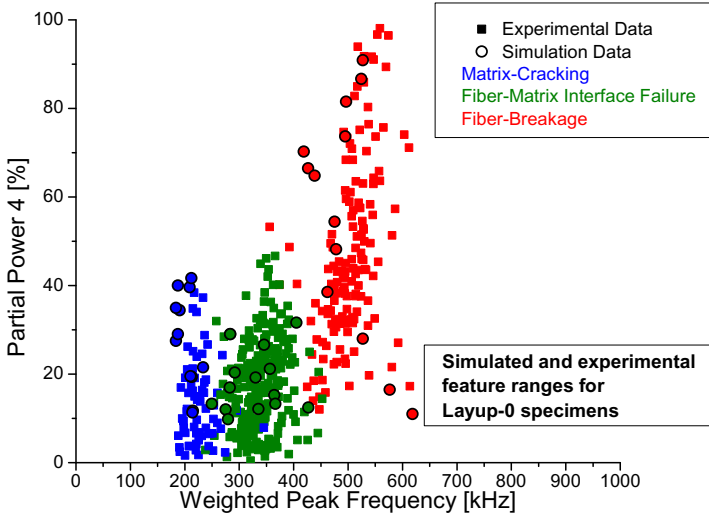


Figure 4.18.: Comparison of feature values extracted from experimental and simulated signals at the microscopically observed source positions in a diagram of Partial Power 4 over Weighted Peak-Frequency.

contributions of interface failure and fiber breakage scatter drastically for the different specimens. As will be demonstrated in the following, this scattering is caused by the differently pronounced types of final failure for the individual specimens and not by a lack of reliability of the pattern recognition method.

For the investigated specimens, the effect of the different ultimate failure types is visualized better as relative signal amplitude of the signals and the average amplitude per signal, both plotted over the recorded mechanical work during loading of the different specimens. The value of mechanical work is obtained from the integration of the load-displacement curve and corrected by the remaining stiffness if the specimen shows no crack-through failure. This procedure was chosen in analogy to the measurement of  $G_{Ic}$ -values as demonstrated in figure 4.37 in section 4.3.1. Typically for fiber reinforced materials a moderate distribution of the obtained mechanical properties is observed, although the specimens were cut out of the same plate. The average amplitude per signal is calculated as sum of all amplitudes within one class and divided by the number of signals from this class. This is understood as the calculated mean amplitude for the signals belonging to the associated failure

## 4. Experimental results

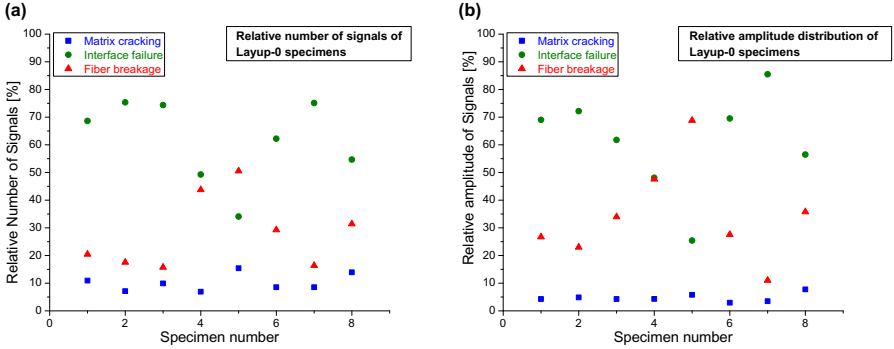


Figure 4.19.: Quantified results for matrix cracking, interface failure and fiber breakage shown in plots of relative number of signals (a) and relative amplitude (b) over specimen identifier.

mechanisms. Based upon the considerations in section 3.4.3, changes in this value can be understood either as change of crack surface per acoustic emission signal release or as respective change in strain energy per acoustic emission signal release.

For the present investigation these diagrams reveal a formation of two groups of specimens plus one distinctly different specimen (see figure 4.20). Both groups of specimens show a systematic dependency between their relative amplitudes and the mechanical work recorded for the respective specimen. With increasing mechanical work the contributions to interface failure grow, while the contribution of fiber breakage systematically decreases. This is caused by the differently emphasized types of failure of the individual specimens. In particular, specimens with large areas of delamination (see figure 4.11) show high contributions of interface failure signals and lower contributions of fiber breakage signals. The contribution of matrix cracking signals is comparable for all specimens. In contrast to all other specimens, the marked specimen in figure 4.20 shows no macroscopic delamination at all, which is reflected in the drastically different contributions to interface failure and fiber breakage. In this case the specimen failure is dominated by fiber breakage at the position of the supports.

The influence of the different failure mechanisms contributions to the work value is also seen in the diagram of average amplitude per signal plotted over the mechanical work in figure 4.20-b. In the given context the observed decay in average amplitude per fiber breakage signals in dependence of work is attributed to a change in crack area per acoustic emission signal. Thus for the



#### 4. Experimental results

high average signal amplitude values a larger number of fiber breakages cause the excitation of one acoustic emission signal. This explains why these specimens fail at lower load levels, since this indicates a higher crack growth rate of fiber breakage at the support positions. In contrast, the average amplitude per matrix cracking signals is almost constant. This is very reasonable, since based on microscopic observations no changes in the fracture behavior of the matrix were observed. The average amplitude of interface failure signals show less systematic contributions. Similar to fiber breakage, these are attributed to changes in the respective crack surface area. However, from the present investigation it cannot be excluded, that these different contributions arise from differences in the respective strain energy release, which could be the result of a locally changed fiber-matrix interfacial strength.

Differences between the two groups of specimen are also observed in the temporal evolution of the different failure mechanisms as shown in figure 4.21-a and 4.21-b in plots of the accumulated number of the signals belonging to one signal cluster in dependence of time. For comparison the respective stress-strain curve is shown. For the group of specimens with high work values a significantly later onset of fiber breakage with higher acoustic emission activity was observed (see figure 4.21-b). Since the accumulated fiber breakages finally cause the crack-through process, this defers ultimate failure to higher load-displacement values. In contrast, specimens with low work values show an almost equal onset of all failure mechanisms at the same time (figure 4.21-a).

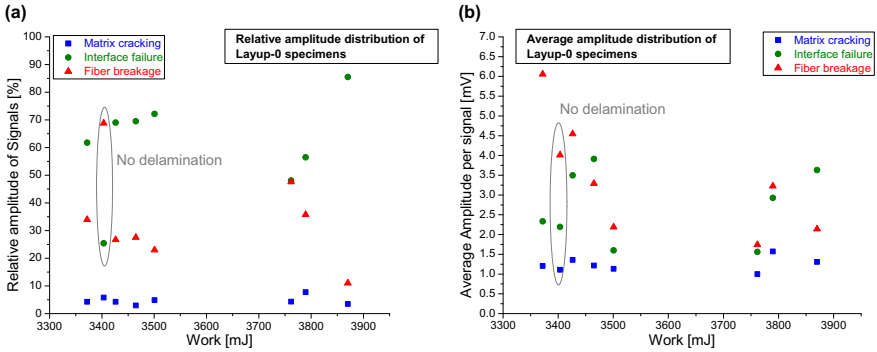


Figure 4.20.: Quantified results for matrix cracking, interface failure and fiber breakage shown in plots of relative amplitude contribution (a) and average amplitude of signals (b) over recorded mechanical work.

#### 4. Experimental results

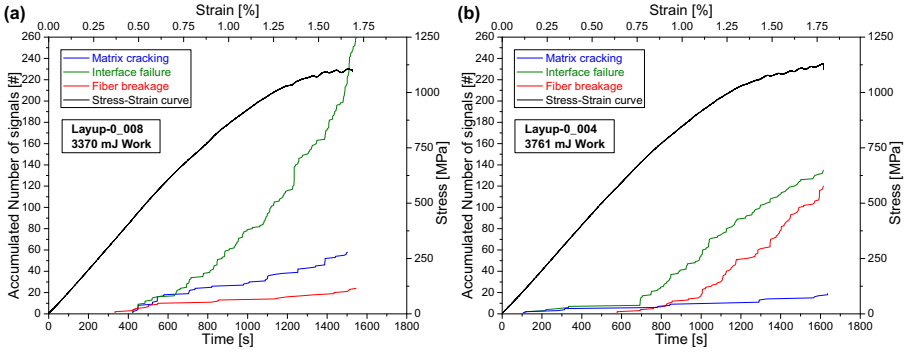


Figure 4.21.: Comparison of temporal evolution of contributions from matrix cracking, interface failure and fiber breakage for specimen with 3370 mJ work (a) and 3761 mJ work (b). For comparison, the stress-strain curve of the respective specimen is shown.

In summary, a strong correlation between the macroscopically observed damage and the relative contributions obtained by pattern recognition of the recorded acoustic emission signals is observed. This strongly supports the proposed correlation of the microscopic failure mechanisms with the respective characteristics of the acoustic emission signals.

### 4.2.2. Loading perpendicular to fiber axis: Layup-90 specimen

Loading in four-point bending of specimen types with  $[90_5]_{sym}$  stacking sequence typically cause ultimate failure by a crack-through process at one or both of the support positions (see figure 4.22). This is a direct consequence of the unidirectional reinforcement with fiber axes parallel to the supports axes. The typical macroscopic appearance of failure with a corresponding scanning electron microscopy image obtained from the crack surface is shown in figure 4.22. The dominant failure mechanism in this type of specimens obviously is inter-fiber matrix cracking and interfacial failure. Fiber breakage in turn is seldom observed and can only occur directed along the y-axis of the specimen.

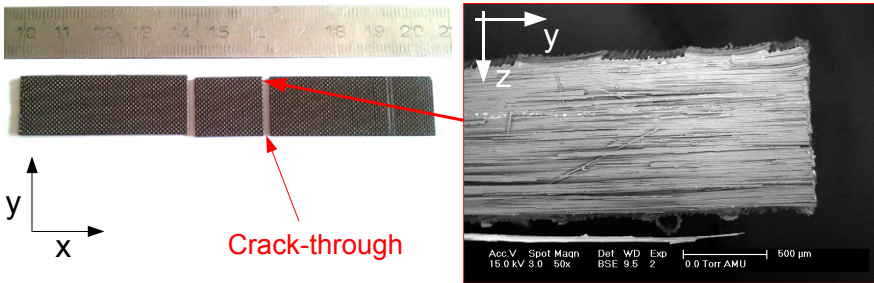


Figure 4.22.: Image of macroscopically observed damage of  $[90_5]_{sym}$  layup specimens and cross-sectional scanning electron microscopy image of crack surface at crack through position

### Interpretation of pattern recognition results

Limiting for the investigation with pattern recognition is the fact, that only few acoustic emission signals are recorded for each specimen failure. After localization these are further reduced in number. In total the amount of signals recorded for all five specimens investigated is only 15. To this end, even a reasonable higher amount of specimens is not expected to show a sufficient number of signals ( $\geq 100$ ) for investigation with pattern recognition techniques. Instead all recorded signals for the five different specimens are investigated in one approach and are plotted as Partial Power 4 over Weighted Peak-Frequency in figure 4.23. With respect to the previous knowledge from section 4.2.1 these are already marked as matrix cracking and interface failure due to their feature ranges in the plot. In the following the validity of this assignment is discussed

#### 4. Experimental results

by comparison to the results obtained from FEM-simulations.

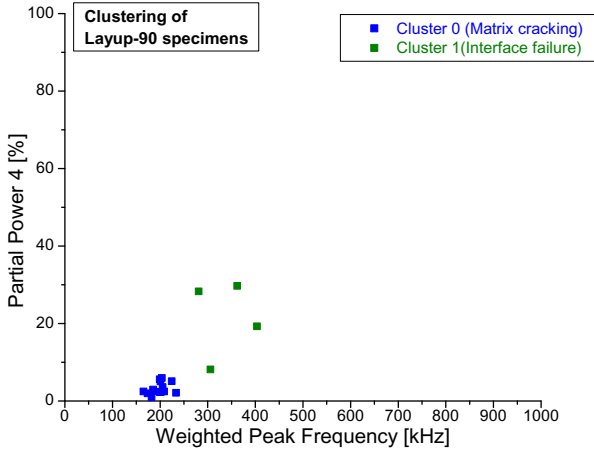


Figure 4.23.: Plot of all acoustic emission signals recorded during failure of  $[90_5]_{sym}$  layup specimens in a diagram of Partial Power 4 over Weighted Peak-Frequency.

#### Comparison with simulation results

The comparison of a representative experimental signal of cluster 0 with a simulated signal of matrix cracking is shown in figure 4.24. Same as for the Layup-0 specimens, the exact (y,z) - source position for the experimental signal is unknown, which can influence the exact comparability of the signals. Both signals show good agreement in their frequency contributions and temporal behavior. In comparison to the signals obtained from matrix cracking in Layup-0 specimens (see figure 4.15), the signals frequencies are shifted to higher frequencies at around 200 kHz. This is caused by the different displacement directions, since no crack surface displacement in z-direction is expected for Layup-90 specimens. Instead the displacement direction in the simulation was chosen along the x-axis with  $d_x = 100$  nm and  $T_{e,x} = 1000$  ns.

The experimental signal of cluster 1 and the simulated signal for interface failure in figure 4.25 shows only minor differences to the respective matrix cracking signal. The only difference is a slightly more pronounced  $S_0$ -mode, visible at the beginning of the signals between  $10 \mu s < t < 20 \mu s$  and a mean

#### 4. Experimental results

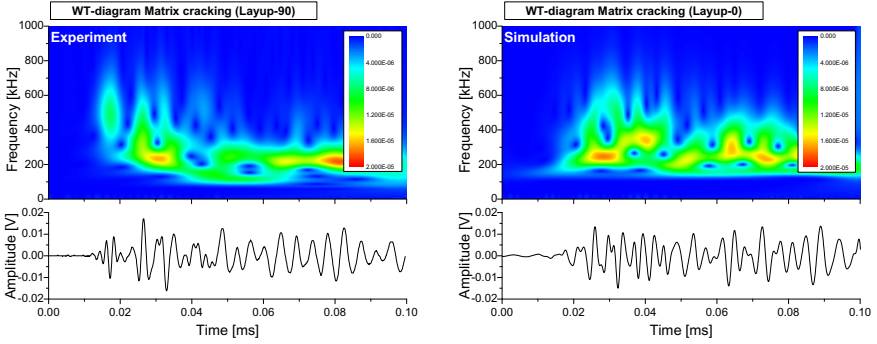


Figure 4.24.: Comparison of WT-diagrams for one representative experimental signal and the simulated result for matrix cracking at  $(x,y,z) = (0,0,0)$  mm with  $d_x = 100$  nm and  $T_{e,x} = 1000$  ns.

shift of energy contribution to higher frequencies in the rest of the signal. These slight differences in turn are strong enough to yield the different feature ranges for matrix cracking and interface failure observed in figure 4.23. In addition no obvious microscopic distinction can be made between interface failure and matrix cracking for the observed failure mode as shown in figure 4.22. Thus, for the given case, the differences in the obtained frequency features can also arise solely from different source-sensor distances.

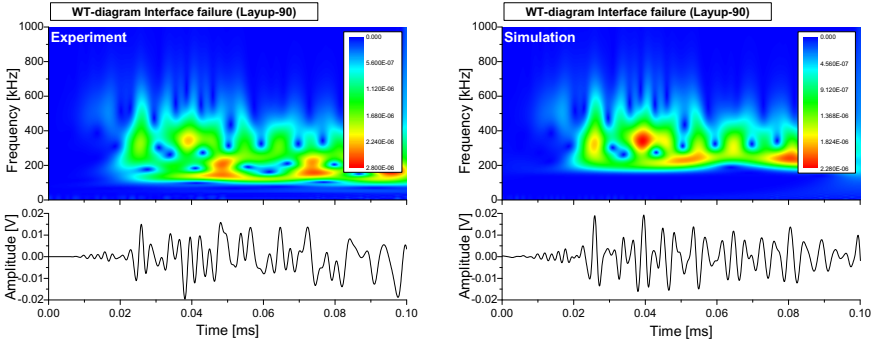


Figure 4.25.: Comparison of WT-diagrams for one representative experimental signal and the simulated result for interface failure at  $(x,y,z) = (0,0,0)$  mm with  $d_x = 50$  nm,  $d_y = d_z = 100$  nm and  $T_{e,x} = T_{e,y} = T_{e,z} = 100$  ns.

### 4.2.3. Loading in varied stacking sequence: Layup-0/90 specimens

Failure in these specimens with  $[0/90_4]_{sym}$  stacking sequence occurs dominantly at the positions of the upper supports as marked in figure 4.26. The clearly visible surface topology originates from the removal of the peel-ply fabric. Similar to the Layup-0 specimens, inter-ply delamination in various extents are observed in the region between the upper supports positions. Here the delamination is induced by the occurrence of inter-fiber matrix cracks within the  $90^\circ$  layers which cause stress raisers at the interface region between  $90^\circ$  and  $0^\circ$  layers as e. g. described by [180]. Due to the changed stacking sequence no complete crack-through is observed. Instead final failure occurs by crack-through in the top (compressive loaded)  $0^\circ$ -layer, propagates through the  $90^\circ$ -layers and stops at the bottom (tensile loaded)  $0^\circ$ -layer. This failure evolution consequently results in different contributions of inter-fiber matrix cracking, fiber breakage and interface failure than for the Layup-0 specimens. As an quantitative approach, the area of inter-ply delamination was quantified by SAM as shown in figure 4.27. Using a transducer with 30 MHz frequency and 12.7 mm focal length, the specimens were examined after mechanical loading. In order to measure the delaminated area, images of depth-staggered ultrasonic scans with 50 ns width were used. For CFRP-Air interfaces or for CFRP-water interfaces the reflection coefficient is between 93 % and 100 %. The ultrasonic images shown in figure 4.27 correspond to depth positions located below the inter-ply delamination. In this case all black areas inside the specimen volume in figure 4.27 can be understood as “shadow” of the inter-ply delaminations, since the ultrasonic signal is totally reflected before reaching this depth position.

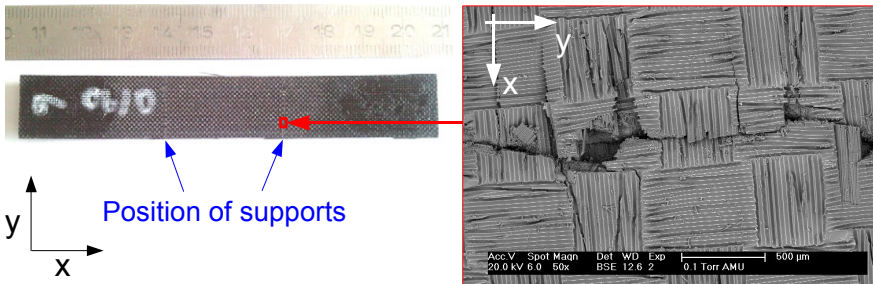


Figure 4.26.: Image of macroscopically observed damage in  $[0/90_4]_{sym}$  layup specimens and top-view scanning electron microscopy image of macroscopically visible crack at surface of specimen.

#### 4. Experimental results

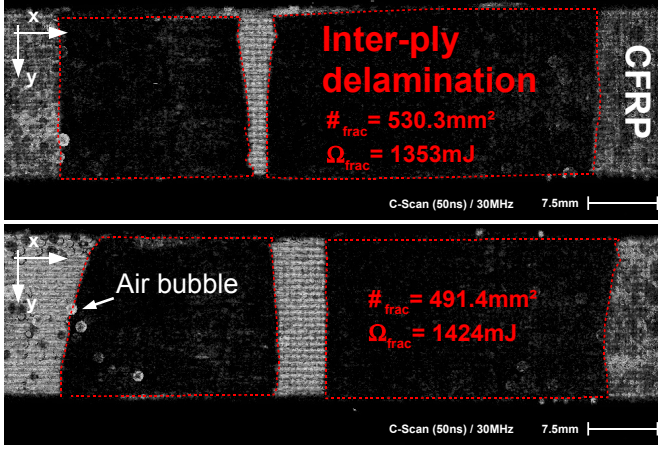


Figure 4.27.: Quantified areas of inter-ply delamination utilizing ultrasonic images. The delaminated area is marked in red.

#### Pattern recognition

The diagrams in figures 4.28-a and 4.28-b show the Davies-Bouldin over Gamma-Index for two representative investigations by the pattern recognition method similar as for the Layup-0 specimens. Again, the lower boundary value for the number of features for the investigations was chosen to be  $Q_{min} = 5$  out of the same selected  $Q = 12$  features. The marked optimal feature combinations indicate optimal index values for either three or four clusters. In contrast to the behavior observed for the Layup-0 specimens the proposed feature combination given in table 4.3 is not the only combination showing good index performance for all specimens investigated. Instead an additional feature combination for partitioning into four clusters as given in table 4.4 is found as well. In comparison to the feature combination given in table 4.3, the only change is the replacement of Partial Power 2 by Partial Power 3. The respective clustering of these two feature combinations are shown in figures 4.29 and 4.30 as diagrams of Partial Power 4 over Weighted Peak-Frequency for two representative specimens.

As exemplarily shown in figures 4.29-a and 4.30-a the clustering using the feature combination from table 4.4 with four clusters yields unique cluster positions for each dataset. For any feature combination suggesting a separation into four clusters no partition type was observed, which shows similar cluster

#### 4. Experimental results

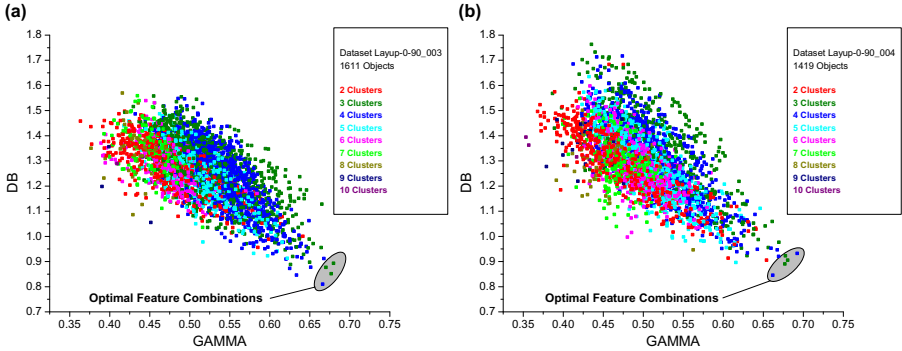


Figure 4.28.: Result of the proposed pattern recognition method for two representative investigations shown as diagram of Davies-Bouldin over Gamma-Index for all feature combinations.

Feature	Remark
Peak Frequency [Hz]	
Weighted Peak-Frequency [Hz]	
Partial Power 1 [%]	Frequency range 0-150 kHz
Partial Power 3 [%]	Frequency range 300-450 kHz
Partial Power 4 [%]	Frequency range 450-600 kHz

Table 4.4.: Alternative feature combination for clustering of acoustic emission signals from Layup-0/90 specimens.

positions for all five specimens investigated. In clear contrast, the feature combination of table 4.3 shown in figures 4.29-b and 4.30-b yields strictly similar cluster positions for all specimens. In addition the so obtained cluster positions agree well with those observed for the Layup-0 specimens. Thus again the feature combination of table 4.3 was used for investigation of correlations between failure mechanisms and the different cluster types. In anticipation of the following discussion, the resulting assignment is already marked in figures 4.29-b and 4.30-b as matrix cracking, interface failure and fiber breakage.



#### 4. Experimental results

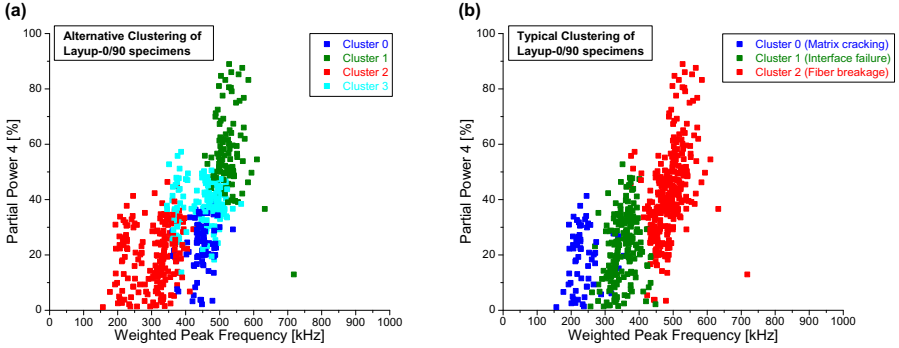


Figure 4.29.: Result of cluster positions for Layup-0/90\_005 as diagram of Partial Power 4 over Weighted Peak-Frequency for feature combination of table 4.4 (a) and feature combination from table 4.3 (b).

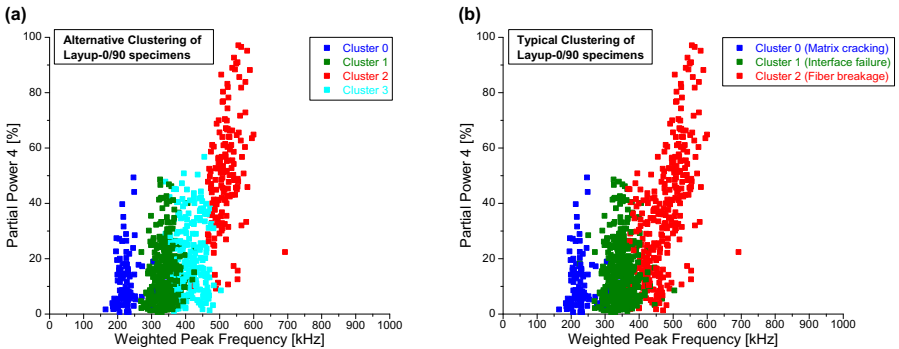


Figure 4.30.: Result of cluster positions for Layup-0/90\_006 as diagram of Partial Power 4 over Weighted Peak-Frequency for feature combination of table 4.4 (a) and feature combination from table 4.3 (b).

## Discussion of the signal clusters

First a comparison is made between the average WT-diagrams as calculated for the three different clusters (see figure 4.31). Similar to the diagrams obtained from the Layup-0 specimens, the three signal clusters show strong differences in their individual time-frequency behavior. While cluster 0 shows strongest contributions below 200 kHz and thus a strong  $A_0$ -mode, cluster 1 shows dominant contributions at intermediate frequency ranges around and above 200 kHz. For this cluster the contributions to  $S_0$ -mode and  $A_0$ -mode are of almost similar magnitude. The remaining cluster 2 shows very strong contributions to the  $S_0$ -mode reflected in the high intensity between 400 kHz and 600 kHz.

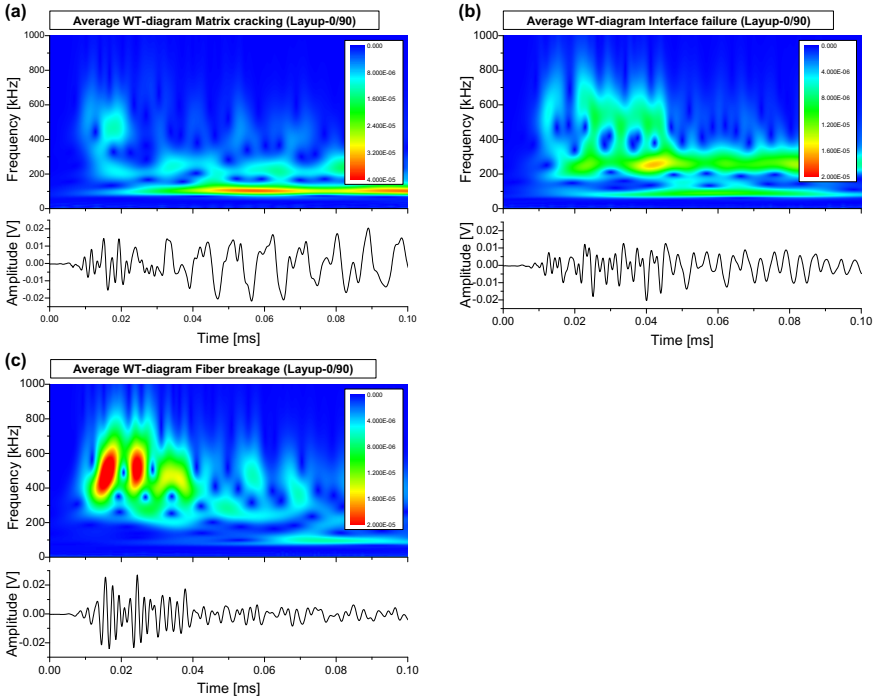


Figure 4.31.: Comparison of the average WT-diagrams for signals from cluster 0 (a), cluster 1 (b) and cluster 2 (c) as obtained by pattern recognition.

## 4. Experimental results

### Comparison with simulation results

In figures 4.32 to 4.34 single representative signals of the obtained clusters are compared to simulated signals of matrix cracking, interface failure and fiber breakage at microscopically observed source positions in a simulated bending specimen geometry with  $[0/90_4]_{sym}$  layup.

For the representative signal of cluster 0 and the simulated signal of matrix cracking with  $d_z = 100$  nm and  $T_{e,z} = 1000$  ns largest frequency contributions are observed at frequencies below 200 kHz. In direct comparison the experimental signal exhibits a stronger pronounced  $A_0$ -mode at around 100 kHz than the simulated signal. This is characteristic for all signals contributing to this class as shown in the average WT diagram in figure 4.31-a and is not reflected exactly in the simulation. As described in section 4.2.1 before, this can result from deviations in the exact source position, since the (y,z)-position of the experimental signal is unknown. An additional influence can arise from the application of the transfer function of the sensor using the full-sensor representation. Since the sensitivity curve was extrapolated below 100 kHz the sensitivity of the sensor in this range might be underestimated. Except for this discrepancy, both signals show qualitative agreement.

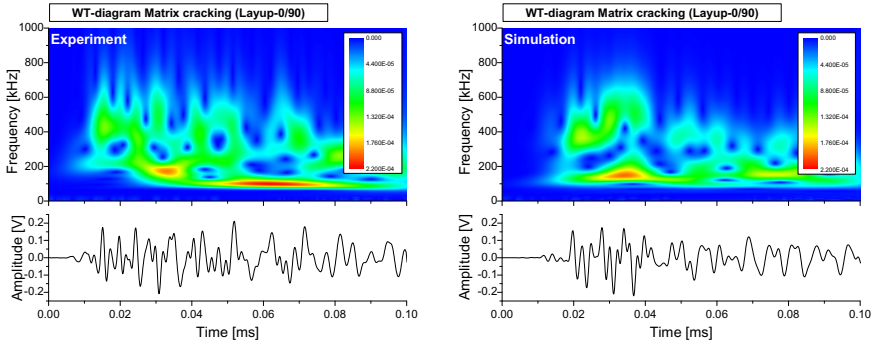


Figure 4.32.: Comparison of WT-diagrams for one representative signal of cluster 0 and the simulated result for matrix cracking at  $(x,y,z) = (0,0,0)$  mm with  $d_z = 100$  nm and  $T_{e,z} = 1000$  ns.

Figure 4.33 shows the representative signal from cluster 1 in comparison to the simulated signal of interface failure. Both signals in figure 4.33 agree well in their time-frequency behavior. The intensities and time-frequency positions of the intensity maxima show almost an exact match.

Figure 125 shows a comparison of one representative signal from cluster 2

#### 4. Experimental results

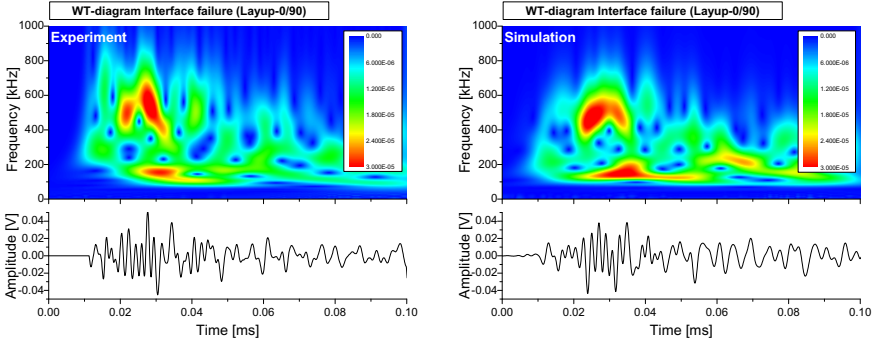


Figure 4.33.: Comparison of WT-diagrams for one representative signal of cluster 1 and the simulated result for interface failure at  $(x,y,z) = (0,0,0)$  mm with  $d_x = 50$  nm,  $d_y = d_z = 100$  nm and  $T_{e,x} = T_{e,y} = T_{e,z} = 100$  ns.

and a respective simulation of fiber breakage. In contrast to simulations of matrix cracking and interface failure, the source position was chosen at  $(x,y,z) = (0,0,0.6)$  mm. This is a consequence of the  $[0/90_4]_{sym}$  stacking sequence, which does not allow fiber breakage in x-direction at the  $(x,y,z) = (0,0,0)$  mm position, since the fiber axis is oriented along the y-axis at this position. Both signals show good agreement in their time-frequency behavior with strongest contributions due to a high  $S_0$ -mode at around 500 kHz.

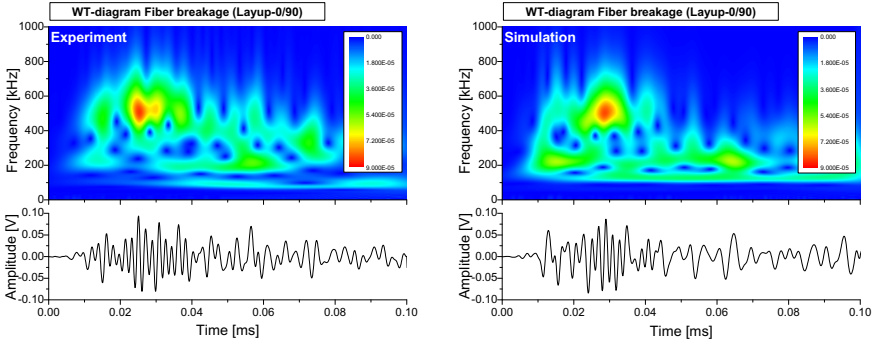


Figure 4.34.: Comparison of WT-diagrams for one representative signal of cluster 2 and the simulated result for fiber breakage at  $(x,y,z) = (0,0,0.6)$  mm with  $d_x = 100$  nm,  $T_{e,x} = 100$  ns.

#### 4. Experimental results

It is worth to point out, that the simulated signals obtained for identical source types and source positions in the Layup-0/90 specimens show characteristic differences to those for the Layup-0 specimens. This difference is solely caused by the variation of the stacking sequence and shows similar consequences for the experimental signals and the simulated signals. Based on these observations and the similarities to the findings in Layup-0 specimens, in the following the three distinct types of signals are again attributed to matrix cracking, interface failure and fiber breakage.

##### **Interpretation of pattern recognition results**

The quantified results of the measurements of all Layup-0/90 specimens are summarized in figure 4.35 as diagram of relative signal amplitude (a) and average signal amplitude (b) plotted over the value of mechanical work obtained from the load-displacement curves.

In figure 4.35-a a strong correlation between the relative amplitude of the different failure mechanisms signals and the measured mechanical work is observed. In particular, the relative contribution of fiber breakage increases with the recorded work value while the contribution of interface failure shows contrary behavior. This is reflected in the macroscopically observed failure modes as well. Here the quantification of the ultrasonic images shows, that specimens with low work values show larger areas of delamination. Similar, it was observed in ESEM-investigations, that specimens with high work values show more pronounced fiber breakage at the supports positions. The quantified relative amplitude contributions of signals identified as matrix cracking increases first in dependence of work and saturates towards higher work values. The increase at the beginning is attributed to a growing number of inter-fiber matrix cracks within the  $90^\circ$ -layers of specimen. At higher work values (reflecting longer loading durations) the number of inter-fiber matrix cracks typically saturates, when the maximum crack density is approached [18].

In contrast to the result for the Layup-0 specimens, no drastic changes in the average amplitudes per signal are observed for all failure mechanisms (see figures 4.20-b and 4.35-b). According to the considerations above this indicates no changes in the associated crack area per acoustic emission signal and a constant value for the respective strain energy release per signal. However, a compensation of both contributions, like lower strain energy release at higher crack surface area per signal could result in very similar behavior. In this context a local variation in the interfacial fracture toughness could be responsible for the changed contributions of the different failure mechanisms. As a direct consequence, despite the strong correlations shown in the diagrams in figure 4.35 it is still hard to conclude which microscopic effect is causing the

#### 4. Experimental results

observed differences in specimen failure.

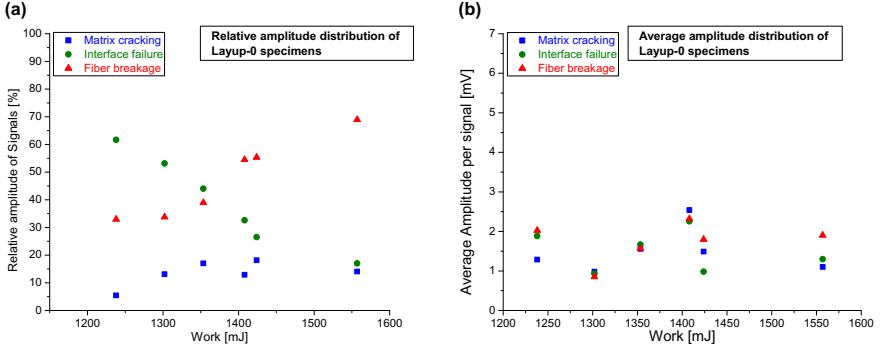


Figure 4.35.: Quantified results for matrix cracking, interface failure and fiber breakage shown in plots of relative amplitude of signals (a) and average amplitude per signal (b) over recorded mechanical work.

### 4.3. Variation of specimen geometry and loading condition

The purpose of this specimen series is the evaluation of the proposed pattern recognition method applied to acoustic emission signals recorded during failure of the same T800/913 material combination as for the bending specimens in section 4.2 but with different specimen geometry and loading condition.

#### 4.3.1. DCB testing of T800/913 specimens

Here the typical failure mechanisms occurring during mode-I crack growth in DCB-tests are expected to be drastically different in their composition than those for flexural testing. As shown in the scanning electron microscopy images in figure 4.36, the typical failure mechanisms during this loading condition is inter-fiber matrix cracking and interfacial failure in form of inter-ply delamination. Fiber breakage can occur due to excessive bending of the beams and locally high adhesion but is observed less frequent than in flexural tests. For the present specimen series strong variations in the measured fracture toughness values were observed and are reported in table 4.5. According to ASTM D 5528 the fracture toughness value  $G_{Ic}$  is obtained from the recorded mechanical energy during specimen loading divided by the measured macroscopic crack surface area. The mechanical energy is given by the integral of the load-displacement curve subtracted by the energy value of the remaining stiffness (red hachured rectangle) as shown in figure 4.37. The respective crack surface area is usually calculated from the measured crack growth during loading multiplied by the width of the specimen. As demonstrated by the scanning electron microscopy images in figure 4.36, similar macroscopic crack surface values do not necessarily coincide with the real microscopic crack surface values. This is demonstrated by comparison of figure 4.36-a showing an almost flat crack surface with figure 4.36-b showing a very rough structured surface caused by splicing into several layers. Such splicing results in a higher microscopic crack surface value and is dominantly observed in those specimens with higher  $G_{Ic}$ -values.

Similar to the investigations of the bending specimen geometries, the acoustic emission signals were first localized with a linear sensor arrangement as given in figure 4.7 using a hyperbolic localization technique. Only the localized signals were used for feature extraction and analysis by pattern recognition. As consequence of the extended propagation length introduced by the specimen dimensions the signals are subject to increased dispersion effects. Consequently, the time interval for the feature extraction was increased from 100  $\mu$ s to the

#### 4. Experimental results

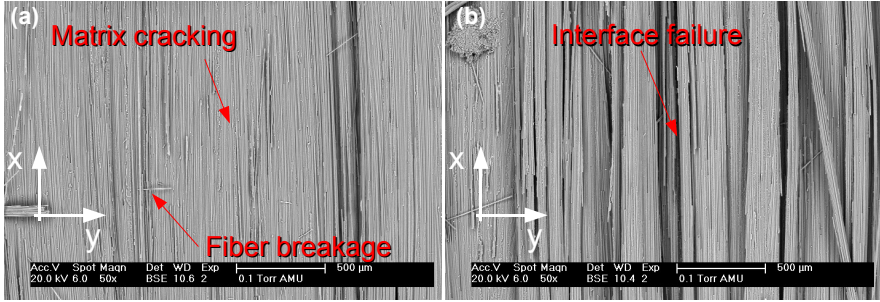


Figure 4.36.: Scanning electron microscopy image of crack surface in top view in regions of weak adhesion (a) and high adhesion (a).

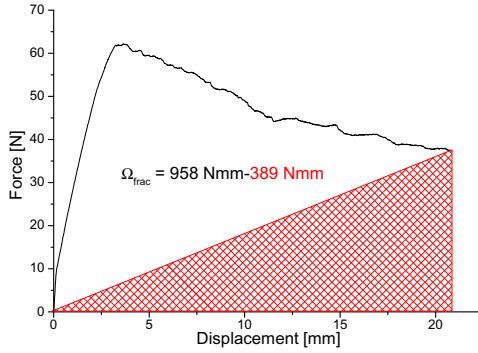


Figure 4.37.: Representative load-displacement curve and calculation of mechanical energy  $\Omega_{frac}$

Specimen number	$G_{Ic}$ -value [J/m <sup>2</sup> ]
DCB_001	284±4
DCB_002	292±4
DCB_003	421±6
DCB_004	527±5
DCB_005	408±3

Table 4.5.: Summary of fracture toughness values for specimen series



## 4. Experimental results

first 200  $\mu\text{s}$  after first arrival of the  $S_0$ -mode.

### Pattern recognition

For further analysis the same  $Q = 12$  frequency features as for the flexural testing specimens were investigated with the proposed pattern recognition technique of section 2.3.3 with  $Q_{min} = 5$  as lower boundary for the number of features to be used for pattern recognition. The result of the investigation is shown in figure 4.38-a as representative diagram for all DCB-measurements as plot of  $DB$  over  $GAMMA$  index. The investigation yields clear preference for one particular feature combination, which is marked in figure 4.38-a. This is actually the same feature combination as found for the clustering of the acoustic emission signals from Layup-0 specimens given in table 4.3. The respective representative clustering result is shown in figure 4.38-b in a diagram of Partial Power 4 over Weighted Peak-Frequency.

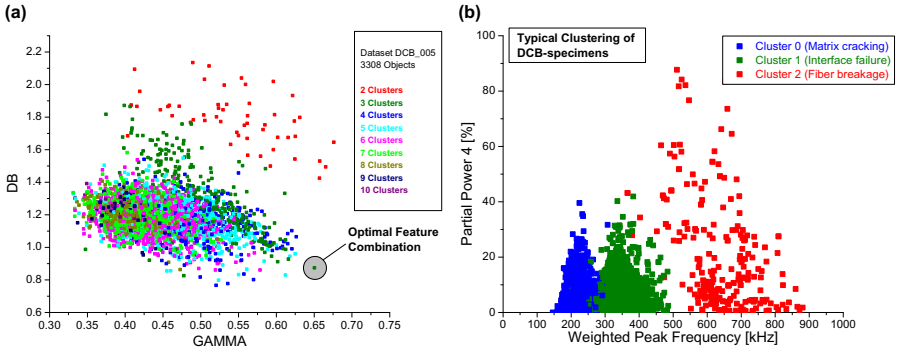


Figure 4.38.: Result of the proposed pattern recognition method for one representative investigation shown as diagram of Davies-Bouldin over Gamma-Index for all feature combinations (a) and respective optimal clustering as diagram of Partial Power 4 over Weighted Peak-Frequency (b).

### Discussion of the signal clusters

In comparison to the cluster positions of the different failure mechanisms in figures 4.13-b, 4.23, 4.29-b and 4.30-b of the Layup-0, Layup-90 and Layup-0/90 specimens, the feature ranges of the respective clusters in figure 4.38-b are larger. This effect is a consequence of the dispersive propagation of Lamb

#### 4. Experimental results

waves, which causes continuous changes of the signals frequency composition in dependence of propagation length. In comparison to the flexural testing geometry this effect is found more pronounced in the DCB-geometry since the maximum propagation length of the signals is extended to 70 mm in comparison to the maximum distance of 55 mm in bending specimens. This ultimately results in overlapping clusters and makes the identification of the exact cluster boundaries more difficult. Consequently an error free classification of acoustic emission signals in such geometries will not be possible after a certain propagation length.

##### **Comparison with simulation results**

To proof the validity of the assignment of the different obtained signal types to the respective microscopic failure mechanisms the different experimental signal types are compared to simulated signals of matrix cracking, interface failure and fiber breakage in analogy to the Layup-0 specimens. The simulated signals were obtained using the DCB-geometry described in section 3.5 utilizing the full sensor representation.

As shown in figures 4.39 to 4.41, the obtained experimental and simulated signals show good agreement to each other. In comparison to the signals obtained in flexural tests, the  $A_0$ -modes typically are less disturbed by boundary reflections, since the incident reflection from the x-edge of the specimen is missing within the shown time-scale. Again the contribution to the  $A_0$ -mode around 100 kHz visible in the experimental signals is not exactly reflected in the simulation (see also section 4.2.3). Except for this discrepancy, the three failure types again follow the observed scheme with intense  $A_0$ -modes for matrix cracking, intense  $S_0$ -modes for fiber breakage and intermediate ratios for interface failure.

Similar to the Layup-0 specimens a quantitative comparison between the ranges of features extracted from experimental signals and simulated signals was made. Here the source model position was varied along the x and y-direction within the specimen volume according to the microscopically observed source positions. No changes along the z-direction of the specimen were made, since this is almost constant during specimen failure. The comparison of the feature values obtained from the experimental signals and the simulated signals is shown in figure 4.42 in a plot of Partial-Power 4 over Weighted Peak-Frequency. Again good agreement of the distribution ranges and locations of the experimental signals to the features from the simulated signals is observed. The characteristic overlap of signals attributed to matrix cracking and to interface failure is also found within the simulated signals and is caused by the strong variations in the simulated source-sensor distances.

#### 4. Experimental results

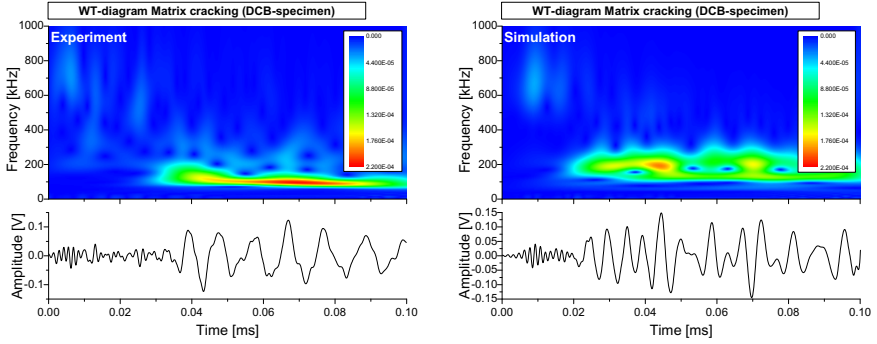


Figure 4.39.: Comparison of WT-diagrams for one representative experimental signal of cluster 0 and the simulated result for matrix cracking at  $(x,y,z) = (0,0,0)$  mm with  $d_x = 100$  nm and  $T_{e,x} = 1000$  ns.

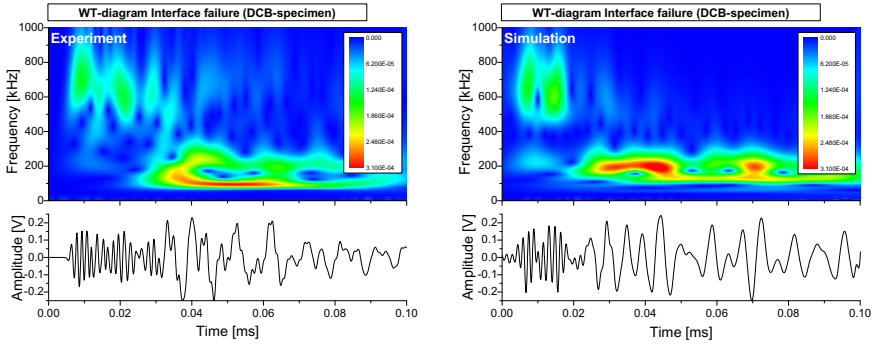


Figure 4.40.: Comparison of WT-diagrams for one representative experimental signal of cluster 1 and the simulated result for interface failure at  $(x,y,z) = (0,0,0)$  mm with  $d_x = 50$  nm,  $d_y = d_z = 100$  nm and  $T_{e,x} = T_{e,y} = T_{e,z} = 100$  ns.

#### Interpretation of pattern recognition results

In figure 4.43-a the quantified results of the relative signal amplitude contribution of the different failure mechanisms are shown in dependence of the measured fracture toughness value. Clearly the obtained signal contributions of interface failure and matrix cracking dominate the overall failure behavior as already expected by microscopical observations. Fiber breakage in turn shows

#### 4. Experimental results

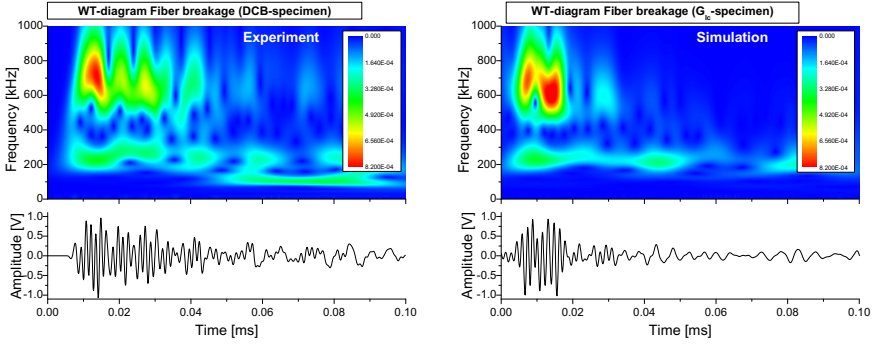


Figure 4.41.: Comparison of WT-diagrams for one representative experimental signal of cluster 2 and the simulated result for fiber breakage at  $(x,y,z) = (0,0,0)$  mm with  $d_x = 100$  nm and  $T_{e,x} = 100$  ns.

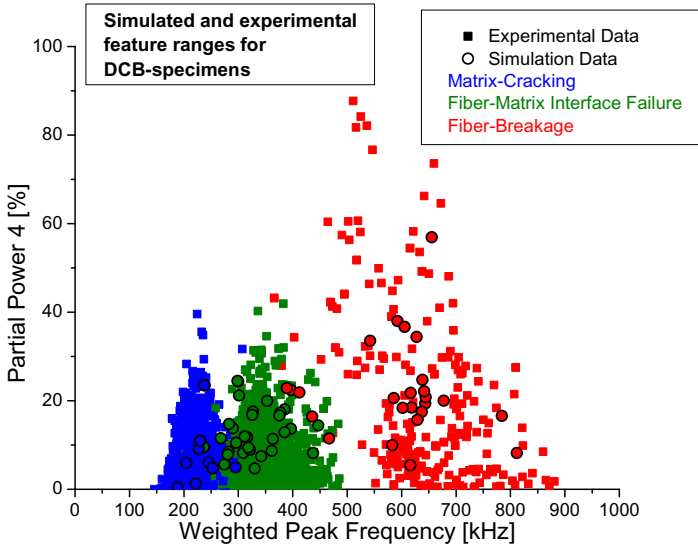


Figure 4.42.: Comparison of feature values extracted from experimental and simulated signals at the microscopically observed source positions in a diagram of Partial Power 4 over Weighted Peak-Frequency.

#### 4. Experimental results

almost negligible contributions in the relative amplitude contributions. With increasing  $G_{Ic}$ -value the signals correlated with interface failure show increasing contributions, while for matrix cracking a contrary behavior is observed. This agrees well with the microscopic observations of the associated failure types as shown in figure 4.36, which indicate the same increased contribution of interface failure for specimens with increased  $G_{Ic}$ -values.

In particular, the linear regression of the relative amplitude contributions of interface failure and matrix cracking predict equal failure contributions, when the specimens  $G_{Ic}$ -value approaches the range of fracture toughness expected for pure resin. Since no fracture toughness values were available for the used Hexply913 resin, for comparison the fracture toughness values for a Hexcel RTM6 and a Hexply914 are shown in figure 4.43 [150, 181, 182]. The latter one is closely related to the used resin system, but is expected to show lower fracture toughness values than the Hexply913 resin, estimated on the tensile strength and modulus provided by the manufacturer.

The fracture toughness value obtained from the intersection of the linear regression of interface failure and matrix cracking is understood as measure of the interfacial fracture toughness between fiber and matrix. For equal contributions of both failure types the interfacial fracture toughness is expected to be at least equal to the fracture toughness of the used resin type. In addition, the extrapolation indicates that specimens with fracture toughness values below those of pure resin should dominantly fail by matrix cracking. For the current specimens this predicts a fracture toughness value of the used resin of  $139 \text{ J/m}^2$ .

Within the standard deviation, the average amplitudes per signal yield a constant value for all failure mechanisms independent of the  $G_{Ic}$  value (see figure 4.43-b). As already discussed for the Layup-0/90 specimens in section 4.2.3 this can indicate a constant crack surface area increment per signal and a constant energy release respectively. But as also discussed in section 4.2.3, the constant amplitude per signal can also originate from diametrical behavior of both contributions.

To analyze the interfacial strength between fiber and matrix, a comparison of average frequency spectra calculated for the signal class attributed to interface failure is shown in figure 4.44 for three specimens with different  $G_{Ic}$ -values. Here a slight increase at frequency contributions around 700 kHz is observed for an increasing  $G_{Ic}$ -value. As discussed in section 3.4.1 the contributions in this frequency range are caused by the  $S_0$ -mode and thus indicate an increased interfacial strength between fiber and matrix with increasing  $G_{Ic}$ -value. In comparison to the simulations shown in figure 3.27, the observed effect is very low. In addition, for an increased  $G_{Ic}$ -value there is also a noticeable increase of contributions observed around 225 kHz, which is indicative for a decreased interfacial strength. Thus it cannot be excluded, that different

#### 4. Experimental results

mechanisms like microscopic inhomogeneities or variations in the microscopic loading conditions are responsible for the large  $G_{IC}$  value range observed for the present specimens.

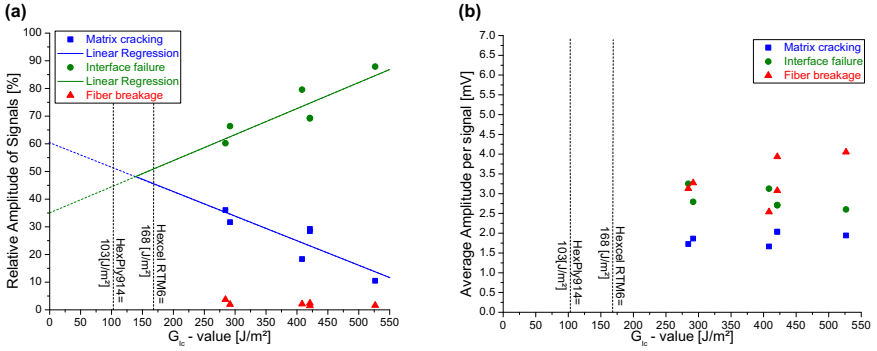


Figure 4.43.: Quantified results for matrix cracking, interface failure and fiber breakage shown in plots of relative energy contribution (a) and average amplitude per signal (b) over measured fracture toughness value in comparison with reference values from two resins [181, 182].

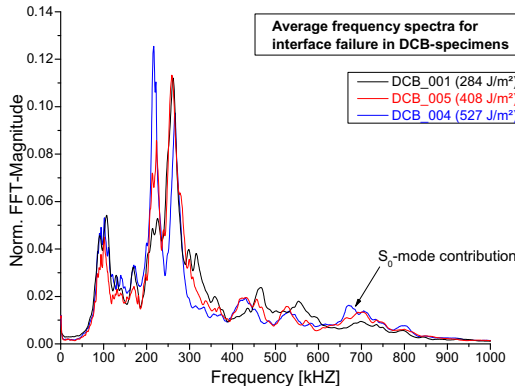


Figure 4.44.: Comparison of average FFT-spectra of interface failure signals for specimens with different  $G_{IC}$ -values.

### 4.3.2. Tensile testing of T800/913 specimens

Similar to the DCB-specimen series before, the acoustic emission techniques established for the flexural testing specimens are investigated within this series of tensile specimens using a different geometry for signal propagation and different loading conditions. This results in an increased mean signal propagation length in comparison to the flexural testing specimens. In addition the influence of the  $[0/90_3/0]_{sym}$  ply-layup on the identification process of different failure mechanisms is analyzed in the following.

During tensile loading, the failure inside the specimens is initialized by inter-fiber matrix cracking occurring in the  $90^\circ$  oriented layers (see figure 4.45-a). In contrast to the expected type of mode-I cracking perpendicular to the loading axis (x-direction), the observed type of inter-fiber crack growth parallel to the x-direction seems to originate from mode-II loading conditions. This type of failure can occur if the outer  $0^\circ$  layers are subject to higher strain rates than the inner  $0^\circ$  layers. This is often caused by insufficient grip forces of the tensile jaws. The growth of these cracks also results in delamination along the interface between  $0^\circ$  and  $90^\circ$  plies with final failure due to fiber breakage in the  $0^\circ$ -layers as discussed by [183] and partially by [180]. The microscopic appearance of the specimen after crack-through is shown in figure 4.45-b in a top-view SEM-image. Here final failure causes severe fragmentation of the specimen. Since this also results in a loss of contact between the acoustic emission sensors and the specimen, this can cause severe damage to the sensors by drop down. Thus only three specimen were loaded till final failure, while all others were only loaded up to a maximum force of  $F = 32$  kN, which is sufficient to initialize inter-fiber matrix cracking, inter-ply delamination and even fiber breakage within the specimen.

Similar to the investigations in sections 4.2 and 4.3.1 the recorded acoustic emission signals were first subjected to a localization routine. Due to the different amounts of carbon fibers oriented in  $0^\circ$  and  $90^\circ$  directions, the measured sound velocities in x- and y-direction differ. These were measured to be  $(6190 \pm 40)$  m/s in x-direction and  $(8518 \pm 98)$  m/s in y-direction, respectively. The attenuation was measured to be  $(100 \pm 10)$  dB/m independently of the chosen direction. Since four sensors in planar geometry were used during the measurements, the source positions could be localized in two dimensions using an anisotropic localization algorithm, which takes into account the different sound velocities. Figure 4.46 shows a representative diagram of the localized source positions in the xy-plane of one specimen. The color range in figure 4.46 marks the density of acoustic emission sources, while the tapered volumes dimension and the reinforcements are marked by white rectangles.

The majority of localized source positions is found within the tapered volume

#### 4. Experimental results

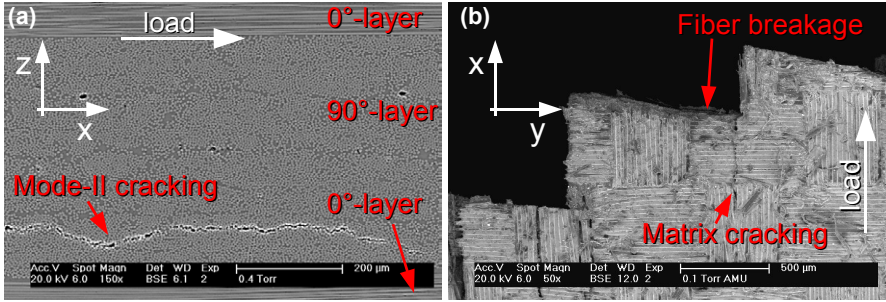


Figure 4.45.: Cross-sectional SEM-image of inter-fiber matrix cracking in tapered specimen volume (a) and top-view SEM-image of crack front at position of crack-through (b).

and is attributed to the occurrence of mode-II inter-fiber matrix cracking and adjacent delamination between the ply layers. In addition spots with high acoustic emission density coincidence with the localized positions of fiber breakage. This agrees with microscopical observations, where fiber breakage was observed to occur within the  $0^\circ$  layers close to the positions of inter-fiber matrix cracking. In this context high acoustic emission density spots are attributed to inter-fiber matrix cracking and subsequent secondary damage due to the increased stress levels at these positions.

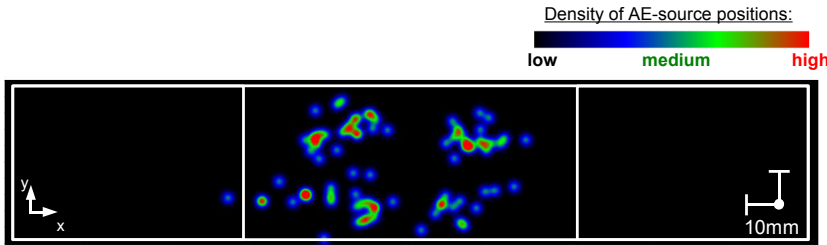


Figure 4.46.: Localized acoustic emission source positions of one representative tensile specimen shown as density diagram. The colour value marks the local density of acoustic emission sources, while the specimen dimensions and reinforcement areas are marked by white rectangles.



### Pattern recognition

In the following only the localized signals were used for further analysis by pattern recognition. Here the same pattern recognition method as introduced in section 2.3.3 was used to determine the best feature combination for partitioning of the recorded acoustic emission signals. Similar to the procedure of the DCB-specimens the signal features were extracted from the first 200  $\mu\text{s}$  after arrival of the  $S_0$ -mode to interpret only the characteristic part of the detected signals. The result of the investigation with  $Q_{min} = 5$  and the same  $Q = 12$  frequency features as used for the flexural testing specimens described in section 4.2 is shown as diagram of  $DB$  over  $GAMMA$  index in figure 4.47-a as representative result of one tensile specimen.

For this specimen series various feature combinations are located within the numerical optimal range. In summary a separation into three clusters with the feature combination given in table 4.4 was found to be suitable for all seven specimens investigated. This is the alternative feature combination also found in the numerical optimal range for clustering of acoustic emission signals of Layup-0/90 specimens. In contrast to the investigations in section 4.2.3, the feature combination yields stable clusters for all tensile specimens investigated. This is a consequence of the changed center-frequency positions of the identified clusters. This changed frequency range is seen best, when comparing the clustering of the tensile specimen shown in figure 4.47-b, with the respective diagram of a Layup-0/90 specimen shown in figures 4.29-b and 4.30-b. For the tensile specimens the diagram of Partial Power 4 over Weighted Peak-Frequency clearly reveals a mean shift to higher Weighted Peak-Frequencies for the interface failure and fiber breakage clusters.

### Comparison with simulation results

This shift of intensities to higher frequencies is also observed in the simulated frequency spectra of interface failure for the three different geometries in chapter 3 (see figure 3.47). In addition to these simulations at the specimen origin, the source positions of the model source was varied according to the microscopically observed positions for the various failure types. For these simulations, the reduced sensor model was included to compare the simulated to experimental signals. In figures 4.48 to 4.50 a comparison is made between the WT-diagrams of simulated signals for matrix cracking, interface failure and fiber breakage with respective experimentally detected signals localized approximately at  $(x,y) = (0,0)$ . As discussed before the WT-diagrams agree satisfactory and change systematically in their characteristics with high intensity  $A_0$ -modes for matrix cracking, high intensity  $S_0$ -modes for fiber breakage and intermediate  $A_0$ - to

#### 4. Experimental results

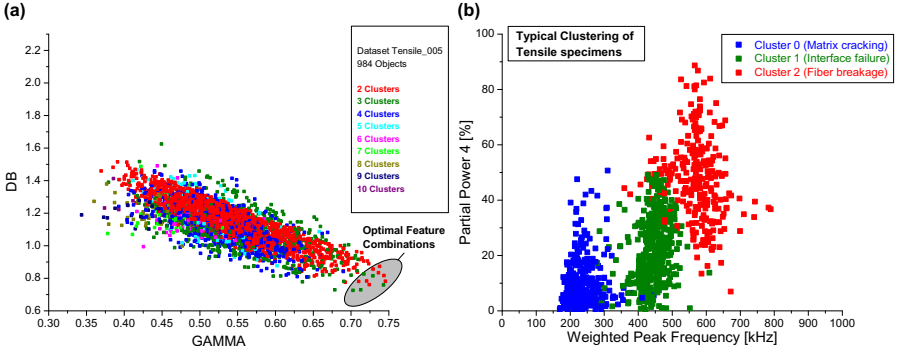


Figure 4.47.: Result of the proposed pattern recognition method for one representative investigation shown as diagram of Davies-Bouldin over Gamma Index for all feature combinations (a) and respective optimal clustering as diagram of Partial Power 4 over Weighted Peak-Frequency (b).

$S_0$ -mode ratios for interface failure.

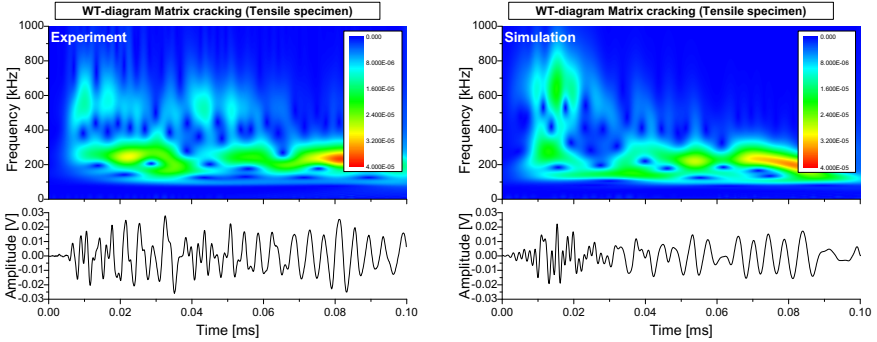


Figure 4.48.: Comparison of WT-diagrams for one representative signal of cluster 0 and the simulated result for matrix cracking at  $(x,y,z) = (0,0,0.455)$  mm with  $d_z = 100$  nm and  $T_{e,z} = 1000$  ns.

In addition, a quantified comparison of the simulation results with experimental data is given in figure 4.51. Here the same feature extraction procedure was applied to the simulated signals and the experimental signals to yield the plot of Partial Power 4 over Weighted Peak Frequency. In summary the

#### 4. Experimental results

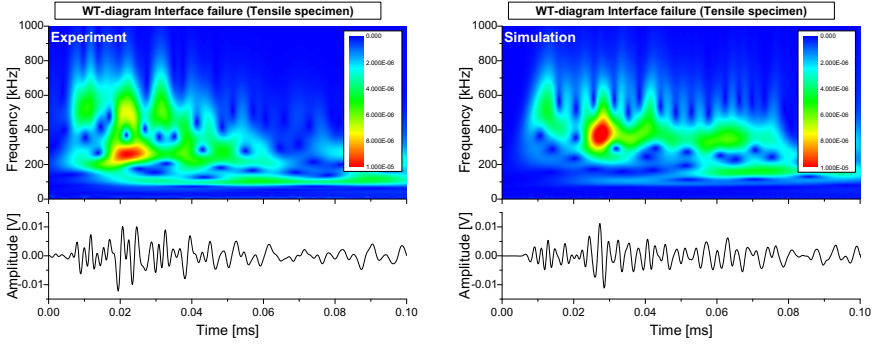


Figure 4.49.: Comparison of WT-diagrams for one representative signal of cluster 1 and the simulated result for interface failure at  $(x,y,z) = (0,0,0.455)$  mm with  $d_y = 50$  nm,  $d_x = d_z = 100$  nm and  $T_{e,x} = T_{e,y} = T_{e,z} = 100$  ns.

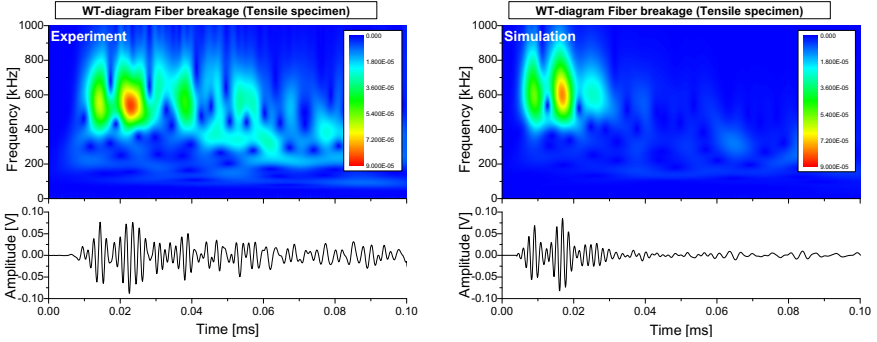


Figure 4.50.: Comparison of WT-diagrams for one representative signal of cluster 2 and the simulated result for fiber breakage at  $(x,y,z) = (0,0,0)$  mm with  $d_x = 100$  nm,  $T_{e,x} = 100$  ns.

agreement between the simulated signals and associated clusters for the three different failure mechanisms is satisfactory. Only for interface failure, larger discrepancies between the simulated and the mean experimental values are observed. Since these types of signals are attributed to a variety of source mechanisms, the present source model may not be representative for all of them. In particular, all interface failure types were simulated with constant excitation times for all directions and constant displacement amplitudes  $d_x$

#### 4. Experimental results

and  $d_y = d_z$ . Since these parameters influence the frequency characteristics of the respective signals they should be varied to fit the type of interface failure under investigation.

In summary the comparison of microscopic investigations and source locations of the associated acoustic emission signals and the comparison of the feature ranges from experimental and simulated signals allows a distinction between matrix cracking, fiber breakage and fiber-matrix interface failure.

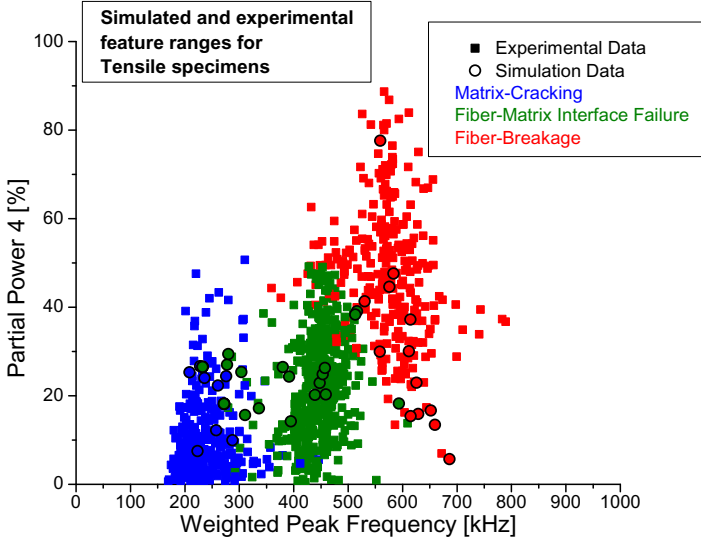


Figure 4.51.: Comparison of feature values extracted from experimental and simulated signals at the microscopically observed source positions in a diagram of Partial Power 4 over Weighted Peak-Frequency.

#### Interpretation of pattern recognition results

A quantification of the experimental results from pattern recognition is shown in figure 4.52 as diagram of relative amplitude (a) and average amplitude per signal (b) over the recorded value of mechanical work.

Since two different load levels were used for the specimens investigated it is best to separate the discussion into two parts. These different load levels are reflected in figure 4.52 by the drastically different values of the recorded mechanical work and could only be visualized by application of an axis break.

#### 4. Experimental results

Thus the shown data points should not be misinterpreted to show strict linear dependency on the recorded work.

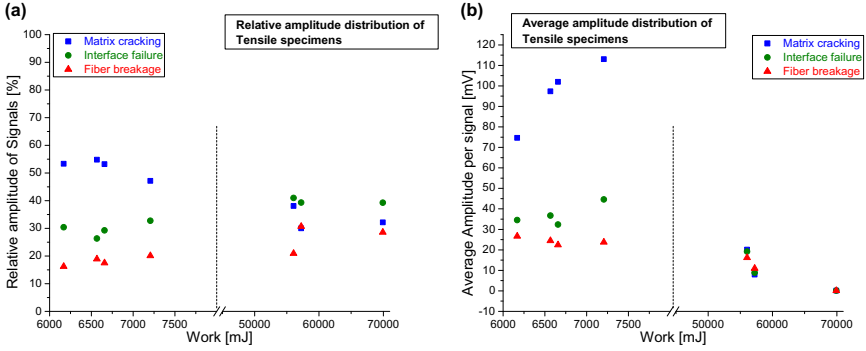


Figure 4.52.: Quantified results for matrix cracking, interface failure and fiber breakage shown in plots of relative amplitude of signals (a) and average amplitude per signal (b) over recorded mechanical work.

The four specimens located at lower work values were only loaded up to a maximum force of  $F = 32$  kN. The dominantly observed failure in these specimens is mode-II inter-fiber matrix cracking, which is expressed in highest relative amplitude contributions to matrix failure and interface failure. In comparison the quantified amount of fiber breakage is only less intense and almost constant in dependence of the recorded mechanical work. The increase of the average amplitude per matrix cracking signal is caused by a drastic reduction in the absolute number of recorded matrix cracking signals. This can be associated with a decreased number of inter-fiber matrix cracks, which translates into a higher residual stiffness of the specimen. This finally causes a higher mechanical work value for constant maximum force. In comparison the average amplitude per fiber breakage and interface failure signals is almost constant, which indicates a very similar progress of these failure types in all four specimens in dependence of loading.

A completely different contribution to the three failure mechanisms is found for the three specimens loaded till final failure. As expected by the microscopic observations at higher load levels, an increased contribution of inter-ply failure between  $0^\circ$  and  $90^\circ$  layers and fiber breakage within the  $0^\circ$ -layers is found. This is reflected in the changed relative amplitude contributions of signals attributed to fiber breakage and interface failure. In addition, numerous signals with lower amplitudes are detected, indicating crack growth with lesser crack surface areas, than for the initial mode-II inter-fiber matrix cracking. These

#### 4. *Experimental results*

additional signals cause a severe drop of the average signal amplitudes down to regions which are typically observed for the DCB-specimens and bending specimens.

#### 4.4. Variation of curing degree of flexural testing specimens

As a consequence of the systematic variation of the curing degree of this specimen series, the macroscopically observed mode of failure in four point bending changes drastically. As depicted in figure 4.53 in a photographic image, the HG60% and HG70% specimens show excessive shear failure along the stacked plies. For this failure mode the dominant contribution of acoustic emission sources is expected to originate from mode-II inter-fiber matrix cracking and interface failure between the ply layers.

The macroscopically observed damage for the HG80% and HG100% specimen types is different. These specimens exhibit the typical failure mode expected for four-point bending of CFRP with most of the damage located at the position of the upper supports and minor delamination in the area between the supports. Consequently the microscopic source mechanisms for acoustic emission is expected to consist of inter-fiber matrix cracking, interface failure in form of delamination and fiber breakage as already discussed in section 4.2.3.

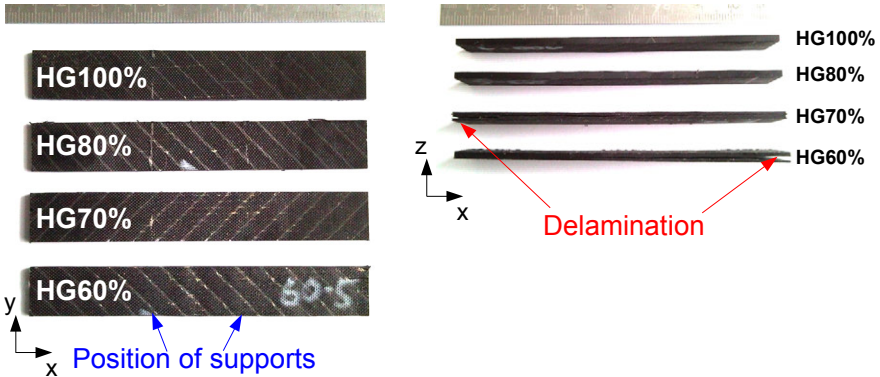


Figure 4.53.: Image of macroscopically observed failure in specimen series in top-view (left) and side-view (right).

In the following, the previously published results [184] are presented and are completed by a short review on the obtained mechanical properties including their correlation to microscopic observations and a reexamination of the recorded acoustic emission signals by the new pattern recognition methodology as proposed in section 2.3.3.

#### 4.4.1. Discussion of mechanical properties and microscopic observations

The diagrams in figure 4.54 show a summary of the measured specimens mean fracture strength and mean flexural modulus in dependence of the degree of curing. The respective mean values are summarized in table 4.6. As already visualized by the failure modes in figure 4.53 the low fracture strength of the HG60% specimens is a consequence of the excessive shear failure. For the HG70% specimens a significant increase of the mean fracture strength is observed, but remains lower than for the HG80% and HG100% specimens. Most noticeable the highest fracture strength of all specimens is observed for the HG80% specimens and not for the HG100% specimens subject to the recommended curing cycle. Similar, the measured flexural modulus shows a significant decrease between the HG80% to the HG100% specimens. A comparable loss of mechanical performance was also observed in DCB tests of the same specimen series.

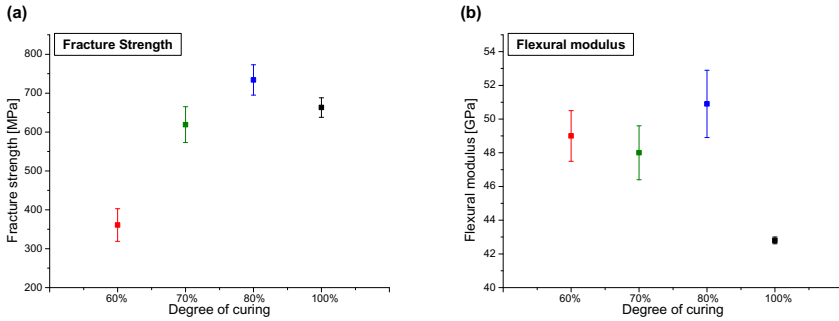


Figure 4.54.: Fracture strength (a) and flexural modulus (b) of all investigated specimens. The different curing degrees are marked in color.

Based upon the fracture behaviour observed in four point bending, a drastic change in the interfacial strength between fiber and matrix in dependence of the cross-linking degree of the resin can be expected. To confirm this assumption, measurements of the apparent interlaminar shear strength according to DIN-EN 2563 were performed [172]. The result of this investigation is shown in figure 4.55 and is summarized in table 4.6. Within the margin of error, similar results are obtained for the HG60% and HG70% specimens. These show a significantly lower shear strength value than the HG80% and HG100% specimens, which is also reflected in the microscopic observations of their fracture surface. Figure 4.56 holds a comparison of scanning electron microscopy pictures in top-view



## 4. Experimental results

of the fracture surface of specimens with different degrees of curing. Generally, shear stress directed along the fiber-axis is transferred to the surrounding matrix as well. During crack progress parallel to the fiber axis, a high adhesion to the matrix causes stronger energy dissipation in the form of crack formation within the matrix. This causes the typical ripple structures growing perpendicular to the fiber axis as observed in all images in figure 4.56 [185]. The strongest pronounced ripple structure is found in the HG80% specimens, which indicates a high interlaminar shear strength. In comparison these structures are less emphasized in the other curing degrees and are least present for the HG60% specimens.

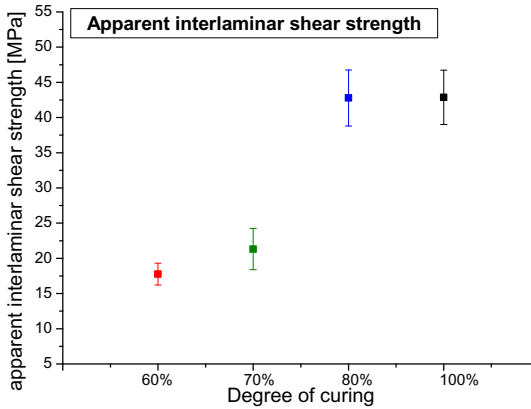


Figure 4.55.: Results of apparent interlaminar shear strength for the different curing degrees.

### 4.4.2. Interpretation of acoustic emission results

For localization of the acoustic emission source positions, the sound velocity was obtained from the average time of travel of 20 test pulses propagating between the two sensors and their respective metric distance. The so obtained velocities of the  $S_0$ -mode are summarized in table 4.7 for the different curing degrees. Within the margin of error no systematic tendency between degree of curing and sound velocity is observed. In particular, the measured sound velocity is most of all dominated by the orientation of the fibers due to their high sound velocity and the thickness of the plate due to the formation of

#### 4. Experimental results

Specimen type	Fracture strength [MPa]	Flexural modulus [GPa]	Apparent interlaminar strength [MPa]
HG60%	$361 \pm 42$	$49.0 \pm 1.5$	$17.8 \pm 1.6$
HG70%	$619 \pm 46$	$48.0 \pm 1.6$	$21.3 \pm 2.9$
HG80%	$734 \pm 39$	$50.9 \pm 2.0$	$42.8 \pm 4.0$
HG100%	$663 \pm 25$	$42.8 \pm 0.2$	$42.9 \pm 3.9$

Table 4.6.: Summary of the average mechanical properties obtained for the different degrees of curing.

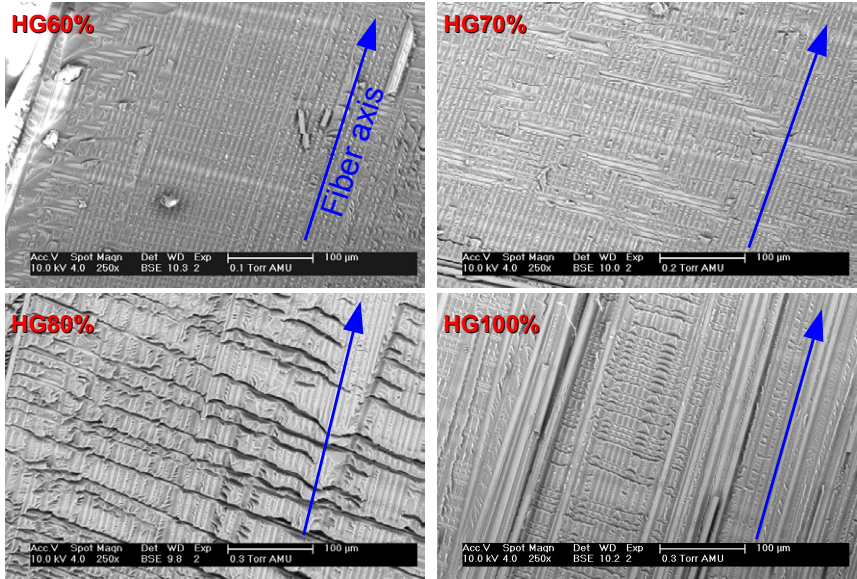


Figure 4.56.: Comparison of scanning electron microscopy pictures showing the fracture surface of specimens used for determination of the apparent interlaminar shear strength in top-view.

Lamb waves (see section 2.2.3). Since the stacking sequence was identical for all specimens the correlation to the plate thickness as given in table 4.7 might

#### 4. Experimental results

explain the observed differences in the sound velocity better than the change in the degree of curing.

Specimen type	$S_0$ -mode velocity [m/s]	Plate thickness [mm]
HG60%	$4670 \pm 50$	$2.2 \pm 0.1$
HG70%	$4490 \pm 80$	$2.4 \pm 0.1$
HG80%	$4510 \pm 90$	$2.4 \pm 0.1$
HG100%	$4600 \pm 20$	$2.3 \pm 0.1$

Table 4.7.: Summary of the measured sound velocities and the measured plate thickness.

The acoustic emission signals were localized using a threshold based hyperbolic localization technique with the linear sensor geometry shown in figure 4.6. Subsequently only the localized signals were used for further analysis. From the remaining signals two datasets (non-defined signals and defined acoustic emission signals) were set up manually within the software package Noesis. This provides training data for a backpropagating neuronal network, which is used for an automated identification and exclusion of the non-defined signals for all datasets.

For the following investigations the acoustic emission signal frequency features as defined in table 2.2 were extracted solely of the initial 100  $\mu$ s of the recorded acoustic emission signals, while the approach already published in [184] used the complete signal for feature extraction. As discussed in section 4.2 the usage of the initial 100  $\mu$ s of the signal is expected to emphasize the frequency characteristics originating from the different failure mechanisms.

In figure 4.57-a the accumulated acoustic emission energy for one representative specimen of each curing degree is shown in dependence of the loading duration. Clearly the onset of acoustic emission signals shifts drastically in dependence of the curing degree. Here the HG60% and HG70% specimens show early acoustic emission onsets caused by the initiation of shear failure. In HG80% and HG100% specimens the acoustic emission onset is shifted to later time (higher loads). Moreover, the accumulated acoustic emission energies show significant dependence on the degree of curing. Thus for HG60% and HG70% a multitude of the signals of HG80% and HG100% specimens are detected. In combination with the macroscopic observation of specimen failure this is explained by the drastic differences in the final size of the crack surface areas. This is also reflected in the representative localization patterns given

## 4. Experimental results

for the different curing degrees in figure 4.57-b. The HG60% and HG70% specimens show a broad distribution of acoustic emission sources along the x-axis reflecting the macroscopically observed inter-ply delamination causing shear failure. In contrast, the HG80% and HG100% specimens typically show narrow source position distributions with accumulations around the x-positions of the upper supports as marked in figure 4.57-b.

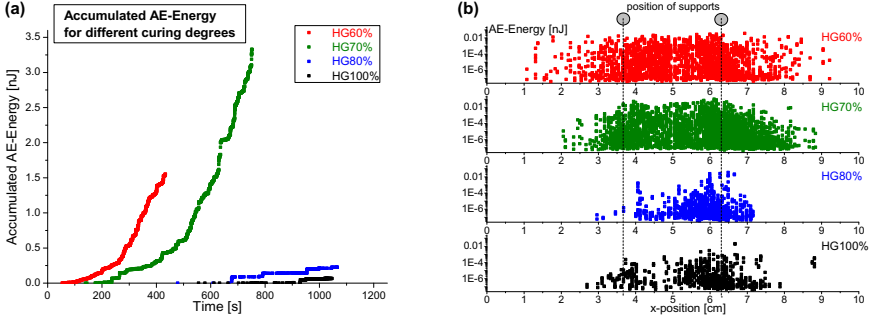


Figure 4.57.: Comparison of the acoustic emission results for the different curing degrees in accumulated acoustic emission energy (a) and source localization patterns along x-axis (b).

### Pattern recognition

For investigation by the pattern recognition approach from section 2.3.3 only the frequency features as introduced in section 4.2 (Average Frequency, Reverberation Frequency, Initiation Frequency, Peak Frequency, Frequency Centroid, Weighted Peak-Frequency, Partial Powers 1-6) and as defined in table 2.2 were investigated. As discussed in section 3.4.3 frequency features are expected to reflect the source mechanisms better than energy criteria. For the features Partial Power 1-6, the same frequency ranges were used as shown in figure 4.10 to allow direct comparison with the results in section 4.2, 4.3.1 and 4.3.2. Again the settings for the investigation were  $Q = 12$  and  $Q_{min} = 5$ . The results of the pattern recognition investigation are shown in figure 4.58 as comparison of one representative specimen for each curing degree in plots of  $DB$  versus  $GAMMA$ .

For the HG60% and HG70% specimens the optimal feature combination as given in table 4.8 was found. This feature combination is also located in the numerical optimal range for the HG80% and HG100% specimens, although some specimens favor the same feature combination as given in table 4.3 for the

#### 4. Experimental results

T800/913 specimens. The only difference between the two feature combinations is the exchange of Partial Power 4 by the Average Frequency. This exchange is caused by the significant change of the failure mechanisms ratios, which introduce strong differences in the variance and distributions of the frequency features for the HG60% and HG70% specimens compared to those of the HG80% and HG100% specimens. In particular, the HG60% and HG70% specimens show strongest contribution of interface failure and matrix cracking (dominant contribution below 450 kHz), which results in less significance of features like Partial Power 4, which characterize the high frequency range (450 - 600 kHz). Thus for this investigation the feature combination given in table 4.8 was chosen, since this was located in the numerical optimal range of all specimens investigated.

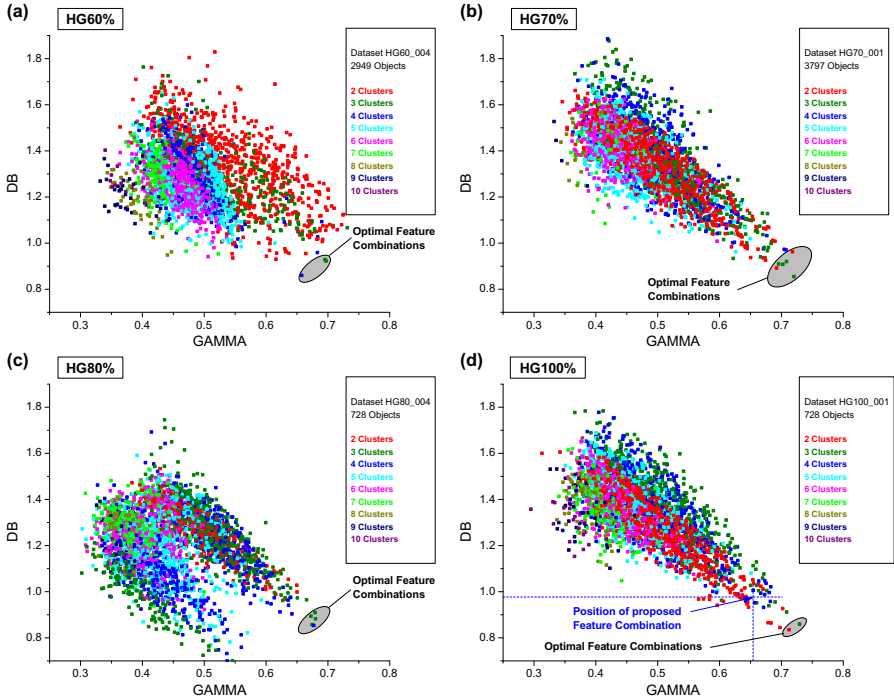


Figure 4.58.: Result of the proposed pattern recognition method for one representative investigation for each degree of curing shown as diagram of Davies-Bouldin over Gamma Index for all feature combinations.

For comparison, the *DB* and *GAMMA* index locations of the feature com-

#### 4. Experimental results

Feature	Remark
Peak Frequency [Hz]	
Weighted Peak-Frequency [Hz]	
Average Frequency [Hz]	
Partial Power 1 [%]	Frequency range 0 - 150 kHz
Partial Power 2 [%]	Frequency range 150 - 300 kHz

Table 4.8.: Feature combination for clustering of acoustic emission signals from HG% specimens.

binations proposed in [184] is marked in figure 4.58-d as well. Clearly, the numerical performance of the partition based on the features proposed in [184] is worse than the optimal feature combination in table 4.8. This is owed to the fact, that the currently used method presented in section 2.3.3 was established after the publication of [184] and the feature selection was solely based on correlation dendrograms. However, the overall classification of signals to the respective clusters is very similar, as shown in figure 4.59-a and 4.59-b for the clustering result according to [184] and following the new approach from section 2.3.3. Since the features of the new approach are obtained from the initial 100  $\mu$ s of the recorded signals and not from the complete signals as in [184], the diagrams in figure 4.59 are not directly comparable. The difference in the feature extraction process is expressed by a shift of the cluster positions to higher frequency ranges. Apart from this, the relative cluster positions are the same and are well comparable to those in sections 4.2, 4.3.1 and 4.3.2.

#### Discussion of signal clusters

The correlation of a particular failure mechanism with a cluster as preliminary given in figure 4.59 is again based on the signals frequency range and is expected to show similar behavior like observed in the Layup-0/90 specimens of the T800/913 material system. The formation of signal classes with distinct time-frequency behavior is shown in figure 4.60 for an exemplarily set of averaged WT-diagrams for the three obtained clusters of a HG100% specimen. Same as for the investigations of the T800/913 material system clear differences between the three different signal types are observed with intense  $A_0$ -modes for matrix cracking (a), intermediate  $A_0$  to  $S_0$ -ratios for interface failure (b) and intense  $S_0$ -mode excitations for the fiber breakage case (c).

## 4. Experimental results

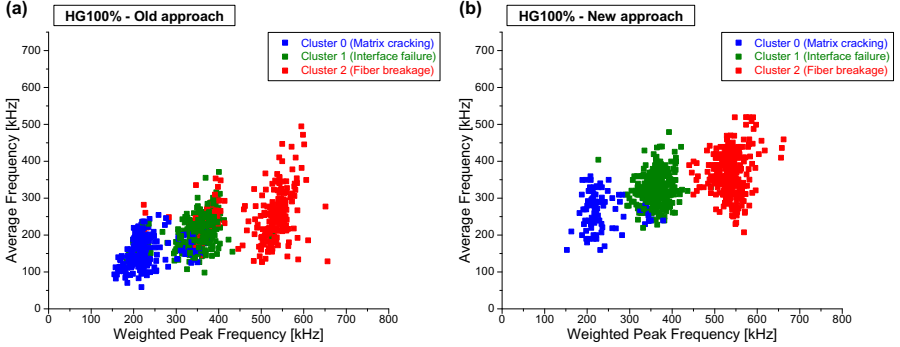


Figure 4.59.: Comparison of clustering result from [184] and new approach from section 2.3.3 using feature combination as given in table 4.8 applied to one HG100% specimen.

### Interpretation of pattern recognition results

Similar to the quantification of the pattern recognition results before, the relative signal amplitude and the average signal amplitude of the different failure mechanisms is shown in figure 4.61-a and 4.61-b for all HTS/RTM6 specimens in dependence of the measured mechanical work. A clear dependency between the degree of curing and the recorded work value was found. The HG60% and HG70% specimens show work values  $\Omega_{frac} \leq 2500$  mJ, while HG80% and HG100% specimens show work values  $\Omega_{frac} > 2500$  mJ.

As shown in figure 4.61-a for increasing mechanical work the contribution of fiber breakage grows, while interface failure shows a significant reduction of contribution. Within the scattering range matrix cracking contributes almost equally for all work values. These complex changes in the contributions of the microscopic failure types are well correlated to the macroscopically observed types of failure. The HG60% and HG70% specimens show dominant interface failure by inter-ply delamination. This is observed less in the HG70% than for the HG60% specimens and is reflected in the decrease of relative amplitude contributions to interface failure. For the HG80% and HG100% specimens the macroscopic failure mode changes from mode-II shear failure to mode-I cracking located dominantly at the supports positions. This results in a higher contribution to fiber breakage and results in comparable contributions of the three failure mechanisms like observed for the T800/913 specimens with  $[0/90_4]_{sym}$  layup.

Within figure 4.61-b the dependencies of the average amplitude per signal

#### 4. Experimental results

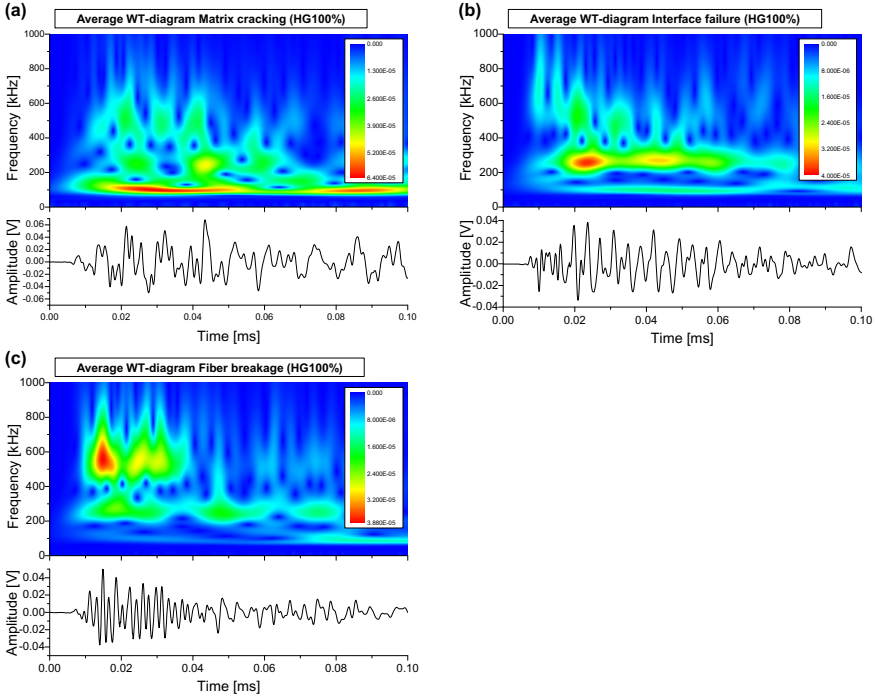


Figure 4.60.: Comparison of the average WT-diagrams from cluster 0 (a), cluster 1 (b) and cluster 2 (c) as obtained by pattern recognition.

and the recorded work is shown. Here fiber breakage and interface failure show similar trends with almost constant average amplitudes for HG60% and HG70% specimens ( $\Omega_{frac} \leq 2500$  mJ) and a significant drop for HG80% and HG100% specimens ( $\Omega_{frac} > 2500$  mJ). In addition, for matrix cracking a maximum of the average amplitude per signal is found for the HG70% specimens. The dependency between the average amplitude for interface failure and the curing degree reflects the respective changes in the interfacial shear strength as shown in figure 4.55. This is concluded from the expected changes in the crack surface increment  $\Delta A$  per acoustic emission signal, which is assumed to be higher for lower interfacial shear strengths. A similar dependency is found for matrix cracking. In this case an additional contribution is expected to originate from changes in the strain energy release per acoustic emission signal, since the different curing degrees will directly influence the fracture toughness value of the resin. This additional contribution can explain the distinct maximum



#### 4. Experimental results

of average amplitude per signal for the HG70% specimens. Instead, for fiber breakage the drop of average amplitude per signal for the HG80% and the HG100% specimens is solely attributed to respective changes in the crack surface increment per acoustic emission signal. Here a strong variation of the carbon fibers fracture toughness value for the different curing degrees is not expected, since all specimens were manufactured using the same Torayca HTS fibers. Instead, the variation of the curing degree and the interfacial strength between fiber and matrix has direct influence on the frequency of occurrence of fiber bundle breakage or single fiber breakage. This changes the effective crack surface increment  $\Delta A$  per acoustic emission signal.

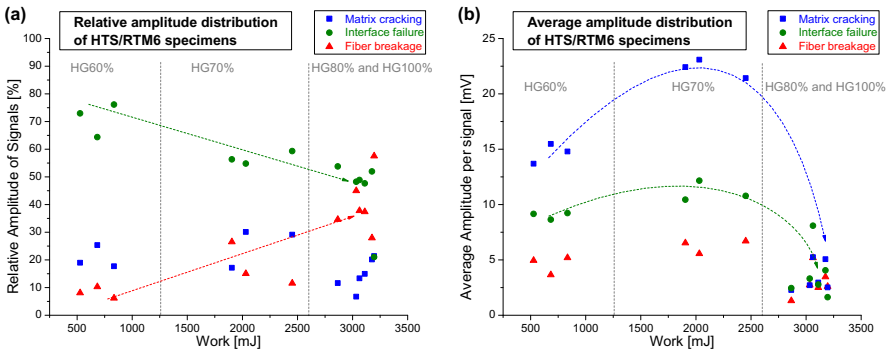


Figure 4.61.: Quantified results for matrix cracking, interface failure and fiber breakage shown in plots of relative number of signals and relative energy contribution over recorded mechanical work.

For the present specimen series a particular interest rests on the signals identified as interface failure. Based upon the measurement of the apparent interlaminar shear strength a respective change of the interfacial strength between fiber and matrix is expected. This is responsible for the drastic changes in the failure mode of the specimens. To demonstrate the analysis capabilities of acoustic emission in this concern, figure 4.62 shows a comparison of the average WT-diagrams of the signal class correlated to interface failure obtained for one representative HG60%, HG70%, HG80% and HG100% specimen. For this specimen series a clear shift of energy contributions to the  $S_0$ -mode as visible at the beginning of the signals for increasing curing degree between HG60% and HG80% is observed. Similar to the measurement of the apparent interlaminar shear strength no further change in the  $S_0$ -mode contribution is observed between the HG80% and HG100% specimen.

#### 4. Experimental results

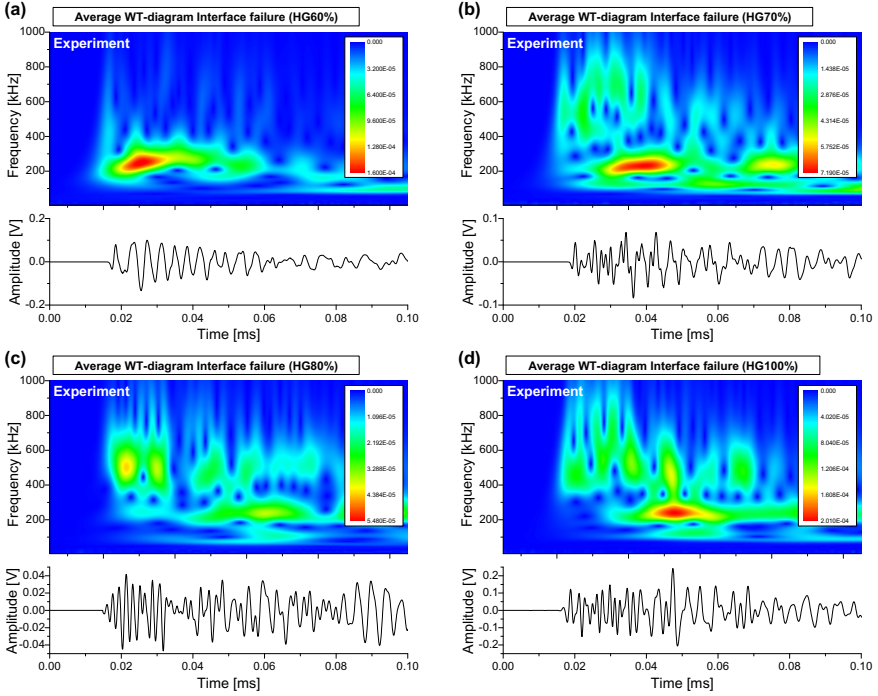


Figure 4.62.: Comparison of average WT-diagrams of class correlating with interface failure for HG60% (a), HG70% (b), HG80% (c) and HG100% specimen (d).

As discussed in section 3.4.1 the increased excitation of the  $S_0$ -mode is attributed to a higher fiber-matrix interfacial strength. For comparison of this effect figure 4.63 shows simulations obtained for the T800/913 elastic properties in  $[0/90_4]_{sym}$  layup with varied excitation ratio  $(d_x):(d_y, d_z)$ . In the simulations an increase of the excitation ratio  $(d_x):(d_y, d_z)$  from  $d_x = 5.0$  nm to  $d_x = 7.5$  nm and  $d_x = 10.0$  nm at constant  $d_y = d_z = 100$  nm and constant excitation time  $T_{e,x} = T_{e,y} = T_{e,z} = 100$  ns yields a very similar shift of contributions to the  $S_0$ -mode. Here the simulated WT-diagrams are not meant to give an exact match to the time-frequency behavior of the interface failure signals observed in the HTS/RTM6 specimens, but should act as comparison of the expected changes when the interfacial strength varies.

However, a similar shift of contributions is expected for a mean shift of the associated sources z-position as discussed in section 3.4.4. Thus if the inter-ply

#### 4. Experimental results

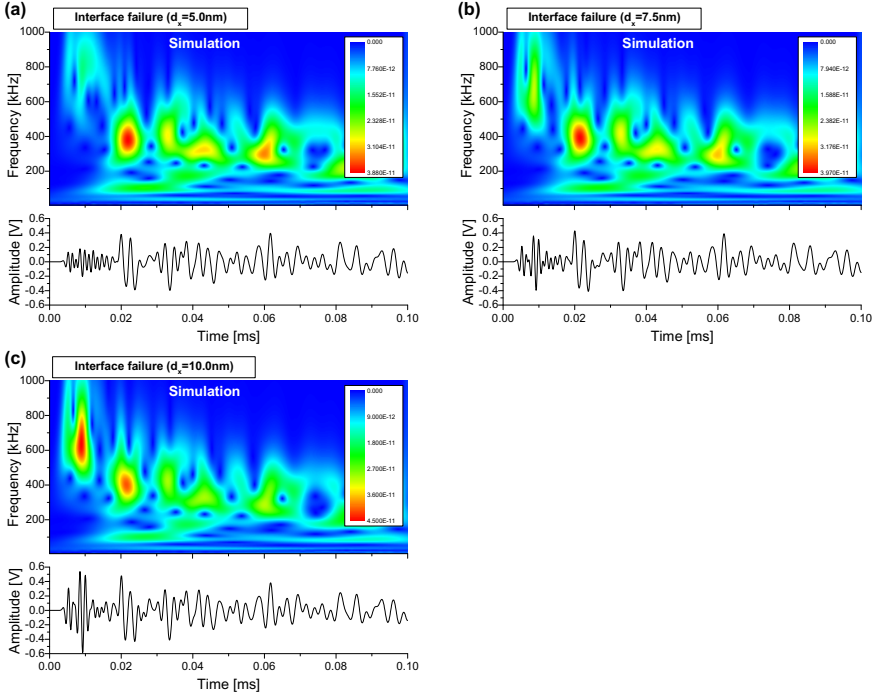


Figure 4.63.: Comparison of WT-diagrams of simulated interface failure signals with T800/913 properties in a  $[0/90_3]_{sym}$  layup at constant  $d_y = d_z = 100$  nm and constant excitation time  $T_{e,x} = T_{e,y} = T_{e,z} = 100$  ns with  $d_x = 5.0$  nm (a),  $d_x = 7.5$  nm (b) and  $d_x = 10.0$  nm (c).

delamination occurs at mean z-positions closer to the surface a shift of intensity from  $S_0$  to  $A_0$ -mode is expected even at constant interfacial strength. For the present specimen series this was not the case. In particular, the HG60% and HG70% specimens show inter-ply delamination located close to the medial plane, while for HG80% and HG100% an approach of the delamination position to the surface was observed. This change of positions would result in an inverse shift of contributions as those observed in figure 4.62. Thus the effect is expected to be even more pronounced for specimen series were such failure occurs at constant z-position, like for DCB-specimens.

## 4.5. Application of pattern recognition method to T-Pull specimens

The T-Pull specimens investigated have a complex stacking sequence and are the specimen geometries with largest dimensions investigated. In particular, the mean source-sensor distance is even larger than for the DCB-specimens. As already discussed in sections 4.3.1 and 4.3.2 large propagation distances and complex stacking sequences make identification of the typical acoustic emission signals correlated with matrix cracking, fiber breakage and interface failure more difficult. Thus the focus within the analysis of the HTS/RTM6 T-Pull specimens is the investigation of the capabilities to separate signals of different failure mechanisms using the same pattern recognition approach as presented in section 2.3.3.

### 4.5.1. Discussion of microscopic observations

All of the specimens investigated show macroscopic failure by complete or partial pull-off between stringer and base-plate (see figure 4.64). The finally observed macroscopic crack surface is located at the interfaces between different ply layers. Here the ultimate failure typically occurs at the top  $45^\circ$  and  $135^\circ$  oriented plies (see figure 4.64). Based on these microscopic investigations, interface failure and inter-fiber matrix cracking are expected to be the dominating source of acoustic emission. In addition fiber breakage is observed randomly distributed over the whole fracture surface (see figure 4.64).

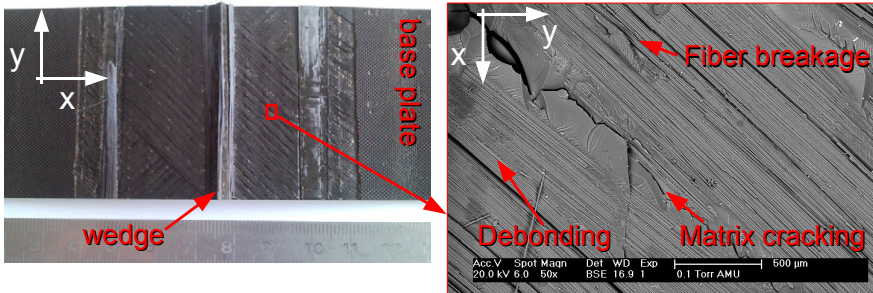


Figure 4.64.: Image of macroscopically observed failure in T-Pull specimen (left) and respective scanning electron microscopy image of the fracture surface in top-view (right).

### 4.5.2. Interpretation of acoustic emission results

Within the margin of error the sound velocity was measured to be isotropic for the base-plate and the stringer, respectively. This is also concluded from the symmetric ply-layup of both components. The measured average sound velocities are  $(5386 \pm 171)$  m/s for the base-plate and  $(5897 \pm 862)$  m/s for the stringer, respectively. As a consequence of the specimen geometry, the recorded acoustic emission signals were localized using two independent sensor groups. The first array of three sensors was used to perform two-dimensional localization of the acoustic emission signals (x,y)-position on the base-plate. The second array of three sensors was used to localize the according source (y,z)-positions on the stringer. The combination of both localization results can act as three-dimensional source positions. For the first sensor group, the missing z-coordinate is chosen to be  $z = 1.5$  mm, while for the second sensor group the x-coordinate is chosen as  $x = 150$  mm. This reflects the location of the source positions within the base-plate and the stringer, respectively. The sufficiency of the localization method was evaluated by pencil lead fracture tests on distinct positions within the area of macroscopically observed failure. Here the calculated source positions show reasonable agreement with the positions of the pencil lead fracture.

A visualization of the localized source positions in projections to the xy-, xz- and yz-plane from failure of one representative specimen at  $\varepsilon \leq 0.65$  % is shown in density diagrams in figure 4.65. Clearly the projections of the acoustic emission source density to the xz- and xy-plane demonstrate that numerous signals originate from the position of the wedge located between base plate and stringer. The projection to the yz-plane reveals additional source positions located within the stringer, which indicate additional failure caused by tensile loading in this region.

The localized acoustic emission source positions can be used to analyze the weak-spots within the specimens joint. For all T-Pull specimens the onset of failure was localized at the position of the wedge. In figure 4.66 a visualization of the failure progress until the first load drop at  $\varepsilon \leq 0.45$  % and the subsequent load levels at  $\varepsilon \leq 0.54$  % and  $\varepsilon \leq 0.65$  % is shown. The failure initiates at the wedge location and grows in intensity with increased strain level. In addition, the size of the damaged region grows asymmetric in x-direction. This asymmetric growth was found to be indicative for an increased mechanical performance. All specimens showing asymmetric source distribution along the x-axis exhibit superior maximum forces at ultimate failure compared to those specimens with symmetric source distribution. In direct comparison, specimens with symmetric crack growth show acoustic emission source positions only close to the wedge position, while specimens with asymmetric crack growth exhibit

#### 4. Experimental results

numerous additional acoustic emission sources in the region  $\pm 20$  mm around the wedge position. Under the assumption of constant fracture toughness this slightly increased crack surface area requires higher amounts of energy for crack progress, which defers failure to higher load levels.

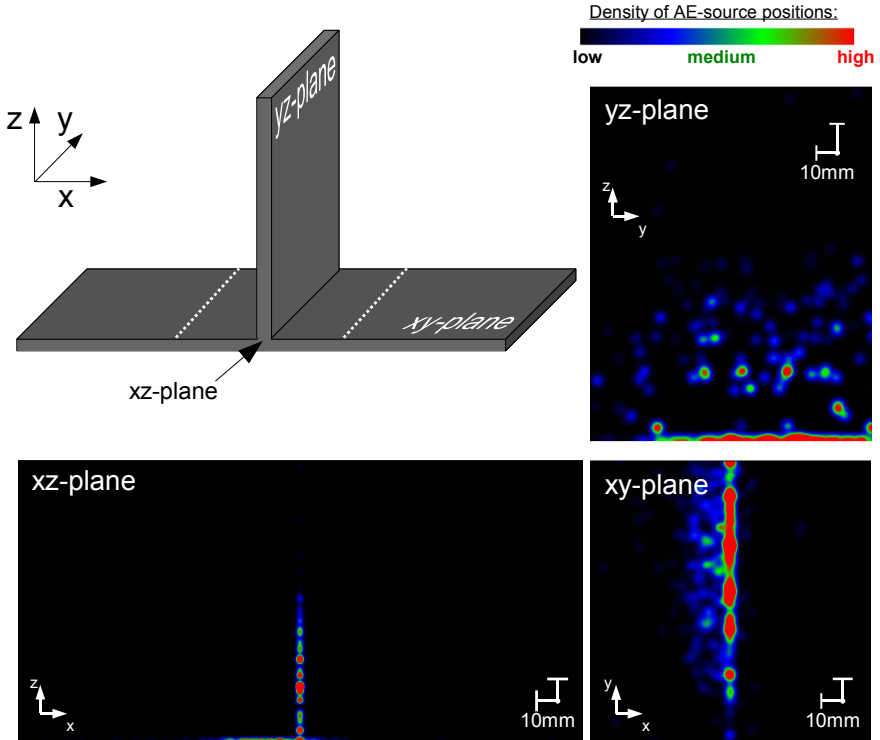


Figure 4.65.: Density diagrams of localized source positions in T-Pull specimen in projections to the xy-, yz- and xz-plane after ultimate failure at  $\varepsilon \leq 0.65$  %.

#### Pattern recognition

In the following only the signals, which were localized by one of the two sensor groups are taken into account for analysis by pattern recognition. Similar to the investigation of the DCB-specimens and the Tensile specimens in section 4.3.1

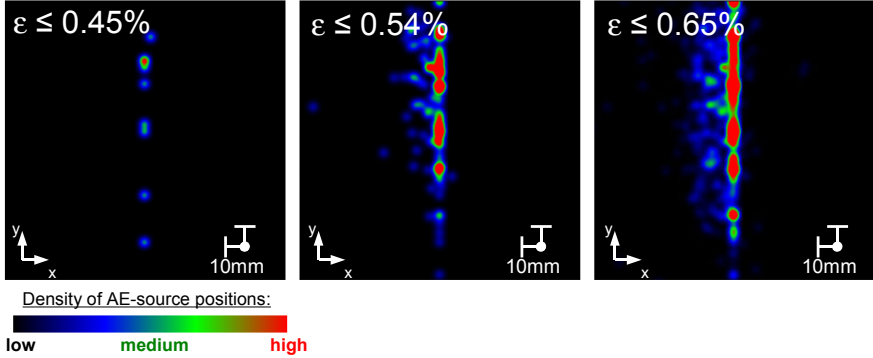


Figure 4.66.: Density diagrams of localized source positions in projection to the xy-plane at increasing load levels of  $\varepsilon \leq 0.45\%$ ,  $\varepsilon \leq 0.54\%$  and  $\varepsilon \leq 0.65\%$ .

and 4.3.2 the frequency features as defined in table 2.2 (Average Frequency, Reverberation Frequency, Initiation Frequency, Peak Frequency, Frequency Centroid, Weighted Peak-Frequency, Partial Powers 1-6) were extracted from the initial  $200\ \mu\text{s}$  of the recorded signals after arrival of the  $S_0$ -mode. Subsequently the obtained signals are investigated by the pattern recognition method from section 2.3.3 similar to the investigations before with  $Q = 12$  and  $Q_{min} = 5$ . The result of this approach is shown as diagram of  $DB$  index and  $GAMMA$  index for one representative specimen in figure 4.67-a. Clearly, within the optimal range of the cluster validity indices a separation into two clusters is suggested for all feature combinations. In particular, the feature combinations given in tables 4.3, 4.4 and 4.8 are all located in the marked optimal range and suggest separation into two clusters as well. The plot of Partial Power 4 over Weighted Peak-Frequency for the feature combination from table 4.3 visualizes the respective clustering result with  $P = 2$ . Under the assumption of similar frequency characteristics for signals correlated with matrix cracking, interface failure and fiber breakage as discussed in the sections before the clusters can be assigned as marked in figure 4.67-b.

In contrast to the specimen types investigated above, the clusters associated with matrix cracking and interface failure are almost completely merged together. This behavior is attributed to the increased mean propagation distances and the complex ply layup, which results in less distinct signal types for a particular failure mechanism. Only the signal types associated with fiber breakage retain distinct differences and are identified as separate cluster.

## 4. Experimental results

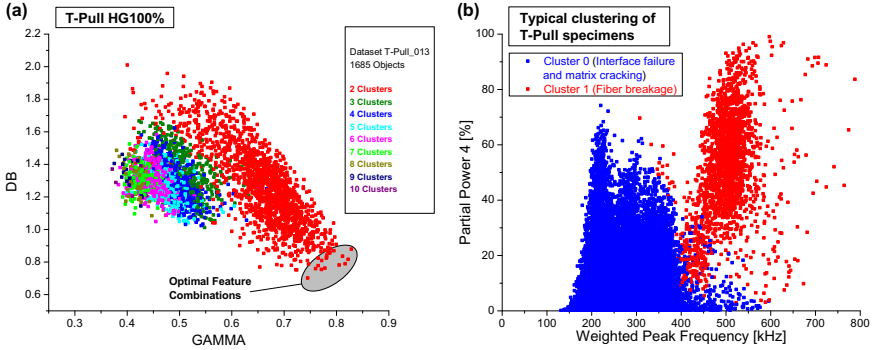


Figure 4.67.: Result of the proposed pattern recognition method for one representative specimen shown as diagram of Davies-Bouldin over Gamma index for all feature combinations (a) and respective optimal clustering as diagram of Partial Power 4 over Weighted Peak-Frequency (b).

### Interpretation of pattern recognition results

As shown in figure 4.68 the onset of fiber breakage signals is found at significantly higher load levels, than those of the remaining signals. As average value of all specimens the acoustic emission onset of fiber breakage was obtained at  $\varepsilon_{AE} = (0.497 \pm 0.006) \%$ , while the acoustic emission onset of the remaining signals was observed at  $\varepsilon_{AE} = (0.154 \pm 0.043) \%$ . The onset of acoustic emission at low strain levels is not unexpected, since numerous voids and resin enclosures were detected in cross-sectional microscopy images and ultrasonic images. These flaws can induce acoustic emission signals with signatures of matrix cracking long before the first significant load drop. As average value, the first load drop visible in the force-strain curves was measured at  $\varepsilon_{drop} = (0.496 \pm 0.051) \%$ . This agrees well with the acoustic emission onset of fiber breakage signals, as obtained from the pattern recognition approach.

In figure 4.69-a the relative signal amplitude of the two identified failure mechanisms is shown in dependence of the value of recorded mechanical work. The diagram clearly reveals the large energetic contributions to the signals attributed to matrix cracking and interfacial failure. Similar to the DCB-tests fiber breakage shows drastically less contributions, which is in good agreement with the microscopic observations (see figure 4.64). For an increased value of mechanical work a slight shift of contributions to the class of signals attributed to matrix cracking and interface failure is observed. This is most likely caused



#### 4. Experimental results

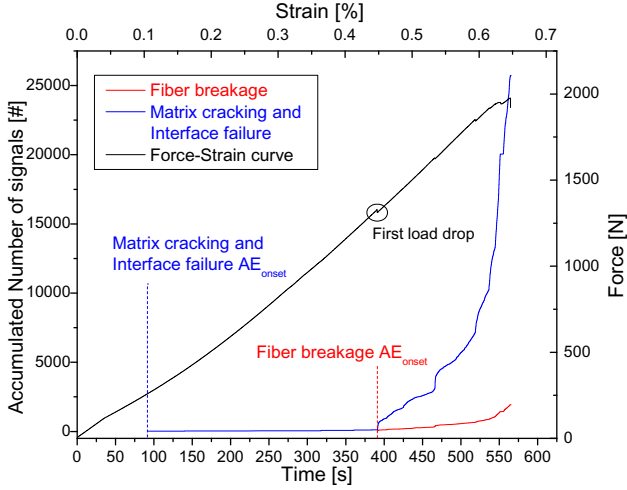


Figure 4.68.: Temporal evolution of accumulated number of signals corresponding to matrix cracking and interface failure and accumulated number of signals corresponding to fiber breakage. For comparison, the force-strain curve of the respective specimen is shown.

by the asymmetric growth of damage around the wedges position, which is associated with a slightly increased crack surface area.

The diagram in figure 4.69-b shows the average signal amplitude of the two identified failure mechanisms in dependence of the value of recorded mechanical work. Within the margin of error, the contribution of signal types correlated to fiber breakage shows comparable values for all specimens. Similar to the investigations in section 4.2.3 and 4.3.1, this is indicative for comparable interfacial fracture toughness. For the signals correlated with matrix cracking and interface failure a slight increase in dependence of mechanical work is observed. As discussed in the sections before, this increase can be attributed to an increased fracture toughness value, which could be responsible for the asymmetric growth of damage. Another possible reason is an increase of the crack volume increment  $\Delta V$  per acoustic emission signal. This increase in  $\Delta V$  could also be expected, since specimens with higher mechanical work values show a broad distribution of acoustic emission source positions.

However, for the T-Pull specimens, strongest tendencies in dependence of mechanical work would be expected for signal types associated with interfacial failure. Same as for the DCB-specimens in section 4.3.1, the separation and

#### 4. Experimental results

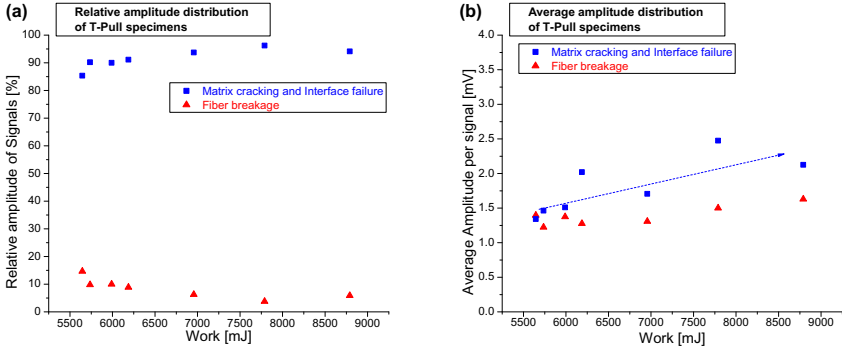


Figure 4.69.: Quantified results for combined contributions of matrix cracking and interface failure and fiber breakage shown in plots of relative amplitude of signals (a) and average amplitude per signal (b) over recorded mechanical work.

quantification of this failure type could yield the most significant dependency, since the measured mechanical properties of T-Pull specimens dominantly depend on the interfacial properties between fiber and matrix.

## 4.6. Application of pattern recognition method to coatings on CFRP substrates

The main focus in the following section is the analysis of acoustic emission signals recorded during failure of nickel and copper coatings applied on CFRP by pattern recognition techniques. Various results of the conducted investigations were already published [128, 129, 186] and are repeated with a global scope in the following. For consistency, the same pattern recognition approach as previously published in [129] is used. First a short review on the failure progress in the investigated coating systems utilizing microscopic analysis is given. In the second part, the obtained acoustic emission signals are analyzed by pattern recognition techniques and are correlated to the different failure mechanisms. The frequency spectra of the signals are compared qualitatively to those of signals from FEM-simulations. In addition the energy content of the signals is quantitatively compared to the respective micromechanical strain energy release as calculated by the fracture mechanics approach already published in [129]. Finally a comparison is made between the results obtained from all coating systems investigated and is discussed in terms of material science.

First it is useful to compare the acoustic emission activity of coated and uncoated specimens loaded in four-point bending. Both the stress-strain curve and the onset of acoustic emission indicate the initiation of failure in the uncoated CFRP substrates to occur at a strain level of  $\varepsilon = 1.0 - 1.2 \%$  (see figure 4.70-a). In contrast, a large number of additional AE signals arise for NiCu-coated samples at  $\varepsilon \leq 1.0 \%$  (see figure 4.70-b). Since the CFRP samples are identical for both specimen series these additional signals are attributed solely to coating failure. This is supported by the fact that the additional AE signals do not correspond to significant changes in the stress-strain curve (fig. 4.70-b). This result is expected since the metallic coating should have a negligible influence on the mechanical properties of the specimen, which are dominated by the elastic properties of the CFRP.

Although signals from coating and CFRP failure are clearly distinguishable by the strain level of their occurrence, the distribution range of acoustic emission energy is comparable in both cases. Consequently, no clear distinction between coating and CFRP failure can be achieved based on energy criteria alone. In the following, it is assumed, that all acoustic emission signals detected below  $\varepsilon \leq 0.8 \%$  arise solely from coating failure, and are therefore denoted “*Coating AE signals*”.

## 4. Experimental results

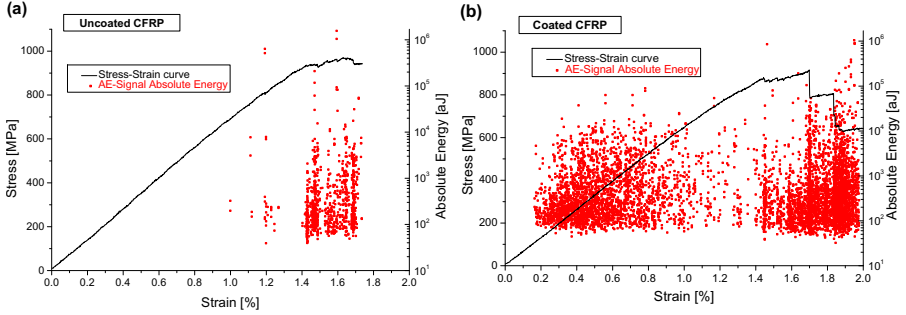


Figure 4.70.: Absolute energy of acoustic emission signal vs. strain (dots) and stress-strain curve (line) in (a) uncoated and (b) NiCu-coated CFRP specimen.

### 4.6.1. Microscopic investigation

For evaluation of the failure progress in the coatings, five specimens were loaded to different strain levels and assessed afterwards by scanning electron microscopy. As representative example for all coatings investigated, microscopy results from a NiCu50 specimen are discussed in the following. At low strain levels ( $\varepsilon = 0.33\%$ ) microscopic cracks develop in the nickel layer at the fringe of the coating (see fig. 4.71-a). With increased loading ( $\varepsilon = 0.65\%$ ) the cracks grow beneath the copper layer and cause extensive delamination at the interface region between copper and nickel (fig. 4.71-b). A similar delamination between nickel and CFRP was not observed. At even higher strain levels ( $\varepsilon = 1.23\%$ ) macroscopic copper cracks evolve in the maximum strain region of the coating which propagate with minor branching at the crack tip. These cracks grow over the whole specimen width perpendicular to the loading axis (fig. 4.71-c). For higher strain levels of  $\varepsilon \geq 1.40\%$  first significant failures of the CFRP-substrates in form of matrix cracking, fiber-matrix debonding and fiber breakage is also observed (fig. 4.71-d).

For quantitative comparison with the results obtained from acoustic emission measurements, the length of crack propagation in the coatings were measured in selected specimens. After unloading of the sample, the whole coating surface was investigated with scanning electron microscopy and the overall crack length  $a$  determined from images in top-view using the software package ImageJ [174] (see figure 4.72-a). Under the assumption that the crack propagation within the copper layer is a “crack-through” process (crack tip stops at Ni–Cu interface),

#### 4. Experimental results

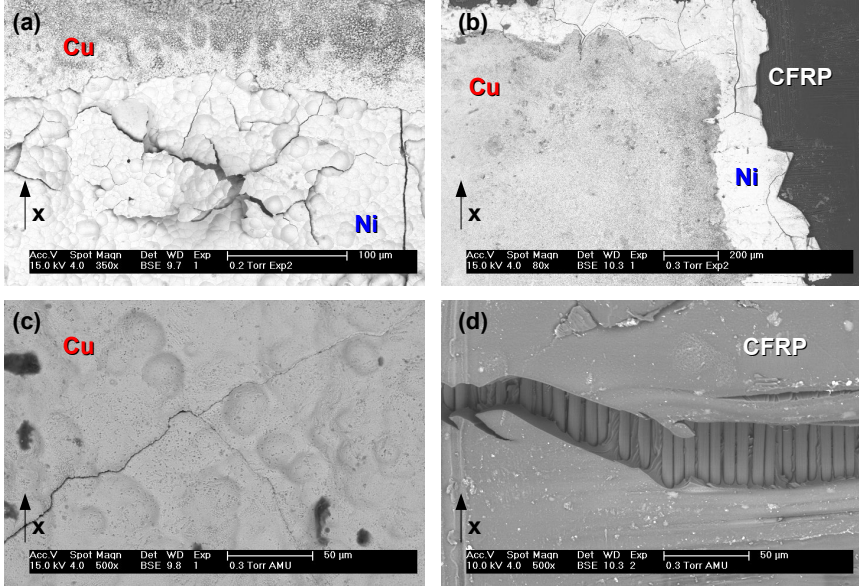


Figure 4.71.: Top view scanning electron microscopy images of NiCu50 specimens at different strain levels. (a) Fringe of coating at  $\varepsilon = 0.33\%$ , (b) fringe of coating at  $\varepsilon = 0.65\%$  and (c) center of coating at  $\varepsilon = 1.23\%$ . Typical CFRP failure at  $\varepsilon \geq 1.40\%$  (d).

the total crack surface area can be estimated as:

$$A = 2az_{ct} \quad (4.1)$$

The thickness  $z_{ct}$  of the different copper layers was estimated from scanning electron microscopy cross-sectional images to be  $(11.1 \pm 2.9) \mu\text{m}$ ,  $(32.3 \pm 3.7) \mu\text{m}$  and  $(48.7 \pm 4.7) \mu\text{m}$  for the different nominal coating thicknesses. An image of the fracture surface originating from a tensile test on an according center-notched specimen is shown in figure 4.72-b. The measurement of the crack growth within the copper layer according to equation (4.1) will be used in section 4.6.3 for calculations within a fracture mechanics approach.

The application of the same procedure to estimate nickel crack growth is more difficult, since the cracks propagate below the copper layer. This means their crack length cannot be determined directly via electron microscopy in top view. An investigation of purely nickel coated CFRP-specimens yielded initial crack networks with varying density, which is representatively shown in

#### 4. Experimental results

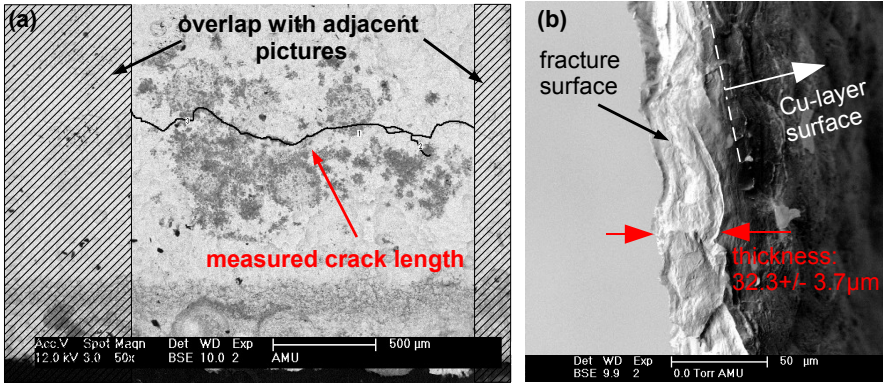


Figure 4.72.: Quantification of copper cracking crack length from top-view scanning electron microscopy images (a) and cross-sectional image of crack surface from 30  $\mu\text{m}$  copper center-notched tensile specimen (b).

figure 4.73-a for one specimen before loading. This crack network grows only slightly during mechanical loading in comparison to the initial crack density (compare fig. 4.73-b). Therefore the crack progress can only be determined very inaccurately from top-view images as in figure 4.73-c, i. e. the standard deviation is unacceptably large.

For measurement of the area of delamination between nickel and copper, the specimens were investigated by scanning ultrasonic microscopy. Using a transducer with 100 MHz frequency and 1.5 mm focal length, selected specimens were examined before and after mechanical loading (see figure 4.74). In order to determine the area of delamination, depth-staggered ultrasonic images with a total penetration depth of 50 ns were used, which correspond to a respective sound propagation path of 240  $\mu\text{m}$  in pure copper. This is much larger than the coatings approximate thickness of 30  $\mu\text{m}$  and therefore reflection signals from the CFRP substrate are expected as well. For delaminated areas the reflection coefficients change from 0.034 % for a Cu-Ni interface to 100 % for Air-Ni interfaces and almost 74 % - 93 % for water-CFRP or water-Ni interfaces. These high intensity reflections can easily be detected within the ultrasonic images. The delamination present after loading at the positions of high reflections could also be verified visually. Here largest delamination is observed at the boundaries of the coating ranging along the coatings x- and y-fringes. In order to quantify the delaminated area correctly, the roving textured

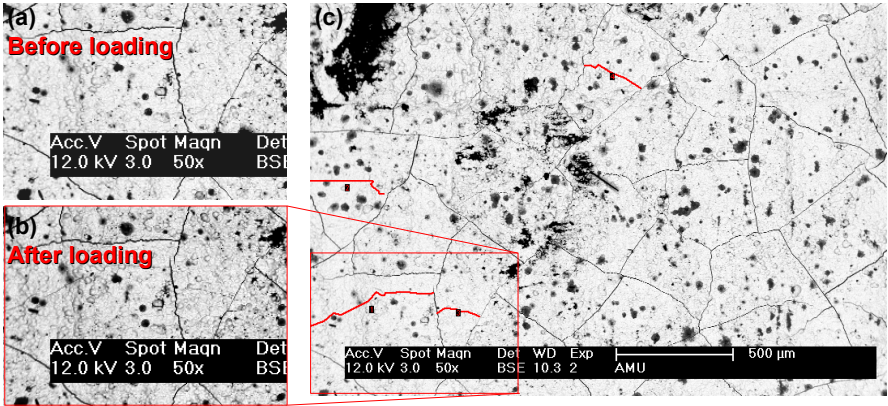


Figure 4.73.: Comparison of crack network observed in nickel coatings before and after loading. The red lines mark the observed difference in crack length.

CFRP-surface and according displacements in the relative depth were taken into account. An example of a delaminated area (marked in white) is shown in figure 4.74. For comparison with the obtained respective acoustic emission signals the delamination area was quantified using the software ImageJ.

### 4.6.2. Pattern recognition approach

In the following, the Coating AE-signals are investigated by the pattern recognition approach previously published in [129] following the method established in [93]. Thus the acoustic emission signals recorded during bending experiments are first localized in one dimension using the linear sensor arrangement shown in figure 4.6 and only signal sources within a distance of 12.5 mm from the specimen center are considered for further investigation. This reflects the position of the coating and is used to exclude transient friction signals that originate from the positions of the lower supports. The sound velocity used for localization was calculated from mutual sensor pulses travel times to be  $(5500 \pm 500)$  m/s. It is well known, that Lamb wave propagation occurs mainly within the CFRP and that the influence of the coating application is negligible. This is consistent with the observation, that the coating thickness has no significant influence on the measured sound velocity within the accuracy of the setup.

In contrast to the measurements on CFRP many “noise” signal types were

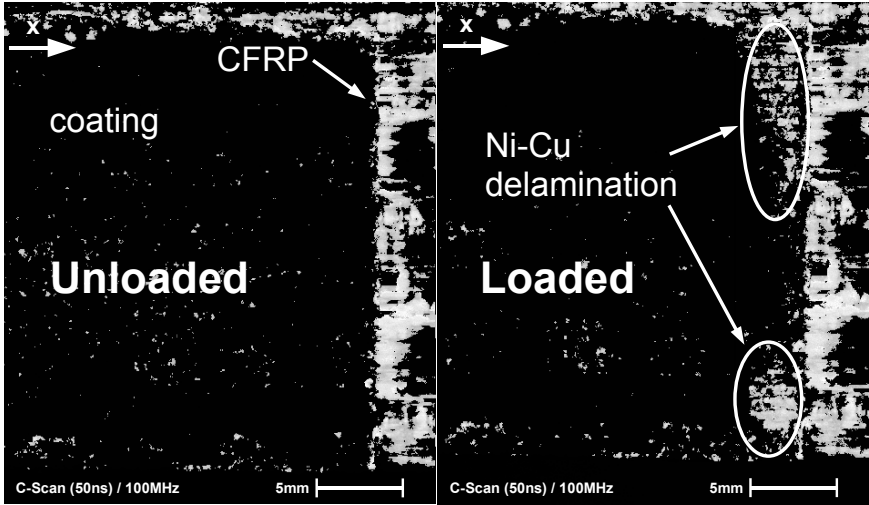


Figure 4.74.: Ultrasonic image of specimen NiCu30 before (left) and after mechanical loading (right).

recorded during coating failure. To remove these, the signals localized were subjected to a “noise” reduction, which consists of a supervised classification algorithm trained to detect signals that could deteriorate clustering results:

- Manual definition of one dataset with “noise” signal types and one dataset with defined signals
- Selection of characteristic signal parameters that allow highest discrimination between noise signals and defined signals
- Training of classification algorithm based on a back-propagating neural network to detect “noise” signal types in any dataset.

To provide higher discrimination efficiency and better algorithm performance, the features were normalized and projected to their principal components axes. The “noise” signal types were excluded from further investigation. From the remaining signals the features given in table 4.9 are extracted as defined in table 2.2. Amplitude, absolute energy and average signal level were used, since the energy of the underlying AE-source is expected to be characteristic in this investigation. In addition, Rise- and Decay-angle were included to take into account the overall shape of the signal. The shape should reflect, at least to



#### 4. Experimental results

some extent, Lamb wave mode ratios which in turn can reflect the underlying source mechanism [76]. Further, four frequency features are used to take into account the slight frequency composition changes, arising from the different source radiation patterns of the different failure types.

After a principal components axis transformation the nine features were projected to the principal axes and normalized to a range from -1 to 1 divided by their standard deviation. Subsequently, the datasets of each specimen are evaluated by an investigation of the *DB* and *TOU* indices in dependence of the number of clusters following reference [93] utilizing the Kohonen LVQ algorithm. This is shown for one representative investigation for a Ni-, NiCu10-, NiCu30- and NiCu50-specimen in figure 4.75.

Feature	Remark
Amplitude [dB]	
Absolute energy [J]	
Average signal level [dB]	
Rise angle [rad]	
Decay angle [rad]	
Partial Power 1 [%]	Frequency range 0 - 180 kHz
Partial Power 2 [%]	Frequency range 180 - 366 kHz
Partial Power 3 [%]	Frequency range 366 - 620 kHz
Partial Power 4 [%]	Frequency range 620 - 1200 kHz

Table 4.9.: Feature combination for clustering of acoustic emission signals from coating failure.

For the nickel coated specimen shown in figure 4.75-a the investigated index values of *DB*, *TOU* and the *DB/TOU*-ratio indicate numerical optimal values at 8 clusters. However, for all investigated Ni specimens very unstable results regarding the number of optimal clusters were found. This is a consequence of the self-similarity of the acoustic emission signals recorded during failure of Ni specimens. In particular no delamination between the Ni-coating and the CFRP substrate was observed microscopically, which means that only one type of failure occurs. Thus it is assumed, that all Coating AE signals recorded during failure of this type of specimens arise from mode-I Ni-cracking.

In contrast, the investigated index values of *DB*, *TOU* and the *DB/TOU*-ratio shown in figures 4.75-b, 4.75-c and 4.75-d indicate numerical optimal partitions for three clusters for the shown NiCu10, NiCu30 and NiCu50 spec-

## 4. Experimental results

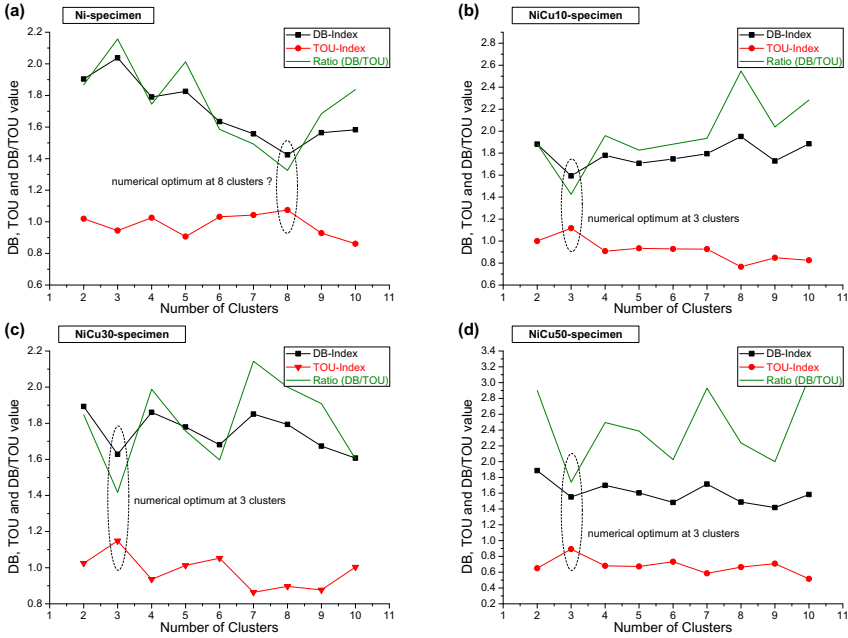


Figure 4.75.: Investigation of  $DB$  and  $TOU$  indices and  $DB/TOU$  ratio in dependence of the number of clusters for one representative Ni (a), NiCu10 (b), NiCu30 (c) and NiCu50 (d) specimen.

imens. In summary, for all NiCu specimens investigated either two or three cluster were found as numerical optimal value for the feature combination from table 4.9. Accordingly either two (copper cracking and nickel cracking) or three (delamination in addition) failure mechanisms were observed microscopically.

Consequently, the next step is the assignment of the different signal types to the respective failure mechanisms. On one hand this is based on the AE-source location, on the other hand this can be concluded from the signals average frequency spectra.

### Source location

An example of the localized positions of the acoustic emission sources of the different clusters is shown for one representative NiCu50 specimen in figure 4.76. Preliminary to the following discussion, the associated failure mechanisms are already marked in figure 4.76. The localized positions of the different clusters

#### 4. Experimental results

coincidence with the observed positions of the respective failure mechanisms as discussed in section 4.6.1.

The signals attributed to Ni-cracking typically occur at the fringe of the coating, and grow slightly in their density at these positions in dependence of loading, which is reflected well in the microscopic observations.

Signals correlated with Ni-Cu delamination typically show broad distribution in the coated area. Since Ni-Cu delamination was observed to occur dominantly at the boundary of the coating (x-fringe and y-fringe) the localized source positions matches these observations. In figure 4.76, signals contributing to these class show localized position even outside the marked coated range. In comparison to the density of signals within the coated area these are almost negligible. These can originate from false localized source positions or arise from delamination of copper surface particles, which were found randomly distributed outside the coated area. These surface particles are typical remainders of the electroplating process.

The last type of signals typically localizes within the center of the coating or at the fringes of the coating. In each case, the localized source positions coincidence with the microscopically observed positions of copper cracks.

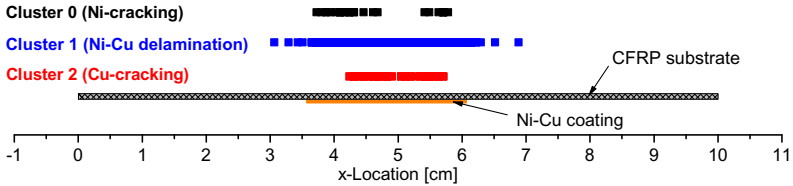


Figure 4.76.: Comparison of AE signal x-location patterns versus cluster number for one representative NiCu50 specimen including schematic representation of sample geometry.

#### Average frequency spectra

The average frequency spectra of each signal class for one representative Ni, NiCu10, NiCu30 and NiCu50 specimen are shown in figure 4.77. Again the following assignment to the respective failure mechanism is preliminary marked in figure 4.77. As demonstrated by the comparative simulations for nickel cracking, copper cracking and nickel-copper delamination in section 3.4.1, little changes in the frequency spectra of the different failure mechanisms are

#### 4. Experimental results

expected. Instead the overall spectrum is dominated by the specimen geometry. As concluded from the investigations before, no other failure types besides mode-I Ni-cracking is observed in purely nickel coated specimens. Thus only one spectrum characteristic for Ni-cracking is shown in figure 4.77-a. For the remaining specimens in figures 4.77-b, 4.77-c and 4.77-d the distinction is made between Ni-cracking, Cu-cracking and Ni-Cu delamination. In the present case the difference of spectral weight between frequencies above and below 400 kHz can indicate a different direction of sound radiation. Here, in-plane crack surface movement typically results in higher  $S_0$ -mode contributions than out-of-plane movement. Consequently, Ni-cracking and especially Cu-cracking (both in-plane) show stronger contributions at frequencies above 400 kHz than Ni-Cu delamination (out-of-plane).

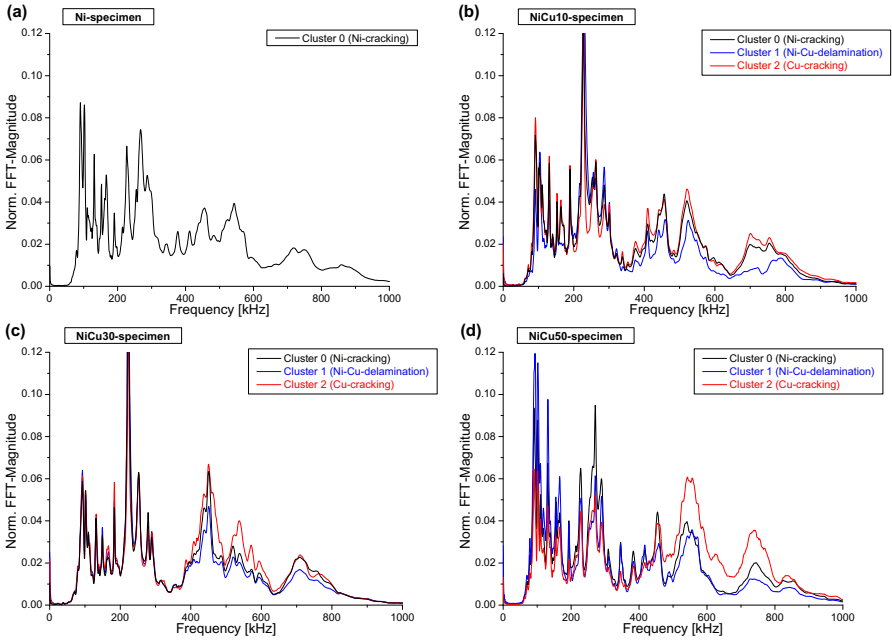


Figure 4.77.: Average frequency spectra of the different acoustic emission signals types for one representative (a) Ni, (b) NiCu10, (c) NiCu30 and (d) NiCu50-specimen.

In particular, for Cu-cracking the contributions to the  $S_0$ -mode seem to increase with an increasing Cu-coating thickness. As shown in figure 4.78, this increase is also observed within the simulations of copper cracking with the

## 4. Experimental results

respective coating thicknesses using the model settings described in section 3.4.1. Based on the considerations in section 3.4.3 this behavior is explained by the anisotropic elastic properties of the CFRP substrate which dominates the signal propagation process. Here the increased coating thickness causes a movement of a larger crack surface area in the in-plane direction. This directly translates into a stronger excitation of the  $S_0$ -mode causing higher frequency contributions at 700 kHz.

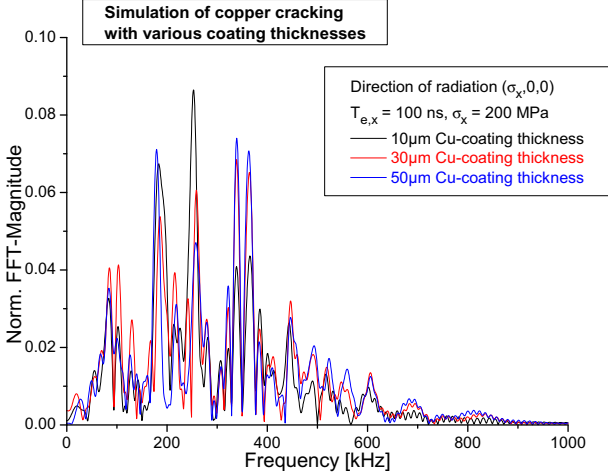


Figure 4.78.: Comparison of simulated frequency spectra of copper-cracking with constant fracture strength  $\sigma_x = 200$  MPa and constant excitation time  $T_{e,x} = 100$  ns using the reduced sensor model.

From the above findings it is thus concluded, that the three signal classes obtained from pattern recognition can be attributed to the three failure mechanisms Ni-cracking, Cu-cracking and Ni-Cu delamination based on their localized source positions and their average frequency spectra.

### 4.6.3. Comparison with fracture mechanics

Based upon equation (3.10) presented in section 3.4.3 one expects a direct proportionality between the microscopic strain energy release and the acoustic emission signal energy for stable crack growth. This linear elastic fracture mechanics approach was already published in [129] and is shortly reviewed in the following. In general, the correlation given in equation (3.10) is fulfilled for each

#### 4. Experimental results

distinct type of failure under the assumption, that the crack volume increment  $\Delta V$  is comparable for each crack propagation step. If these assumptions are fulfilled, this should result in distinct proportionality constants  $\beta$  for nickel cracking, copper cracking and nickel-copper delamination. To calculate  $\beta$ , equation (3.10) was integrated over the duration of the experiment. Therefore it is possible to compare the micromechanical energy calculated from the observed damage after unloading of the specimen with the accumulated acoustic emission energy:

- The integral of  $\partial W_{AE}/\partial t$  is given by summation of the measured signals acoustic emission energies
- The micromechanical strain energy release  $\partial \Omega/\partial t$  is calculated from the measured fracture toughness  $G_c$  and the microscopically measured crack surface  $A$

In the following this investigation was only conducted for copper cracking and nickel-copper delamination, since the error ranges for the measured values of nickel crack growth were unacceptably large. In addition only the NiCu10 and NiCu30 specimens were investigated, since the number of NiCu50 and CuCu50 specimens provided was not sufficient to conduct all of the presented investigations<sup>12</sup>. The respective fracture toughness values were determined from tensile tests on center-notched copper coatings and peeling tests on nickel-copper coatings.

##### Measurement of copper coating fracture toughness

For calculation of  $G_{Ic}$  the critical stress-intensity factor  $K_{Ic}$  of the copper coatings was measured. The coatings were lifted off their substrates and a centre-notched specimen as shown in figure 2.8 was prepared. This provides a suitable geometry according to numerical simulations and measurements on Ni-based metal foils [26]. Assuming plane stress conditions, the fracture toughness  $G_{Ic}$  can subsequently be calculated according to equation (2.5) using a Young's modulus for the copper coatings of 120 GPa. Figure 4.79 shows a set of representative curves used for determination of the critical load  $F_c$  from the intersection of the load-displacement curve and the 5%-secant of the linear-elastic range analogous to ASTM-E399 [173]. As described in section 2.1.3 the geometric dimensions of the specimens entering the calculation are foil-thickness  $z_{ct}$ , width  $2x_{ct}$  and pre-crack length  $2a$ . Using equations (2.7), (2.8)

---

<sup>12</sup>The NiCu50 and CuCu50 specimens were investigated previously to the other coating types.

#### 4. Experimental results

and (2.5) this finally yields a fracture toughness value of  $(7460 \pm 2932) \text{ J/m}^2$  for  $10 \text{ }\mu\text{m}$  Cu-coatings and  $(5412 \pm 2376) \text{ J/m}^2$  for  $30 \text{ }\mu\text{m}$  Cu-coatings, respectively.

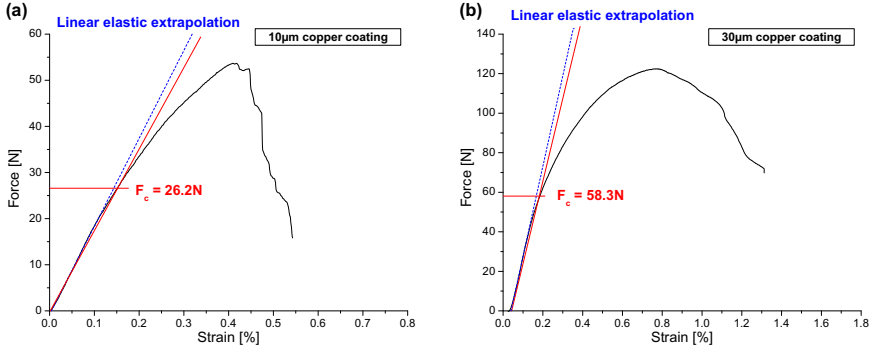


Figure 4.79.: Typical load-strain curves measured for  $10 \text{ }\mu\text{m}$  copper coatings (a) and  $30 \text{ }\mu\text{m}$  copper coatings (b) used for determination of the mode-I fracture toughness value.

The fracture toughness values reported on copper coatings with similar thickness show scattering in their order of magnitude, depending on treatment and crystal structure [27, 28]. While [27] and [28] report an increase in  $G_{Ic}$  with coating thickness in ranges below  $300 \text{ }\mu\text{m}$ , a decrease with increasing thickness was observed for the coatings investigated within this thesis. In general, the thickness dependence of  $G_{Ic}$  is attributed to boundary effects, which can change the relative amount of energy dissipation at the crack tip. This is due to the fact, that the stress-fields are different in the boundary (surface) region compared to the bulk and that the surface microstructure can lead to an increased strain concentration at the crack tip, which reduces the macroscopic fracture toughness. With decreasing coating thickness boundary effects become more important. To explain the observed decrease in fracture toughness with increasing thickness in the present case, the shape of the crack tips was analyzed using scanning electron microscopy. Figures 4.80-a and 4.80-b show SEM-images in top-view of crack patterns of the two different coatings. In the  $30 \text{ }\mu\text{m}$  Cu-coatings the crack propagates orthogonal to the loading axis with a very sharp crack tip opening displacement. In contrast, in the  $10 \text{ }\mu\text{m}$  Cu-coatings large branching is observed ahead of the crack tip and in addition, the crack orientation angle changes during tensile loading, driven by the crack growth along flaws. Both effects increase the total amount of energy necessary for crack propagation and thus the fracture toughness. The different appearance of the cracks in the two coatings could be attributed to

#### 4. Experimental results

the growing influence of surface inhomogeneities for the thinner coating. Such surface inhomogeneities are expected to play only a minor role in metal foils as investigated by [27], but are more important in the electroplated coatings applied on rough substrates as in the current investigation.

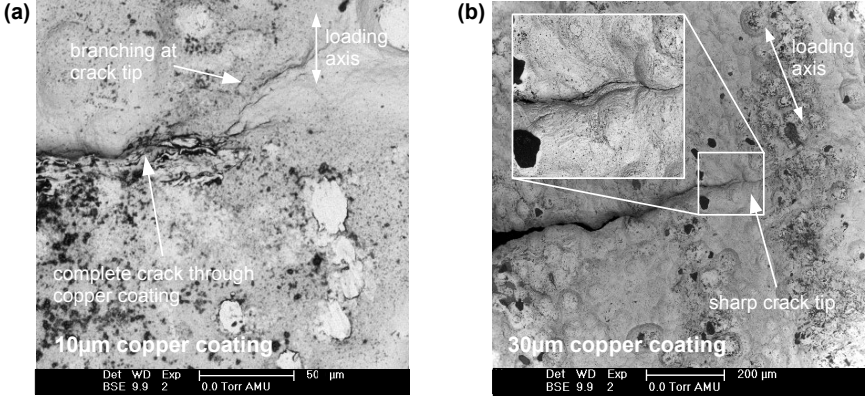


Figure 4.80.: Scanning electron microscopy pictures (top-view) of the crack tip in 10  $\mu\text{m}$  copper coating showing branching of crack tip (a) and similar picture of 30  $\mu\text{m}$  copper coating with sharp crack tip (b).

Another reason for a change in fracture toughness can be differences in the tensile or compressive stress level present within the coating. Such stress should be reflected in the peak-shape and -position of X-Ray diffraction patterns. Eight coatings were analyzed by X-Ray diffraction applied on the CFRP and again after pull-off as exemplarily shown in figure 4.81-a for a NiCu10 specimen. The diffraction patterns of the respective coating type exhibit a peak shift before and after pull-off, characteristic for tensile<sup>13</sup> macro-stress calculated from the peak positions before  $2\theta_{\text{before}}$  and after  $2\theta_{\text{after}}$  pull-off as:

$$\sigma_{ct} = E \left( 1 - \frac{\sin(2\theta_{\text{before}})}{\sin(2\theta_{\text{after}})} \right) \quad (4.2)$$

The calculated value of  $(151 \pm 19)$  MPa is the same in both coatings within the margin of error (see peak-shifts in figure 4.81-b). Thus it is concluded that a pre-existent macro-stress is not responsible for the differences in the observed fracture toughness values.

<sup>13</sup>In [129] this was mistakenly reported as “compressive” macro-stress. However, the respective conclusion does not change, since both coatings show equal stress levels.



## 4. Experimental results

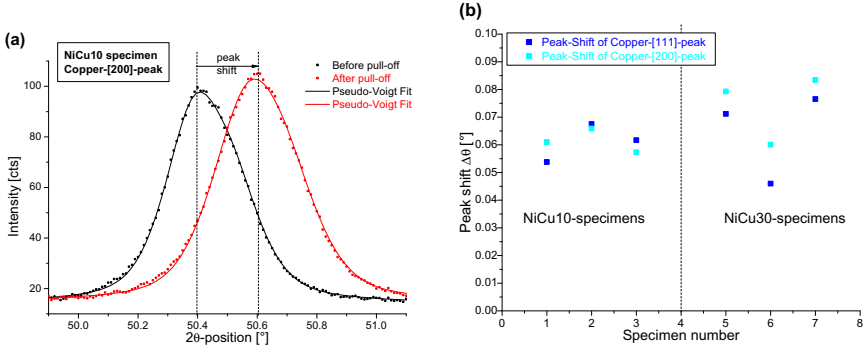


Figure 4.81.: Representative X-Ray diffraction pattern of Cu-[200]-peak before and after coating pull-off (a) and comparison of peak shifts for NiCu10 and NiCu30 specimens (b).

### Measurement of nickel-copper interfacial fracture toughness

To obtain the strain energy release rate for mode-I/II delamination, peeling tests according to ASTM B533-85 were conducted, although the geometry of the specimens does not completely correspond to ASTM B533-85 [170]. As stated in [30], the influence of plastic deformation at the interfacial crack tip is negligible, if the interfacial tensile adhesion is much smaller than the yield strength of the coating material. Therefore, the calculated peeling strength is assumed to reflect the interfacial fracture toughness value  $G_{I/IIc}$ . The peeling test was conducted by pulling at a preliminary peeled edge and measurement of the necessary force. At the beginning of the peeling test, the load sharply increases until crack growth is initiated and reaches a constant peeling force during stable crack propagation. At the end of the measurement, the detected force increases drastically. This is most likely caused by inhomogeneities of the coating at its fringes. Therefore the average peeling force was calculated between the onset of constant peeling strength and the sharp increase at the end as indicated in figure 4.82. The values for  $G_{I/IIc}$  were calculated from the recorded mean peeling force divided by the coating width to be  $(202 \pm 51) \text{ J/m}^2$  for  $10 \text{ } \mu\text{m}$  coatings and  $(385 \pm 15) \text{ J/m}^2$  for  $30 \text{ } \mu\text{m}$  coatings.

### Comparison with acoustic emission energy

In combination with the quantification of the crack surface area for copper cracking and Ni-Cu delamination as described in section 4.6.1 the total microscopic strain energy release for copper cracking and nickel-copper delamination

#### 4. Experimental results

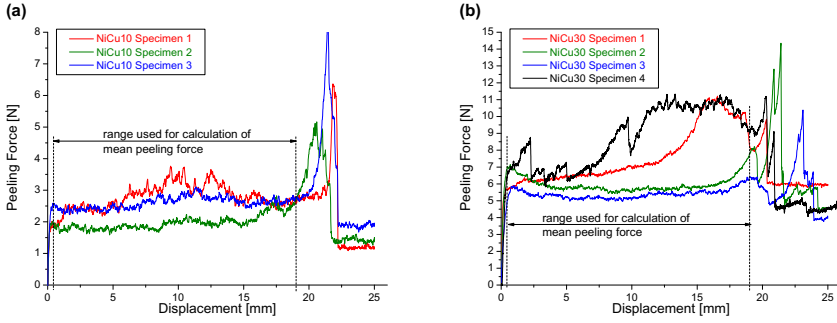


Figure 4.82.: Typical force-displacement curves used for measurement of interfacial fracture toughness values  $G_{I/IIc}$  for NiCu10 (a) and NiCu30 specimens (b).

at the end of the experiment is calculated and compared to the measured acoustic emission energy of the associated signals. This yields the proportionality constant  $\beta$  as given in equation (3.10), which is plotted in figure 4.83 for all specimens investigated.

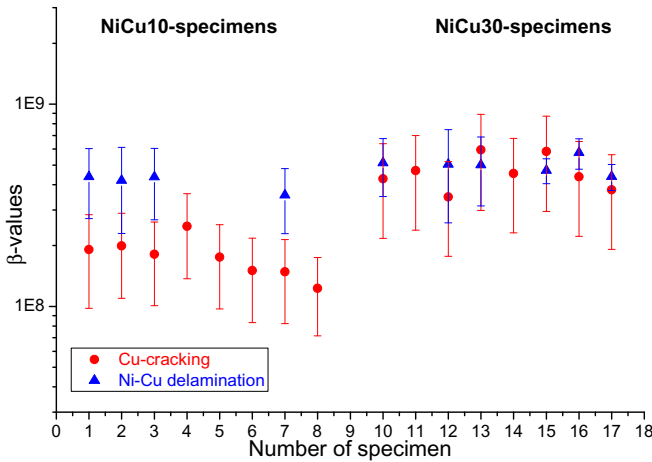


Figure 4.83.: Comparison of proportionality factors  $\beta$  for Cu-cracking and Ni-Cu delamination of all specimens investigated.

#### 4. Experimental results

In the case of delamination failure, the error in the determination of  $\beta$  is large, since the quantification of the delaminated area is error-prone. In addition, the standard deviation of the  $G_{I/IIc}$ -value derived from peeling tests also contributes to the error in  $\beta$ . In the case of copper cracking failure, large errors in  $\beta$  originate from the size of standard deviations in the experimentally determined  $G_{Ic}$  values. These large standard deviations are attributed to inhomogeneous coatings on one hand and the uncertainty in the range of linear elastic behavior which defines the critical load  $F_c$  necessary for the calculation of  $G_{Ic}$  on the other hand (see figure 4.79). In comparison, the inaccuracy of crack length determination via electron microscopy is negligible.

For delamination failure, the proportionality between calculated micro-mechanical energy and accumulated acoustic emission energy is remarkably good for both coating thicknesses (see figure 4.83). This becomes especially clear, comparing the changes of acoustic emission energy contributions to delamination between the different specimens (see table 4.10). Here, changes of more than one order of magnitude are observed. Accordingly the delaminated area measured via scanning acoustic microscopy changes, which results in a constant value for  $\beta$  within the experimental error.

In contrast, the  $\beta$ -values for copper cracking failure agree very well only within one coating thickness, but decrease by an approximate factor of three going from 30  $\mu\text{m}$  Cu-coating to 10  $\mu\text{m}$  Cu-coating thickness. This is consistent with the theoretical descriptions of acoustic emission sources presented in section 2.2.2, which all assume that in case of a crack-through process, the emitted acoustic emission energy during fracture geometrically only depends on the crack length increment. Since the micromechanical fracture energy is proportional to the newly formed crack surface, the proportionality constant between AE-energy and micro-mechanical energy changes as a function of coating thickness. As discussed in section 3.4.3 this direct correlation is only fulfilled, if the strain energy release per crack increment is almost constant. Since the measured proportionality constants  $\beta$  show constant values for each coating type, this seems to be fulfilled for the present case. In addition, the drop by an approximate factor of three in the mean  $\beta$ -values for NiCu30 and NiCu10 reflects the expected change of the crack surface area based on the different coating thicknesses.

#### 4. Experimental results

Failure type	Specimen	AE-energy [ $10^{-13}$ J]	Crack area [mm <sup>2</sup> ]	G-value [J/m <sup>2</sup> ]	$\beta$ [ $10^{-8}$ ]
Cu-cracking	NiCu10-1	3.5	0.009 $\pm$ 0.001	7460 $\pm$ 2932	1.91 $\pm$ 0.19
	NiCu10-2	32.0	0.085 $\pm$ 0.004	7460 $\pm$ 2932	1.99 $\pm$ 0.89
	NiCu10-3	41.0	0.099 $\pm$ 0.005	7460 $\pm$ 2932	1.81 $\pm$ 0.80
	NiCu10-4	32.0	0.107 $\pm$ 0.005	7460 $\pm$ 2932	2.49 $\pm$ 1.12
	NiCu10-5	67.5	0.159 $\pm$ 0.008	7460 $\pm$ 2932	1.75 $\pm$ 0.78
	NiCu10-6	51.5	0.104 $\pm$ 0.005	7460 $\pm$ 2932	1.50 $\pm$ 0.67
	NiCu10-7	100.0	0.199 $\pm$ 0.010	7460 $\pm$ 2932	1.48 $\pm$ 0.66
	NiCu10-8	268.0	0.441 $\pm$ 0.011	7460 $\pm$ 2932	1.23 $\pm$ 0.52
	NiCu30-1	47.4	0.374 $\pm$ 0.019	5412 $\pm$ 2376	4.27 $\pm$ 2.10
	NiCu30-2	46.0	0.398 $\pm$ 0.020	5412 $\pm$ 2376	4.69 $\pm$ 2.31
	NiCu30-3	55.7	0.358 $\pm$ 0.018	5412 $\pm$ 2376	3.48 $\pm$ 1.71
	NiCu30-4	23.6	0.259 $\pm$ 0.013	5412 $\pm$ 2376	5.94 $\pm$ 2.96
	NiCu30-5	104.0	0.873 $\pm$ 0.044	5412 $\pm$ 2376	4.54 $\pm$ 2.23
	NiCu30-6	37.3	0.402 $\pm$ 0.020	5412 $\pm$ 2376	5.83 $\pm$ 2.88
	NiCu30-7	49.0	0.396 $\pm$ 0.020	5412 $\pm$ 2376	4.38 $\pm$ 2.16
	NiCu30-8	68.4	0.477 $\pm$ 0.024	5412 $\pm$ 2376	3.77 $\pm$ 1.86
Ni-Cu delamination	NiCu10-1	39.0	8.4 $\pm$ 1.1	221.3 $\pm$ 22.1	4.37 $\pm$ 1.65
	NiCu10-2	73.0	15.2 $\pm$ 2.9	221.3 $\pm$ 22.1	4.20 $\pm$ 1.91
	NiCu10-3	177.0	38.2 $\pm$ 4.8	221.3 $\pm$ 22.1	4.36 $\pm$ 1.68
	NiCu10-7	1260.0	221.3 $\pm$ 22.1	221.3 $\pm$ 22.1	3.55 $\pm$ 1.26
	NiCu30-1	27.5	3.66 $\pm$ 0.9	385 $\pm$ 15	5.13 $\pm$ 1.63
	NiCu30-3	1.3	0.2 $\pm$ 0.1	385 $\pm$ 15	5.04 $\pm$ 2.45
	NiCu30-4	23.6	3.1 $\pm$ 0.9	385 $\pm$ 15	5.01 $\pm$ 1.87
	NiCu30-6	87.6	10.7 $\pm$ 1.1	385 $\pm$ 15	4.71 $\pm$ 0.66
	NiCu30-7	5.9	0.9 $\pm$ 0.1	385 $\pm$ 15	5.76 $\pm$ 0.99
	NiCu30-8	24.9	2.8 $\pm$ 0.3	385 $\pm$ 15	4.38 $\pm$ 0.64

Table 4.10.: Quantification of the accumulated acoustic emission energies, crack surface areas and the respective fracture toughness value for Cu-cracking and Ni-Cu delamination of all specimens investigated.

#### 4.6.4. Discussion of different coating types

As shown in figure 4.84 in a comparison of the recorded acoustic emission energies, the coating systems investigated show drastic different acoustic emission energy release when subjected to the same loading conditions. As presented in the previous section this is correlated with the respective micromechanical energy release and is discussed in its consequence on the coatings loading capability in the following.

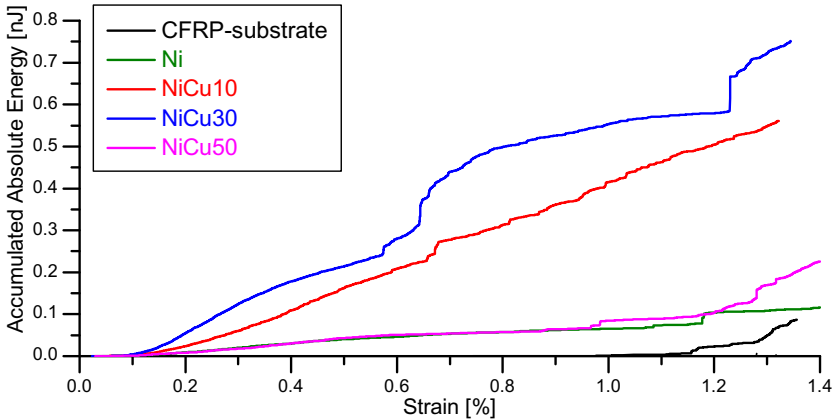


Figure 4.84.: Comparison of recorded acoustic emission energies for one representative specimen of Ni, NiCu10, NiCu30 and NiCu50 coating systems. For comparison the accumulated acoustic emission energy of a CFRP specimen is shown as well.

For pure Ni-coatings, microscopic observations indicate solely mode-I crack propagation and no delamination at the interface between nickel and CFRP. As discussed before this is also reflected in the pattern recognition approach since no feature combination allows reproducible separation of the recorded signals [186]. In addition all Ni specimens investigated show systematic correlation in their localization patterns along the x-axis, their acoustic emission onset and their mean frequency spectra. In particular, the minor crack surface increase as shown in figure 4.73 is also reflected in the acoustic emission energies of figure 4.84. Due to the lower fracture toughness values of nickel and the marginal crack surface increase the accumulated acoustic emission energy is typically smaller for nickel than for copper crack growth.

In contrast, the pattern recognition approach applied to acoustic emission

#### 4. Experimental results

signals from NiCu10 specimens yields either two or three distinct types of signals. As discussed in section 4.6.2 these are attributed to the occurrence of nickel cracks, copper cracks and occasionally Ni-Cu delamination. This correlates well with the microscopic investigations of the respective specimens. For specimens with two classes no delamination is observed. Specimens with three identified signal types show copper cracking, nickel cracking and delamination in addition<sup>14</sup>. The lack of copper delamination for some of the specimens is attributed to deviations of the interfacial strength between nickel and copper coating close to the fringe, which inhibits initiation of delamination. Moreover, the localization pattern of the class associated with nickel cracking of all specimens shows great resemblance to those observed for pure nickel coatings.

The acoustic emission energy release of NiCu30 specimens is typically higher than those of all other coating systems investigated. For these, the pattern recognition method indicates the occurrence of three different types of failure, again attributed to nickel cracks, Ni-Cu delamination and copper cracks. In contrast to the NiCu10 specimens the amount of signals attributed to delamination is decreasing, while copper cracks are observed more often. This strictly correlates with the decrease of the delaminated area quantified by scanning acoustic microscopy. This change of contributions is attributed to the mean increase in interfacial fracture toughness from  $(202 \pm 51)$  J/m<sup>2</sup> for NiCu10 and  $(385 \pm 15)$  J/m<sup>2</sup> for NiCu30 specimens. Consequently, crack growth within the copper coating is energetically more preferential than for the NiCu10 specimens and causes even higher acoustic emission energy release.

The pattern recognition results for NiCu50 specimens indicate three distinct classes comparable in their localization patterns to those of nickel cracking, copper cracking and Ni-Cu delamination observed in NiCu10 and NiCu30 specimens. In contrast to the other coated specimens a strong reduction in the recorded acoustic emission energies is found for the NiCu50 specimens. Same as for the NiCu30 specimens, the relative contributions to the signal class correlated with delamination decreases again. Similar the contribution of copper cracking rises compared to the NiCu30 specimens. Nickel cracking shows almost comparable contributions to those observed for the other coating types. Same as for the NiCu30 specimens this is attributed to the further increase of interfacial fracture toughness to  $(825 \pm 113)$  J/m<sup>2</sup>. The reduced total acoustic emission energy in turn indicates an overall higher loading capacity of the NiCu50 coatings.

---

<sup>14</sup>Another typical failure behaviour of NiCu10 specimens is discussed in [186].

#### 4. Experimental results

Since none of the above discussed coating systems yielded a load capacity comparable in any way to that of pure CFRP other types of coating compositions were investigated as well. In particular, the early onset of nickel cracks is responsible for failure initiation of the coating system since it causes an early onset of delamination between the nickel and copper layer as discussed in section 4.6.1. To avoid this failure initiation the nickel coating was exchanged by a comparable copper coating to investigate its influence. A comparison of the strain dependency of the recorded acoustic emission energy of a NiCu50 specimen with a CuCu50 specimen is shown in figure 4.85. Clearly, the CuCu50 specimen shows a drastically reduced number of signals below  $\varepsilon = 0.7 \%$  with lower mean acoustic emission energies than for the NiCu50 specimen. The recorded signals of the CuCu50 specimen do not even correspond to similar failure types as observed in NiCu specimens. Instead the minor number of signals below  $\varepsilon = 0.7 \%$  are attributed to chipping of surface particles. This also explains the sporadically appearance of these signals and their large distribution in the localized source positions. In addition, no failure in form of copper cracking or delamination was observed up to strain levels of  $\varepsilon < 0.7 \%$ . For higher strain levels, failure in the CFRP also cause crack initiation in the coating.

Thus the load capacity of the CuCu50 coating system is expected to be above  $\varepsilon = 0.7 \%$ . Compared to those of the NiCu coatings, these superior mechanical properties are caused by the high interfacial fracture toughness expected for the Cu-Cu coatings. While the initial layer in both coating systems shows very high adhesion to the CFRP substrate, the governing factor for the coatings load capacity is the onset of failure at the interface between the initial layer and the subsequent electroplated layer. Here nickel layers initialize failure at lower loads than copper layers, due to their lower mode-I fracture toughness. The resulting stress at the Ni-Cu interface is than reduced by delamination or crack propagation into the copper layer. Thus functional failure of the NiCu coating types is observed earlier than for the CuCu coating.

#### 4. Experimental results

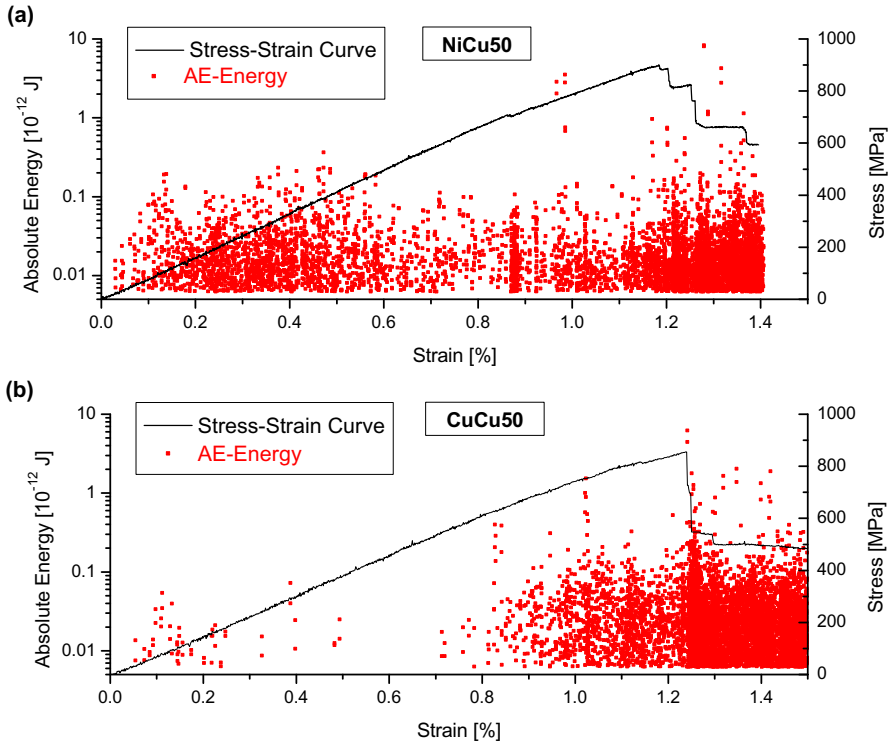


Figure 4.85.: Comparison of recorded acoustic emission energy in one representative NiCu50 (a) and one representative CuCu50 specimen (b) in dependence of strain level. For comparison the respective stress-strain curve is given as well.



## 5. Summary and Discussion

In this section the results presented within this thesis are summarized and discussed with a focus on three different topics. Firstly, the results of finite element simulations are summarized and compared to predictions of analytical theories and experimental results. Secondly, the proposed pattern recognition method is critically reviewed and their results are discussed regarding the correlations to microscopic observations and fracture mechanics results. Finally the experimental results are reviewed under material scientific scope and discussed with respect to their relevance regarding failure prediction, failure analysis and material optimization.

### 5.1. Finite element simulation

From the view-point of finite element simulations, three basic components are required to model the complete acoustic emission measurement. These are the acoustic emission source, the signal propagation and the detection of the signal by a sensor. Only if all three components describe the inherent physical processes adequately, the model can be used to analyze the influence of different failure mechanism, different geometry of the specimen and variations in the material properties. Ultimately, only a valid model allows a direct correlation between simulated and experimental acoustic emission signals.

The advantage of the source model established within this thesis in comparison to previous acoustic emission source descriptions [37–39, 43–45] consists of the fact, that it takes into account the finite extent of acoustic emission sources and the inhomogeneous elastic properties in its vicinity. The driving mechanism of the source model is solely based on an initial deflection of the crack surface, which is based on considerations of fracture mechanics [34] and seismology [35]. In particular, no driving oscillatory force was used as source mechanism. Instead, the resulting crack surface oscillations in the source model are solely the result of the crack geometry and the elastic response of the material to the initial deflection. These oscillations are damped due to the energy propagation away from the source into the adjacent medium. Consequently, a quicker decay of the oscillation is observed for cracking media exhibiting a higher longitudinal sound velocity. A comparison of the simulated crack surface

## 5. Summary and Discussion

movement and the various analytical descriptions [37, 38, 45] shows good agreement for the investigated materials with high sound velocities (copper, nickel, carbon fiber). In contrast, for materials with low sound velocities (resin) a less damped crack surface oscillation was found, which is not adequately described within the current analytical models. For the current investigation of CFRP the respective differences of the source behavior play a key role in the source identification process of carbon fiber breakage and matrix cracking. Here the differently damped oscillations result in characteristically different excitations of Lamb wave modes, which can be used for the respective identification. In addition, the response of the model to an increase in initial excitation time is expressed by a shift of the frequency weight to lower frequencies. This effect is qualitatively comparable to analytical solutions obtained by M. Giordano et al. [45] and is taken into account in the simulations by material and failure specific excitation times.

In the investigated planar specimen geometries the proposed source model excites Lamb waves with distinct symmetric and antisymmetric modes that propagate within the model specimen. The modeling and finite element simulation of such Lamb wave propagation within isotropic and anisotropic media is already well established in literature [152–154, 187]. In the present simulations the velocities of the Lamb waves excited by the acoustic emission source compare well to the calculated results based on plate-wave theory [48].

To compare the simulated acoustic emission signals to experimental signals, the influence of the used acoustic emission sensor has to be taken into account, since the sensor significantly alters the shape and frequency content of the detected signals [1, 62, 67, 155]. Within this thesis a three dimensional model of the experimentally used sensor of type WD including piezoelectric conversion was established. The simulated frequency dependent sensitivity of this sensor model is consistent with experimental data obtained in a setup for reciprocity calibration according to [155]. In addition, the shape and intensity of simulated signals resulting from pencil lead fracture tests agree well to respective experimental signals. Due to the large computational resources required for this full sensor model, reasonable reduction steps were introduced to yield a computationally more efficient sensor model. It was demonstrated, that the aperture of the sensor's PZT-elements is the dominating parameter for the shape and frequency content of the simulated sensor signal. This is in accordance with reports from L. Goujon et al. [67]. In addition, they found a distinct dependency of the sensor response on the material of the used calibration block during reciprocity calibration. This effect was also observed in the current simulations for different elastic properties assigned to the calibration block. Consequently, a direct application of experimental sensor calibration curves to signal deconvolution is limited to investigations on materials identical to

the respective calibration block. This is of great disadvantage for materials like CFRP, since it is not feasible to provide the typical volumetric calibration block geometries required for sensor calibration. With the current approach of sensor simulation it is possible to obtain the simulated frequency dependent sensitivity curve of any calibration block material.

Within the used planar model specimen geometries simulations of the various source mechanisms result in excitations exhibiting different ratios of  $S_0$ - and  $A_0$ -modes. The interpretation of the various Lamb wave modes to identify particular failure mechanisms was introduced by W. Prosser and M. Gorman [56,143,144] and was also previously investigated by finite element simulations [76,146]. Using the proposed source model it was demonstrated, that solely the different elastic properties of the cracking medium can result in distinctly different ratios of excited Lamb wave modes. The current simulations show that a distinction of matrix-cracking and fiber-breakage at the same source position is possible based on different intensity ratios of symmetric and antisymmetric Lamb wave modes. A high intensity of antisymmetric modes corresponds to a strong frequency contribution in the lower frequency range, while high intensity of symmetric modes corresponds to contributions in the higher frequency range. These characteristic differences in the frequency distributions for matrix cracking (lower frequencies) and fiber breakage (higher frequencies) are expected by various authors based on their experimental observations [4–8]. In addition to frequency spectra dominated by either the  $S_0$ - or the  $A_0$ -mode, frequency spectra with significant contributions of both modes are often observed experimentally. Within this thesis it was demonstrated, that such spectra can be simulated best by simultaneous excitation in fiber axis direction (x) and perpendicular to the fiber axis direction (y,z). Based on fracture mechanics considerations this type of displacement is expected in the case of failure processes with significant interaction between fiber and matrix. In this context the loss of contact between fiber and matrix (y,z-displacement) is expected to cause a relaxation of the fiber (x-displacement). This type of failure can be interpreted as either fiber-matrix debonding or fiber pull-out. Here the increase of the ratio of the displacement amplitudes  $d_x:(d_y,d_z)$  results in a systematic shift of the frequency weight to higher frequencies, which is correlated to a stronger excitation of the  $S_0$ -mode. This type of frequency shift was experimentally observed in specimens as a function of the apparent interlaminar shear strength (see section 4.5). Thus it is assumed, that an increase of  $d_x:(d_y,d_z)$  is correlated to an increase of adhesive strength between fiber and matrix.

As indicated by equation (2.57) the final appearance of the detected acoustic emission signal is not only dependent on the source mechanism, but also on the propagation medium. Within this thesis the influence of the propaga-

## 5. Summary and Discussion

tion medium was investigated by comparing simulation results of different specimen geometries. Although the different geometries significantly influence the simulated acoustic emission signal, a distinct dependency of the signal characteristics on the source mechanism is still retained. In general, an increase in propagation length results in stronger dispersion of the Lamb waves with different attenuation levels of  $S_0$ - and  $A_0$ -mode [56, 159, 168, 169]. This consequently alters the frequency spectra and can even result in false assignment of signals to failure mechanisms, when detected for propagation distances above 40 - 50 mm. Similarly, the position of the acoustic emission source within the specimen geometry is very important for the formation process of Lamb waves. Variation of the source position towards one of the specimens surfaces results in a stronger excitation of the  $A_0$ -mode. This is caused by the asymmetric source position with respect to the specimen's surfaces. This break of symmetry in turn is required for strong excitation of  $A_0$ -modes and agrees with previously reported results of simulations using isotropic propagation media [76]. It is worth to notice, that the proposed source model for matrix cracking results in significant excitation of lower frequencies even at symmetric positions and thus can be used to identify this particular failure mechanism at these positions. In summary, for the investigated specimen geometries the frequency spectra obtained by simulation of failure mechanisms in CFRP are characteristic for by the type of microscopic failure for all source positions and can be classified accordingly by appropriate frequency based parameters.

This does not apply to the different simulated failure mechanisms occurring in coatings on CFRP substrates. Here the source position at the substrates surface results in strong similarities of the simulated signals for mode-I nickel cracking and mode-I copper cracking. Slight differences in the frequency spectra are only found for the simulated signals of nickel-copper delamination, which is due to the different excitation direction of delamination (out-of-plane) and mode-I cracking (in-plane). This emphasizes the importance of such simulations to assess suitable parameters for identification of the different failure types. In the case of coatings, the drastic differences in the observed energy content thus suggests to use a combination of frequency and energy parameters to successfully identify all three failure types.

Within the current simulations, for all materials and for all failure mechanisms a linear dependency between acoustic emission signal amplitude and crack volume increment was found. This is in agreement with the generalized theory of acoustic emission [38, 39]. Variations in the crack volume increment can either result from a variation in the local microscopic fracture toughness of the material or from microscopic changes of loading conditions. Thus, measurement of acoustic emission amplitudes will sensitively depend on both. Consequently, a direct interpretation of the acoustic emission amplitude as measure of the

microscopic crack progress is only valid, if either the fracture toughness or the microscopic loading conditions are constant. In the simulations a correlation between the microscopic strain energy release  $\Omega$  during crack progress and the detected acoustic emission signal energy  $W_{AE}$  is observed. For isotropic media one finds  $\Omega = \beta W_{AE}$  with constant proportionality factor  $\beta$ . In contrast, for anisotropic media the proportionality factor  $\beta$  depends significantly on the geometry of the acoustic emission source. This dependency is caused by the energetic inequality of the directions of the crack surface displacement within anisotropic media. Consequently, different strain energy releases can result from equal crack volume increments due to the anisotropic elasticity. Thus, the common experimental approach to correlate the energy of the acoustic emission signals with the energy of the microscopic failure mechanisms is only valid if the geometry of the acoustic emission source is retained and the strain energy release during crack growth occurs under similar loading conditions.

The frequency content of the simulated and experimental signals agrees satisfactory and changes systematically for all investigated specimen geometries and source mechanism. In addition, frequency features extracted from the simulated signals exhibit the same distribution ranges as those of the experimental signals associated with the respective failure mechanism. Thus the obtained classification process relating failure mechanism and acoustic emission signals can act as proof of principle for the presented geometries, materials and acoustic emission sensor type. For a generalized application of the presented approach to arbitrary CFRP-structures, attenuation effects and other geometric boundary conditions and their influence on the detected frequency spectra should be investigated further. Especially dispersive wave propagation, source position relative to the sensor and stacking sequence of the CFRP can significantly affect the obtained frequency spectra [56, 76, 145].

## 5.2. Pattern recognition

As mentioned in section 2.3.3 the goal of the application of the proposed pattern recognition techniques is the identification of similar types of signals. To correlate these types of signals with distinct failure mechanisms is not part of the pattern recognition process. Instead, such correlation can only be achieved by proper interpretation of the results of the pattern recognition process and by including additional results from experiment or simulation. Consequently, the pattern recognition method presented within this thesis is only a tool to achieve the numerically best separation of the natural clusters [84] of signal types (signal classification).

Based on the considerations of A. Anastassopoulos and T. Philippidis [93]

## 5. Summary and Discussion

feature based pattern recognition techniques were used for identification of the natural clusters of acoustic emission signals. The first critical step is the selection of suitable feature combinations for description and classification of the acoustic emission signals. To a certain extent the feature selection can be supported utilizing correlation dendrograms. In addition, the feature selection can be based on the assumption of a correlation between a feature and the observed failure mechanisms. Within the current thesis a generalized approach to identify the feature combination with best numerical performance was used. This approach is based on exhaustive screening of the clustering results using all possible feature combinations. For each feature combination the number of clusters leading to the best separation of the dataset is chosen based on a voting scheme [127] utilizing the cluster validity indices introduced by J. Dunn [109], J. Tou [110], D. Davies and D. Bouldin [111] and L. Hubert [112]. Subsequently, the optimum of all feature combinations is evaluated by the global cluster validity index performance.

For the investigated experimental datasets the optimal feature combination is typically not easy to identify. In particular, the different datasets originating from one specimen series can yield different feature combinations as numerical optimum. Consequently, near optimal feature combinations were investigated as well. For each specimen series one characteristic feature combination with satisfactory high cluster validity index performance is found. The feature combinations found, show strong similarities for all CFRP-specimens investigated. Differences in the features numerical ranges can induce changes in the selected globally optimal feature combinations. In the case of CFRP failure a typical feature combination consists solely of frequency features as given in table 4.3 for a bending specimen. Differences in these features numerical range originate from characteristic shifts in the mean signal frequency caused by different specimen geometries, different stacking sequences and variations of material processing. As a consequence, a different optimal feature combination is found, e.g. for tensile specimens compared to bending specimens, as given in table 4.4 and 4.3. However, the only change concerning the selected features is a replacement of one Partial Power range by another. It is worth to point out, that the presence of noise signals can drastically influence the outcome of the presented pattern recognition approach. In this context it was observed, that distinct noise signal types result in formation of additional natural clusters. This is a direct consequence of the distinctly different features of noise signals [128]. Moreover, a noise signal cluster often can act as super-dominating cluster (see section 2.3.3), which inhibits successful separation of the remaining signals.

In this thesis it was demonstrated that a stable distinction between signals correlated with matrix cracking, fiber breakage and interface failure is possible in the case of acoustic emission signals originating from CFRP failure. The

## 5. Summary and Discussion

correlation of the distinct signal types with the respective failure mechanism was achieved by various methods. Firstly, the localized source positions of the different signal classes show strict correlation to the microscopically observed positions of the associated failure type. Secondly, the feature ranges of the different signal classes agree with the feature ranges from simulated signals of the associated failure mechanism. Finally, the quantified contribution of the different signal classes corresponds systematically to the expected type and degree of damage, which depends on the respective specimen type and loading condition.

In the case of acoustic emission signals from coating failure the obtained distinct signal types were correlated to mode-I nickel cracking, mode-I copper cracking and mode-I/II nickel-copper interface delamination. Here the applied cluster validity index method [93] indicates the existence of two (nickel cracking, copper cracking) or three (in addition nickel-copper delamination) distinct signal types. Again the correlation is based on the localized source positions of the different signal types, which is consistent with microscopically observed locations of the associated failure type. In addition, the mean frequency spectra of the different signal classes agree in their frequency shift with the respective simulated signals and principle considerations [56, 62, 76, 143, 144].

Dispersion and attenuation during signal propagation drastically influences the detectability and separability of signal types correlated with different failure mechanisms. The range of experimental features characteristic for the different signal types shows larger overlap with increasing mean signal propagation distance. This is obvious comparing the cluster positions of the T800/913 bending specimens and the T800/913 DCB-specimens in figures 4.13 and 4.47. Due to the increased mean propagation length in the DCB-specimens the signal classes of matrix cracking and interface failure show significant overlap. This overlap is even larger in the HTS/RTM6 T-Pull specimens shown in figure 4.67. Here both signal classes appear completely merged and cannot be separated by the current pattern recognition method utilizing the k-means algorithm. In addition the overlap depends on the stacking sequence of the CFRP specimens. For non-unidirectional stacking sequences or woven fabric larger overlap was observed experimentally than for unidirectional stacking sequences. Consequently, the degree of error during classification of acoustic emission signals will depend on the signals propagation length and the specimens stacking sequence. Thus successful separation of signals originating from matrix cracking or interface failure requires a high density sensor network in larger specimens, which ensures a mean source-sensor distance less than 40 - 50 mm. In contrast, the range of signal features characteristic for fiber breakage is less susceptible to the influence of propagation and stacking sequence. Here only a minor overlap between the fiber breakage cluster and the remaining signal clusters is

## 5. Summary and Discussion

observed in the investigated specimens. Based on the present investigations and considerations of various authors [56, 62, 76] it is assumed, that such distinction will be possible for signal propagation distances up to 100 mm, although further investigations are necessary to determine the exact limitations.

Concerning the exhaustive search procedures various authors [84, 91] already pointed out, that these search procedures are generally devastating in their performance. For the method presented here, the required computational resources depend dominantly on the following parameters:

- the number of feature combinations  $N_{tot}$ ,
- the number of acoustic emission signals  $N$  and
- the maximum number of clusters  $P$  to investigate

Since the various feature combinations are the focus of the investigation, an excessive reduction of  $N_{tot}$  is generally not recommendend. As indicated above a suitable pre-selection of features based on physical concepts in combination with correlation dendrograms can act as suitable tool for the reduction of  $N_{tot}$ . In the given context it was demonstrated in section 2.3.3 that a higher efficiency of the complete procedure can be achieved by random selection of a statistically representative subset  $N_{subset} \leq 0.5 \cdot N$  of the complete dataset. For experimental investigations a suitable subset size is initially unknown, unless further assumptions are made concerning the number of signals belonging to a cluster. Additional reduction of the required computational resources can be achieved by limiting the maximum number of clusters  $P$  investigated for each feature combination. Again this requires knowledge or estimation of the number of natural clusters within the dataset. Consequently, the applicability of non-exhaustive screening methods should be further investigated. The decrease in the required computational resources would also facilitate the application of alternative cluster algorithms instead of the currently used k-means algorithm. The latter is not necessarily the best cluster algorithm for feature based classification of transient ultrasonic signals [93, 128, 129, 188]. Similarly, the introduction of new signal features in addition to the standardized features [77, 78], like the Weighted Peak-Frequency can improve the capabilities of the current pattern recognition approach. In this context, features derived from Wavelet-Transformations appear to be the most promising candidates for further improvement of the current acoustic emission source identification method.



### 5.3. Material Analysis

In recent years the aerospace and automotive industry has developed a lively interest in hybrid materials with lightweight potential. Reducing overall weight is the key for energy efficiency, a larger carrying capacity and, therefore, greater competitiveness. Here the light-weight potential of CFRP is still not completely utilized since a reliable prediction of ultimate or functional failure is still difficult. Therefore, industrially used structures are typically oversized. Thus a successful identification of the microscopic origin of failure initiation is of high practical interest.

With the proposed pattern recognition method it is possible to identify similar types of acoustic emission signals. In combination with finite element simulations of the microscopically observed failure in CFRP these can be correlated with matrix cracking, interface failure and fiber breakage. Within the context of this discussion, matrix cracking should always be understood as inter-fiber matrix cracking. Interface failure is attributed to microscopic failure mechanisms, which involve fiber and matrix, like debonding, delamination, fiber bridging and related failure mechanisms. Signals identified as fiber breakage refer to the occurrence of single fiber failure and failure of fiber bundles.

The identification of these different failure mechanisms as a function of loading can yield valuable informations about failure evolution in fiber reinforced composites. In the present thesis it was demonstrated that quantification of the occurrence of these failure mechanisms by acoustic emission analysis correlates directly with the measured mechanical properties of the specimens. In particular, for specimens of the same production process changes in the relative contributions of different failure mechanisms correlate well to the measured mechanical properties. Since for composite specimens mechanical properties often scatter over a large range, acoustic emission measurements can form a vital part in investigations of their microscopic origin. The quantified occurrence of different failure types and their load dependent onsets can further be compared with predictions of modern engineering theories regarding the occurrence of inter-fiber matrix cracking and fiber breakage [18, 20–23, 180, 189]. In addition, the acoustic emission onset and load-dependent evolution of a particular failure type is found to be more suitable for prediction of the composites ultimate failure than the general onset of acoustic emission signals. This is observed best in the Layup-0 specimen series in section 4.2.1. Here the onset of fiber breakage signals is strictly correlated to the final load level at ultimate failure. A similar conclusion cannot be achieved by the accumulated number of acoustic emission signals alone. A limiting factor for the mechanical performance of CFRP is the interfacial strength between fiber and matrix [18]. Within the HTS/RTM6 specimen series it was demonstrated, that an increased apparent interlaminar

## 5. Summary and Discussion

shear strength is indicated by an increased mean  $S_0/A_0$ -mode excitation ratio for signal types associated with interface failure. Here further investigations are required to clarify if these correlations are sufficiently strong to assess the interfacial strength between fiber and matrix. In particular, changes of source position and signal propagation distance can have a similar effect and thus have to be considered. Testing of micro-composites by fiber pull-out [190] and fiber fragmentation [2, 5, 45, 191, 192] accompanied by acoustic emission analysis have already shown the valuable capabilities for analysis of interfacial strength between fiber and matrix and should be enhanced by the analysis capabilities of pattern recognition techniques.

The presented investigations on coating failure demonstrate that the proposed pattern recognition techniques can be used to successfully identify different failure mechanisms occurring within coatings. Beyond correlating acoustic emission signals and failure mechanisms, it was shown that the failure specific acoustic emission energies can act as measure of the corresponding fracture energies, as derived from a LEFM approach. The quantification of fracture energies by acoustic emission measurements offers the possibility to use the presented method for comparative studies of different coating-substrate systems. In particular, these findings suggest that acoustic emission analysis is generally applicable for health monitoring of the coating-substrate combinations investigated. By comparative acoustic emission measurements it was also demonstrated that the CuCu-coatings are superior to the NiCu-coatings in their mechanical performance (see section 4.6.4). In general the functional load limit of thin coating systems is not easy to predict, since the residual stress level after coating application alters the real load limit of the coating substrate system drastically. Here the presented acoustic emission techniques can be used to assess the quality or functional load limit of such coating systems under realistic loading conditions.

Apart from the presented results, closely related acoustic emission investigations within the scope of this thesis demonstrated the broad capabilities of the proposed pattern recognition approaches. Thus the fracture toughness values of graphite electrodes were estimated based on acoustic emission measurements and the obtained localization patterns were compared to computer tomography images [82, 193, 194]. Similar to the failure of coatings applied to CFRP substrates, the load limit of ceramic coatings applied on steel substrates was investigated [195]. Within a cooperation with the University of Applied Science Munich the failure behavior of smart CFRP structures with embedded carbon-fiber strain gauges was investigated. The comparative acoustic emission measurements during loading of specimens with and without carbon-fiber strain gauges were used to assess the influence of the integrated sensor system [196, 197]. Within the project "Mehrstufige Verfahren zur Her-

## *5. Summary and Discussion*

stellung von CFK-Integralstrukturen” various mechanical tests of CFRP were accompanied by acoustic emission measurements. Similar to the presented results, the conducted measurements correlate with microscopical observations of the identified failure mechanisms and were used to optimize new production technologies for integral manufacturing of CFRP structures.

In summary, if the respective source mechanisms show significant differences in their signal characteristics, identification of different failure mechanisms in hybrid materials by pattern recognition applied to acoustic emission signals is generally possible. These differences can originate from variations in the local elastic properties of the cracking media, the direction of source radiation or the energy release of the acoustic emission source. The possibility to interpret the load dependent evolution of otherwise undistinguishable failure mechanisms is an outstanding chance to understand and predict the occurrence of functional failure in hybrid materials.

## 6. Outlook

The next steps towards a broad applicableness of the presented acoustic emission methods are the investigation of the proposed techniques in application to acoustic emission signals from larger CFRP structures than those investigated. The faced problems are attenuation and dispersion effects of the guided waves that carry the source information. These were partially addressed within this thesis and have to be investigated in more detail for larger mean propagation distances than 50 mm. Similar investigations should also be performed for CFRP specimens with complex stacking sequences and combinations of unidirectional reinforcements and woven fabric. A suitable tool to assess the influence of these changes is finite element simulation. The simulations should be improved in their numerical efficiency to enable calculation of larger specimen volumes and screening of larger numbers of source excitation parameters. In particular, the source model should be improved to yield a geometrically more accurate representation of the microscopic source type. Currently the chosen geometry is only understood as approximation to realistic acoustic emission sources. In addition, measurements of the crack surface displacement magnitude and the source excitation time are required to ensure the applicableness of the chosen simulation settings. Ultimately the simulation of the acoustic emission source should be based on an accurate finite element description of crack growth. As recently shown by A. Livne et al. it is still a challenging task to validate the input parameters for such simulations by experimental means [198]. To this end, analysis of acoustic emission signals from microscopic mechanical tests with controlled loading conditions is one promising approach to obtain these parameters. Here analysis of matrix cracking with various loading rates could elucidate the influence of the Deborah-number on the signals frequency spectra. The combination of single fiber pull-out experiments with acoustic emission measurements should yield the missing information of characteristic signal contributions when the interfacial strength is changed. In addition a suitable experimental setup should be developed to measure the acoustic emission source excitation time, since its value is still subject to assumptions. Finally the technology readiness of the proposed identification methods of distinct failure types should be proven by statistically firm approaches, which demonstrate their stableness. In this way acoustic emission measurements are expected to become an even more powerful and reliable tool for interpretation

## 6. *Outlook*

of material failure.

## **A. AWARE++ User's manual**

The following pages hold a copy of the user's manual of the software package AWARE++, since this was established within the scope of this thesis and was extensively used to achieve the interpretation of the experimental results. It is copied in its original appearance, as provided with the software. Therefore the following pages do not confirm to the symbol conventions annotated on pages 282 - 285 as within the rest of the thesis.

AWARE++  
Advanced Waveform Analysis Research Engine

Software Manual  
Rev. 1.2

(c) 2008-2010 Markus Sause

# Contents

<b>1</b>	<b>Softwares Aim</b>	<b>3</b>
1.1	Basic Idea . . . . .	3
1.2	Purpose . . . . .	3
1.3	System Requirements . . . . .	4
1.4	License Information . . . . .	4
<b>2</b>	<b>Using the software</b>	<b>5</b>
2.1	Basic Operation . . . . .	5
2.2	File . . . . .	5
2.3	Calculation . . . . .	5
2.3.1	Fast Fourier Transformation (single file) . . . . .	5
2.3.2	Wavelet Transformation (single file) . . . . .	7
2.3.3	Average FFT (multiple files) . . . . .	7
2.3.4	Average WT (multiple files) . . . . .	8
2.3.5	Convolution and Deconvolution . . . . .	10
2.4	ASCII-Operators . . . . .	10
2.4.1	Event Linking . . . . .	10
2.4.2	Columns . . . . .	11
2.4.3	Accumulate . . . . .	12
2.5	View . . . . .	12
2.6	Help . . . . .	12
<b>3</b>	<b>Compatibility</b>	<b>13</b>
3.1	Data formats . . . . .	13
3.2	Using other data formats . . . . .	15
3.3	Errors and Bug Reports . . . . .	15
	<b>Literature</b>	<b>15</b>



# 1 Softwares Aim

## 1.1 Basic Idea

The Advanced Waveform Analysis and Research Engine (AWARE) was developed as a fast software program, that can be used for automated calculations of Fast-Fourier-Transformation (FFT) spectra and Wavelet-Transformation (WT) coefficients. Originally the software was developed for advanced interpretation of acoustic emission signals, but the software can also be used for calculations on other transient waveform types. The latest release version AWARE++ 1.0 offers a graphical user interface in addition to the earlier release version AWARE beta. This results in faster access to calculation parameters and faster visualization of the calculation result.

## 1.2 Purpose

AWARE++ is a useful tool for advanced signal analysis of ASCII-based waveforms provided in .txt format. Its main features are:

- Calculation of Fast Fourier Transforms
- Calculation of Continuous Wavelet Transforms
- Calculation of average FFT-Spectra of multiple waveforms
- Calculation of average WT-Spectra of multiple waveforms
- Automated signal convolution and deconvolution of single or multiple waveforms

The AWARE++ software can calculate FFT frequency spectra of ASCII-based signals. An implementation of several window functions is planned, but not realized yet and will be adopted in future release versions. More advantageous, the software can automatically process a large number of files. Additionally the average frequency spectra of these signals, their standard deviation, maximum and minimum values can be calculated. As a second method for signal analysis, the Continuous Wavelet Transformation of ASCII-based signals is implemented. The scale and time ranges can be chosen as real values, each range adopted to the current signal's needs. The wavelet coefficients can either be saved as complex values for further calculation, or magnitude for visualization. The wavelet size is decreased from infinity to a fixed size chosen before calculation. This can boost the computation time with only a small lack of accuracy, and was already realized in the software package AGU-Vallen wavelet as well [1]. Currently only the Gabor mother wavelet is implemented, but future release versions will perhaps include some other commonly used mother wavelet types. Analogous to the FFT-options a calculation of an average WT-diagram is realized, although there is no option for standard deviation, maximum and minimum values available. This may be realized in future release versions. Apart from these basic operations, the AWARE++ software can

convolute and deconvolute large number of files with a given transfer function. This could be a sensors sensitivity curve, transfer properties of a material or any other function. This option is implemented as calculation in the frequency domain, using the FFT-calculation for transformation from time to frequency space.

### 1.3 System Requirements

Due to the computation complexity, a fast microsoft windows based pc-system should be available. This release version was tested within an 32-bit and 64-bit Microsoft Windows XP<sup>TM</sup>-environment. Fastest results will be obtained on workstations with multi-core processors or single-core CPUs with clock speeds above 2 GHz. Besides CPU-power a reasonable amount of RAM should be provided to enhance computation time. At least 1024 MB are recommended, although the maximum usable amount of 2.5 GB RAM available on 32-bit Windows-XP<sup>TM</sup> systems can get used during excessive calculations. Installation requires typically less than 10 MB free disc space. In contrast, the necessary amount of free disc space during calculation depends on your input data. Many operations produce converted copies of the input data. Provide at least an amount equal to your input data size times 1.2 of free harddisc space.

*Example:*

*Your input data are 1000 ASCII-waveforms with each 13kB datsize. This results in 13MB datsize in total. Hence you should provide at least 15.6MB free disc space for this calculation.*

### 1.4 License Information

*AWARE++ is free software: you can redistribute it and/or modify it under the terms of the GNU Lesser Public License as published by the Free Software Foundation, either version 3 of the License, or (at your option) any later version.*

*AWARE++ is distributed in the hope that it will be useful, but WITHOUT ANY WARRANTY; without even the implied warranty of MERCHANTABILITY or FITNESS FOR A PARTICULAR PURPOSE. See the GNU Lesser Public License for more details.*

*You should have received a copy of the GNU Lesser Public License along with AWARE++. If not, see <http://www.gnu.org/licenses>.*

Part of the softwares routines are licensed to other authors, especially:

- The routine for quick folder selection was implemented by Walter Storm (c) 2006
- The FFT-routine was published by Paul Bourke 1993 [2]
- The WT-routine was published by Suzuki et al. 1996 [3]

Microsoft and Windows XP are registered trademarks of Microsoft Corporation. AEwin is a registered trademark of Physical Acoustics Limited and MISTRAS Group Incorporated. Other brands and their products are trademarks or registered trademarks of their respective holders and should be noted as such.

## 2 Using the software

### 2.1 Basic Operation

Start the program executable **AWARE++**.exe. You will see the main window, like shown in fig. 2.1. Choose the option of your choice from the drop-down menu. Depending on the menu item you choose, you will be asked for several input parameters necessary for the choosen operation. For file- and folder-selection another window will pop-up, which allows you to select the path to your input data.

### 2.2 File

Select **File** → **View AE-file** or

Select **File** → **View FFT-file** or

Select **File** → **View WT-file**

Using "View AE-file" you can choose a single \*.txt file and quickly display it. Using the other two options you can quickly re-display the results of preceeding calculations (WT-coefficients magnitude or FFT-spectra magnitude). In any case a new window will open which displays the respective content.

Select **File** → **Exit**

This option closes the application.

### 2.3 Calculation

For all selections a window will pop up, which allows you to select different calculation parameters. All parameters can be saved to a \*.ini file using the button "Save Setup". Using the button "Load Setup" you can load an appropriate \*.ini file. The default values are loaded from the **Setup.ini** file located in the installation folder.

#### 2.3.1 Fast Fourier Transformation (single file)

Select **Calculation** → **Single FFT** from the drop-down menu. A new window will pop-up, which is shown in fig. 2.2. The only parameter necessary for the calculation is the path to the ASCII-waveform. In order to load a file click on the activated "Load" button. When you are done click the button "Calculate!". The FFT-magnitude of the calculation result is displayed in a new window. The results are saved as ASCII-data and as \*.bmp file for a quick preview to the folder containing the input data.

Details on implementation:

The implementation of the Fast Fourier Transform uses procedures adopted from Paul Bourke, which were modified by Peter Cusack and are described in detail elsewhere [2].

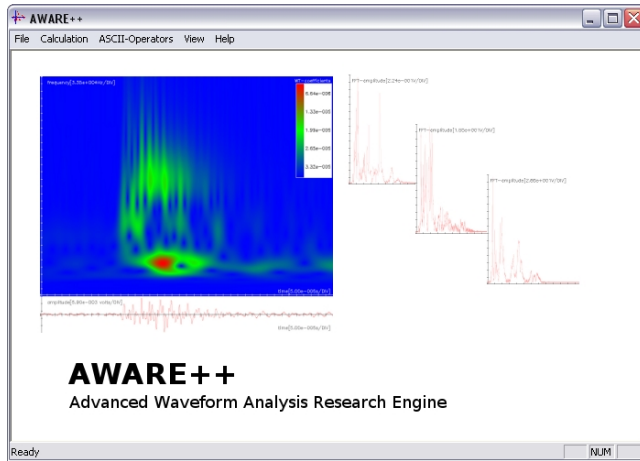


Figure 2.1: Main Window of AWARE++

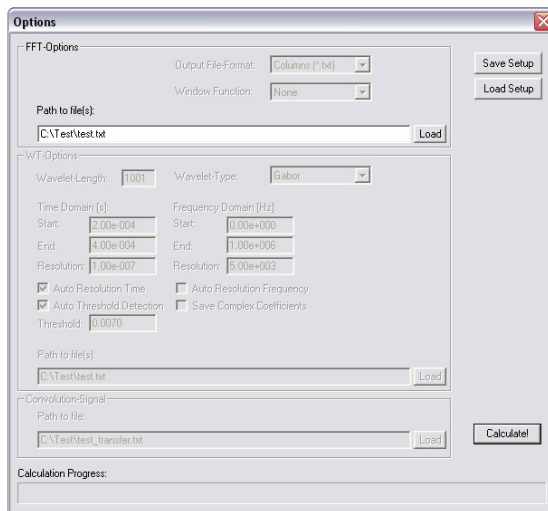


Figure 2.2: Options for FFT-calculation

### 2.3.2 Wavelet Transformation (single file)

Select **Calculation** → **Single WT** from the drop-down menu. A new window will pop-up, which is shown in fig. 2.3. There are several parameters, that are necessary to calculate the WT-coefficients. The "Wavelet-Length" is simply the size of the wavelet in samples. In order to obtain the WT-coefficient at time position  $t$  the calculation is only performed within the interval  $t \pm (\text{waveletlength} - 1)/2$ . Therefore reducing the wavelet length can decrease the computation time, but should be used with care. If the wavelet length gets to short, the remaining size may not be enough to allow a convenient decay of the envelope. The next parameter to choose is the "Wavelet-Type". Currently only the Gabor mother wavelet is implemented. Further parameters are start, end and optionally resolution of both, time and frequency domain. These parameters should match your input data and can be entered in real values. If you use the option "Auto Resolution Time", the sampling interval will automatically be read from the input file. Using the option "Auto Resolution Frequency" will automatically subdivide the given frequency range linearly in 100 steps. Enabling the option "Save Complex Coefficients" will store the WT-coefficients as complex values, disabling will save the coefficients magnitude value (see also 3). In order to load a file for calculation, click on the activated "Load" button. When you are done click the button "Calculate!". The WT-coefficients magnitude and the respective input signal is displayed in a new window. The results are saved as ASCII-data and as \*.bmp file for a quick preview to the folder containing the input data.

*Warning:*

*After the result of the calculation is displayed, the software will save the WT-coefficients. Depending on your input parameters (e.g. resolution) this will take some time to complete. Eventually the software will not respond! Do not force the software to close, or your results may be lost!*

Details on implementation:

The routine for WT-calculation follows the source-code published by Suzuki et al. and is described in detail there [3].

### 2.3.3 Average FFT (multiple files)

Select **Calculation** → **Average FFT** from the drop-down menu. A new window will pop-up, which is shown in fig. 2.2. In order to calculate an average FFT-spectra of several waveform files within a folder, the only parameter necessary is the path to the folder which contains the ASCII-waveforms. To load a folder for calculation, click on the activated "Load" button. When you are done click the button "Calculate!". The average FFT-magnitude is displayed in a new window. The resulting average is saved as ASCII-file **average\_fft.txt** and as picture-file **average\_fft\_preview.bmp** for a quick preview into the subfolder avgFFTDdata.

Details on implementation:

The average complex FFT-amplitude  $\langle A \rangle$  is defined as FFT-Amplitude  $A$  at frequency  $f$  summed over all waveforms and divided by the number of waveforms  $N$ :

$$\langle A(f) \rangle = \frac{1}{N} \sum_{i=1}^N A_i(f) \quad (2.1)$$

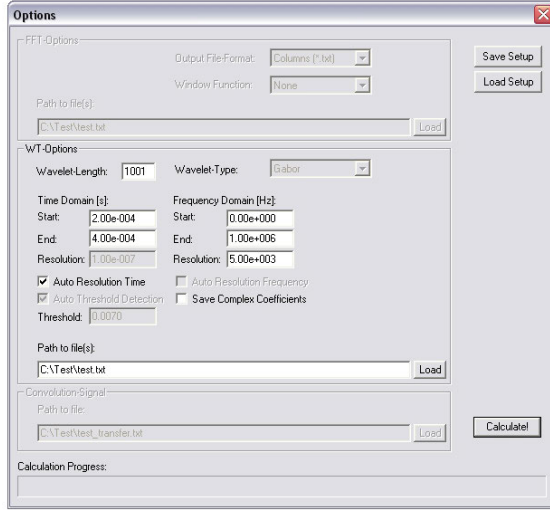


**Figure 2.3:** Options for WT-calculation

The corresponding real and imaginary FFT-amplitudes are defined as real and imaginary part of  $\langle A \rangle$  respectively. The average FFT-Magnitude  $\langle M \rangle$  is defined as absolute value of the average FFT-amplitude  $\langle A \rangle$ :

$$\langle M(f) \rangle = \frac{1}{N} \sum_{i=1}^N |A_i(f)| \quad (2.2)$$

The extremal values at a frequency value  $f$  are defined as:

$$\langle M_{min}(f) \rangle = \min(|A_i(f)|) \quad (2.3)$$

$$\langle M_{max}(f) \rangle = \max(|A_i(f)|) \quad (2.4)$$

The standard deviation  $\sigma$  of  $\langle M \rangle$  is calculated applying the parallel axis theorem to the conventional definition as follows:

$$\sigma(f) = \sqrt{\frac{1}{N} \left( \sum_{i=1}^N |A_i^2(f)| - \langle M(f)^2 \rangle \right)} \quad (2.5)$$

### 2.3.4 Average WT (multiple files)

Select **Calculation** → **Average WT** from the drop-down menu. A new window will pop-up, which is shown in fig. 2.3. In order to calculate average WT-coefficients of several waveform files within a folder, the same parameters are necessary like described in section 2.3.2. In addition the option "Auto threshold detection" is now enabled. Using this option together

with an entry in the field "Threshold" can improve calculation results on time-shifted waveforms. In this case the onset of each waveform is not fixed at a specific position within the dataset, but scatters arbitrary from waveform to waveform. To overcome this problem, the specific onset of each waveform is determined by the first crossing of the threshold value given by "Threshold" in units of the waveforms amplitude. The software now shifts the waveforms within the dataset to start at their new (common) zero position. This is defined as 20% of the timeframe given by the values for time start and end. This option should be used with care, as unrealistic threshold values can significantly influence the outcome of the calculation results! To load a folder for processing, click on the activated "Load" button. When you are done click the button "Calculate!". The average WT-coefficients magnitude and the respective input signal is displayed in a new window. The resulting average is saved as ASCII-file **average\_wt.txt** and as picture-file **average\_wt\_preview.bmp** for a quick preview into the subfolder avgWTData.

*Warning:*

*After the result of the calculation is displayed, the software will save the WT-coefficients. Depending on your input parameters (e.g. resolution) this will take some time to complete. Eventually the software will not respond! Do not force the software to close, or your results may be lost!*

Details on implementation:

If the option for "Auto threshold detection" is disabled the average WT-coefficients are obtained in a similar manner like the average FFT-magnitude. First of all, the average FFT-magnitude of all waveforms is calculated, like defined in equation 2.2. Afterwards, the inverse Fourier-Transformation is applied to yield the average waveform amplitude in time domain. This signal is now used to calculate the associated WT-coefficients. This is numerically identical to a direct averaging of each waveforms WT-coefficients  $C_{\psi}(a, b)$ , but computationally much more efficient.

The WT-Transformation of a single waveform  $i$  with signal amplitude  $a$  is defined as:

$$C_{i,\psi}(a, b) = \frac{1}{\sqrt{a}} \int_{-\infty}^{\infty} a_i(t) \psi\left(\frac{t-b}{a}\right) dt \quad (2.6)$$

Here  $\psi\left(\frac{t-b}{a}\right)$  denotes the wavelet-function at scale position  $a$  and location parameter  $b$ . After application of the convolution theorem the corresponding WT-Transformation in the frequency domain can be obtained as:

$$C_{i,\psi}(a, b) = \frac{\sqrt{a}}{2\pi} \int_{-\infty}^{\infty} A_i(f) e^{jbf} \langle \psi(af) \rangle df \quad (2.7)$$

Here  $A(f)$  denotes the Fourier-Transformation of  $a(t)$  and  $e^{jbf} \langle \psi(af) \rangle$  the respective Fourier-Transformation of the wavelet-function. Consequently, the average WT-coefficient at position  $a$  and  $b$  of  $N$  waveforms is:

$$\frac{1}{N} \sum_{i=1}^N C_{i,\psi}(a, b) = \langle C_{i,\psi}(a, b) \rangle = \frac{1}{N} \sum_{i=1}^N \frac{\sqrt{a}}{2\pi} \int_{-\infty}^{\infty} A_i(f) e^{jbf} \langle \psi(af) \rangle df \quad (2.8)$$

Using the linearity of the integral for finite boundaries  $f_{low}$  and  $f_{high}$  the summation can be switched with the integration, which results in:

$$\langle C_{i,\psi}(a, b) \rangle = \frac{\sqrt{a}}{2\pi} \int_{f_{low}}^{f_{high}} \frac{1}{N} \sum_{i=1}^N A_i(f) e^{jbf} \langle \psi(af) \rangle df \quad (2.9)$$

Hence, using the definition of the average FFT-amplitude from equation 2.1 we can finally write:

$$\langle C_{i,\psi}(a, b) \rangle = \frac{\sqrt{a}}{2\pi} \int_{f_{low}}^{f_{high}} \langle A(f) \rangle e^{jbf} \langle \psi(af) \rangle df \quad (2.10)$$

This is the Wavelet-Transformation of the waveforms averaged FFT-amplitude, which is identical to the average of the signals wavelet-coefficients.

If the "Auto threshold detection" is enabled, the only the time-shift of the original waveforms changes as described above, before the Fourier-Transformation is applied.

### 2.3.5 Convolution and Deconvolution

Select **Calculation** → **Signal Convolution** or

Select **Calculation** → **Signal Deconvolution** from the drop-down menu.

A new window will pop-up, which is shown in fig. 2.4. In order to (de)convolute several waveform files within a folder, click on the activated upper "Load" button to load a folder path. To load the respective (de)convolution signal, click on the activated lower "Load" button to load a signal file. For the output file format two options are available. Using "Single \*.txt" (de)convolutes each waveform file and stores the result into the procData subfolder. Using "Columns \*.txt" appends the (de)convoluted waveform to a column separated single file instead (see also section 3), where each column corresponds to the result of a single waveform.

Details on implementation:

The software uses the application of the convolution theorem, which means the convolution takes place in the frequency domain:

$$A^*(f) = A(f) \cdot H(f); \quad (2.11)$$

Here  $A(f)$  is the Fourier-Transformation of the waveforms amplitude  $a(t)$  and  $H(f)$  the respective convolution signal in the frequency domain. The deconvolution procedures is defined equivalently as:

$$A^*(f) = \frac{A(f)}{H(f)}; \quad (2.12)$$

## 2.4 ASCII-Operators

The main purpose of this section is the treatment of several kinds of ASCII input data, to obtain special output formats, without changing the data content itself.

### 2.4.1 Event Linking

Select **ASCII-Operators** → **Event Linking** and select the path to the folder, which contains the files to be linked together.

Multi-channel recording equipment for ultrasonic waves usually either uses independent triggering for each channel or one guard channel as trigger. Due to the varying source-sensor distance, the waveforms arrive at different times at each sensor and are recorded for a fixed length (i. e. fixed data size). To obtain a time-linked datafile for each singular source event recorded with all sensors, the timelines of each sensor is shifted, to obtain a common timeline



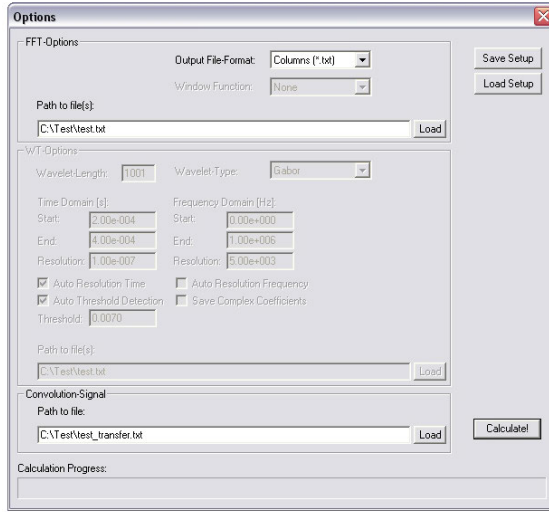


**Figure 2.4:** Options for signal (de)convolution

for all sensors. This is shown in fig. 2.5 in an example for three sensors. The output is saved in the subfolder convData and one file per source event with incremental filenames.

#### Details on implementation:

At first, the absolute recording times are read from each waveforms file header. Only waveforms belonging to one source event as defined in the filenames (see section 3) are taken into account. Afterwards, a threshold based arrival time extraction is used to obtain the waveforms onset relative to the absolute recording time. The first waveform arrival is choosen as beginning of the new common time line. Relative to this waveform, the corresponding sensors datasets are shifted in time using zero padding at the beginning and data removal at the end. This is only possible if the overall recording time is sufficiently large, so that data removal only takes place after the waveforms decay. It should be noted, that the maximum loss of data points can be estimated from the maximum difference in arrival time with respect to the source-sensor distance.

### 2.4.2 Columns

Select **ASCII-Operators** → **Columns** and select the path to the folder, which contains the files to be linked together.

All waveforms inside the folder are pasted into one single ASCII-file. Inside the new file, each waveform corresponds to one tabulator separated column with a header definition as described in section 3. The output is saved to the file **Columns\_ASCII\_waveforms.txt**

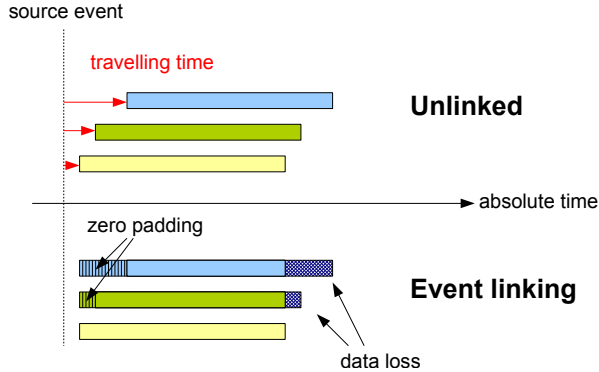


Figure 2.5: ASCII-handling scheme for event linking

### 2.4.3 Accumulate

Select **ASCII-Operators** → **Accumulate** and select the path to the folder, which contains the files to be accumulated.

Each waveforms time of record is read out and is assumed to reflect the waveforms time of occurrence on a macroscopic scale. This neglects the time difference between time of record and the real arrival time, which could for instance be defined by threshold crossing time. In comparison to the timespan of a recording this time difference is often negligible. The software now calculates the cumulative number of waveforms over time. The output is saved in the convData subfolder to the file **Accumulated\_waveforms.txt** as two tabulator separated columns.

## 2.5 View

Select **View** → **Status Bar**

Enabling or disabling the option enables or disables the status bar on the bottom of the window.

## 2.6 Help

Select **Help** → **About AWARE++...**

Show version and copyright information.

## 3 Compatibility

This section should familiarize the user to the ASCII-formats used for calculation routines. Unless otherwise stated each character is important. Especially white-spaces, row- and column delimiting characters should be used exactly in the form as shown here.

### 3.1 Data formats

The input waveforms ASCII-format should exhibit the following form:

```
SOURCE FILE NAME: C:\test\test.dta
DATE: Friday, April 18, 2008
TIME: 17:13:15
SAMPLE INTERVAL (Seconds): 0.0000001000
UNITS: volts
CHANNEL NUMBER: 1
HIT NUMBER: 5
TIME OF TEST: 1058.7284030000
```

```
-0.00091553
0.00030518
0.00030518
...
```

This is the standard ASCII-format obtained by exporting the proprietary data format used by Physical Acoustics Ltd. software AEwin<sup>TM</sup>. As the primary reason for this software was treatment of these data format, no other input type formats are supported right now, but may be adopted in the future, if requested.

The FFT-calculation on a single waveform results in the following data structure:

```
AWARE - Single FFT - (c) Markus Sause 2008
Channel: 1
Time of Record: 1.058728e+003
Timeresolution: 1.000000e-007
Frequency: Real: Imaginary:
0.000000e+000 -6.277465e-001 0.000000e+000
6.103516e+002 -3.027721e-001 4.537087e-001
1.220703e+003 1.373423e-001 3.093146e-001
...
```

In comparison the average FFT calculation has four columns in addition:

```
AWARE - Average FFT - (c) Markus Sause 2008
Frequency: Real: Imaginary: Amplitude: Standard Deviation: Minimum: Maximum:
0.000000e+000 -1.089320e+000 0.000000e+000 2.900359e+000 1.037893e+000 4.705822e-001 2.354950e+001
6.103516e+002 5.511800e+000 2.012331e+000 6.053717e+000 1.220635e+000 4.009856e+000 1.734421e+001
1.220703e+003 5.921892e+000 9.640371e-001 6.014118e+000 1.162506e+000 4.580478e+000 1.289064e+001
...
```

The output file for a single waveforms wavelet coefficients magnitude looks like this:

```
Channel: 2
Time of Record: 5.377976e+002
Timeresolution: 1.000000e-007
Frequency [Hz]/Time[s] 1.000000e-007 2.000000e-007 3.000000e-007 4.000000e-007 5.000000e-007 ...
1.100000e+004 3.164919e-001 3.162870e-001 3.160431e-001 3.158377e-001 3.155941e-001 ...
2.200000e+004 4.486387e-001 4.484015e-001 4.481202e-001 4.478821e-001 4.476018e-001 ...
3.300000e+004 5.514869e-001 5.512926e-001 5.510643e-001 5.508667e-001 5.506385e-001 ...
...
```

### A. AWARE++ User’s manual

Here, the tabulator separated columns are the time domain, while the rows reflect the frequency domain. The first line holds the values for the time scaling, while the first column holds the frequency scaling.

The output file for a single waveforms complex wavelet coefficients should look like this:

```
Channel: 2
Time of Record: 5.377976e+002
Time resolution: 1.000000e-007
Frequency [Hz]/Time[s] 1.0000000e-007 2.0000000e-007 ...
5.0000000e-003 -2.684406e-007,2.936274e-007 -2.703595e-007,3.021117e-007 ...
1.0000000e-004 -2.693933e-007,2.978707e-007 -2.703595e-007,3.021117e-007 ...
1.5000000e-004 -2.684406e-007,2.936274e-007 -2.703595e-007,3.021117e-007 ...
```

The structure of the file is the same, like for coefficient magnitudes, but each coefficient entry is written in complex form. Real and imaginary part are separated by a comma.

The ASCII-structure of a transfer signal used for (de)convolution should be provided, as follows:

Real	Imaginary
6.70484E-4	6.70484E-4
7.18419E-4	7.18419E-4
6.60511E-4	6.60511E-4
6.50789E-4	6.50789E-4
7.71938E-4	7.71938E-4
6.70374E-4	6.70374E-4

The first column provides the real part of the signal, the tabulator separated second column provides the imaginary part. In this option, the signal length (the number of rows) is crucial! The signal length has to match the padded size of the waveforms FFT-spectra. During FFT-calculation the size of the waveform is increased until it matches the next binary based length, e.g. the natural waveform length of 13660 is padded with zeros at the end until it reaches  $2^{14} = 16384$ . In order to use the (de)convolution described in section 2, the respective (de)convolution signal should exhibit the same size of 16384 datapoints. The output format for (de)convolution with option Columns(\*.txt) looks like this:

[illegible]

The first row holds the channel, which recorded the waveform, the second row holds the time of record in seconds. The third row is the sampling rate in kHz. The following 16 rows hold 0 as entry. Row 20 finally holds the number of samples belonging to the waveform. The following rows hold the time ordered values for the signal amplitude.

ASCII-Event linking results in the following data:

```
0.000000e+000 0.000000e+000 0.000000e+000 0.000000e+000 0.000000e+000 6.103500e-004 0.000000e+000
5.000000e-007 0.000000e+000 0.000000e+000 0.000000e+000 0.000000e+000 3.051800e-004 0.000000e+000
1.000000e-006 0.000000e+000 0.000000e+000 0.000000e+000 0.000000e+000 0.000000e+000 0.000000e+000
1.500000e-006 0.000000e+000 0.000000e+000 0.000000e+000 0.000000e+000 -3.051800e-004 0.000000e+000
2.000000e-006 0.000000e+000 0.000000e+000 0.000000e+000 0.000000e+000 0.000000e+000 0.000000e+000
2.500000e-006 0.000000e+000 0.000000e+000 0.000000e+000 0.000000e+000 0.000000e+000 0.000000e+000
3.000000e-006 0.000000e+000 0.000000e+000 0.000000e+000 0.000000e+000 0.000000e+000 0.000000e+000
...
```

The above shows an example for six recording channels. The first column holds the time information. The other six tabulator separated columns correspond to channel one to six, respectively. Each column holds the waveforms amplitude in units as read from the source files. The input files have to be in the format **yourfilename\_M\_N.txt**. Here the value of N is the associated incremental source event and M is the recording channel. The file **yourfilename\_1\_1.txt** has to exist within the folder. The output filenames are order by events. The first linked event is saved to file **00000001.txt** and so on.

The output format for ASCII-Columns is the same like for (de)convolution with Columns(\*.txt) option.

ASCII-Accumulate results in two tabulator separated columns, the first one holds the number of the waveform, the second the respective recording time.

## 3.2 Using other data formats

To begin calculation using data from other software, you have to change the ASCII-format according to the entries like mentioned above. If this is impossible, feel free to ask, if further formats can be included within AWARE++.

## 3.3 Errors and Bug Reports

For any compatibility issues, errors, bug reports or suggestions do not hesitate to contact me via mail at markus.sause@physik.uni-augsburg.de

## Bibliography

- [1] Aoyama Gakuin University (Tokyo Japan) Vallen Systeme GmbH (Munich, Germany), 2001. <http://www.vallen.de/wavelet/index.html>.
- [2] P. Cusack P. Bourke. Fast fourier transformation, 1998. <http://local.wasp.uwa.edu.au/~pbourke/miscellaneous/dft/index.html>.
- [3] Y. Hayashi M. Takemoto H. Suzuki, T. Kinjo and K. Ono. Wavelet transform of acoustic emission signals. *Journal of Acoustic Emission*, 14:69–84, 1996.

## B. Deriving elastic coefficients from micromechanical properties

While the mechanical properties used for FEM-simulation of isotropic materials are easily accessible throughout the literature and via experiments, this is not the case for CFRPs. These are strongly dependent on the chosen type of fiber, the type of resin and the fiber-volume fraction. For simulation of CFRP with distinct ply stacking sequences the anisotropic elastic coefficients for a single unidirectional layer are required. Although B. Hosten et al. established a suitable method for direct measurement of the elastic coefficients [199] this is still an experimentally difficult task. As alternative approach, H. Schürmann suggests a method to derive the elastic coefficients based on micromechanical properties of the chosen fiber and resin in combination with experimentally accessible macroscopic properties [18] for unidirectional lamina. In the case of woven fabric another comprehensive approach was established by N. Naik and P. Shembekar to calculate the macroscopic elastic properties of such laminates based on the structure of the woven fabric and the microscopic elastic properties of the chosen fiber and resin [200–202].

For these transversal isotropic materials the elastic coefficients matrix  $C_{iklm}$  is generally written as:

$$\begin{pmatrix} \sigma_{xx} \\ \sigma_{yy} \\ \sigma_{zz} \\ \tau_{yz} \\ \tau_{xz} \\ \tau_{xy} \end{pmatrix} = \begin{pmatrix} C_{xxxx} & C_{xxyy} & C_{xxzz} & 0 & 0 & 0 \\ C_{zzxx} & C_{yyyy} & C_{yyzz} & 0 & 0 & 0 \\ C_{zzxx} & C_{zzyy} & C_{zzzz} & 0 & 0 & 0 \\ 0 & 0 & 0 & C_{yzyz} & 0 & 0 \\ 0 & 0 & 0 & 0 & C_{xzzz} & 0 \\ 0 & 0 & 0 & 0 & 0 & C_{xyxy} \end{pmatrix} \cdot \begin{pmatrix} \varepsilon_{xx} \\ \varepsilon_{yy} \\ \varepsilon_{zz} \\ \gamma_{yz} \\ \gamma_{xz} \\ \gamma_{xy} \end{pmatrix} \quad (\text{B.1})$$

## B.1. Unidirectional lamina

In the case of unidirectional lamina this can also be written using the compliance matrix  $(C_{iklm})^{-1}$  as:

$$(C_{iklm})^{-1} = \begin{pmatrix} \frac{1}{E_{||}} & \frac{-\nu_{||\perp}}{E_{\perp}} & \frac{-\nu_{||\perp}}{E_{\perp}} & 0 & 0 & 0 \\ \frac{-\nu_{\perp||}}{E_{||}} & \frac{1}{E_{\perp}} & \frac{-\nu_{\perp\perp}}{E_{\perp}} & 0 & 0 & 0 \\ \frac{-\nu_{\perp||}}{E_{||}} & \frac{-\nu_{\perp\perp}}{E_{\perp}} & \frac{1}{E_{\perp}} & 0 & 0 & 0 \\ 0 & 0 & 0 & \frac{1}{E_{S\perp\perp}} & 0 & 0 \\ 0 & 0 & 0 & 0 & \frac{1}{E_{S\perp||}} & 0 \\ 0 & 0 & 0 & 0 & 0 & \frac{1}{E_{S\perp||}} \end{pmatrix} \quad (\text{B.2})$$

All subscripts  $||$  indicate a direction parallel to the fibers axis, while  $\perp$  indicates a direction perpendicular to the fiber axis. For the transversal isotropy often faced in unidirectional CFRP this reduces the number of values necessary for determination of the elastic coefficients to 5 independent values  $E_{||}, E_{\perp}, E_{S\perp||}, \nu_{\perp||}, \nu_{\perp\perp}$  since the remaining quantities in equation (B.2) are linked by the relations:

$$\frac{E_{||}}{\nu_{\perp||}} = \frac{E_{\perp}}{\nu_{||\perp}} \quad (\text{B.3})$$

$$E_{S\perp\perp} = \frac{E_{\perp}}{2(1 + \nu_{\perp\perp})} \quad (\text{B.4})$$

Values for  $E_{||}$  and  $E_{\perp}$  can be obtained experimentally from tensile tests in  $0^\circ$  and  $90^\circ$  directions on unidirectional lamina, which were measured as  $E_{||} = 152.0$  GPa and  $E_{\perp} = 7.4$  GPa for T800/913 [196]. For calculation of the remaining values the fiber-volume fraction  $\phi$  is required, which is given by the “Rule of Mixture”:

$$E_{||} = \phi E_f + E_m(1 - \phi) \quad (\text{B.5})$$

The modulus for resin  $E_m$  and carbon-fiber  $E_f$  can either be determined experimentally by tensile tests, or used as provided by the manufacturer. In alternative  $\phi$  can be measured by experimental methods. Typically it is either quantified by ash analysis of the composite or from cross-sectional images as shown in figure B.1. For this case the fiber-volume fraction is obtained from the black-to-white ratio after threshold based binarization of the image [174]. For the investigated material combination T800/913 this yields as:



## B. Deriving elastic coefficients from micromechanical properties

$\phi = 0.511$  according to equation (B.5), using values from table B.1  
 $\phi = 0.516 \pm 0.027$  using average of 10 cross-sectional images

Since both values agree well within the error-margin, the values for  $E_m$  and  $E_f$  derived from the manufacturer's datasheet seem to be appropriate to describe the macroscopic properties of the lamina. Thus in the following it is assumed  $\phi = 0.511$ .

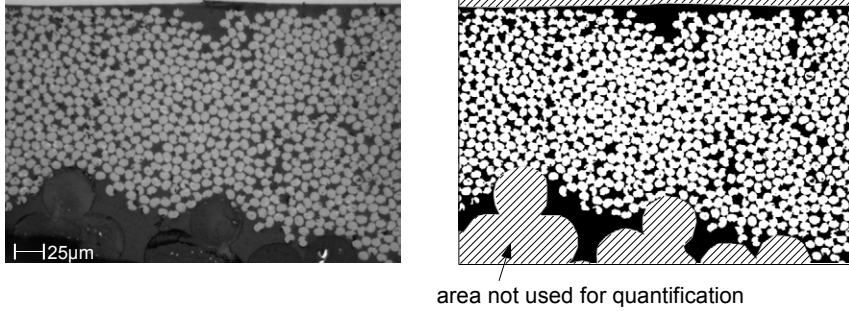


Figure B.1.: Cross-sectional image of CFRP (left) and image prepared for quantification of fiber-volume fraction (right).

To obtain the shear-modulus  $E_{S\perp||}$ , R. Förster et al. presented a semi-empirical formula obtained from a micromechanical approach using the shear-modulus of carbon fiber  $E_{Sf\perp||}$  and resin  $E_{Sm}$  [203]:

$$E_{S\perp||} = E_{Sm} \cdot \frac{1 + 0.4 \cdot \sqrt{\phi}}{(1 - \phi)^{29/20} + \frac{E_{Sm}}{E_{Sf\perp||}} \cdot \phi} \quad (\text{B.6})$$

Using the values from table B.1 the shear-modulus  $E_{S\perp||}$  for T800/913 yields as:

$$E_{S\perp||} = 4.2 \text{ GPa}$$

The poisson-number  $\nu_{\perp||}$  is obtained directly from the Rule of Mixture as:

$$\nu_{\perp||} = \phi \cdot \nu_{f\perp||} + (1 - \phi) \cdot \nu_m \quad (\text{B.7})$$

Using the values from table B.1 for T800/913 this yields as:

$$\nu_{\perp||} = 0.27$$

## B. Deriving elastic coefficients from micromechanical properties

The value for  $\nu_{\perp\perp}$  is obtained in a similar approach based on the Rule of Mixture, which was refined by R. Foye to include the limitation in shrinkage of the resin caused by the presence of the carbon fibers [204]:

$$\nu_{\perp\perp} = \phi \cdot \nu_{f\perp\perp} + (1 - \phi) \cdot \nu_m \left( \frac{\left(1 + \nu_m - \nu_{\perp||} \cdot \frac{E_m}{E_{||}}\right)}{\left(1 + \nu_m^2 + \nu_m \nu_{\perp||} \cdot \frac{E_m}{E_{||}}\right)} \right) \quad (\text{B.8})$$

This evaluates for T800/913 as:

$$\nu_{\perp\perp} = 0.46$$

Subsequently, the remaining unknowns in equation (B.3) and (B.4) can be calculated for T800/913 as:

$$\begin{aligned} E_{S\perp\perp} &= 2.5 \text{ GPa} \\ \nu_{||\perp} &= 0.01 \end{aligned}$$

Property	Value for T800/913	Source
$E_{  }$	152.0 GPa	[196]
$E_{\perp}$	7.4 GPa	[196]
$E_m$	3.4 GPa	[150]
$E_f$	294.0 GPa	[151]
$E_{Sf\perp  }$	50.0 GPa	[18]
$E_{Sm}$	1.21 GPa	[205]
$\nu_{f\perp  }$	0.20	[151]
$\nu_{f\perp\perp}$	0.50	[206]
$\nu_m$	0.35	[150]

Table B.1.: Properties used for calculation of the elastic coefficients of T800/913

These are all values required for calculation of the elastic coefficients used to describe the anisotropic properties of orthotropic lamina. An application of the Gauss-Jordan algorithm to equation (B.2) finally yields the elastic coefficients

matrix  $C_{iklm}$  for T800/913:

$$C_{iklm} = \begin{pmatrix} 154.0 & 3.7 & 3.7 & 0 & 0 & 0 \\ 3.7 & 9.5 & 5.2 & 0 & 0 & 0 \\ 3.7 & 5.2 & 9.5 & 0 & 0 & 0 \\ 0 & 0 & 0 & 2.5 & 0 & 0 \\ 0 & 0 & 0 & 0 & 4.2 & 0 \\ 0 & 0 & 0 & 0 & 0 & 4.2 \end{pmatrix} GPa \quad (B.9)$$

## B.2. Woven fabric lamina

In the case of woven fabric the direct calculation of  $C_{iklm}$  from microscopic elastic properties is more burdensome. N. Naik et al. established an approach to obtain the in-plane elastic coefficients of woven fabric based on the microscopic elastic properties of the used fiber and matrix [200–202]. This approach requires the elastic coefficients of the respective unidirectional lamina as derived from the approach above for the same fiber-matrix combination and fiber-volume fraction  $\phi$  as the woven fabric. Subsequently, the in-plane elastic coefficients of the woven fabric lamina are derived from the unidirectional properties based on the undulation of the fibers, their crimp, the number of fill and warp yarns and the repeat [200]. The out-of-plane elastic coefficients are assumed to be identical to those of the unidirectional lamina. Finally the symmetry of the stacking sequence and the woven fabric has to be taken into account by further modifications [201, 202].

In the following these steps are elucidated for the investigated KDK8054/120 material system. Following the approach by H. Schürmann above, the five basic elastic properties  $E_{||}$ ,  $E_{\perp}$ ,  $E_{S\perp||}$ ,  $\nu_{\perp||}$ ,  $\nu_{\perp\perp}$  for the unidirectional layup are calculated by equations (B.3), (B.4), (B.6) and (B.8) based on the material properties given in table B.2 and a fiber-volume fraction of  $\phi = 0.6$ . In contrast to the approach above, the transversal modulus  $E_{\perp}$  was not measured, so instead the semi-empirical formula established by [207] was used:

$$E_{\perp} = \frac{E_m}{1 - \nu_m^2} \cdot \frac{1 + 0.85 \cdot \phi^2}{(1 - \phi)^{1.25} + \frac{E_m}{(1 - \nu_m^2) \cdot E_{f\perp}} \cdot \phi} \quad (B.10)$$

Thus the five basic elastic properties are calculated as:

$$\begin{aligned} E_{||} &= 135.0 \text{ GPa} \\ E_{\perp} &= 12.9 \text{ GPa} \\ E_{S\perp||} &= 5.8 \text{ GPa} \\ \nu_{\perp||} &= 0.31 \\ \nu_{\perp\perp} &= 0.47 \end{aligned}$$

## B. Deriving elastic coefficients from micromechanical properties

In combination with equations (B.3) and (B.4) the remaining quantities  $\nu_{||\perp}$  and  $E_{S\perp\perp}$  are calculated:

$$\begin{aligned}\nu_{||\perp} &= 0.029 \\ E_{S\perp\perp} &= 4.386 \text{ GPa}\end{aligned}$$

Property	Value for KDK8054/120	Source
$E_{  }$	135.0 GPa (unidirectional)	[208]
$E_m$	3.5 GPa	[200]
$E_{f\perp}$	27.6 GPa	[206]
$E_{Sf\perp  }$	26.2 GPa	[206]
$E_{Sm}$	1.3 GPa	[200]
$\nu_{f\perp  }$	0.28	[206]
$\nu_{f\perp\perp}$	0.50	[206]
$\nu_m$	0.35	[200]

Table B.2.: Elastic properties used for calculation of the elastic coefficients of KDK8054/120

Finally the entries of the compliance matrix in equation (B.2) can be calculated and an application of the Gauss-Jordan algorithm to the compliance matrix yields the elastic coefficients matrix  $C_{iklm}$  for the unidirectional KDK8054/120 material system:

$$C_{iklm} = \begin{pmatrix} 139.7 & 7.6 & 7.6 & 0 & 0 & 0 \\ 7.6 & 16.9 & 8.1 & 0 & 0 & 0 \\ 7.6 & 8.1 & 16.9 & 0 & 0 & 0 \\ 0 & 0 & 0 & 4.9 & 0 & 0 \\ 0 & 0 & 0 & 0 & 5.8 & 0 \\ 0 & 0 & 0 & 0 & 0 & 5.8 \end{pmatrix} GPa \quad (B.11)$$

Following the approach in [200] the geometry of the woven fabric is required for further calculation of the lamina properties, which is summarized in table B.3.

Since the exact solution to obtain the elastic properties is very lengthy, it will not be repeated in detail in the following. Instead, the reader is referred to the publications of N. Naik et al. to deduce the lamina properties out of the  $C_{iklm}$ -matrix from equation (B.11) and table B.3 using the Parallel-Series model [200]. Subsequently the macroscopic properties of the  $[(0,90)_{f3}]_{sym}$

## B. Deriving elastic coefficients from micromechanical properties

stacking sequence according to [201,202] for the present twill 4/4 lamina can be calculated, which finally yields:

$$C_{iklm} = \begin{pmatrix} 67.5 & 7.6 & 7.6 & 0 & 0 & 0 \\ 7.6 & 67.5 & 8.1 & 0 & 0 & 0 \\ 7.6 & 8.1 & 16.9 & 0 & 0 & 0 \\ 0 & 0 & 0 & 4.9 & 0 & 0 \\ 0 & 0 & 0 & 0 & 4.6 & 0 \\ 0 & 0 & 0 & 0 & 0 & 4.6 \end{pmatrix} GPa \quad (B.12)$$

Compared to the experimentally determined value of  $C_{xxxx} = 68.0$  GPa the calculated properties seem very reasonable.

Property	Value for KDK8054/120	Source
Fabric thickness	0.4 mm	[208]
Counts warp	7 cm <sup>-1</sup>	[208]
Counts fill	7 cm <sup>-1</sup>	[208]
Yarn width warp	200 tex	[208]
Yarn width fill	200 tex	[208]
Fabric weight	280 g/m <sup>2</sup>	[208]

Table B.3.: Geometric properties of KDK8054/120 used for calculation of the elastic coefficients

## C. Finite element simulations of acoustic emission signals

Based on the constitutive equation (2.11) and the principle of virtual work  $W$  the Comsol program solves the differential equations, expressed in global or local stress and strain vector components  $\vec{\sigma}$  and  $\vec{\varepsilon}$  for an external stimulation [149]. Similar, the description of piezoelectricity in Comsol is based on the coupled equations in stress-charge form (2.54) and (2.55) and the variation principle of electrical energy  $\Omega_E$ . The acoustic emission signals are then deduced from the respective  $\vec{\varepsilon}$ -components at the model geometry's surface in the area of detection or from the electric field strength  $\Phi_m$  generated by the piezoelectric sensor material.

The principle of virtual work states that the variation of  $W$  induced by forces  $F_i$  and virtual displacements  $\delta u_i$  in an equilibrium state equals zero:

$$\delta W = \sum_i F_i \cdot \delta u_i = 0 \quad (\text{C.1})$$

Generally, the external applied virtual work equals the internal virtual work and in the case of a deformable body with volume  $V$  and surface  $A$ , results in a deformation state with new internal stress and strain components.

$$\int_A \delta \vec{u}^t \cdot \vec{F}_A \, dA + \int_V \delta \vec{u}^t \cdot \vec{F}_V \, dV - \int_V \delta \vec{\varepsilon}^t \cdot \vec{\sigma} \, dV = 0 \quad (\text{C.2})$$

The external applied forces  $\vec{F}_A$  and  $\vec{F}_V$  act on the surface and volume of the body, respectively. The constraint forces within the material are expressed by consistent internal stress  $\vec{\sigma}$  and strain  $\vec{\varepsilon}$  components, with the superscript  $t$  indicating the transposed vectors.

To extend the principle of virtual work for dynamic systems, mass accelerations are introduced. This yields the formulation of the d'Alembert principle which states that a state of dynamic equilibrium exists if the virtual work for arbitrary virtual displacements vanishes. Taking this into account and

introducing the material density  $\rho$  equation (C.2) becomes:

$$\int_A \delta \vec{u}^t \cdot \vec{F}_A dA + \int_V \delta \vec{u}^t \cdot \vec{F}_V dV - \int_V \delta \vec{\varepsilon}^t \cdot \vec{\sigma} dV - \int_V \rho \frac{\partial^2 \vec{u}}{\partial t^2} \cdot \delta \vec{u} dV = 0 \quad (\text{C.3})$$

For application of the piezoelectric effect for signal generation the stress  $\vec{\sigma}$  and strain  $\vec{\varepsilon}$  vectors are coupled to respective charge density displacement  $\vec{D}$  and electric field strength  $\vec{\Phi}$  vectors as given in equations (2.54) and (2.55). Here the variation principle of electrical energy states that the variation of  $\Omega_E$  equals  $\vec{D} \cdot \vec{\Phi}$  within the Volume  $V$  in an equilibrium state:

$$\delta \Omega_E = \int_V \vec{D} \cdot \vec{\Phi} dV \quad (\text{C.4})$$

This defines the basic differential equations solved within the Comsol environment for every finite element. For a closer review on FEM-simulation of continuum mechanics including discussions on boundary conditions and solver strategies, comprehensive information can be found in [156, 157] and in the software manual [149].

# Definitions and parameter conventions

<b>Fracture Mechanics</b>	
Strain-Energy Release Rate, Fracture toughness	$G, G_c$
Work	$W$
Strain energy	$\Omega$
Surface energy	$\Omega_{surface}$
Force, acting on surface, acting on volume, critical	$F, F_A, F_V, F_c$
Displacement vector, magnitude, virtual	$\vec{u}, u, \delta\vec{u}$
Stress-intensity factor, critical	$K, K_c$
Geometry correction tensor, function	$Y_{ik}(\theta), Y(\theta)$
Stress-Tensor, vector	$\sigma_{ik}, \vec{\sigma}$
Stress, parallel, perpendicular to fiber axis	$\sigma, \pm\sigma_{  }, \pm\sigma_{\perp}$
Shear stress, parallel, perpendicular to fiber axis	$\tau, \tau_{  }, \tau_{\perp}$
Fracture strength, fiber, matrix, fiber-matrix interface	$\sigma_{frac}, \sigma_f, \sigma_m, \sigma_{fm}$
Compressive macro-stress (coating)	$\sigma_{ct}$
Deformation-Tensor, vector	$\varepsilon_{lm}, \vec{\varepsilon}$
Deformation, normal	$\varepsilon$
Deformation, shear	$\gamma$
Elasticity-Tensor, complex	$C_{iklm}, C_{iklm}^*$
Modulus Young's, compressive, shear, fiber, matrix	$E, E_C, E_S, E_f, E_m$
Poisson number, fiber, matrix	$\nu, \nu_f, \nu_m$
Lame's constants	$\kappa, \mu$
Density	$\rho$
Fiber volume fraction	$\phi$
Crack motion vector, normal, normal magnitude	$\vec{b}, \vec{d}, d$
Moment tensor	$M_{ik}$



<b>Geometry</b>	
Coating width	$2x_{ct}$
Coating thickness	$z_{ct}$
Plate thickness	$z_d$
Crack length, increment	$a, \Delta a$
Area, crack increment	$A, \Delta A$
Volume, crack increment	$V, \Delta V$
Angle, polar coordinate	$\theta$
Distance, polar coordinate	$r = \sqrt{x^2 + y^2 + z^2}$
Cartesian vector, coordinates	$\vec{r}, (x, y, z)$
Unit vector	$\vec{e}$
<b>Elastic waves</b>	
Scalar potential	$\zeta$
Vector potential	$\vec{\psi}$
Sound velocity, longitudinal, transversal,	$c_i, c_L, c_T, c_R, c_P, c_G$
Rayleigh, phase, group	
Surface velocity, component	$\vec{v}, v_i$
Surface pressure, component	$\vec{p}, p_i$
Wave number	$k$
Wave length	$\lambda$
Time	$t$
Frequency, angular	$f, \omega$
Acoustic impedance	$Z$
Coefficient reflection, transmission	$R, \bar{R}$
See equation (2.46)	$\xi$
See equation (2.47)	$\eta$
Attenuation coefficient	$\alpha$
<b>Piezoelectricity</b>	
Electric energy	$\Omega_E$
Charge density displacement	$D_i$
Electrical permittivity	$\chi_{im}$
Electric field strength	$\Phi_m$
Piezoelectric constants, inverse	$S_{ikm}, S_{ikm}^{-1}$

---

**Acoustic emission**

---

Signal voltage	$U$
Maximum signal voltage	$U_{\max}$
Acoustic emission signal energy	$W_{AE}$
Counts to signal peak	$N_{peak}$
Counts of signals threshold crossings	$N_{AE}$
Time between first and last threshold crossing of signal	$t_{AE}$
Time of maximum signal voltage	$t_{peak}$
Time of first threshold crossing (arrival time)	$t_0$
Reverberation and initiation frequency	$f_{rev}, f_{init}$
Frequency of maximum signal contribution	$f_{peak}$
Frequency centroid	$f_{centroid}$
Proportionality constant	$\beta$
Sampling rate	$\Delta T^{-1}$
Source excitation time	$T_e$
Materials relaxation time	$T_r$
Crack separation mode functional [37]	$v(\theta)$

---

**Pattern recognition**

---

Number of clusters	$P$
Number of features, minimum	$Q, Q_{min}$
Number of objects in dataset	$N$
Number of feature combinations	$N_{tot}$
Feature vector, element	$\vec{q}, q_i$
Vector of features, element	$\vec{g}, g_j$
Node weight vector, element, total	$\vec{w}, w_i, \vec{w}_{tot}$
Partition	$B = \{B_1, B_2, ..., B_P\}$
Distance in feature space	$X$
Scatter matrix, within, total	$\vec{\vec{X}}_W, \vec{\vec{X}}_T$
Number of object pairs	$\Lambda$
Rand Index	$RAND$
Wilks $\lambda$ -value	$WILK$
Dunn Index	$DUNN$
Tou Index	$TOU$
Davies-Bouldin Index	$DB$
Hubert's $\gamma$ Index	$GAMMA$
See equation (2.74)	$\Xi_{ij}$
Error surface function	$L$
Learning rate	$\iota$

---

Other	
Nabla-operator	$\nabla f = \left( \frac{\partial f}{\partial x} e_x + \frac{\partial f}{\partial y} e_y + \frac{\partial f}{\partial z} e_z \right)$ $\vec{\nabla} \cdot \vec{f} = \left( \frac{\partial f_x}{\partial x} + \frac{\partial f_y}{\partial y} + \frac{\partial f_z}{\partial z} \right)$ $\vec{\nabla} \times \vec{f} = \left( \frac{\partial f_z}{\partial y} - \frac{\partial f_y}{\partial z} \right) e_x + \left( \frac{\partial f_x}{\partial z} - \frac{\partial f_z}{\partial x} \right) e_y + \left( \frac{\partial f_y}{\partial x} - \frac{\partial f_x}{\partial y} \right) e_z$
Laplace-operator	$\Delta = \nabla \cdot \nabla$
Einstein notation	$(X \cdot Y)_{ij} = \sum_{k=1}^n X_{ik} Y_{kj} \equiv (X \cdot Y)_{ij} = X_{ik} Y_{kj}$
Green function	$\Gamma_{ipq}$
Heavyside function	$H(t)$
Angle	$\varphi$
Function input, output	$h_E(t), h_A(t)$
Transfer function	$J(t)$
Mean value of $N$ objects	$\langle x \rangle = \sum_{i=1}^N \frac{x_i}{N}$
Variance of $N$ objects	$var(x) = \sum_{i=1}^N \frac{x_i - \langle x \rangle}{N}$
Standard deviation of $N$ objects	$stdev(x) = \sqrt{\frac{1}{N} \sum_{i=1}^N (x_i - \langle x \rangle)^2}$
Number of samples	$2N_S$
Wavelet function	$\Psi$
Wavelet Transformation scales	$\vartheta, \varsigma$
Wavelet Transformation coefficient	$\aleph_{CWT}$

# Bibliography

- [1] C. Grosse, M. Ohtsu, editors. *Acoustic Emission Testing in Engineering - Basics and Applications*. Springer, 2008.
- [2] M. Giordano, A. Calabro, C. Esposito, A. D'Amore, L. Nicolais. An acoustic-emission characterization of the failure modes in polymer-composite materials. *Composites Science and Technology*, **58**, 1923–1928, 1998.
- [3] J. Bohse, J. Chen, A. Brunner. Acoustic Emission Analysis and Micro-Mechanical Interpretation of Mode I Fracture Toughness Tests on Composite Materials. *Fracture of Polymers and Composites and Adhesives*, **27**, 15–26, 2000.
- [4] J. Bohse, J. Chen. Acoustic Emission Examination of Mode I, Mode II and Mixed-Mode I/II Interlaminar Fracture of Unidirectional Fiber-Reinforced Polymers. *Journal of Acoustic Emission*, **19**, 01–10, 2001.
- [5] W. Haselbach, B. Lauke. Acoustic emission of debonding between fibre and matrix to evaluate local adhesion. *Composites Science and Technology*, **63**:15, 2155 – 2162, 2003.
- [6] C. R. Ramirez-Jimenez, N. Papadakis, N. Reynolds, T. Gan, P. Purnell, M. Pharaoh. Identification of failure modes in glass/polypropylene composites by means of the primary frequency content of the acoustic emission event. *Composites Science and Technology*, **64**, 1819–1827, 2004.
- [7] A. Marec, J.-H. Thomas, R. Guerjouna. Damage characterization of polymer-based composite materials: Multivariable analysis and wavelet transform for clustering acoustic emission data. *Mechanical Systems and Signal Processing*, **22**, 1441–1464, 2008.
- [8] X. Li, C. Ramirez, E. L. Hines, M. S. Leeson, P. Purnell, M. Pharaoh. Pattern Recognition of Fiber-reinforced Plastic Failure Mechanism using Computational Intelligence Techniques. *Neural Networks*, pages 2340–2345. IEEE World Congress on Computational Intelligence, 2008.

- [9] C. Lin, S. Leigh, C. Berndt. Acoustic emission responses of plasma-sprayed alumina-3% deposits. *Thin Solid Films*, **310**, 108–11, 1997.
- [10] X. Q. Ma, S. Cho, M. Takemoto. Acoustic emission source analysis of plasma sprayed thermal barrier coatings during four-point bend tests. *Surface and Coatings Technology*, **139**, 55–62, 2001.
- [11] S. Nikulin, V. Khanzhin, A. Rozhnov, A. Babukin, V. Belov. Analysis of Crack Resistance and Quality of Thin Coatings by Acoustic Emission. *The 8th International Conference of the Slovenian Society for Non-Destructive Testing, Portoroz, Slovenia*, 2005.
- [12] J. Miguel, J. Guilemany, B. Mellor, Y. Xu. Acoustic emission study on WC/Co thermal sprayed coatings. *Materials Science and Engineering A*, **352**, 55–63, 2003.
- [13] H. P. Tada, C. Paris, G. R. Irwin. *The Stress Analysis of Cracks Handbook*. Paris Productions, 2nd ed., 1985.
- [14] A. A. Griffith. The phenomena of rupture and flow in solids. *Philosophical Transactions of the Royal Society of London Series A*, **221**, 163–198, 1921.
- [15] G. Irwin. Analysis of stresses and strains near the end of a crack traversing a plate. *Journal of Applied Mechanics*, **24**, 361–364, 1957.
- [16] N. E. Dowling. *Mechanical Behavior of Materials*. Prentice Hall, New Jersey, 2nd ed., 1999.
- [17] L. Issler, H. Ruoff, P. Häfele. *Festigkeitslehre Grundlagen*. Springer, Berlin, 1995.
- [18] H. Schürmann. *Konstruieren mit Faser-Kunststoff-Verbunden*. Springer, Berlin, 2nd ed., 2007.
- [19] F. L. Matthews, R. D. Rawlings. *Composite Materials: Engineering and Science*. Woodhead Publishing Ltd., Cambridge, 1999.
- [20] A. Puck. *Festigkeitsanalyse von Faser-Matrix-Laminaten Modelle für die Praxis*. Carl Hanser Verlag, Munich, 1996.
- [21] Z. Hashin. Analysis of cracked laminates - A variational approach. *Mechanics of Materials*, **4**, 121–136, 1985.

- [22] J. A. Nairn. The Strain Energy Release Rate of Composite Microcracking: A Variational Approach. *Journal of Composite Materials*, **23**, 1106–1129, 1989.
- [23] J. A. Nairn, S. Hu. Matrix Microcracking. *Damage Mechanics of Composite Materials*, **9**, 187–243, 1994.
- [24] T. Tanaka, H. Nakayama, A. Sakaida, N. Horikawa. Estimation of Tensile Strength Distribution for Carbon Fiber with Diameter Variation Along Fiber. *Materials Science Research International*, **5:2**, 90–97, 1999.
- [25] P. R. Chalkera, S. J. Bulla, D. S. Rickerby. A review of the methods for the evaluation of coating-substrate adhesion. *Materials Science and Engineering: A*, **140**, 583–592, 1991.
- [26] L. Liu, J. W. Holmes. Experimental Technique for Elevated Temperature Mode I Fatigue Crack Growth Testing of Ni-Base Metal Foils. *Journal of Engineering Materials*, **129**, 594–602, 2007.
- [27] H. W. Wang, Y. L. Kang, Z. F. Zhang, Q. H. Qin. Size Effect on the Fracture Toughness of Metallic Foil. *International Journal of Fracture*, **123**, 177–185, 2003.
- [28] A. Hadrboletz, B. Weiss, G. Khatibi. Fatigue And Fracture Properties Of Thin Metallic Films. *International Journal of fracture*, **107**, 307–327, 2001.
- [29] ASTM B533-85: Peel Strength of Metal Electroplated Plastics. Technical report, ASTM International, 2004.
- [30] Y. Wei, J. W. Hutchinson. Interface strength, work of adhesion and plasticity in the peel test. *International Journal of Fracture*, **93**, 315–333, 1998.
- [31] R. Beydon, G. Bernhart, Y. Segui. Measurement of metallic coatings adhesion to fibre reinforced plastic materials. *Surface and Coatings Technology*, **126**, 39–47, 2000.
- [32] B. A. Auld. *Acoustic Fields and Waves in Solids*. Krieger Publishing Company, Malabar, 2nd ed., 1990.
- [33] L. D. Landau, E. M. Lifschitz. *Elastizitätstheorie*. Akademie Verlag GmbH, Berlin, 1987.

- [34] L. B. Freund. The initial wave front emitted by a suddenly extending crack in an elastic solid. *Journal of Applied Mechanics*, **39**, 601–602, 1972.
- [35] K. Aki, P. G. Richards. *Quantitative seismology, theory and methods*. University Science Books, Sausalito, 1980.
- [36] M. Ohtsu. Source Mechanism and Waveform Analysis of Acoustic Emission in Concrete. *Journal of Acoustic Emission*, **2**:1, 103–112, 1982.
- [37] M. Lysak. Development of the theory of acoustic emission by propagating cracks in terms of fracture mechanics. *Engineering Fracture Mechanics*, **55**:3, 443–452, 1996.
- [38] M. Ohtsu, K. Ono. A generalized theory of acoustic emission and Green's function in a half space. *Journal of Acoustic Emission*, **3**, 27–40, 1984.
- [39] M. Ohtsu, K. Ono. The generalized theory and source representation of acoustic emission. *Journal of Acoustic Emission*, **5**, 124–133, 1986.
- [40] C. U. Grosse. *Quantitative Non-destructive Testing of Construction Materials Using Acoustic Emission Technique and Ultrasound*. PhD thesis, University of Stuttgart, 1996.
- [41] H. N. G. Wadley, C. B. Scruby. *Acoustic Emission Source Characterization*. *Advances in Acoustic Emission*. Dunhart Publishers, Knoxville, 1981.
- [42] M. Ohtsu. Source Inversion of Acoustic Emission Waveform. *Structural Engineering Earthquake Engineering*, **5**:2, 275–283, 1988.
- [43] E. R. Green. Acoustic emission sources in a cross-ply laminated plate. *Composites Engineering*, **5**, 1453–1469, 1995.
- [44] E. R. Green. Acoustic Emission in Composite Laminates. *Journal of Nondestructive Evaluation*, **17**:3, 117–127, 1998.
- [45] M. Giordano, L. Condelli, L. Nicolais. Acoustic emission wave propagation in a viscoelastic plate. *Composites Science and Technology*, **59**, 1735–1743, 1999.
- [46] R. Stoneley. Elastic Waves at the Surface of Separation of Two Solids. *Proceedings of the Royal Society of London. Series A, Containing Papers of a Mathematical and Physical Character*, **106**:738, 416–428, 1924.

- [47] A. E. H. Love. *Some problems of geodynamics*. Cambridge University Press, 1911.
- [48] H. Lamb. On Waves in an Elastic Plate. *Proceedings of the Royal Society of London. Series A, Containing Papers of a Mathematical and Physical Character*, **93**, 114–128, 1917.
- [49] L. Rayleigh. On Waves Propagated along the Plane Surface of an Elastic Solid. *Proceedings of the London Mathematical Society*, **1-17**, 4–11, 1885.
- [50] J. Krautkrämer, H. Krautkrämer. *Ultrasonic Testing of Materials*. American Society for Testing and Materials, 4th ed., 1990.
- [51] L. Cremer, M. Heckl. *Körperschall Physikalische Grundlagen und technische Anwendungen*. Springer Verlag, Berlin, 1996.
- [52] J. Yin, Y. Shui, W. Jiang. The generation of bulk acoustic waves by interdigital transducers. *Chinese Physical Letters*, **6**:10, 461–465, 1989.
- [53] E. H. Bergman, R. Shahbender. Effect of statically applied stresses on the velocity of propagation of ultrasonic waves. *Journal of Applied Physics*, **29**, 1736–1738, 1958.
- [54] M. J. Eaton, R. Pullin, K. M. Holford, C. A. Featherston. AE Wave Propagation and Novel Source Location in Composite Plates. *28th European Conference on Acoustic Emission Testing, Berlin, Germany*, 2008.
- [55] A. A. Pollock. Classical Wave Theory in Practical AE Testing. *Proceedings of the 8th International AE Symposium*, pages 708–721, 1986.
- [56] W. H. Prosser. Advanced AE Techniques in Composite Materials Research. *Journal of Acoustic Emission*, **14**:3-4, 1–11, 1996.
- [57] G. Neau, M. Deschamps, M. J. S. Lowe. Group velocity of Lamb waves in anisotropic plates: Comparison between theory and experiments. *AIP Conference Proceedings*, volume 557, pages 81–88, 2001.
- [58] I. M. Ward. *Mechanical Properties of Solid Polymers*. John Wiley & Sons Ltd., New York, 1971.
- [59] A. G. Beattie. Acoustic emission, principles and Instrumentation. *Journal of Acoustic Emission*, **2**:1-2, 95–128, 1983.



- [60] G. Gautschi. *Piezoelectric Sensorics*. Springer, Berlin, 2002.
- [61] J. Keprt, P. Benes. The determination of uncertainty in the calibration of acoustic emission sensors. *International Journal of Microstructure and Materials Properties*, **4**:1, 85–103, 2009.
- [62] J. Bohse. Acoustic Emission Examination of Polymer-Matrix Composites. *Journal of Acoustic Emission*, **22**, 208–223, 2004.
- [63] P. D. Wilcox, C. K. Lee, J. J. Scholey, M. I. Friswell, M. Wisnom, B. W. Drinkwater. Progress Towards a Forward Model of the Complete Acoustic Emission Process. *Advanced Materials Research*, **13-14**, 69–75, 2006.
- [64] ASTM-E1106-86: Standard Method for Primary Calibration of Acoustic Emission Sensors. Technical report, ASTM International, 1997.
- [65] NDIS 2109-91: Methods for Absolute calibration of Acoustic Emission Transducers by Reciprocity Technique. Technical report, Japanese Society for Nondestructive Inspection, 1991.
- [66] F. R. Breckenridge, M. Greenspan. Surface-Wave Displacement: Absolute Measurements using a Capacitance Transducer. *Journal of the Acoustic Society of America*, **69**:2, 1177–1185, 1981.
- [67] L. Goujon, J. C. Baboux. Behaviour of acoustic emission sensors using broadband calibration techniques. *Measurement Science and Technology*, **14**, 903–908, 2003.
- [68] P. Theobald, B. Zeqiri, J. Avison. Couplants and Their Influence on AE Sensor Sensitivity. *Journal of Acoustic Emission*, **26**, 91–97, 2008.
- [69] M. A. Hamstad, A. O’Gallagher, J. Gary. A Wavelet Transform Applied To Acoustic Emission Signals: Part 2: Source Location. *Journal of Acoustic Emission*, **20**, 62–82, 2002.
- [70] H. Kühnicke, E. Schulze, D. Voigt. Verbesserte Lokalisation mittels Signalformanalyse. *DGZfP-BB*, volume 105, pages 44–51, 2007.
- [71] D. O. Harris, H. L. Dunegan. Continuous Monitoring of Fatigue-crack Growth by Acoustic-emission Techniques. *Experimental Mechanics*, **14**:2, 71–81, 1974.
- [72] A. Berkovits, D. Fang. Study of fatigue crack characteristics by acoustic emission. *Engineering Fracture Mechanics*, **51**:3, 401–409, 1995.

- [73] O. Ceysson, M. Salvia, L. Vincent. Damage Mechanisms Characterisation Of Carbon Fibre/Epoxy Composite Laminates By Both Electrical Resistance Measurements And Acoustic Emission Analysis. *Scripta Materialia*, **34**, 1273–1280, 1996.
- [74] J. Martinez-Fernandez, G. Morscher. Room and elevated temperature tensile properties of single tow Hi-Nicalon, carbon interphase, CVI SiC matrix minicomposites. *Journal of the European Ceramic Society*, **20**, 2627–2636, 2000.
- [75] P. Alander, L. Lassila, A. Tezvergil, P. Vallittu. Acoustic emission analysis of fiber-reinforced composite in flexural testing. *Dental Materials*, **20**, 305–312, 2004.
- [76] M. A. Hamstad, A. O’Gallagher, J. Gary. A Wavelet Transform Applied To Acoustic Emission Signals: Part 1: Source Identification. *Journal of Acoustic Emission*, **20**, 39–61, 2002.
- [77] ASTM E1316-10a: Standard Terminology for Nondestructive Examinations. Technical report, ASTM International, 2010.
- [78] DGZfP-SE 3: Richtlinie zur Charakterisierung des Schallemissions-Prüfgeräts im Labor. Technical report, DGZfP, 1991.
- [79] J. H. Kurz. *Verifikation von Bruchprozessen bei gleichzeitiger Automatisierung der Schallemissionsanalyse an Stahl- und Stahlfaserbeton*. PhD thesis, University of Stuttgart, 2006.
- [80] H. Akaike. Markovian representation of stochastic process and its application to the analysis of autoregressive moving average processes. *Annals of the Institute of Statistical Mathematics*, **26**, 363–387, 1974.
- [81] S. Bancroft. An algebraic solution of the GPS equations. *IEEE Transactions on Aerospace and Electronic Systems*, **21**:7, 56–59, 1985.
- [82] W. Skopalik, M. G. R. Sause. *Density Ville Rev. 0.99*. University of Augsburg, <http://www.physik.uni-augsburg.de/exp2/downloads.de.shtml>, 2009.
- [83] W. Skopalik, M. G. R. Sause, T. Köck, S. Horn. Visualisierung von Schallemissionslokalisierungen. *DGZfP-BB*, volume 118, pages 62–69, 2009.

- [84] R. Polikar. Pattern Recognition. *Wiley Encyclopedia of Biomedical Engineering*, chapter Pattern Recognition. John Wiley & Sons, Inc., New York, 2006.
- [85] M. Theus. Interactive Data Visualization using Mondrian. *Journal of Statistical Software*, **7**:11, 1–9, 2002.
- [86] K. Florek, J. Lukaszewicz, J. Perkal, H. Steinhaus, S. Zubrzchi. Sur la liason et la division des points d'un ensemble fini. *Colloquium Mathematicum*, **2**, 282–285, 1951.
- [87] K. Pearson. On lines and planes of closest fit to a system of points in space. *The London, Edinburgh, and Dublin Philosophical Magazine and Journal of Science*, **6**:2, 559–572, 1901.
- [88] M. Loeve. *Probability Theory*. Van Nostrand, New York, 1963.
- [89] H. Zha, C. Ding, M. Gu, X. He, H. Simon. Spectral Relaxation for K-means Clustering. *Neural Information Processing Systems*, **14**, 1057–1064, 2001.
- [90] C. Ding, X. He. K-means Clustering via Principal Component Analysis. *Proceedings of International Conference on Machine Learning*, pages 225–232, 2004.
- [91] B. S. Everitt. *Cluster Analysis*. John Wiley & Sons Inc., New York, 3rd ed., 1993.
- [92] K. Fukunaga, J. Mantock. Nonparametric discriminant analysis. *IEEE Transactions on Pattern Analysis and Machine Intelligence*, **5**:6, 671–678, 1983.
- [93] A. A. Anastassopoulos, T. P. Philippidis. Clustering Methodology for the Evaluation of Acoustic Emission from Composites. *Journal of Acoustic Emission*, **13**, 11–21, 1995.
- [94] N. Ativitavas, T. Pothisiri, T. J. Fowler. Identification of Fiber-reinforced Plastic Failure Mechanisms from Acoustic Emission Data using Neural Networks. *Journal of Composite Materials*, **40**:3, 193–226, 2006.
- [95] T. Philippidis, V. Nikolaidis, A. Anastassopoulos. Damage Characterisation of C/C laminates using Neural Network Techniques on AE signals. *NDT&E International*, **31**, 329–340, 1998.

- [96] N. R. Pal, K. Pal, J. M. Keller, J. Bezdek. A possibilistic fuzzy c-means clustering algorithm. *IEEE Transactions on Fuzzy Systems*, **13**:4, 517–530, 2005.
- [97] S. Haykin. *Neural Networks, A Comprehensive Foundation*. Prentice Hall, Englewood Cliffs, 2nd ed., 1998.
- [98] T. Kohonen. *Self Organizing Maps*. Springer, Berlin, 2000.
- [99] C. M. Bishop. *Neural Networks for Pattern Recognition*. Clarendon Press, Oxford, 1995.
- [100] G. A. Carpenter, S. Grossberg. The ART of adaptive pattern recognition by a selforganizing neural network. *Computer*, **21**:3, 77–88, 1988.
- [101] S. Huguet, N. Godin, R. Gaertner, L. Salmon, D. Villard. Use of acoustic emission to identify damage modes in glass fibre reinforced polyester. *Composites Science and Technology*, **62**, 1433–1444, 2002.
- [102] H. Steinhaus. Sur la division des corps matériels en parties (in French). *Bulletin de l'Academie Polonaise des Sciences*, **4**:12, 801–804, 1956.
- [103] J. B. MacQueen. Some Methods for classification and Analysis of Multivariate Observations. *Proceedings of 5th Berkeley Symposium on Mathematical Statistics and Probability*, pages 281–297, 1967.
- [104] S. P. Lloyd. Least squares quantization in PCM. *IEEE Transactions on Information Theory*, **28**:2, 129–137, 1982.
- [105] D. Arthur, S. Vassilvitskii. k-means++: the advantages of careful seeding. *Proceedings of the eighteenth annual ACM-SIAM symposium on Discrete algorithms*, pages 1027–1035, 2007.
- [106] Enviroacoustics S.E. *NOESIS - Advanced Acoustic Emission Data Analysis and Pattern Recognition & Neural Networks Software for Acoustic Emission Applications*, 2006.
- [107] D. Hebb. *The organization of behavior: a neuropsychological theory*. Wiley, New York, 1949.
- [108] W. M. Rand. Objective criteria for the evaluation of clustering methods. *Journal of the American Statistical Association*, **66**, 846–850, 1971.
- [109] J. C. Dunn. Well separated clusters and optimal fuzzy partitions. *Journal of Cybernetics*, **4**, 95–104, 1974.

- [110] J. T. Tou. DYNOC - A dynamic optimal cluster-seeking technique. *International Journal of Computer and Information Sciences*, **8**:6, 541–547, 1979.
- [111] D. L. Davies, D. W. Bouldin. A Cluster Separation Measure. *IEEE Transactions on Pattern Analysis and Machine Intelligence*, **1**:2, 224–227, 1979.
- [112] L. J. Hubert, P. Arabie. Comparing partitions. *Journal of Classification*, **2**, 193–218, 1985.
- [113] V. S. Tseng, C.-P. Kao. Efficiently Mining Gene Expression Data via a Novel Parameterless Clustering Method. *IEEE/ACM Transactions on Computational Biology and Bioinformatics*, **2**:4, 355–365, 2005.
- [114] M. S. Aldenderfer, R. K. Blashfield. *Cluster Analysis*. Sage Publications, Beverly Hills, 1984.
- [115] L. Hubert, J. Schultz. Quadratic assignment as a general data-analysis strategy. *British Journal of Mathematical and Statistical Psychology*, **29**, 190–241, 1976.
- [116] P. Rousseeuw. Silhouettes: a graphical aid to the interpretation and validation of cluster analysis. *Journal of Computational and Applied Mathematics*, **20**, 53–65, 1987.
- [117] L. Goodman, W. Kruskal. Measures of associations for cross-validations. *Journal of the American Statistical Association*, **49**, 732–764, 1954.
- [118] A. Anastassopoulos, A. Tsimogiannis, D. Kouroussis. Unsupervised Classification of Acoustic Emission Sources from Aerial Man Lift Devices. *15th World Conference on NDT, Roma, Italy*, 2000.
- [119] A. N. Tsimogiannis, V. N. Nikolaidis, A. A. Anastassopoulos. Hydrogen Cylinder Acoustic Emission Testing and Data Evaluation with Supervised Pattern Recognition. *NDT.net*, **7**:9, 1–6, 2002.
- [120] A. A. Anastassopoulos, D. A. Kouroussis, V. N. Nikolaidis, A. Proust, A. G. Dutton, M. J. Blanch, L. E. Jones, P. Vionis, D. J. Lekou, D. R. V. vanDelft, P. A. Joosse, T. P. Philippidis, T. Kossivas, G. Fernando. Structural Integrity Evaluation of Wind Turbine Blades Using Pattern Recognition Analysis on Acoustic Emission Data. *Proceedings of the 25th European Conference on Acoustic Emission Testing, Prague, Czech Republic*, 2002.

- [121] A. Waibel, T. Hanazawa, G. Hinton, K. Shikano, K. Lang. Phoneme recognition using time delay neural networks. *IEEE Transactions on Acoustics, Speech, & Signal Processing*, **37**:3, 328–339, 1989.
- [122] J. R. Jang, C. Sun, E. Mizutani. *Neuro-Fuzzy and Soft Computing: A Computational Approach to Learning and Machine Intelligence*. Prentice-Hall, Englewood Cliffs, 1997.
- [123] G. A. Carpenter, S. Grossberg, S. Markuzon, J. H. Reynolds, D. B. Rosen. Fuzzy ARTMAP: A neural network architecture for incremental supervised learning of analog multidimensional maps. *IEEE Transactions on Neural Networks*, **3**:5, 698–713, 1992.
- [124] M. Mitchell. *An Introduction to Genetic Algorithm (Complex Adaptive Systems)*. The MIT Press, Cambridge, 1998.
- [125] R. C. Eberhart, Y. Shi, J. Kennedy. *Swarm Intelligence*. Morgan Kaufmann Publishers, Burlington, 2001.
- [126] J. R. Quinlan. *Programs for Machine Learning*. Morgan Kaufmann Publishers, Burlington, 1992.
- [127] S. Günter, H. Bunke. Validation indices for graph clustering. *Pattern Recognition Letters*, **24**, 1107–1113, 2003.
- [128] M. G. R. Sause, D. Schultheiß, S. Horn. Acoustic emission investigation of coating fracture and delamination in hybrid carbon fiber reinforced plastic structures. *Journal of Acoustic Emission*, **26**, 1–13, 2008.
- [129] M. G. R. Sause, F. Haider, S. Horn. Quantification of metallic coating failure on carbon fiber reinforced plastics using acoustic emission. *Surface and Coatings Technology*, **204**:3, 300 – 308, 2009.
- [130] C. E. Shannon. Communication in the Presence of Noise. *Proceedings of the I.R.E.*, **37**:1, 10–21, 1949.
- [131] Q. Q. Ni, E. Jinen. Fracture Behavior And Acoustic Emission In Bending Tests On Single-Fiber Composites. *Engineering Fracture Mechanics*, **56**, 779–796, 1997.
- [132] Q. Q. Ni, M. Iwamoto. Wavelet transform of acoustic emission signals in failure of model composites. *Engineering Fracture Mechanics*, **69**, 717–728, 2002.

- [133] P. Addison, J. Watson, T. Feng. Low-Oscillation Complex Wavelets. *Journal of Sound and Vibration*, **254**:4, 733–762, 2002.
- [134] B. Vidakovic. *Statistical Modeling by Wavelets*. John Wiley & Sons Inc., New York, 1999.
- [135] H.-I. Choi, W. Williams. Improved Time-Frequency Representation of Multicomponent Signals Using Exponential Kernels. *IEEE Transactions on Acoustics, Speech and Signal Processing*, **37**:6, 862–872, 1989.
- [136] G. Qi, A. Barhorst, J. Hashemi, G. Kamala. Discrete wavelet decomposition of acoustic emission signals from carbon-fiber-reinforced composites. *Composites Science and Technology*, **57**, 389–403, 1997.
- [137] H. Suzuki, T. Kinjo, Y. Hayashi, M. Takemoto, K. Ono. Wavelet Transform of Acoustic Emission Signals. *Journal of Acoustic Emission*, **14**, 69–84, 1996.
- [138] Vallen Systeme GmbH (Munich, Germany), Aoyama Gakuin University (Tokyo, Japan). *AGU-Vallen Wavelet*, 2001.
- [139] M. A. Hamstad. Comparison of Wavelet Transform and Choi-Williams Distribution to Determine Group Velocities for Different Acoustic Emission Sensors. *Journal of Acoustic Emission*, **26**, 40–59, 2008.
- [140] D. M. Egle, C. A. Taturo. Analysis of Acoustic-Emission Strain Waves. *Journal of the Acoustical Society of America*, **41**:2, 321–327, 1967.
- [141] R. W. B. Stephens, A. A. Pollock. Waveforms and Frequency Spectra of Acoustic Emissions. *Journal of the Acoustical Society of America*, **50**:3, 904–910, 1971.
- [142] D. M. Egle, A. E. Brown. Considerations for the Detection of Acoustic Emission Waves in Thin Plates. *Journal of the Acoustical Society of America*, **57**:3, 591–597, 1975.
- [143] M. R. Gorman, W. H. Prosser. AE Source Orientation by Plate Wave Analysis. *Journal of Acoustic Emission*, **9**, 283–288, 1991.
- [144] W. H. Prosser. *The Propagation Characteristics of the Plate Modes of Acoustic Emission Waves in Thin Aluminum Plates and Thin Graphite/Epoxy Composite Plates and Tubes*. PhD thesis, Johns Hopkins University, Baltimore, 1991.

- [145] W. H. Prosser, K. E. Jackson, S. Kellas, B. T. Smith, J. McKeon, A. Friedman. Advanced Waveform-Based Acoustic Emission Detection of Matrix Cracking in Composites. *Materials Evaluation*, **53**:9, 1052–1058, 1995.
- [146] W. H. Prosser, M. A. Hamstad, J. Gary, A. O. Gallagher. Finite Element and Plate Theory Modeling of Acoustic Emission Waveforms. *Journal of Nondestructive Evaluation*, **18**:3, 83–90, 1999.
- [147] J. Bohse. Acoustic emission characteristics of micro-failure processes in polymer blends and composites. *Composites Science and Technology*, **60**, 1213–1226, 2000.
- [148] C. Scruby, D. Buttle. Quantitative Fatigue Crack Measurement by Acoustic Emission. K. J. Marsh, R. Smith, R. O. Ritchie, editors, *Crack Measurement: Techniques and Applications*, pages 207–287, 1992.
- [149] Comsol AB. *COMSOL Multiphysics - Structural Mechanics Module*, 2008.
- [150] *HexPly 913 - Manufacturers datasheet*, 2009.
- [151] *Torayca T800S - Manufacturers datasheet*, 2009.
- [152] M. Castaings, C. Bacon, B. Hosten, M. V. Predoi. Finite element predictions for the dynamic response of thermo-viscoelastic material structures. *Journal of the Acoustic Society of America*, **115**:3, 1125–1133, 2004.
- [153] D. W. Greve, J. J. Neumann, J. H. Nieuwenhuis, I. J. Oppenheim, N. L. Tyson. Use of Lamb waves to monitor plates: experiments and simulations. *Proceedings of the Society of Photo-Optical Instrumentation Engineers, SPIE-5765*, pages 281–292, 2005.
- [154] J. H. Nieuwenhuis, J. Neumann, D. W. Greve, I. J. Oppenheim. Generation and detection of guided waves using PZT wafer transducers. *IEEE Transactions Ultrasonics, Ferroelectrics and Frequency Control*, **52**, 2103–2111, 2005.
- [155] H. Hatano, T. Chaya, S. Watanabe, K. Jinbo. Reciprocity calibration of impulse responses of acoustic emission transducers. *IEEE Transactions on Ultrasonics, Ferroelectrics, and Frequency Control*, **45**:5, 1221–1228, 1998.



- [156] G. A. Mohr. *Finite Elements for Solids, Fluids and Optimization*. Oxford Science Publications, 1992.
- [157] O. C. Zienkiewicz. *The Finite Element Method for Solid and Structural Mechanics*. Elsevier, Oxford, 6th ed., 2005.
- [158] DIN-EN-ISO 14125: Determination of flexural properties. Technical report, Deutsches Institut für Normung, 1998.
- [159] L. Gaul, S. Hurlebaus, L. Jacobs. Localization of a "Synthetic" Acoustic Emission Source on the Surface of a Fatigue Specimen. *Research in Nondestructive Evaluation*, **13**:2, 105–117, 2001.
- [160] M. A. Hamstad, A. O’Gallagher, J. Gary. Effects of Lateral Plate Dimensions on Acoustic Emission Signals from Dipole Sources. *Journal of Acoustic Emission*, **19**, 258–274, 2001.
- [161] C. B. Scruby, H. N. G. Wadley. A calibrated capacitance transducer for the detection of acoustic emission. *Journal of Physics D: Applied Physics*, **11**, 1487–1494, 1978.
- [162] H. C. Kim, H. K. Park. Laser interferometry system for measuring displacement amplitude of acoustic emission signals. *Journal of Physics D: Applied Physics*, **17**, 673–675, 1984.
- [163] K. Ono, H. Cho, T. Matsuo. Transfer functions of acoustic emission sensors. *Journal of Acoustic Emission*, **26**, 72–90, 2008.
- [164] H. N. Hsu, F. R. Breckenridge. Characterization and calibration of acoustic emission sensors. *Materials Evaluation*, **39**:1, 60–68, 1981.
- [165] T. Boczar, M. Lorenc. Determining the Repeatability of Acoustic Emission Generate by the Hsu-nielsen Calibrating Source. *Molecular and Quantum Acoustics*, **25**, 177–192, 2004.
- [166] M. G. R. Sause, S. Horn. Simulation of acoustic emission in planar carbon fiber reinforced plastic specimens. *Journal of Nondestructive Evaluation*, **29**:2, 123–142, 2010.
- [167] M. Hamstad. Frequencies and Amplitudes of AE Signals in a Plate as a Function of Source Rise Time. *29th European Conference on Acoustic Emission Testing, Vienna, Austria*, 2010.
- [168] J. Lee, Y. Kim, H. Kim. Group Velocity of Lamb Wave  $S_0$  Mode in Laminated Unidirectional CFRP Plates. *Key Engineering Materials*, **297-300**, 2213–2218, 2005.

- [169] M. Calomfirescu, A. Herrmann. Attenuation of Lamb Waves in Composites: Models and possible Applications. *Proceedings of the 6th International Workshop on Structural Health Monitoring*, 2007.
- [170] ASTM D 5528-01: Standard Test Method for Mode I Interlaminar Fracture Toughness of Unidirectional Fiber-Reinforced Polymer Matrix Composites. Technical report, ASTM International, 2007.
- [171] D. Schultheiß. *Permeation Barrier for Lightweight Liquid Hydrogen Tanks*. PhD thesis, University of Augsburg, 2007.
- [172] DIN-EN 2563: Determination of the apparent interlaminar shear strength. Technical report, Deutsches Institut für Normung, 1997.
- [173] ASTM E399-09: Standard Test Method for Linear-Elastic Plane-Strain Fracture Toughness  $K_{Ic}$  of Metallic Materials. Technical report, ASTM International, 1997.
- [174] U.S. National Institute of Health. *ImageJ - Image Processing and Analysis in Java*, 2010.
- [175] L. Reimer. *Scanning electron microscopy*. Springer, Berlin, 1985.
- [176] Z. Yu, S. Boseck. Scanning acoustic microscopy and its applications to material characterization. *Reviews of Modern Physics*, **67**:4, 863–891, 1995.
- [177] N. Toyama, T. Okabe. Effect of transverse cracks on lamb wave velocity in CFRP cross-ply laminates. *Journal of Materials Science Letters*, **21**, 271–273, 2002.
- [178] N. Toyama, J. Noda, T. Okabe. Quantitative damage detection in cross-ply laminates using Lamb wave method. *Composites Science and Technology*, **63**, 1473–1479, 2003.
- [179] S. Pierce, W. Philp, B. Culshaw, A. Gachagan, A. McNab, G. Hayward, F. Lecuyer. Surface-bonded optical fibre sensors for the inspection of CFRP plates using ultrasonic Lamb waves. *Smart Materials and Structures*, **5**:6, 776–787, 1996.
- [180] J. Nairn, S. Hu. The Initiation and Growth of Delaminations Induced by Matrix Microcracks in Laminated Composites. *International Journal of Fracture*, **57**, 1–24, 1992.

- [181] *HexFlow RTM6 180° C epoxy system for Resin Transfer Moulding mono-component system - Manufacturers datasheet.*
- [182] *HexPly 914 - Manufacturers datasheet.*
- [183] S. Salpekar, I. Raju, T. O'Brien. Strain Energy Release Rate Analysis of Delamination in a Tapered Laminate Subjected to Tensile Load. *NASA Technical Memorandum*, **102592**, 1–52, 1990.
- [184] M. G. R. Sause, M. Klug, J. Scholler, S. Horn. Anwendung von Muster-erkennungsverfahren zur Schadensanalyse in faserverstärkten Kunststoffen. *DGZfP-BB*, volume 118, pages 9–17, 2009.
- [185] E. Greenhalgh, M. Hiley. Fractography of Polymer Composites: Current Status and Future Issues. *13th European Conference on Composite Materials*, 2008.
- [186] M. G. R. Sause, S. Horn. Schallemissionsanalyse an beschichteten kohlenstofffaserverstärkten Kunststoffen. W. Krenkel, editor, *Verbundwerkstoffe*, pages 474–481. Wiley-VCH, Weinheim, 2009.
- [187] B. Lee, W. Staszewski. Modelling of Lamb waves for damage detection in metallic structures: Part I. Wave propagation. *Smart Materials and Structures*, **12**, 804–814, 2003.
- [188] A. Anastassopoulos, V. Nikolaidis, T. Philippidis. A Comparative Study of Pattern Recognition Algorithms for Classification of Ultrasonic Signals. *Neural Computing & Applications*, **8**, 53–66, 1999.
- [189] A. Puck, M. Mannigel. Physically based stress-strain relations for the inter-fibre-fracture analysis of FRP laminates. *Composites Science and Technology*, **67**:9, 1955–1964, 2007.
- [190] A. Hampe, C. Marotzke. The Energy Release Rate of the Fiber/Polymer Matrix Interface: Measurement and Theoretical Analysis. *Journal of Reinforced Plastics and Composites*, **16**, 341–352, 1997.
- [191] A. Netravali, Z.-F. Li, W. Sachse. Determination of fibre/matrix interfacial shear strength by an acoustic emission technique. *Journal of Materials Science*, **26**, 6631–6638, 1991.
- [192] J.-M. Park, W.-G. Shin, D.-J. Yoon. A study of interfacial aspects of epoxy-based composites reinforced with dual basalt and SiC fibres by means of the fragmentation and acoustic emission techniques. *Composites Engineering Science and Technology*, **59**, 355–370, 1999.

- [193] W. Skopalik. Untersuchung der Bruchzähigkeit von Elektrodengraphit mit Hilfe der Schallemissionsanalyse. Master's thesis, University of Augsburg, 2010.
- [194] T. Köck, W. Skopalik, M. G. R. Sause, S. Horn. Fracture Behavior of Coarse Grain Graphites Investigated by Acoustic-Emission and CT-Analysis. *Annual World Conference on Carbon, Clemson, United States*, 2010.
- [195] H. Middelhoff. Schallemissionsanalyse an keramischen Kompositsystem unter mechanischer Belastung. Master's thesis, University of Augsburg, 2009.
- [196] C. Christner. Verifikation des Monitoringpotentials strukturintegrierter Carbonfasersensoren. Master's thesis, University of Applied Science Munich, 2009.
- [197] T. Müller, A. Horoschenkoff, H. Rapp, M. G. R. Sause, S. Horn. Einfluss von Zwischenfaserbrüchen in 0/90-laminaten auf die elektrische Widerstandsänderung von eingebetteten Carbonfasern. *Deutscher Luft- und Raumfahrtkongress 2010, Hamburg, Germany*, 2010.
- [198] A. Livne, E. Bouchbinder, I. Svetlizky, J. Fineberg. The Near-Tip Fields of Fast Cracks. *Science*, **327**, 1359–1363, 2010.
- [199] B. Hosten. Heterogeneous structure of modes and Kramers-Kronig relationship in anisotropic viscoelastic materials. *Journal of the Acoustic Society of America*, **104**:3, 1382–1388, 1998.
- [200] N. K. Naik, P. S. Shembekar. Elastic Behavior of Woven Fabric Composites: I - Lamina Analysis. *Journal of Composite Materials*, **26**, 2196–2225, 1992.
- [201] P. S. Shembekar, N. K. Naik. Elastic Behavior of Woven Fabric Composites: II - Laminate Analysis. *Journal of Composite Materials*, **26**, 2226–2246, 1992.
- [202] N. Naik, P. Shembekar. Elastic Behavior of Woven Fabric Composites: III - Laminate Design. *Journal of Composite Materials*, **26**, 2522–2541, 1992.
- [203] R. Förster, W. Knappe. Experimentelle und theoretische Untersuchungen zur RiSSbildungsgrenze an zweischichtigen Wickelrohren aus Glasfaser/Kunststoff unter Innendruck. *Kunststoffe*, **61**, 583–588, 1971.

## Bibliography

- [204] R. L. Foye. The transverse poisson's ratio of composites. *Journal of Composite Materials*, **6**, 293–295, 1972.
- [205] A. Kueh, O. Soykasap, S. Pellegrino. Thermo-Mechanical Behavior of Single-Ply Triaxial Weave Carbon Fiber Reinforced Plastic. *Proceedings of European Conference on Spacecraft Structures, Materials & Mechanical Testing, ESA/ESTEC, Noordwijk, The Netherlands*, 2005.
- [206] P. Morgan. *Carbon fibers and their composites*. Taylor & Francis Group, 2005.
- [207] A. Puck. Zur Beanspruchung und Verformung von GFK-Mehrschichtenverbund-Bauelementen. Teil 1. Grundlagen der Spannungs- und Verformungsanalyse. *Kunststoffe 57*, volume 4, pages 284–293, 1967.
- [208] *SIGRAFIL prepreg and SGRATEX prepreg - Manufacturers datasheet*.

# Acknowledgments

I'd like to thank

- **Prof. Dr. S. Horn** for giving me the opportunity to conduct scientific research within the field of acoustic emission science at his chair, for the inspiring discussions and his encouraging support throughout my thesis
- **Prof. Dr. F. Haider** for the possibility to use the laboratory equipment for mechanical testing, the discussions on acoustic emission and for acting as second referee
- **Prof. Dr. M. Hamstad** for the discussions on simulation of acoustic emission signals and for acting as external referee
- **Prof. Dr. A. Horoschenkoff** and **Dipl. Ing. T. Müller** for providing a majority of the customized CFRP specimens
- **Dipl. Ing. M. Klug** and **J. Scholler** from Premium Aerotec for providing the remaining CFRP specimens
- **Dr. D. Schultheiß** from BMW Group “Research and Technology” for providing the coated CFRP specimens
- **Dr. habil. J. Bohse** for the inspiring discussions about acoustic emission analysis on CFRP at several conference meetings
- My colleague **Dr. J. Moosburger-Will** for proof-reading of this thesis
- And **Prof. Dr. U. Eckern**, **Dr. G. Obermeier**, **Dr. M. Klemm**, **Dipl. Phys. M. Krispin**, **Dipl. Phys. A. Santos-Abreu** for proof-reading of the various publications
- All companies who provided supplementary specimens within the scope of this thesis namely **Dr.-Ing. T. Köck** from SGL Group, **Dipl. Ing. H. Vallen** from Vallen Systeme and **Dipl. Ing. C. Wellhausen** from Eurocopter

## *Acknowledgments*

- All PhD, diploma, master and bachelor students, who conducted scientific research within the scope of this thesis, namely **Dipl. Phys. J. Wolfert**, **M. Sc. H. Middelhoff**, **Dipl. Phys. W. Skopalik**, **B. Sc. A. Monden**, **B. Sc. M. Plöckl**, **B. Sc. D. Gyoery**, **B. Sc. M. Parrot** and **Dipl. Ing. C. Christner**
- **Dr. J. Hanss**, **S. Denzer**, **S. Bessel** and **D. Trojak** for specimen preparation, microscopy results and supplementary data
- **A. Hupfer**, **A. Spörhase**, **A. Sturm** and the staff from the “Feinmechanikwerkstatt” for designing and manufacturing last-minute items for mechanical testing
- All members of the chair for experimental physics II which are not already mentioned in personal for the great time and opportunity to work together
- For the financial support provided by the program “Mehrstufige Verfahren zur Herstellung von CFK-Integralstrukturen“
- And finally my parents **B. Sause** and **D. Sause** for the great possibility to study physics and their continuous support in all belongings.

# Curriculum Vitae

## Persönliche Daten:

Name:	Markus Günther Ronny Sause
Geburtsdatum:	14. Oktober 1982
Geburtsort:	Augsburg
Nationalität:	Deutsch

## Berufserfahrung:

Seit 08/2007	Wissenschaftlicher Mitarbeiter am Lehrstuhl für Experimentalphysik II am Institut für Physik der Universität Augsburg
04/2004 - 08/2007	Studentische Hilfskraft am Lehrstuhl für Experimentalphysik II an der Uni Augsburg mit Schwerpunktgebiet Tieftemperaturphysik
10/2000 - 08/2007	Selbständige Tätigkeit im Bereich Entwicklung von Hard- und Software, Webdesign und Beratung, insbesondere Konzeption von Sprachschnittstellen und Applikationsschaltungen für Automationstechnik

## Aus und Weiterbildung:

2002 - 2007	Diplom Physik an der Universität Augsburg
1993 - 2002	Holbein Gymnasium Augsburg
1989 - 1993	Grundschule Augsburg - Inningen



## Publikationen:

1. **Influence of Specimen Geometry on Acoustic Emission Signals in Fiber Reinforced Composites: FEM-Simulations and Experiments.**  
*Markus G. R. Sause and Siegfried Horn*  
Conference Proceedings: 29th European Conference on Acoustic Emission Testing, Vienna, Austria (2010)
2. **Einfluss von Zwischenfaserbrüchen in 0/90-Laminaten auf die elektrische Widerstandsänderung von eingebetteten Carbonfasern.**  
*Tobias Müller, Alexander Horoschenkoff, Helmut Rapp, Markus G. R. Sause und Siegfried Horn*  
Conference Proceedings: Deutscher Luft- und Raumfahrtkongress 2010, Hamburg, Germany (2010)
3. **Fracture Behavior of Coarse Grain Graphites Investigated by Acoustic-Emission and CT-Analysis.**  
*Thomas Köck, Wolfgang Skopalik, Markus G. R. Sause and Siegfried Horn*  
Conference Proceedings: Annual World Conference on Carbon, Clemson, United States (2010)
4. **Simulation of acoustic emission in planar carbon fiber reinforced plastic specimens.**  
*Markus G. R. Sause, Siegfried Horn*  
Journal of Nondestructive Evaluation 29:2 (2010), pp. 123-142  
doi: 10.1007/s10921-010-0071-7
5. **Quantification of metallic coating failure on carbon fiber reinforced plastics using acoustic emission.**  
*Markus G. R. Sause, Ferdinand Haider, Siegfried Horn*  
Surface and Coatings Technology 204:3 (2009), pp. 300-308  
doi: 10.1016/j.surfcoat.2009.07.027
6. **Anwendung von Mustererkennungsverfahren zur Schadensanalyse in faserverstärkten Kunststoffen.**  
*M. G. R. Sause, M. Klug, J. Scholler und S. Horn*  
DGZfP-BB 18 (2009), pp. 9-17
7. **Visualisierung von Schallemissionslokalisierungen.**  
*W. Skopalik, T. Köck, M. G. R. Sause und S. Horn*  
DGZfP-BB 18 (2009), pp. 62-69

8. **Schallemissionsanalyse an beschichteten kohlenstofffaserverstärkten Kunststoffen.**

*Markus G. R. Sause und Siegfried Horn*

in: Verbundwerkstoffe, W. Krenkel (Hrsg.), Viley-VCH, Weinheim, (2009)  
pp. 474-481

9. **Acoustic emission investigation of coating fracture and delamination in hybrid carbon fiber reinforced plastic structures.**

*Markus G. R. Sause, Daniel Schultheiß and Siegfried Horn*

Journal of Acoustic Emission 26 (2008) pp. 1-13



**mbv**berlin | 59,00 Euro  
ISBN: 978 3 86664 889 0



9 783866 648890 >

